

**A SEMI-PASSIVE THERMAL MANAGEMENT SYSTEM  
FOR TERRESTRIAL AND SPACE APPLICATIONS**

**by**

**Sven du Clou**

In fulfillment of the academic requirements for the degree of Master of Science in Mechanical Engineering, College of Agriculture, Engineering and Science, University of KwaZulu-Natal

Supervisor: Mr. Michael J. Brooks

Co-supervisor: Prof. Lance W. Roberts

January 2013

## DECLARATION 1 - PLAGIARISM

I, ....., declare that

1. The research reported in this thesis, except where otherwise indicated, is my original research.
2. This thesis has not been submitted for any degree or examination at any other university.
3. This thesis does not contain other persons' data, pictures, graphs or other information, unless specifically acknowledged as being sourced from other persons.
4. This thesis does not contain other persons' writing, unless specifically acknowledged as being sourced from other researchers. Where other written sources have been quoted, then:
5. Their words have been re-written but the general information attributed to them has been referenced
6. Where their exact words have been used, then their writing has been placed in italics and inside quotation marks, and referenced.
7. This thesis does not contain text, graphics or tables copied and pasted from the Internet, unless specifically acknowledged, and the source being detailed in the thesis and in the References sections.

Signed:

.....

Mr. Sven du Clou

As the candidate's supervisor I have approved this dissertation for submission.

Signed:

.....

Mr. Michael J. Brooks

As the candidates co-supervisor I have approved this dissertation for submission.

Signed:

.....

Prof. Lance W. Roberts

## DECLARATION 2 - PUBLICATIONS

1. du Clou, S.\*, Brooks, M.J., Lear, W.E., Sherif, S.A., Khalil, E.E., Pulsed Ejector Cooling System, *10<sup>th</sup> International Energy Conversion Engineering Conference*, American Institute of Aeronautics and Astronautics, Atlanta, Georgia, USA, July 2012
2. du Clou, S.\*, Brooks, M.J., Lear, W.E., Sherif, S.A., Khalil, E.E., An Ejector Transient Performance Model for Application in a Pulse Refrigeration System, *9<sup>th</sup> International Energy Conversion Engineering Conference*, American Institute of Aeronautics and Astronautics, San Diego, California, USA, July 2011
3. du Clou, S.\*, Brooks, M.J., Bogi, B., Lear, W.E., Sherif, S.A., Khalil, E.E., Modeling of Transient Ejector Performance with Application to a Pulse Refrigeration System, *8<sup>th</sup> International Energy Conversion Engineering Conference*, American Institute of Aeronautics and Astronautics, Nashville, Tennessee, USA, July 2010
4. Brooks, M.J.\*, du Clou, S., Mhlongo, M., Olivier, J.P., Lear, W.E., Sherif, S.A., Pulse-Driven Refrigeration: Progresses and Challenges, *7<sup>th</sup> International Energy Conversion Engineering Conference*, American Institute of Aeronautics and Astronautics, Denver, Colorado, USA, August 2009
5. du Clou, S.\*, Brooks, M.J., Roberts, L.W., Design of a Solar-Driven Ejector Cooling System, *Second Postgraduate Renewable Energy Symposium*, Centre for Renewable and Sustainable Energy Studies, Lynedoch, Cape Town, South Africa, November 2011
6. du Clou, S.\*, Brooks, M.J., Roberts, L.W., Solar-Driven Thermal Management Research at UKZN, *First Postgraduate Renewable Energy Symposium*, Centre for Renewable and Sustainable Energy Studies, Lynedoch, Cape Town, South Africa, November 2010

\* Primary author

Signed:

.....

Sven du Clou

## ACKNOWLEDGEMENTS

I would like to thank my primary supervisor, Michael Brooks, for his excellent guidance, personal encouragement and understanding during my studies. I am grateful for his assistance and technical expertise.

Thank you to the academic and the workshop staff at the School of Mechanical Engineering for their willing assistance during my studies. My fellow Aerospace Systems Research Group (ASReG) and Sustainable Energy Research Group (SERG) colleagues have assisted in experiments and contributed to technical discussions.

I greatly appreciate the contribution of the co-authors to the various publications that have resulted from this research. This includes Michael Brooks and Prof. Lance Roberts of UKZN, Dr. William Lear, Dr. S.A. Sherif, and Bhageerath Bogi of the University of Florida, and last but not least Dr. Essam Khalil of Cairo University.

I wish to thank the Centre for Renewable and Sustainable Energy Studies at Stellenbosch University for supporting this research.

My family has always encouraged me, and without their support this work would not have been possible. My Oupa has always been there for me, providing a wealth of technical advice. Last but certainly not least, I would like to express my heartfelt appreciation to my partner, Tamryn, for her love and support throughout my academic career.

## ABSTRACT

In this study a semi-passive pulse thermal loop (PTL) was designed and experimentally validated. It provides improved heat transfer over passive systems such as the loop heat pipe in the moderate to high heat flux range and can be a sustainable alternative to active systems as it does not require an electric pump. This work details the components of the engineering prototype and characterizes their performance through the application of compressible and two-phase flow theory. A custom LabVIEW application was utilized for data acquisition and control. During operation with refrigerant R-134a the system was shown to be robust under a range of heat loads from 100 W to 800 W. Operation was achieved with driving pressure differentials ranging from 3 bar to 12 bar and pulse frequencies ranging from 0.42 Hz to 0.08 Hz. A smaller pressure differential and an increased pulse frequency results in improved heat transfer at the boilers.

An evolution of the PTL is proposed that incorporates a novel, ejector-based pump-free refrigeration system. The design of the pulse refrigeration system (PRS) features valves at the outlet of two PTL-like boilers that are alternately actuated to direct pulses of refrigerant through an ejector. This is intended to entrain and raise the pressure of a secondary stream of refrigerant from the cooling loop, thereby replacing the compressor in a conventional vapor-compression cycle. The PRS is therefore characterized by transient flow through the ejector. An experimental prototype has been constructed which is able to operate as a conventional PTL when the cooling section is bypassed, although full operation of the refrigeration loop remains to be demonstrated. The design of the ejector is carried out using a one-dimensional model implemented in MATLAB that accounts for compressibility effects with NIST REFPROP vapor data sub-routines. The model enables the analysis of ejector performance in response to a transient pressure wave at the primary inlet.

The high driving pressures provided by the PTL permit operation in a micro-gravity environment with minimal power consumption. Like the PTL, the proposed PRS is therefore well suited to terrestrial and aerospace applications where it could be driven by waste heat from electronics or solar thermal energy. As a novel semi-passive thermal management system, it will require complex control of the valves. Further analysis of the transient thermodynamic cycle is necessary in order to characterize and effect successful operation of the PRS.

# CONTENTS

DECLARATION 1 - PLAGIARISM.....	i
DECLARATION 2 - PUBLICATIONS .....	ii
ACKNOWLEDGEMENTS .....	iii
ABSTRACT.....	iv
CONTENTS.....	v
LIST OF FIGURES.....	ix
LIST OF TABLES .....	xix
LIST OF SYMBOLS .....	xx
1 INTRODUCTION.....	1
1.1 The pulse thermal loop .....	1
1.2 The pulse refrigeration system.....	2
2 REVIEW OF SPACECRAFT AND TERRESTRIAL THERMAL MANAGEMENT ....	5
2.1 The space environment .....	5
2.2 History of spacecraft thermal management .....	5
2.3 Future missions.....	7
2.4 Technology drivers .....	7
2.5 Types of thermal management systems .....	8
2.5.1 Passive technologies.....	8
2.5.2 Active technologies.....	11
2.5.3 Niche area of research.....	13
2.6 Pulse thermal loop (PTL) review.....	13
2.6.1 PTL cycle description .....	13
2.6.2 PTL advantages.....	16
2.6.3 PTL development history .....	17
2.7 Pulse refrigeration system (PRS) review .....	21
2.7.1 Vapor-compression refrigeration .....	21
2.7.2 Ejector cooling systems (ECS).....	22
2.7.3 PRS concept development.....	27
2.7.4 PRS for terrestrial applications .....	29
3 PULSE THERMAL LOOP DESIGN.....	31
3.1 PTL design.....	31
3.2 Refrigerant selection.....	33

3.3	Boiler design.....	33
3.3.1	Boiler block material.....	34
3.3.2	Sight glass window .....	35
3.3.3	Boiler stress computational analysis .....	36
3.3.4	Boiler valves and instrumentation.....	38
3.4	Refrigerant charging cylinder .....	41
3.5	Condenser design.....	42
3.5.1	Application of concentric tube heat exchanger theory.....	42
3.5.2	Condenser analytical model .....	45
3.5.3	Condenser model results .....	46
3.5.4	Final condenser design.....	49
3.5.5	Condenser assembly.....	50
3.6	Adiabatic transfer lines (VTL and LRL) .....	51
3.7	System head losses.....	52
3.8	Final assembly .....	53
3.9	Instrumentation uncertainty .....	54
4	CONTROL SYSTEM.....	55
4.1	$\Delta P$ control features.....	55
4.2	$\Delta P$ control logic .....	56
4.3	Servo control with PWM .....	58
4.4	Heater power control with PWM.....	59
4.5	Hardware.....	59
4.5.1	Power supply.....	59
4.5.2	DAQ chassis and modules.....	59
4.5.3	Instrumentation .....	60
4.6	Summary.....	60
5	PULSE THERMAL LOOP PERFORMANCE.....	61
5.1	Experimental procedure.....	61
5.1.1	Evacuating procedure.....	61
5.1.2	Charging procedure .....	61
5.1.3	Start-up procedure.....	64
5.1.4	Steady-state operation .....	65
5.1.5	Shut-down procedure .....	65
5.2	Experimental results .....	65
5.2.1	PTL - ideal start-up .....	65
5.2.2	PTL - non-ideal start-up .....	66

5.2.3	PTL – asymmetric operation.....	68
5.2.4	PTL – varied $\Delta P_{set}$ .....	70
5.2.5	PTL – varied heater power input.....	77
5.3	Summary.....	79
6	PULSE REFRIGERATION SYSTEM PROTOTYPE.....	80
6.1	Ejector theory.....	81
6.2	Ejector literature.....	83
6.2.1	Nozzle.....	84
6.2.2	Suction chamber.....	86
6.2.3	Constant area chamber.....	87
6.2.4	Diffuser.....	87
6.3	Governing equations of the ejector analytical model.....	88
6.4	Steady-state ejector design model.....	90
6.4.1	Design model validation.....	91
6.4.2	Design model results.....	93
6.5	Transient ejector nozzle performance model.....	95
6.5.1	Transient model validation.....	97
6.5.2	Transient model results.....	99
6.5.3	Optimizing ejector geometry.....	100
6.6	PRS components.....	103
6.6.1	Expansion valve.....	103
6.6.2	The ejector.....	104
6.7	PRS variants.....	105
6.8	PRS experimental results.....	107
6.8.1	Unsteady PRS operation.....	107
6.8.2	Steady PRS operation.....	109
6.9	Summary.....	112
7	CONCLUSION.....	114
	REFERENCES.....	117
	APPENDIX.....	124
A.	TABLES.....	124
B.	CALCULATIONS.....	134
B.1.	Boiler design.....	134
B.2.	System head loss.....	138
B.3.	System charge mass.....	141



B.4.	Condenser performance .....	143
B.5.	Effectiveness NTU method.....	144
C.	DRAWINGS.....	145
D.	DATA ACQUISITION SOFTWARE AND HARDWARE .....	154
D.1.	LabVIEW GUI.....	154
D.2.	DAQ chassis and modules .....	155
D.3.	VI diagrams .....	156
E.	PHOTOGRAPHY .....	160
F.	MATLAB SCRIPT FILES .....	(On disk)
G.	VIDEO.....	(On disk)

## LIST OF FIGURES

Figure 2.1	Schematic of a simple constant conductance heat pipe. ....	9
Figure 2.2	Schematic of a capillary pumped loop (CPL) [17]. Loop operation is limited to the pump capacity of the capillary wick. ....	10
Figure 2.3	Schematic of a loop heat pipe (LHP) [6]. The design is similar to a CPL other than the CC that is incorporated before the evaporator. ....	11
Figure 2.4	Schematic of a mechanically-pumped fluid loop. ....	12
Figure 2.5	Conceptual map of thermal control system applications showing niche research area [18] for where the PTL and the PRS are being developed. ....	13
Figure 2.6	Schematic of the pulse thermal loop [3]. Heat is transferred from the source to the sink by sequentially isolating, pressurizing and pulsing refrigerant around the loop using multiple boilers. ....	14
Figure 2.7	Upper diagrams (a, b, c and d) describe PTL operation. The lower graph (e) shows a typical experimental pressure trace of a PTL operating with $\Delta P_{set}$ of 10 bar. ....	15
Figure 2.8	Top view photograph of Weislogel's prototype PTL #1 [3]. The design includes two thermally decoupled constant volume evaporators, a 3-way valve, a condenser, flow restrictors and check valves. ....	18
Figure 2.9	Micro-PTL [20]. This 10 cm <sup>3</sup> PTL includes two 3.5 cm <sup>3</sup> evaporators and is predicted to transfer up to 200 W of thermal energy. ....	19
Figure 2.10	PTL developed by Brooks <i>et al.</i> [4] consisting of two thermally decoupled boilers. The loop is capable of dissipating heat up to 800 W with $\Delta P_{set}$ up to 8 bar. ....	19
Figure 2.11	PTL developed by du Clou <i>et al.</i> [21]. The inner loop included the components required to test the PRS concept, but this was not demonstrated. ....	20
Figure 2.12	Schematic of a compressor-driven vapor-compression refrigeration system. ....	22

Figure 2.13	Temperature - entropy diagram for vapor-compression refrigeration. [24].....	22
Figure 2.14	Schematic of an ejector cooling system (ECS).....	23
Figure 2.15	Temperature - Entropy diagram for an ECS.....	24
Figure 2.16	Thermally pumped ECS investigated by Huang <i>et al.</i> [36]. The system relies on a 1.8 m gravity head and intermittent cooling of the generator tanks.....	27
Figure 2.17	Solar integrated thermal management and power (SITMAP) system [25].....	27
Figure 2.18	Schematic of PRS. Pulses from the PTL boilers are directed through the ejector cooling loop. ....	28
Figure 2.19	Temperature - Entropy diagram for the PRS.....	29
Figure 3.1	The assembled PTL including thermally coupled boilers, a VTL, a condenser, and a LRL. Flow in an anti-clockwise direction is controlled through the use of check valves and a 3-way servo valve. Two VTL lengths were investigated.....	31
Figure 3.2	Complete PTL boiler section including valves and instrumentation.....	34
Figure 3.3	Sight glass windows (a) threaded end cap, and (b) flat gauge glass.....	35
Figure 3.4	Mesh applied to boiler block before simulation. Arrows indicate the applied bolt forces and the internal pressures.....	37
Figure 3.5	Von Mises analysis of boiler block showing a maximum stress of 22.35 MPa, at the minimum cross-section.....	37
Figure 3.6	Safety Factor contour plot of the boiler block showing a minimum of 11.18.....	37
Figure 3.7	Displacement analysis of the boiler block showing a maximum of 0.0025 mm.....	38
Figure 3.8	(a) Poppet check valve and, (b) lift check valve [52,53].....	39
Figure 3.9	3-Way valve operation [54].....	39
Figure 3.10	3-Way servo valve assembly.....	40

Figure 3.11 Refrigerant charging cylinder includes a pressure gauge and a thermocouple. It allows for accurate measurement of the mass of refrigerant with which the system is charged. ....	41
Figure 3.12 A double pipe heat exchanger setup in (a) parallel flow and (b) counter flow arrangement with the corresponding temperature profile plots [47,58].....	42
Figure 3.13 Concentric tube annulus showing inner and outer tube diameters .....	43
Figure 3.14 Pseudo-code flow chart for the analytical model of the PTL condenser. ....	46
Figure 3.15 Condenser annulus diameter vs. Reynolds number. Increased fluid viscosity results in a lower Reynolds number. ....	48
Figure 3.16 Condenser annulus diameter vs. condenser length. Increased fluid viscosity results in a longer condenser length requirement. ....	48
Figure 3.17 Condenser annulus diameter vs. annulus flow velocity. The velocity profiles are similar due to the different fluids having similar saturated liquid densities. ....	49
Figure 3.18 Concentric tube counter-flow condenser design.....	49
Figure 3.19 Concentric tube condenser inlet manifold with the hot and cold fluid inlet and exit thermocouples and the VTL check valve.....	50
Figure 3.20 LRL components including necessary valves and instrumentation.....	52
Figure 4.1 Control hardware for PRS experimental prototype. ....	55
Figure 4.2 Instrument locations for the PTL and PRS. Other variants were investigated incorporating the same instruments.....	57
Figure 4.3 Schematic of $\Delta P$ control logic for manual, PTL and PRS operation.....	58
Figure 4.4 PWM signals with different duty cycles.....	58
Figure 5.1 Schematic of refrigerant mass distribution before a 16 bar pulse with a $\Delta P_{set}$ of 8 bar. [16] .....	62

Figure 5.2	Charging cylinder connected to the boiler using quick connects. The ball valves are opened to fill the boilers with refrigerant. ....	63
Figure 5.3	Boiler liquid level viewed through the sight glass.....	63
Figure 5.4	Ideal PTL start-up pressure and temperature response. Short VTL with $x = 0.65$ , $Q = 500$ W and $TWI = 20^\circ\text{C}$ . After initiating pulses with a $\Delta P_{set}$ of 4 bar, the average boiler pressure reduced from 24 bar to 12.5 bar, and temperature reduced from $80^\circ\text{C}$ to $54^\circ\text{C}$ .....	66
Figure 5.5	PTL start-up from a low $\Delta P_{set}$ of 1 bar. ....	67
Figure 5.6	PTL start-up with high charge mass. Large VTL with $x = 0.52$ , $Q = 500$ W and $TWI = 15^\circ\text{C}$ . The system pressure increases, and the test is aborted. ....	67
Figure 5.7	PTL start-up with low charge mass. Large VTL with $x = 0.79$ , $Q = 300$ W and $TWI = 15^\circ\text{C}$ . The boiler temperature increases, and the test is aborted. ....	68
Figure 5.8	Asymmetric pulsing. Small VTL with $x = 0.65$ , $Q = 400$ W and $TWI = 20^\circ\text{C}$ . The macro view shows the temperature and pressure response to $\Delta P$ feedback control. The boiler containing the lesser mass ( $P1$ ) is intermittently pulsed at a lower $\Delta P_{set}$ forcing less R-134a into the alternate boiler ( $P2$ ). Operation becomes more symmetric. ....	70
Figure 5.9	Typical pressure and temperature history as a function of $\Delta P$ control. Large VTL with $x = 0.64$ , $Q = 500$ W and $TWI = 15^\circ\text{C}$ . Although pulse detail is lost, the macro view highlights how the boiler temperature reduces from $60^\circ\text{C}$ to $45^\circ\text{C}$ with a reduction in $\Delta P_{set}$ from 10 bar to 4 bar. ....	71
Figure 5.10	Frequency and temperature response to $\Delta P_{set}$ . Large VTL with $x = 0.64$ , $Q = 500$ W and $TWI = 15^\circ\text{C}$ . (a) $\Delta P_{set} = 10$ bar, (b) $\Delta P_{set} = 4$ bar.....	72
Figure 5.11	$\Delta P_{set}$ vs. $f$ and $TB$ . Large VTL with $x = 63.72\%$ , $Q = 500$ W and $TWI = 15^\circ\text{C}$ . ....	73
Figure 5.12	Frequency vs. $\Delta P_{set}$ for a range of heat inputs, charge mass and VTL size.....	74

Figure 5.13 Block temperature vs. $\Delta P_{set}$ for a range of heat inputs, charge mass and VTL size. ....	74
Figure 5.14 Average condenser heat transfer vs. $\Delta P_{set}$ for a range of heat inputs, charge mass and VTL size. ....	74
Figure 5.15 Frequency vs. $\Delta P_{set}$ performance map including results from the literature [16,4]. The operating envelope is indicated by the dashed lines and can be used to design a PTL for a particular application. Increased $Q$ improves the circulation limit, the pulse limit and $f$ . ....	76
Figure 5.16 $TB$ vs. $\Delta P_{set}$ performance map including results from the literature [16]. ....	76
Figure 5.17 Power input ( $Q$ ) vs. boiler temperature ( $TB$ ) for varied $\Delta P_{set}$ . ....	78
Figure 5.18 Power input ( $Q$ ) vs. pulse frequency ( $f$ ) for varied $\Delta P_{set}$ . ....	78
Figure 5.19 Power input ( $Q$ ) vs. average condenser heat transfer for varied $\Delta P_{set}$ . ....	78
Figure 6.1 Ejector schematic. The primary flow expands in the CD nozzle and entrains a secondary flow. Pressure is recovered with a normal shock wave during steady operation. [59]. ....	81
Figure 6.2 Ejector operating modes dependant on the driving pressure ratio, $\phi$ . [63] ....	82
Figure 6.3 PTL pulse showing anticipated ejector driving pressure ratio ( $\phi$ ) increasing to unity within 2 s as the pulse pressure ( $P_2$ ) falls to meet the lower condenser pressure ( $P_c$ ). ....	83
Figure 6.5 Pseudo-code flow chart for the ejector design model. [78] ....	91
Figure 6.6 The design model area ratios are compared to the experimental results of Huang <i>et al.</i> [63]. The model shows good agreement with the experimental results. ....	92
Figure 6.7 The design model area ratio results are compared with the results from the model developed by Huang <i>et al.</i> [63]. The models are directly proportional but are offset by a constant term. ....	92
Figure 6.8 Ejector geometry designs for a range of steady inlet stagnation pressures. [78]. ....	94

Figure 6.9	Static pressure plot at different cross-section locations (diameter) along the ejector axis. The vertical lines represent normal shock waves in the constant area section. (100 kPa = 1 bar). [78] .....	94
Figure 6.10	Static pressure and Mach number profiles along the ejector axis (100 kPa = 1 bar) for varied input stagnation pressure. [78] .....	95
Figure 6.11	Transient performance logic flow chart for the analysis of unsteady flow through an ejector CD nozzle. [78].....	96
Figure 6.12	Static pressure at different nozzle locations during transient blow-down. The real gas solution (solid lines) is compared with the ideal gas solution (dotted lines) from Equations 6.16 and 6.22. The error ranges from 3.0% to 12%. [78] .....	98
Figure 6.13	Mach number for different nozzle locations during the transient blow-down. The real gas solution (solid line) is compared with the ideal gas solution (dotted line) from Equation 6.17. The error reduces from 12% to 1%. [78] .....	98
Figure 6.14	Choked mass flow rate reduces as the boiler empties. The real gas solution (solid line) is compared with the ideal gas solution (dotted line) from Equation 6.20. The error reduces from 11% to 1%. [78].....	98
Figure 6.15	Operating modes of a CD nozzle (0.9 mm to 1.4 mm) during 3 second blow-down, indicating transient oblique and normal shocks. [59] .....	100
Figure 6.16	Mach number at different locations in the CD nozzle in response to the 3 second transient blow-down. [59].....	100
Figure 6.17	Mach number profiles for different ejector nozzle geometries (a) $D_e = 0.9$ mm, (b) $D_e = 1.1$ mm, and (c) $D_e = 1.3$ mm. [59].....	102
Figure 6.18	Periods of supersonic and subsonic flow for different CD nozzle exit diameters, and constant throat diameter of 0.9 mm. ....	102
Figure 6.19	Operating modes of a CD nozzle (0.9 mm to 1.1 mm) during 3.1 second blow-down, indicating transient oblique and normal shocks.....	103
Figure 6.20	Expansion valve and evaporator tube in the ejector cooling loop. ....	104

Figure 6.21 Ejector installed with pressure transducers and thermocouples .....	104
Figure 6.22 PRS variant I integrates a VTL bypass which enables normal PTL operation. Valve 2 is actuated to direct pulses of refrigerant through the ejector cooling loop during PRS operation.....	105
Figure 6.23 Schematic of PRS variant II. The second 3-way valve is located in the LRL.....	106
Figure 6.24 PRS variant II includes a 3-way valve in the LRL and no VTL bypass loop.....	107
Figure 6.25 PRS variant I where operation is switched from PTL to PRS mode. $Q = 300$ W, $x = 0.67$ , $TWI = 15^{\circ}\text{C}$ . The system stalls within 3 pulses. The trend indicates a low charge mass. The initial pulse with $\Delta P_{set} = 7.5$ bar provides compression ( $PJ3$ - $PJ2$ ) to the secondary inlet of 0.4 bar. ....	108
Figure 6.26 PRS variant I, operating with unsteady pulses and decreasing $\Delta P_{set}$ , increasing in temperature and about to stall. Pulses are diverted through the VTL bypass at 4220 s to reduce boiler block temperature. This highlights the importance of having a bypass loop in the PRS.....	109
Figure 6.27 PRS variant II operation with $x = 0.68$ . The system is both condenser and pressure limited, indicating a low charge mass. The initial pulse with $\Delta P_{set} = 11.5$ bar results in 1 bar compression ( $PJ3$ - $PJ2$ ) of the secondary stream.....	109
Figure 6.28 Steady (asymmetric) operation of variant II results in asymmetric compression of the secondary inlet to the ejector. $\Delta P_{set} = 9$ bar to 11 bar, $x = 55\%$ , $TWI = 15^{\circ}\text{C}$ .....	110
Figure 6.29 Low $\Delta P$ pulsing through ejector of variant II results in uneven compression. $\Delta P_{set} = 4.2$ bar, $x = 55\%$ , $TWI = 15^{\circ}\text{C}$ .....	111
Figure 6.30 $\Delta P_{set}$ vs. Frequency for three PRS tests. Two PTL curves are superimposed for comparison. The inversely proportional relationship is characteristic of a PTL pumped system. ....	112
Figure 6.31 $\Delta P_{set}$ vs. Compression achieved by the ejector. Compression increases with $\Delta P_{set}$ . ....	112



Figure A.1	Temperature vs. Entropy diagrams for a) a wet vapor refrigerant, and b) a dry vapor refrigerant. A wet vapor refrigerant has a negative slope saturated vapor line. As it undergoes isentropic expansion, it passes through the two-phase region and condensed bubbles form in the vapor flow. The vapor may be superheated to avoid this. A dry vapor refrigerant has a positive slope saturated vapor line. It remains a superheated vapor during expansion.....	129
Figure A.2	Nusselt number for laminar flow tabulated values curve fit approximation, used in the condenser analytical model, Equation 3.16.....	131
Figure B.1	(a) Soft clamped members with a rigid bolt, and (b) bolt force diagram used to calculate initial tightening force ( $F_i$ ). [50].....	135
Figure B.2	Cut-away cross section of boiler chamber showing sight glass cavity detail .....	137
Figure C.1	Boiler block design (a) top view and (b) isometric view.....	145
Figure C.2	Cross-sectioned isometric view of the boilers showing the minimum thickness where the maximum stress occurs .....	145
Figure C.3	Boiler block machine drawing.....	146
Figure C.4	Boiler block glass cover plate machine drawing .....	147
Figure C.5	Servo valve bracket.....	148
Figure C.6	Tube from boiler outlet to the 3-way valve .....	149
Figure C.7	Condenser inlet manifold.....	150
Figure C.8	Condenser return manifold .....	151
Figure C.9	Ejector body (design).....	152
Figure C.10	Ejector nozzle .....	153
Figure D.1	LabVIEW GUI. The tabbed control is used to select manual, PTL, or PRS operating modes. $\Delta P_{set}$ and $Q$ can be varied on demand. The application .VI is available on the included disk.....	154

Figure D.2	NI module connections and DAQ chassis. ....	155
Figure D.3	Generate 200 Hz frequency signal for servo 1 with a 30% duty cycle from the NI 9474 module counter, and start the task. This is repeated for servo 2. ....	156
Figure D.4	Manual servo control with user defined duty cycle. The sub-VI writes the task to the output channel. The logic computes the alternative servo position ( $\pm 90^\circ$ ) which is used in the PTL and PRS automated control logic. This is repeated for servo 2. ....	156
Figure D.5	PTL automated valve toggling. Writes the new position to the output task and computes the alternative position. The embedded loop only executes when the input is true, ( $\Delta P > \Delta P_{set}$ ). ....	156
Figure D.6	PRS automated valve toggling for variant I, using a flat sequence structure. There are four steps to the sequence when the input condition is true; i) actuate second servo valve to ejector loop, ii) a small time delay is imposed, iii) actuate the boiler servo valve to pulse refrigerant through the ejector loop, iv) a small time delay is imposed and, v) actuate ejector servo valve to allow the latter portion of the pulse to pass through the VTL bypass. The same case structure is applied to variant II with steps i and iii swapped. ....	157
Figure D.7	Tabbed control is manually selected on the front panel to enable manual, PTL automated or PRS automated operation. The logic structure is used to determine which operating mode is selected. The included switch and wait tabs prevent unwanted valve cycling since $\Delta P$ may not reduce before the next iteration causing the valve to cycle unnecessarily. ....	157
Figure D.8	The start task acquires and initializes the signals from the DAQ modules. A spreadsheet file is created, opened, and the column labels are assigned. The file is left open to improve the loop iteration speed. ....	158
Figure D.9	Measurement loop. The data are unbundled, displayed, and written to a spreadsheet file at a frequency of 10 Hz. ....	158
Figure D.10	Fail-safe logic. The pressure and temperature limits are compared with the real-time measurements. If the output logic is true, the heaters are turned off. ....	159

Figure D.11 The stop button terminates the loop. The tasks are cleared and the spreadsheet file is closed .....	159
Figure D.12 Software generated PWM loop for the heater power control .....	159
Figure E.1 Photographs of nominal refrigerant injection, boiling and pulsing. Flow is from right to left. Video of this process is given on the disk in Appendix G .....	160
Figure E.2 Photographs of refrigerant injection, boiling and pulsing with excess mass. Flow is from left to right. Video of this process is given on the disk in Appendix G. ....	161
Figure E.3 Pull down resistor of 10 k $\Omega$ grounds floating signals present in PWM.....	162

## LIST OF TABLES

Table 3.1	User defined parameters for the condenser design and selected results. [59].....	47
Table 3.2	System component guideline volumes based on reported ratios. ....	51
Table 5.1	Average and local heat flux compared with the theoretical maximum .....	77
Table A.1	Comparison of various thermal management technologies for space applications.....	125
Table A.2	Comparison of different PTL designs.....	126
Table A.3	Pair-wise comparison of the project requirements giving relative importance .....	127
Table A.4	Quality Function Development technique for ranking engineering requirements .....	128
Table A.5	Refrigerant comparison [22,82].....	129
Table A.6	Specifications of candidate materials for boiler block.....	130
Table A.7	3-Way valve specifications [53,54].....	130
Table A.8	Servo specifications (HS-7980 TH Monster Torque) [55] .....	130
Table A.9	Tabulated Nusselt numbers for laminar flow in an annulus [46].....	131
Table A.10	Comparison of ejector geometries from the literature .....	132
Table A.11	Control hardware specifications .....	133
Table B.1	List of fittings and loss coefficients in vapor portion [6,57].....	139
Table B.2	List of fittings and loss coefficients in liquid portion [6,57] .....	140

## LIST OF SYMBOLS

### Nomenclature

$A$	Area	[m <sup>2</sup> ]
$a$	Sonic velocity	[m/s]
$C_p$	Specific heat at constant pressure	[kJ/kg.K]
$C_v$	Specific heat at constant volume	[kJ/kg.K]
$C_v$	Flow coefficient	
$D_h$	Hydraulic diameter	[m]
$D$	Diameter	[m]
$F_i$	Bolt tightening force	[N]
$f$	Friction factor	
	Pulse frequency	[Hz]
$h$	Convection heat transfer coefficient	[W/m <sup>2</sup> .K]
	Enthalpy	[kJ/kg]
$h_f$	Major head loss	[m]
$h_{lm}$	Minor head loss	[m]
$h_T$	Total head loss	[m]
$k$	Thermal conductivity of material or fluid	[W/m.K]
$I$	Current	[Amp]
$ID_a$	Inner diameter annulus	[m]
$ID_t$	Inner diameter tube	[m]
$L$	Length	[m]
$M$	Mach number	
	Modulus of Rupture (MOR strength)	[MPa]
$\dot{m}$	Mass flow rate	[g/s]
$Nu$	Nusselt number	
$NXP$	Nozzle exit position inside ejector	[m]
$OD_a$	Outer diameter annulus	[m]
$OD_t$	Outer diameter tube	[m]
$P$	Absolute Pressure (1 bar = 10 <sup>5</sup> Pa)	[bar]
$P1$	Absolute pressure in boiler 1	[bar]
$P2$	Absolute pressure in boiler 2	[bar]
$PJ1$	Absolute pressure at the ejector primary inlet	[bar]
$PJ2$	Absolute pressure at the ejector secondary inlet	[bar]
$PJ3$	Absolute pressure at the ejector exit	[bar]

$P_R$	Back pressure ratio across CD nozzle, $P_1/P_{p0}$	[bar]
$P_w$	Wetted perimeter in annulus tube flow	[m]
$Q$	Power or heat input	[W]
$Q_{in}$	Heat input	[W]
$Q_{out}$	Heat removed	[W]
$q$	Heat transfer rate	[W]
$q''$	Heat flux	[W/cm <sup>2</sup> ]
$Re$	Reynolds number	
$r$	Radius	[m]
$T$	Temperature	[°C]
$TB$	Temperature of the boiler block	[°C]
$TC1$	Temperature of refrigerant at condenser inlet	[°C]
$TC2$	Temperature of refrigerant at condenser outlet	[°C]
$T_i$	Bolt tightening torque	[N.m]
$TW1$	Temperature of cooling fluid at condenser inlet	[°C]
$TW2$	Temperature of cooling fluid at condenser outlet	[°C]
$t$	Thickness	[m]
$U$	Overall heat transfer coefficient	[W/m <sup>2</sup> .K]
$V$	Velocity	[m/s]
	Volume	[cm <sup>3</sup> ]
$x$	Vapor quality (or fraction)	
$x1$	Vapor quality in boiler 1	
$x2$	Vapor quality in boiler 2	

### Greek Symbols

$\Delta P$	Pressure differential between boiler and condenser	[bar]
$\Delta P_{set}$	Set pressure differential at which the valves toggle	[bar]
$\Delta T_{lm}$	Logarithmic mean temperature difference	
$\delta$	Displacement	[m]
$\varepsilon$	Emittance	
$\eta_h$	Efficiency of heat engine	
$\mu$	Kinematic viscosity	[N.s/m <sup>2</sup> ]
$\rho$	Density	[kg/m <sup>3</sup> ]
$\sigma$	Stress	[MPa]
	Stefan-Boltzmann constant ( $5.669 \times 10^{-8}$ W/m <sup>2</sup> .K <sup>4</sup> )	
$\varphi$	Ejector driving pressure ratio, $P_c/P_{p0}$	

$\psi$	Ejector compression ratio, $P_c/P_{s0}$
$\omega$	Entrainment ratio, $\dot{m}_s/\dot{m}_p$
$\eta_{is}$	Isentropic efficiency

### Subscripts

<i>ave</i>	Average
<i>c,i</i>	Cold fluid at condenser inlet
<i>c,o</i>	Cold fluid at condenser outlet
<i>e</i>	Converging diverging nozzle exit
<i>h,i</i>	Hot fluid at condenser inlet
<i>h,o</i>	Hot fluid at condenser outlet
<i>i</i>	Inner tube surface
<i>is</i>	Isentropic property
<i>m</i>	Ejector mix section
<i>o</i>	Outer tube surface
<i>p</i>	Ejector primary inlet
<i>s</i>	Ejector secondary inlet
<i>t</i>	Converging-diverging nozzle throat property
<i>x</i>	Before shock
<i>y</i>	After shock, or yield
<i>0</i>	Total stagnation property
<i>l</i>	Position in ejector, downstream of CD nozzle before mix

### Superscripts

*	Critical point
”	Inches (1 inch = 25.4 mm)

### Abbreviations

AU	Astronomical unit $\sim 149.6 \times 10^6$ km
CD	Converging-diverging nozzle
COP	Coefficient of performance
COP <sub>o</sub>	Overall coefficient of performance
CPL	Capillary-pumped loop
ECS	Ejector-based cooling system

GUI	Graphical user interface
GWP	Global warming potential
LHP	Loop heat pipe
LRL	Liquid return line in PTL
NPT	National pipe thread (tapered)
ODP	Ozone depleting potential
PWM	Pulse width modulation
PRS	Pulse refrigeration system
PTL	Pulse thermal loop
QC	Quick connect fitting
SITMAP	Solar integrated thermal management and power cycle
TMS	Thermal management system
UTS	Ultimate tensile stress
UKZN	University of KwaZulu-Natal
VI	Virtual instrument
VCR	Vapor-compression refrigeration
VTL	Vapor transfer line in PTL



# 1 INTRODUCTION

Spacecraft thermal management systems (TMS) are vital for the success of any mission. They maintain temperature sensitive equipment within safe operating margins, even when subjected to the extreme fluctuations from  $-200^{\circ}\text{C}$  to  $+200^{\circ}\text{C}$  that can occur in space [1]. In this study, two systems are investigated that could provide engineers with alternate cooling options for future spacecraft. These are a semi-passive two-phase pulse thermal loop and an ejector-based pulse refrigeration system. Both are powered by a low-grade heat source and could find terrestrial application as sustainable alternatives to mechanically-pumped cycles.

## 1.1 The pulse thermal loop

The pulse thermal loop (PTL) is an oscillatory heat transport system that may be a viable solution for future spacecraft thermal control. Advances in spacecraft design utilizing sophisticated batteries and electronics are leading towards smaller vehicles with increasing capabilities. The cooling requirements continue to expand, necessitating innovative TMS that are generally tailored for each application. These systems must be designed to comply with the heat flux requirements, weight and volume limitations, and the available electrical power of the spacecraft.

The PTL combines the benefits of both passive and active cooling technologies. Passive technologies (including thermosyphons and heat pipes) are well suited to small scale systems and continue to meet the cooling requirements at progressively larger heat loads. Active technologies (including mechanically-pumped loops) are well suited to large scale systems and continue to meet the cooling requirements at progressively smaller heat loads [2]. The PTL was proposed by Weislogel [3] in response to the need for a lightweight satellite cooling system that falls between these limits, having better performance than passive systems and less complexity than active systems. The PTL is therefore suitable for niche applications where passive systems are heat flux - or heat transport - limited, or where active systems are weight - or power draw - limited.

The PTL concept is relatively new and there is potential for improvement on the system design and operation. This study expands on previous work in which an experimental PTL was constructed but not adequately tested. A laboratory scale PTL is designed including revised boilers, valves, condenser, control hardware and a custom control application with data acquisition. Unique to this effort are the boilers which are twice as large as previous versions by Brooks *et al.* [4,5], and incorporate large borosilicate sight glass windows to enable flow

visualization. Performance is characterized through experimental testing over a range of operating conditions, including variable power ( $Q$ ), pulse frequency ( $f$ ) and differential driving pressure ( $\Delta P$ ) between each boiler chamber and the condenser.

The PTL research objectives include:

- Establishing thermal design requirements or constraints
- Developing an engineering prototype PTL, with large thermally coupled boilers which are powered by cartridge heaters
- Incorporation of sight glass windows in the boilers for visual inspection
- Developing a custom data acquisition and control application using NI LabVIEW software
- Benchmarking the PTL against previous prototypes

The PTL is intended for use as a TMS on board spacecraft but there are potential terrestrial applications for the technology. In this work an evolution of the PTL is proposed that incorporates a novel, ejector-based pump-free pulse refrigeration system, or PRS [4].

## **1.2 The pulse refrigeration system**

The proposed pulse refrigeration system (PRS) is a development of the PTL that aims to provide refrigeration without requiring a compressor. It is powered by low grade waste heat or solar thermal energy resulting in a cost effective and sustainable alternative to conventional mechanically-pumped cooling systems. It is suitable for both terrestrial and space applications provided there is a heat source that can be exploited. The PRS concept has not been experimentally demonstrated and requires the construction and testing of a novel engineering prototype. This includes a redesign of the PTL to include a cooling loop incorporating an ejector and an expansion valve.

The ejector (also known as a jet pump or a thermo-compressor) is critical to the functioning of the PRS. It has no moving parts, is intended to entrain and compress a secondary fluid and its performance can be described using compressible flow theory. It is designed to operate under steady state conditions, however, is highly inefficient during transients. The ejector in the PRS receives transient pulses of refrigerant at its primary inlet from PTL-like boilers and is expected to operate inefficiently for most of the cycle.

The design and performance of the PRS ejector is analyzed using two one-dimensional (axisymmetric) models implemented in MATLAB. These two-phase models take

compressibility effects into account with NIST REFPROP vapor data sub-routines. A novel aspect of this work is that the quasi-steady performance model enables an analytical method of determining ejector transient operating modes in response to a varying back pressure ratio ( $P_R$ ) across the inlet nozzle. To the author's knowledge, this is the first such analytical transient ejector model to be published.

A PRS experimental prototype is constructed from the PTL components and is tested. It is able to operate as a conventional PTL when the ejector-based cooling section is bypassed, however, attempts to operate the PRS as a refrigeration device were unsuccessful due to the ejector not functioning as intended since the  $\Delta P$  rapidly reduced to zero, limiting entrainment. This aspect of the work remains to be demonstrated.

The PRS research objectives include:

- Evaluation of the additional components required to convert a PTL to a PRS
- Investigation of various ejector flow theories and designs
- Modeling of the ejector in MATLAB for the unique transient operating conditions
- Design of an optimal ejector for use in the PRS
- Evaluation of the PRS concept through a testing program

Refinement of the PTL and PRS would broaden the options available to spacecraft TMS design engineers. Terrestrial applications are also of interest as these systems could provide a sustainable alternative to the well established mechanically-pumped cooling cycles. The PTL is suitable for replacing the heat pipes on central processing units (CPUs) or it can be used to manage the waste heat of industrial equipment to improve thermal efficiencies and reduce failures due to overheating. The PRS would be suited to providing refrigeration in off-grid or mid-latitude sunny regions where solar radiation can be exploited.

### **Structure of this dissertation**

A review focusing on spacecraft thermal management systems is presented in Chapter 2. It provides an overview of the history and relevance of spacecraft temperature control, the various technologies currently available, as well as emerging technologies. This includes the development of the PTL and the PRS. Their terrestrial applications are also discussed.

A new PTL design is detailed in Chapter 3, incorporating thermally coupled boilers, large sight glass windows and a counter-flow concentric tub heat exchanger. The heat exchanger design is

based on a simplified analytical model implemented in MATLAB.

The custom LabVIEW control application is discussed in Chapter 4. This includes the hardware, software and logic.

The PTL experimental results are discussed in Chapter 5. Various nominal and off-nominal results are discussed and the performance of the system is mapped. The results are compared with data obtained from previous variants demonstrated by Weislogel *et al.* [2] and Brooks *et al.* [4].

Chapter 6 presents the design of the additional components required in the PRS, with focus on the ejector. Two ejector models are described including a steady state design model and a transient performance model. The models are validated and used to investigate the design and performance of an ejector for the PRS. Experimental attempts at operating a PRS that incorporates a commercial ejector are presented.

The research conclusions are described in Chapter 7. Recommendations are made for further research into both the PTL and the PRS. The Appendices follow including tables, calculations, design drawings, MATLAB codes, description of the LabVIEW control application and experimental video footage.

## 2 REVIEW OF SPACECRAFT AND TERRESTRIAL THERMAL MANAGEMENT

Thermal management is required for all spacecraft from simple satellites to complex manned space vehicles. A TMS is responsible for maintaining equipment within safe temperature limits and, in manned vehicles, for controlling cabin temperature for human survivability. In this chapter, various thermal control technologies are discussed, including systems that have flown on previous missions, and novel cycles that could be developed for future spacecraft or terrestrial applications, including the PTL and the PRS.

### 2.1 The space environment

The space environment ranges from low Earth orbits to the gravity-free expanses between celestial objects. Extreme thermal loads on a vehicle result from its position and orientation with respect to nearby planets and the Sun as well as waste heat generated from onboard equipment. This can cause degradation of materials and failure of the spacecraft structure and sub-systems.

Environmental heat loads on Earth-orbiting satellites include direct sunlight, reflected sunlight off of the Earth (albedo) and infrared (IR) energy emitted from the Earth [6]. Direct sunlight intensity is the largest environmental heat source, which at the Earth's mean distance from the Sun (1 AU) is  $1367 \text{ W/m}^2$  [6,1]. An orbit usually includes periods of eclipse, resulting in temperature fluctuations on the outside of a spacecraft ranging from  $-200^\circ\text{C}$  to  $+200^\circ\text{C}$ , and equipment inside the spacecraft ranging from  $-130^\circ\text{C}$  to  $+100^\circ\text{C}$  [1]. In addition, the spacecraft generates heat at high heat flux densities from the propulsion systems, electronics and battery packs. The thermal loads must be dissipated through a TMS to keep sensitive equipment within their operating temperature range. Typically electronics must be maintained between  $-20^\circ\text{C}$  and  $50^\circ\text{C}$ , batteries between  $0^\circ\text{C}$  and  $20^\circ\text{C}$ , and various mechanisms such as solar array drives and attitude control components between  $0^\circ\text{C}$  and  $50^\circ\text{C}$  [6,4].

### 2.2 History of spacecraft thermal management

Careful consideration of thermal control is evident with the earliest spacecraft. Passive and active technologies (described in section 2.5) have been employed from the start of the space age and have evolved as the cooling requirements have increased with mission capabilities.

*Prosteishy Sputnik* (or Sputnik-1) was the first artificial satellite to be launched into space in 1957. The sphere measured 585 mm in diameter with a mass of 83.6 kg [7]. It employed a combination of passive and active thermal control. The top hemisphere was coated with a 1 mm

thick passive thermal protective layer. The temperature inside the sphere was actively maintained between 23°C and 30°C by controlling a fan that circulated nitrogen gas. Sputnik-3 (or Object-D) was launched in 1958 and included 16 active louvered shutters which were controlled to alter the radiation view factor of the external heat exchanger [8].

America's first satellite, Explorer-1, was launched after Sputnik-1 in 1958. It was superior in many ways, especially in its operational life. Its success was largely due to the passive (power-free) TMS that it employed. White and dark green stripes were painted on the outer surface of the instrument section and the vehicle was spun along its longitudinal axis, evenly distributing heat [9]. The Gemini spacecraft (launched from 1964 to 1966) had a thermal control system that provided life support for two astronauts [10]. It was able to dissipate heat at three times the rate of the thermal control system used on the earlier Mercury spacecraft (1961 to 1963). It included advanced coatings and an active fluid cooling system (using a positive displacement pump) for regulating the temperature of the cabin, astronauts' suits and equipment. The 165 ft<sup>2</sup> outer surface of the docking adapter module doubled as a radiator to space. The space shuttle orbiter was flown from 1981 to 2012 and made use of an active liquid cooling TMS [6]. Heat was collected from the cabin, fuel cell, hydraulics, ground support equipment, and payload heat exchangers, and radiated to space.

Cassini was launched in 1997 to probe Saturn and its moons, and is still in operation today. The TMS includes multi-layer insulation, reflective louvers and heat exchangers. It is designed to dissipate 700 W of waste heat from electronics in order to maintain them between 5°C and 50°C [11]. In the same year of Cassini's launch, the Mars Pathfinder landed on the Martian surface. It was the first American satellite to use an actively pumped-liquid TMS [6] using refrigerant R-11. It made use of a centrifugal pump (with a pressure rise of 0.3 bar) requiring 10 W of electrical power to provide 90 W to 180 W of cooling power [12].

The international space station (ISS) assembly began in 1998. It makes use of an actively pumped single-phase cooling system for thermal control [13]. The inside of the spacecraft is cooled using water heat exchangers, to provide a habitable atmosphere for humans. The internal heat is exchanged with two liquid ammonia loops that are circulated externally through deployed aluminum radiators. Ammonia, having a freezing point of -77°C, is necessary since water would otherwise freeze in the external pipes. Ammonia is not used in the internal cooling loop as a leak would endanger crew members. Reliability of pumped devices is of concern, as evidenced by the failure that occurred in 2010 which required two spacewalks, or EVAs, to swap out the pump unit [14].

It is evident that spacecraft require varied levels of thermal control, that thermal management is a rapidly evolving field, and that there are numerous options available to designers.

### **2.3 Future missions**

Future missions will provide new science and observational capabilities as technologies evolve. Improved capabilities require greater power requirements and pointing accuracy, improved instrument resolution and thermal control. The demand on engineering sub-systems will increase in order for spacecraft to operate in more challenging environments with improved performance.

Conventional TMS including multi-layer insulation, coatings, louvers and heat pipes are already becoming inadequate for today's spacecraft [6]. Newly developed two-phase systems and long-life mechanical pumps have been implemented on recently launched spacecraft (e.g. high-powered communication satellites, Mars Pathfinder, Mars Exploration Rovers, Swift, and ICESat) to meet the growing mission requirements [6].

Ambitious missions of the future (including the establishment of lunar and Mars bases) require continued innovation and development of the thermal control subsystems whilst decreasing the size and weight of the TMS. The two-phase, oscillatory heat-transport cycles described in this study could find application terrestrially or on future spacecraft.

### **2.4 Technology drivers**

Spacecraft technology drivers include increasing capabilities and operational life, reducing power consumption, working in challenging space environments, decreasing the weight of equipment, and adapting systems for terrestrial application. These are achieved through the development of modern materials, coatings, electronics, novel structures, renewable power generation, and minimizing the size and weight of components. Miniaturization of power devices generates increased heat flux densities relative to the size and weight of the spacecraft.

One of the greatest opportunities for TMS weight savings lies in the development of lightweight composite materials and pumped phase-change fluid cycles. Examples of modern composites include K1100 and P-140 fibers which have been developed as alternative thermal conductors to copper and aluminum. The thermal conductivity of K1100 fibers is 1100 W/m.K, which is three times that of copper at one-quarter the density [6]. Such composites can be integrated into electronic circuit-board enclosures and structural heat sinks. They are, however, ineffective at transporting heat loads to a heat sink that is some distance away from the heat source. In

comparison, pumped phase-change fluid cycles can transport large amounts of heat from a source to a sink.

Developing these technologies will ultimately reduce spacecraft weight and minimize launch costs, or allow for a larger payload.

## **2.5 Types of thermal management systems**

TMS can be divided into two categories: passive and active technologies [1,15].

### **2.5.1 Passive technologies**

Passive thermal technologies include materials, coatings, insulation, radiating heat fins, sun shields, and heat pipes [6]. They are suited to relatively small scale heat loads at low heat flux densities in comparison to active technologies. The flow of thermal energy can be controlled by conductive and radiative heat paths of materials, coatings, and insulations to achieve a desired thermal balance. Heat pipes use a phase-change fluid to regulate the temperature of components. In some texts they are considered as active technologies as they employ a working fluid. They can, however, be categorized as passive as they do not require a mechanical pump to drive the flow, and operate without electrical power.

Various heat pipes include constant conductance heat pipes, one-way or diode heat pipes, variable conductance heat pipes, capillary-pumped loops (CPLs), and loop heat pipes (LHPs) [6]. They all transport heat over a distance from an evaporator to a condenser (or radiator), exploiting the latent heat of phase change. Fluid is pumped back to the evaporator by capillary action of a wick structure. They are suited to small scale systems as they are able to transfer large amounts of heat without the use of electrical power, are more reliable, and have less weight in comparison to active technologies. Passive heat pipes are however limited in driving pressure, heat flux capability and microgravity sensitivity due to their weak capillary forces (typically less than 0.7 bar [16,2]). This constrains the radiator design since the fluid channels cannot be reduced in size. Smaller tubes increase the viscous pressure drop beyond the capillary pump capacity of the loop [4].

#### **i) Constant conductance heat pipe**

Operation of a horizontal tube constant conductance heat pipe is shown in Figure 2.1. It consists of a simple tube with a wick structure annulus. The cycle operates when there is a small temperature difference between the evaporator and the condenser. A phase-change working



fluid absorbs heat in the evaporator section and is evaporated out of the wick. The vapor flows to the condenser where heat is rejected and the fluid condenses back into the wick structure. The condensed liquid is then pumped by weak capillary forces generated in the wick to replenish the evaporator section of the tube.

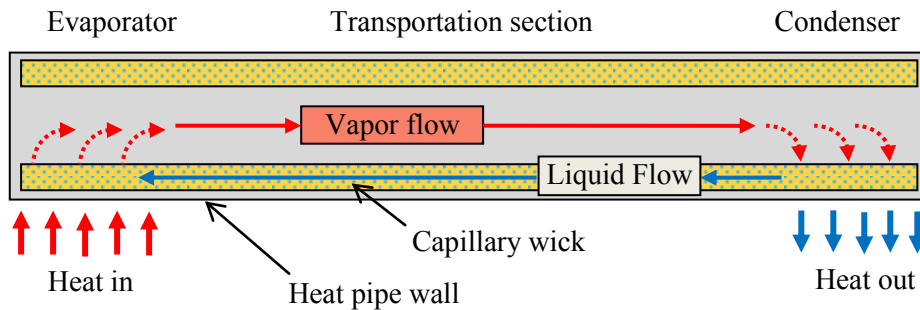


**Figure 2.1** Schematic of a simple constant conductance heat pipe.

## ii) Capillary-pumped loop (CPL)

Similar to a heat pipe, the CPL operates by absorbing heat at an evaporator through evaporating a phase-change fluid, and rejecting heat at a condenser through condensation. The key differences are that the wick structure in a CPL is located in the evaporator section only, and the condenser can be placed at some distance away from the evaporator. There is no wick in the transport tubes or the condenser. A CPL can also have multiple evaporators and condensers.

A typical single-stage CPL is shown in Figure 2.2. The loop functions when the condenser is at a lower temperature than the evaporator. A porous wick (typically high-density polyethylene) is situated in the evaporator and is saturated with liquid. As heat is applied, the liquid at the outer surface of the wick evaporates and the slightly superheated vapor moves to the condenser where it is condensed and slightly subcooled. The driving pressure due to the capillary action at the wick returns the subcooled liquid to the evaporator core. Capillary forces draw fluid in radially from the liquid core into the pores of the wick. A CPL also includes a reservoir that is connected to the liquid line through a small diameter tube. The reservoir contains saturated working fluid (liquid and vapor) at the set loop pressure (and temperature). A small heater is required to maintain the reservoir temperature which controls the CPL set-point.

CPLs are capable of pumping fluid with up to 3 m head against terrestrial gravity depending on the flow geometry and the wick structure [17]. They cannot function in an adverse gravity environment, such as during launch acceleration.

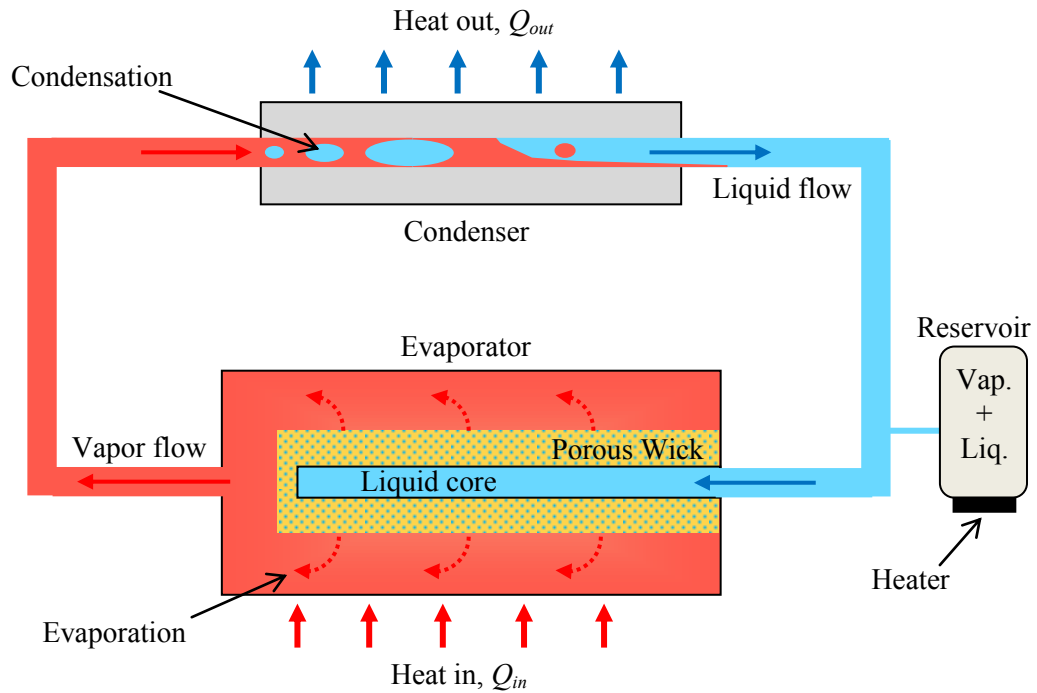


**Figure 2.2** Schematic of a capillary pumped loop (CPL) [17]. Loop operation is limited to the pump capacity of the capillary wick.

### iii) Loop heat pipe (LHP)

An LHP is similar in design to a CPL but has an in-line compensation chamber (CC) coupled to the evaporator inlet, rather than an external reservoir. The CC may sometimes contain a weaker secondary wick (with different properties to the primary evaporator wick) to improve performance [6]. Excess fluid is stored in the CC before being drawn in to the wick by capillary force. The basic configuration is shown in Figure 2.3. The wick performs the same capillary pump action as with a CPL.

Two-phase systems generally require some form of pre-conditioning before start-up. The wick and vapor line of a CPL must first be flooded with liquid by heating the reservoir 5°C to 15°C above the evaporator temperature [6]. In contrast, an LHP traditionally requires less pre-conditioning. When sufficient heat is applied at the evaporator a threshold temperature gradient across the wick (between the evaporator and the CC) results in a pressure difference initiating circulation. For both CPLs and LHPs, start-up can be assisted by using a starter heater at the evaporator to maximize heat flux. An LHP is considered to be the more robust of the two. If a CPL has inadequate subcooling, it will deprime (or dry-out). If an LHP has inadequate subcooling, the operating temperature will increase to create sufficient subcooling. Both cycles are unable to cool the evaporator to temperatures below that of the condenser.

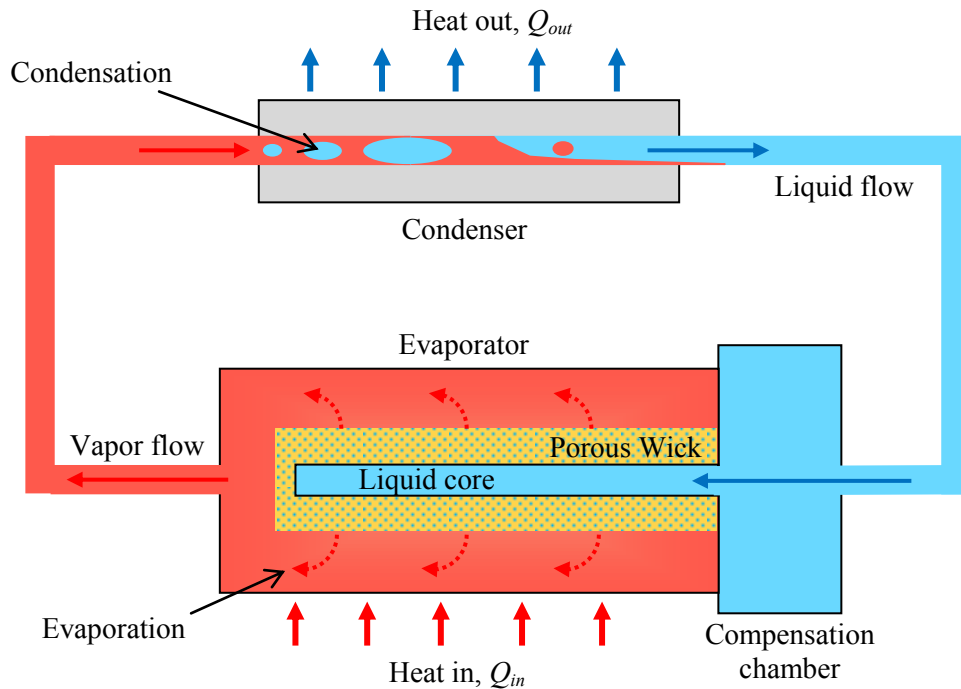


**Figure 2.3** Schematic of a loop heat pipe (LHP) [6]. The design is similar to a CPL other than the CC that is incorporated before the evaporator.

CPLs and LHPs have flown on numerous missions with NASA, the European Space Agency (ESA), and the Russian Federal Space Agency. They have become the baseline thermal-control technology for spacecraft. They offer performance advantages over other heat pipes including longer heat transport distances which allow for complicated layouts of the transport tubing, and increased heat transfer capability. They have been demonstrated to transport from 20 W to 24 kW of thermal energy [6].

### 2.5.2 Active technologies

Active thermal technologies include heaters, louvers and mechanically-pumped loops (typically single-phase) [6]. They are well suited for relatively high heat loads at high heat flux densities in comparison to passive technologies. Louvers are mechanically operated blinds placed on the outside of a spacecraft to modulate the radiation heat transfer to space by opening and closing. A mechanically-pumped system uses a feedpump or compressor to generate fluid flow in a loop.

#### i) Single-phase mechanically-pumped loop

A single-phase pumped fluid loop can transport moderate to large amounts of thermal energy (100 W to 1000 W) through forced liquid convective cooling, over long transport distances [6]. This is due to the high mass flow rate achieved through using an electric pump. Increased pump

pressure enables the use of smaller tubes, which offer an improved strength-to-weight ratio and are especially important in preventing system failure due to micro-meteor strikes.

A simplified schematic is shown in Figure 2.4. The loop consists of a feedpump, a heat exchanger where heat is absorbed, and a space radiator where heat is rejected. Like the CPL or LHP, the cycle is unable to cool the evaporator to temperatures below that of the radiator. In comparison to heat pipes the disadvantages include increased power consumption, weight, size, cost, and mechanical complexity. A disadvantage inherent to single-phase systems is that the fluid temperature at the evaporator is highly variable and depends on the heat load.

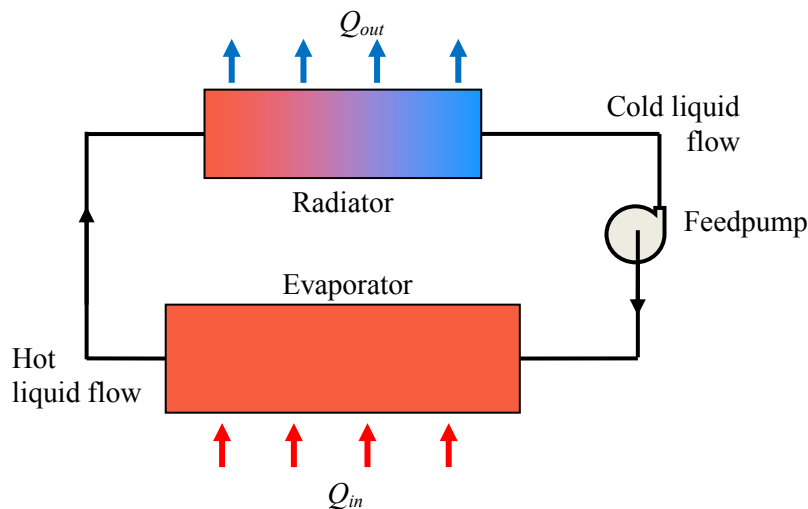


**Figure 2.4** Schematic of a mechanically-pumped fluid loop.

## ii) Two-phase pumped loops

Typical Earth-based vapor-compression refrigeration (VCR) cycles enable refrigeration at temperatures below that of the condenser. They are power-intensive, difficult to operate in a gravity-free environment, and have seen little or no use in space [15].

Two-phase pumped loops are particularly attractive for future spacecraft as they enable smaller transport tubes, less working fluid and less pumping power in comparison to single-phase systems. The evaporative heat transfer allows for isothermal cooling of equipment experiencing variable heat loads.

There is potential for the development of alternate two-phase cycles that are not limited by condenser temperature or the use of a compressor to drive the flow. Ejector cooling systems (ECS) make use of an ejector rather than a mechanical compressor in the vapor-compression part of the cycle, providing two-phase cooling with reduced power consumption.

### 2.5.3 Niche area of research

Weislogel [18] conceptualized a map of heat pipe and mechanically-pumped loop applications in terms of non-dimensional heat transfer and heat flux density requirements, presented in Figure 2.5. The unshaded region represents applications where heat pipes are incapable due to pool boiling heat flux limitations and mechanically-pumped systems have unacceptable weight, size, and complexity. Also, miniaturization of mechanically-pumped systems is uneconomical. An example would be for the cooling of high-powered electronics where small scale and high thermal conductance is required without the cost of a mechanical pump.

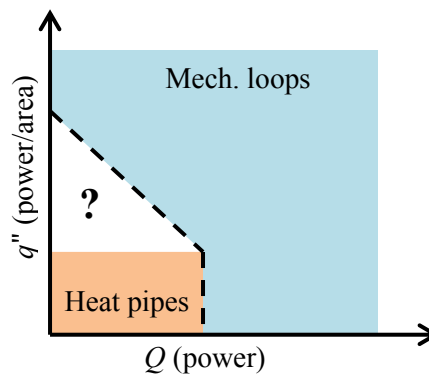


**Figure 2.5** Conceptual map of thermal control system applications showing niche research area [18] for where the PTL and the PRS are being developed.

To address this gap researchers are developing passive and active two-phase systems including novel heat pipe designs and ejector-based vapor-compression systems. It is in this region where novel two-phase concepts such as the semi-passive PTL and the PRS find potential application. In the context of this study, semi-passive refers to a system which does not require a pump or external power supply, but does include valves with moving parts.

## 2.6 Pulse thermal loop (PTL) review

The PTL is a semi-passive oscillatory heat transport cycle. It makes use of multiple constant volume boilers that exploit waste heat to generate two-phase flow. This relatively new concept requires further development before it can find commercial application.

### 2.6.1 PTL cycle description

The basic components of a PTL include two or more constant volume boilers, a radiator or condenser, transport tubing, flow control valves and a two-phase working fluid. A simple schematic is shown in Figure 2.6, but there are conceivably many variations possible. Each boiler is fitted with check-valves at the inlet and shut-off valves (solenoid or actuated ball

valves) at the exit. This ensures one-way flow around the loop. Heat is supplied to the boilers and rejected at the condenser. The valves at the boiler exits toggle to alternately couple each chamber to the low pressure condenser, thereby isolating each one in turn. This sequentially pressurizes and pulses (forces) the working fluid around the loop. Saturated fluid in the liquid return line (LRL) flows through a check-valve into the isolated (empty) boiler because, for a brief period just after an emitted pulse, the isolated boiler's pressure is lower than the loop's pressure. The isolated boiler pressurizes whilst the alternate boiler, open to the condenser, depressurizes due to expansion and condensation. The resulting cycle is therefore characterized by steady, periodic, non-equilibrium evaporation and condensation processes. A control scheme monitors the absolute pressure differential,  $\Delta P$ , between the boilers and activates the valves when a predetermined value,  $\Delta P_{set}$ , is reached. Passive valves, such as diaphragm controlled valves, can be employed to enable power-free operation.

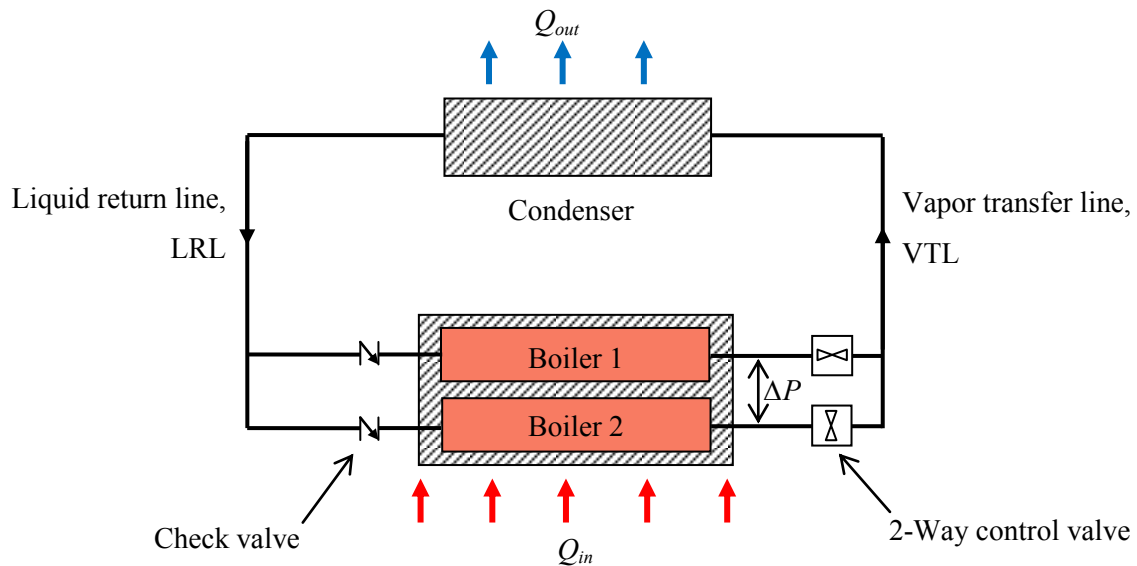
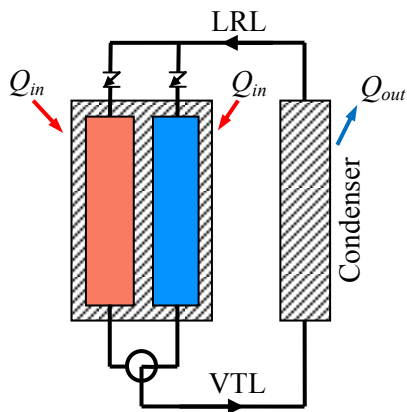
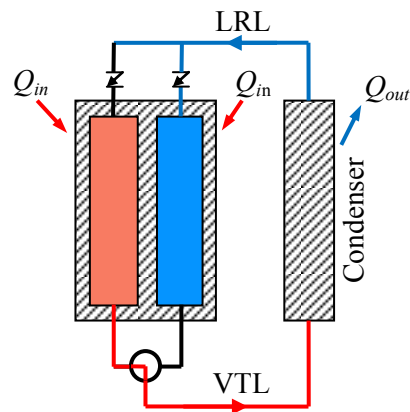


**Figure 2.6** Schematic of the pulse thermal loop [3]. Heat is transferred from the source to the sink by sequentially isolating, pressurizing and pulsing refrigerant around the loop using multiple boilers.

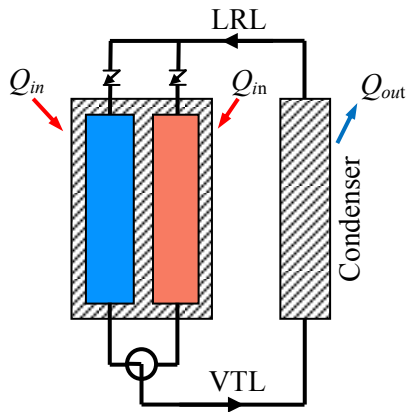
One complete PTL cycle consists of two pulses that include seven steps. This is described with the aid of Figure 2.7. For simplicity the PTL schematics include a 3-way control valve at the outlet of the boilers rather than using two two-way valves. The characteristic pressure trace of the two boilers is shown to aid in the description of the seven steps. The pulses are initially at a high pressure (peaks of  $P1$  and  $P2$ ) and dissipate to the lower condenser pressure (troughs of  $P1$  and  $P2$ ). A pulse period consists of two pulses that are  $90^\circ$  out of phase. The oscillatory pulsing is maintained as long as heat is supplied to the boilers. This has been demonstrated with the cycle operating at steady state for up to 60 hours [3].



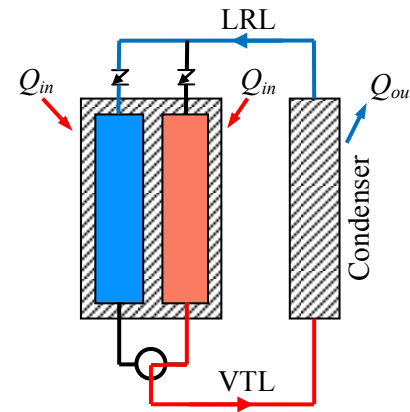
(a) Boiler 1 is sealed, contains refrigerant, and is pressurizing. Boiler 2 is open to condenser and is depressurizing. (Steps 1 & 2)



(b) Boiler 2 is empty and sealed. At  $\Delta P_{set}$  boiler 1 is opened to the condenser. Pulse from boiler 1 forces fluid into boiler 2. Boiler 2 begins to pressurize. (Steps 3 & 4)



(c) Boiler 2 is sealed, contains refrigerant, and is pressurizing. Boiler 1 is open to the condenser and is depressurizing. (Step 5)



(d) Boiler 1 is empty and sealed. At  $\Delta P_{set}$  boiler 2 is opened to the condenser. Pulse from boiler 2 forces fluid into boiler 1. Boiler 1 begins to pressurize. (Steps 6 & 7)

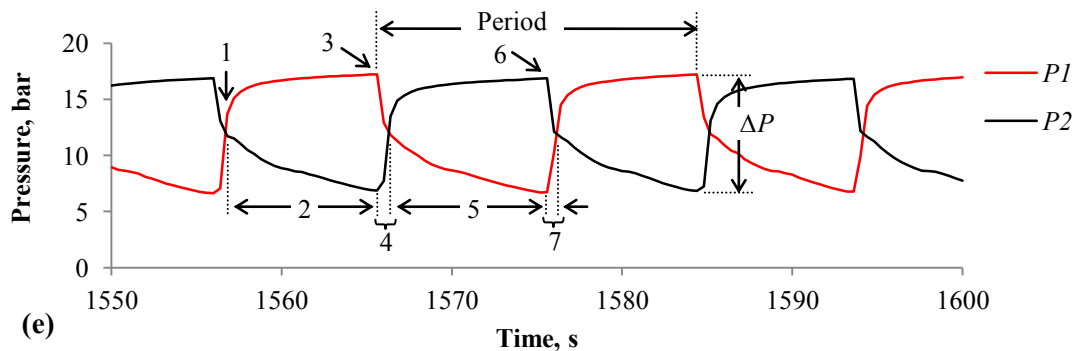


**Figure 2.7** Upper diagrams (a, b, c and d) describe PTL operation. The lower graph (e) shows a typical experimental pressure trace of a PTL operating with  $\Delta P_{set}$  of 10 bar.

Variations in the PTL design include multiple stacked boilers which could be thermally isolated or coupled, different size and types of condensers, different diameter and lengths of transport tubing, different valve technologies for controlling the flow (check valves, shut-off valves, 2-way valves and 3-way valves, diaphragm valves), and different control schemes (frequency control, temperature control and pressure control). The performance of the PTL is affected by the variations in the system design, heat input ( $Q$ ), condenser temperature ( $T_{WI}$ ), driving pressure differential ( $\Delta P$ ), pulse frequency ( $f$ ), thermophysical fluid properties, refrigerant charge vapor fraction ( $x$ ), and mass distribution.

The PTL cycle meets the requirements of the niche area identified in Figure 2.5. The high driving pressures coupled with exploiting the latent heat of phase-change enables the use of small tubes and can result in significant spacecraft weight savings, especially with the radiator. Spacecraft radiators are often the largest/heaviest part of the TMS weighing as much as  $12 \text{ kg/m}^2$  for deployable types [6].

### 2.6.2 PTL advantages

The PTL offers advantages over passive heat pipes and mechanically-pumped loops which make it suitable for advanced thermal control applications. In Table A.1, Appendix A, a non-dimensional comparison between the PTL and conventional thermal management technologies is made in terms of heat flux, transport distances, gravity independence and power consumption.

There are two major benefits of a PTL [16]:

1. The PTL is not limited by a wick structure. Unlike a CPL or an LHP, there is greater flexibility in designing for larger systems with increased thermal capacity and transport distances. The increased  $\Delta P$  reduces the impact of tube lengths and fittings, and enables operation in adverse gravity environments. They are able to operate at increased heat flux densities as they are not limited by nucleate pool boiling or weak capillary forces.
2. The PTL is pump-free. It requires fewer moving parts and near zero power consumption whilst being able to generate similar  $\Delta P$  to that of a mechanically-pumped loop. A PTL can transport approximately 25% heat in comparison to a pumped loop having the same  $\Delta P$ . (i.e. A PTL operating with a  $\Delta P_{set}$  of 12 bar will be able to transfer the same heat as a mechanically-pumped loop operating at 3 bar.)

The main disadvantage of a PTL is difficulty in predicting the performance and reliability of operation. This study increases the data base which maps the performance of the PTL, for a range of operating conditions. Reliability is closely related to the valves employed. Check



valves and electrically powered solenoid valves have been used in previous examples, which were sometimes unable to achieve symmetric pulsing [16]. This could be due to uneven calibration or internal leaking of the valves. Also, the solenoid valves here are electrically powered. The loop can be configured to require no auxiliary power by using diaphragm operated 3-way valves with hysteresis [2], but requires further investigation.

### 2.6.3 PTL development history

The PTL was initially conceived and patented by Weislogel at NASA's Lewis Research Centre in 1992 [3]. The patent became public domain in 1995. Weislogel, Hitch and Bacich continued development of the PTL in 1998 with an analytical system model and demonstrated the loop's capabilities using refrigerant R-134a [2,16,3]. Their last publication was in 2004, but PTL development at TDA Research Inc. appears to be ongoing [19]. Brooks and du Clou commenced PTL research in 2007 and 2008 respectively [4,5]. A summary of various prototypes developed to date is presented in Table A.2 of Appendix A.

By 1998 over 700 hours of operation were logged. Long duration steady states (up to 50 hours) with a range of heat rates (400 W to 2100 W), local heat flux densities ( $1.18 \text{ W/cm}^2$  to  $16 \text{ W/cm}^2$ ), and  $\Delta P_{set}$  (1 bar to 12.4 bar) were demonstrated [3]. Four experimental prototypes were developed:

1. Thermally decoupled 7/8" ID by 254 mm long copper evaporators (boilers) having a volume of  $98 \text{ cm}^3$  each, with a large condenser, and 3/16" ID copper transport tubing, photographed in Figure 2.8. Flow restrictors with different coefficients ( $C_v$ -values) simulated increased tube lengths without changing the flow quality.
2. Thermally coupled 3/4" ID by 318 mm long copper boilers with a volume of  $90 \text{ cm}^3$  each, and a small condenser.
3. Design #2, with  $55 \text{ cm}^3$  vapor reservoirs giving a total volume of  $145 \text{ cm}^3$  per boiler, and a small condenser.
4. Design #3 with a large condenser.

In designs 3 and 4, vapor reservoirs are included to reduce the loop pulse frequency ( $f$ ). The lower  $f$  enables improved data acquisition and solenoid valve control but reduces the performance. The principal dependant variables were identified as frequency ( $f$ ) and the mean saturation pressure and temperature of the working fluid. Independent variables include heat input ( $Q$ ), condenser temperature ( $TB$ ), driving pressure differential ( $\Delta P_{set}$ ), volume ratios of the components with respect to the boiler, charge vapor quality ( $x$ ), flow resistance and the type of

working fluid. It was experimentally determined that the loop must be charged with sufficient refrigerant such that the vapor fraction ( $x$ ) at 20°C is in the range of  $0.6 < x < 0.8$ .

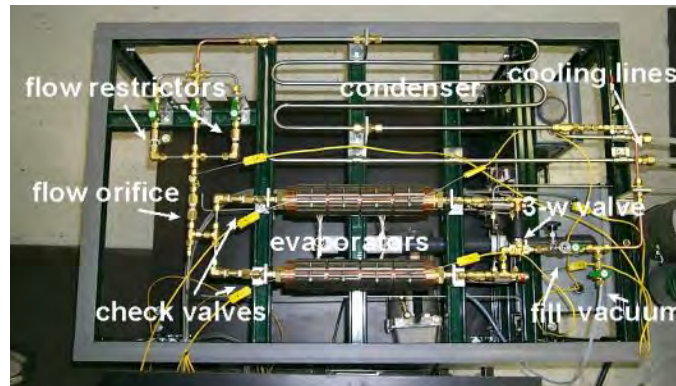


**Figure 2.8** Top view photograph of Weislogel's prototype PTL #1 [3]. The design includes two thermally decoupled constant volume evaporators, a 3-way valve, a condenser, flow restrictors and check valves.

The PTL can be scaled to transfer a range of heat loads from 10 W to 100 kW (up to 10-times greater than high performance heat pipes) [16]. It can transfer up to  $129 \text{ W/cm}^2$  if ammonia is used as the working fluid [2]. This is a 30-fold improvement over comparably sized CPLs. The use of ammonia would also enable increased  $\Delta P_{set}$  of up to 18 bar. Increased  $\Delta P_{set}$  allows for even longer transport distances, through smaller tube diameters and operation in adverse gravity environments (i.e. under launch accelerations). The PTL can find terrestrial application for high end electronics cooling or industrial scale thermal management.

By 2004 over 15 PTL variants had been built logging over 10000 hours of operation, with individual tests lasting up to 500 hours [16,2]. Horizontal and vertical designs were investigated employing counter-flow and parallel-flow condensers. A number of working fluids have been tested including water, methanol, R-134a, R-410a and ammonia. Heat rates ranging from 25 W to 2330 W with  $\Delta P_{set}$  ranging from 0.5 bar to 18 bar have been demonstrated. Condenser temperatures were varied from 5°C to 25°C, with minimal effect on pulse frequencies ( $f$ ) for  $\Delta P_{set}$  above 3 bar. The PTL operating window ( $\Delta P_{set}$  vs.  $f$ ) was investigated using different charge levels with  $x$  ranging from 0.63 to 0.73. A lower charge mass (increased  $x$ ) enables operation at lower  $\Delta P_{set}$ , decreased system mean pressure, and increased  $f$ , but with greater variance in the boiler temperatures. A  $10 \text{ cm}^3$  micro-pulsed thermal loop (MPTL), pictured in Figure 2.9, was developed but not demonstrated [20]. The loop is constructed of 1.17 mm ID tubing having two  $3.5 \text{ cm}^3$  serpentine evaporators, and is charged with less than 3 ml of R-134a. The heat transfer capacity is predicted to be in the range of 5W to 200 W.

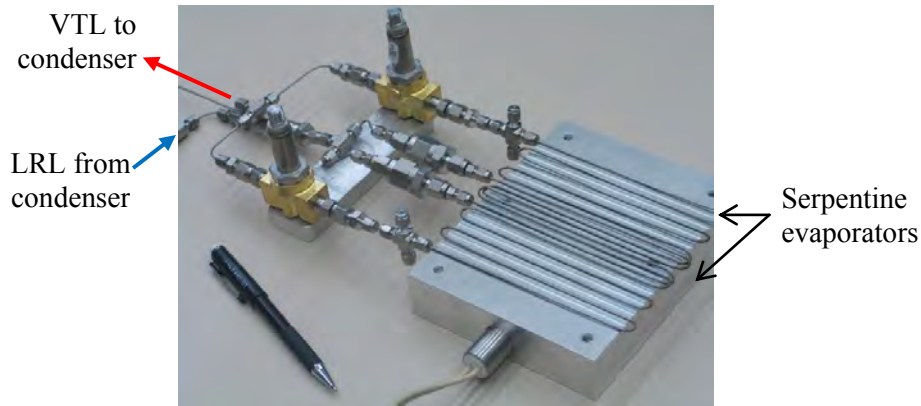


**Figure 2.9** Micro-PTL [20]. This 10 cm<sup>3</sup> PTL includes two 3.5 cm<sup>3</sup> evaporators and is predicted to transfer up to 200 W of thermal energy.

At the University of KwaZulu-Natal (UKZN), Brooks *et al.* [4] constructed a PTL in 2007 to validate the concept and investigate different control schemes. The experimental prototype (Figure 2.10) included two thermally decoupled 31.5 cm<sup>3</sup> boilers, 4.55 mm ID transport tubing, a 39.2 cm<sup>3</sup> condenser, and R-134a as the working fluid. Greater detail is provided in Table A.2 of Appendix A. The loop operated with  $\Delta P_{set}$  ranging from 4 bar to 8 bar (limited by valve constraints) and power inputs ranging from 400 W to 800 W. The system was unable to operate at pressures below 3 bar but the cycle pressure trace was prone to asymmetry.

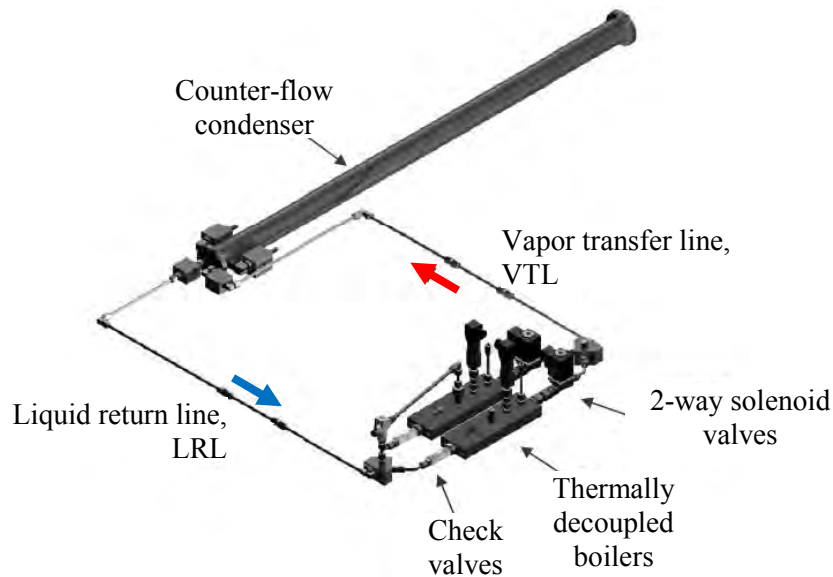


**Figure 2.10** PTL developed by Brooks *et al.* [4] consisting of two thermally decoupled boilers. The loop is capable of dissipating heat up to 800 W with  $\Delta P_{set}$  up to 8 bar.

Four methods of controlling the PTL were investigated including frequency control,  $\Delta P$  control, absolute pressure control and hybrid control (combined  $\Delta P$  and absolute pressure control). Stable operation is best achieved using the  $\Delta P$  method of control. This is the same method employed by Weislogel and Bacich [16]. With this method, a software algorithm monitors the pressures at the two boilers and actuates the outlet valves when the absolute  $\Delta P$  reaches a set value,  $\Delta P_{set}$ . Operation is the same as described in Figure. 2.7.

The potential applications of the PTL have not yet been fully realized. Thermodynamically speaking, it is a heat engine where the work output is used to circulate refrigerant. One can imagine utilizing a PTL as a heat-driven pump to replace a conventional electrically-driven pump in a loop. Brooks *et al.* [4] proposed a novel ejector-based pulse refrigeration system (PRS) that makes use of PTL-like boilers to pump refrigerant around a cooling loop.

In 2008 a revised PTL including two thermally coupled 36 cm<sup>3</sup> boilers, was constructed and tested (Figure 2.11) [5]. This PTL included the components required to test the PRS concept. Although the PTL performance was an improvement on the previous version, the PRS concept could not be demonstrated due to excessive pressure drops that limited circulation. The PTL (outer loop in the figure) enabled heat transfer from 80 W to 150 W with  $\Delta P_{set}$  ranging from 3 bar to 8 bar. The system was prone to asymmetry with respect to the cyclic boiler pressure histories. It was determined that asymmetry may not only be caused by thermally decoupled boilers (as was the case in 2007), but also by the quality of the valves employed.

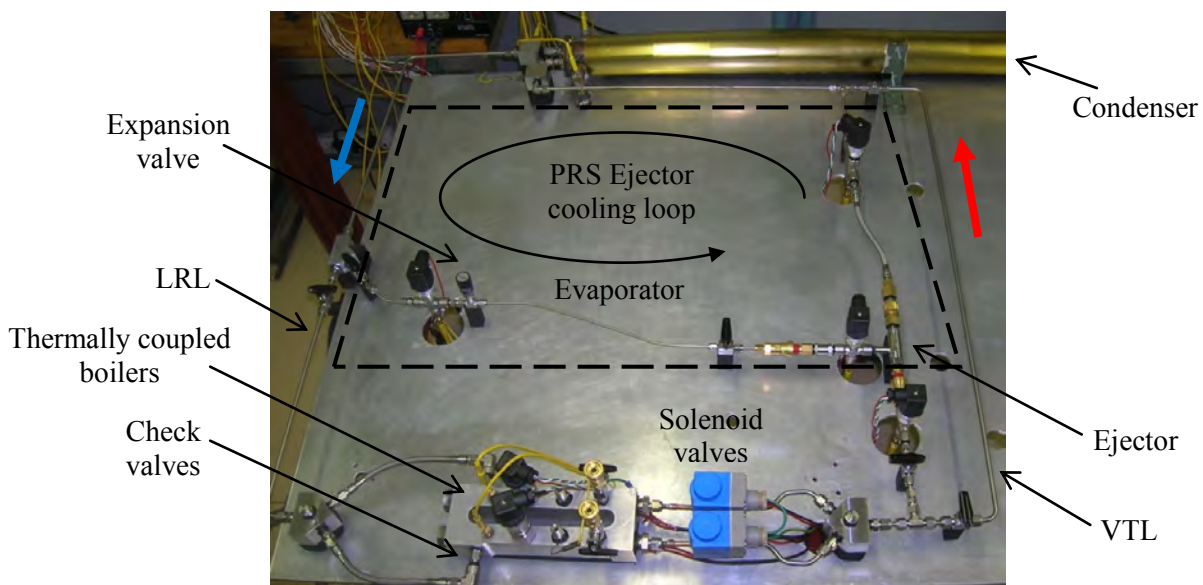


**Figure 2.11** PTL developed by du Clou *et al.* [21]. The inner loop included the components required to test the PRS concept, but this was not demonstrated.

## 2.7 Pulse refrigeration system (PRS) review

The present study aimed to develop the PTL into a new type of refrigeration system, the PRS. The PRS combines the PTL-pump with an ejector-based cooling system (ECS) to provide pump-free heat-driven refrigeration (shown in Figure 2.11 and Figure 2.14). More detail regarding the PRS is described below and in Chapter 6. Many researchers have investigated ECS with particular focus on the ejector design. An ECS is principally similar to conventional vapor-compression refrigeration (VCR), except that the compressor is replaced with an ejector, a boiler and a low energy feedpump. The PRS proposed here eliminates the pump required in the ECS and competes with compressor-driven cycles, conventional ECS, thermoelectrics (Peltiers) and absorption cycles [22].

### 2.7.1 Vapor-compression refrigeration

Most refrigeration cycles are thermodynamically similar to the compressor-driven VCR cycle in Figure 2.12. The cycle includes an evaporator, a condenser, a compressor, and an expansion valve. The condenser and the evaporator are isobaric heat exchanging devices.

The typical thermodynamic cycle is sketched on the temperature-entropy diagram in Figure 2.13. Refrigerant is pumped out of the condenser as a saturated liquid at point 4 and passes through an irreversible expansion/throttle valve in process 4-5. Adiabatic flash evaporation lowers the temperature of the refrigerant resulting in a two-phase mixture. Heat is transferred from the cold space to the evaporator during process 5-1, vaporizing the liquid fraction of the refrigerant at constant pressure to give saturated vapor. Note that the evaporator operates at a lower temperature than the condenser. The refrigerant then passes through an electrically driven compressor, in process 1-2, which compresses the refrigerant to a superheated vapor. The condenser removes the superheat by cooling the vapor in the isobaric process 2-3, and condensing it to saturated liquid in process 3-4. A great amount of energy is associated with the phase change of the working fluid which enables heat to be absorbed at the evaporator to achieve the cooling effect [23]. The coefficient of performance (COP) is defined as the ratio of the heat removed from the cold space ( $Q_{in}$ ) to the work input, Equation 2.1.

$$COP = Q_{in}/W_{in} = Q_{in}/(Q_{out} - Q_{in}) \quad (2.1)$$

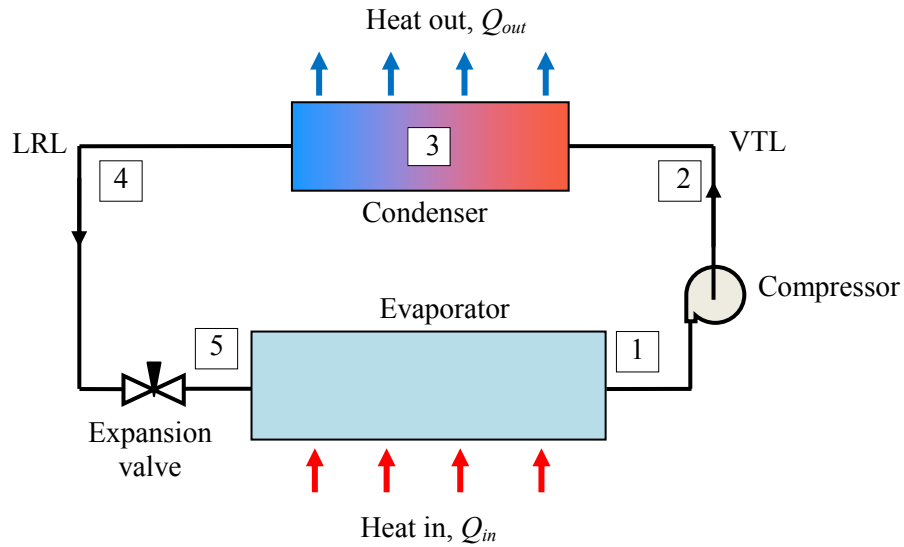


**Figure 2.12** Schematic of a compressor-driven vapor-compression refrigeration system.

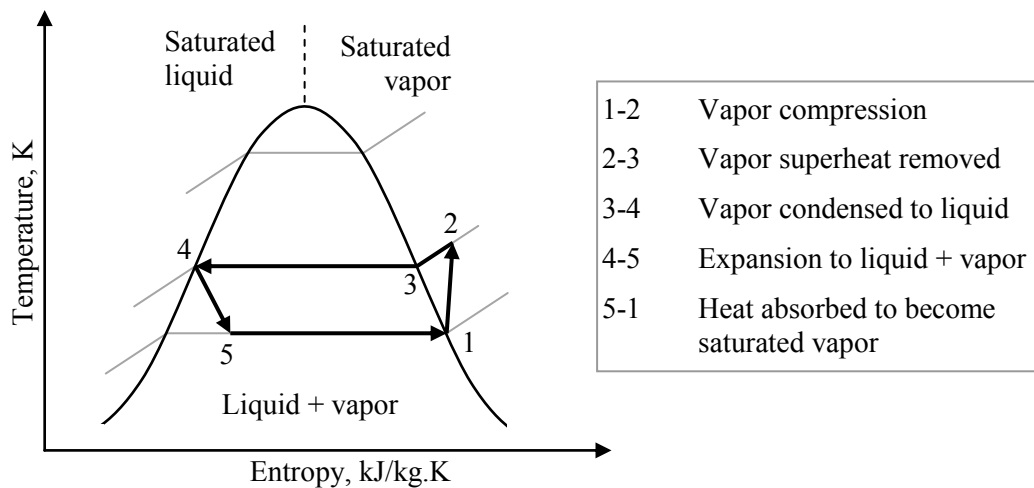


**Figure 2.13** Temperature - entropy diagram for vapor-compression refrigeration. [24]

### 2.7.2 Ejector cooling systems (ECS)

ECS eliminate the need for a compressor in the refrigeration part of the cycle. This is attractive for space applications as the ejector offers the advantage of having no moving parts. This improves long term reliability whilst decreasing weight and vibration levels [25]. An ECS is also attractive for terrestrial applications as it can be powered by low grade thermal energy from vehicle engines, industrial processes or solar thermal sources. The mechanically simple ejector utilizes a high pressure motive fluid to entrain and compress a lower pressure secondary fluid. This compression is required to raise the pressure of the secondary stream to that of the condenser. The primary disadvantage is that ejector based systems, whether driven by solar or waste heat, require the refrigerant to be circulated by an electric feedpump [22]. In comparison

to the conventional compressor-driven VCR cycle in Figure 2.12, ECS reduce power consumption but suffer from a reduced COP. The overall efficiency of a heat-driven ECS ( $COP_o$ ) is defined as the product of the heat engine efficiency ( $\eta_h$ ) and the COP of the refrigerator, Equation 2.2.

$$COP_o = \eta_h \times COP \quad (2.2)$$

**i) Operation of an ECS**

A simple ECS is given in Figure 2.14 where the cooling loop is comparable to the VCR cycle and follows the thermodynamic process shown in Figure 2.15. An ejector replaces the compressor in the VTL. The fluid flow is split in the LRL where a portion is expanded in the cooling loop (process 4-5) and evaporates to produce the cooling effect in process 5-1. The remaining portion of the fluid flow in the LRL is pumped to the waste heat recovery boiler in process 4-6. The boiler absorbs heat during process 6-7 superheating the fluid to produce the primary (motive) flow. The primary flow is then expanded through the ejector supersonic nozzle in process 7-e. The high velocity low pressure region in the ejector entrains the secondary fluid in process 1-s1, expanding the flow due to a reducing flow area. The two streams mix at point m and recompress to the condenser pressure at 2, due to a normal shock wave.

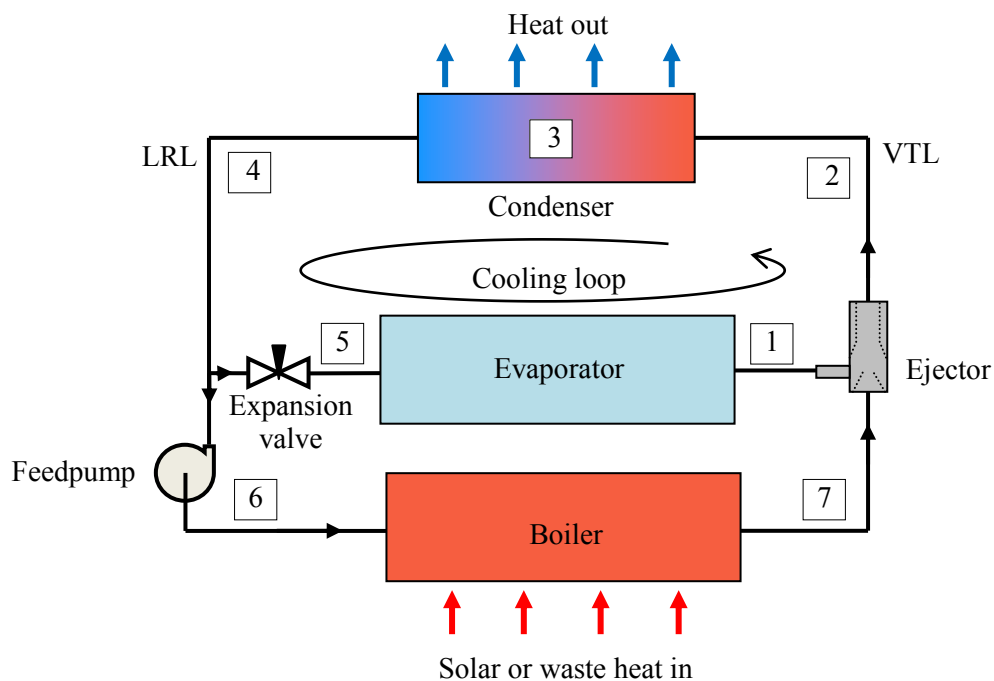


**Figure 2.14** Schematic of an ejector cooling system (ECS).

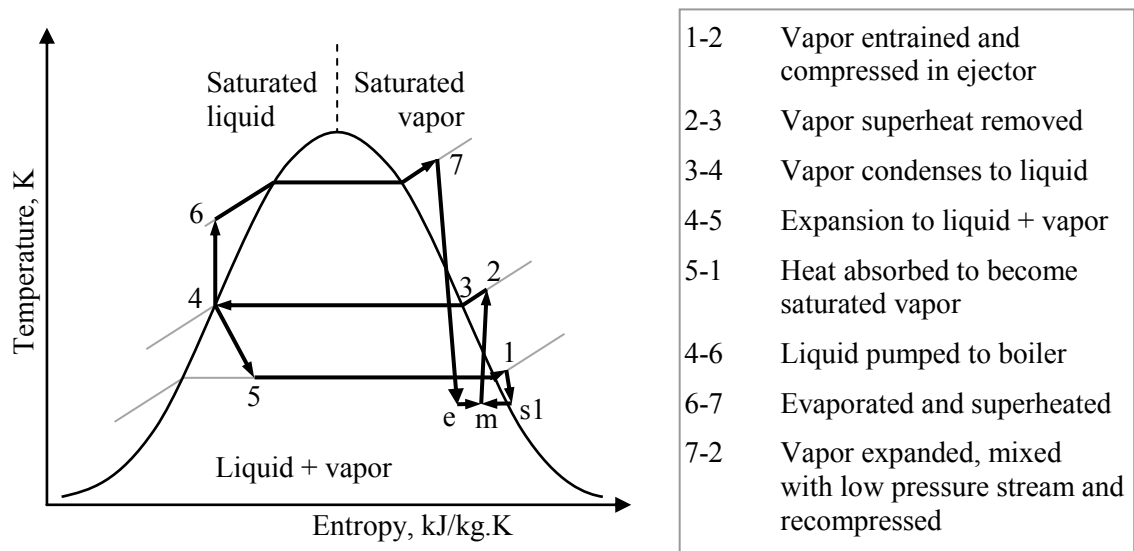


**Figure 2.15** Temperature - Entropy diagram for an ECS.

## ii) ECS in the literature

Ejector cooling systems have largely been supplanted by electrically driven vapor-compression systems where a superior COP is achievable. Due to environmental considerations, researchers have mainly investigated steam-jet refrigerators, or ECS, as alternatives [22,26]. They make use of low grade solar thermal energy or waste heat to drive the boiler in the cycle.

Although the ECS is promoted as a renewable system, it still requires an electric pump to circulate the working fluid. It has been argued that the ECS pump power required is negligible in comparison to the heat input at the boilers (typically less than 1% [27]) and is often neglected in the thermodynamic performance equations [28].

Eames *et al.* [28] provided a comprehensive literature review on ECS and selected water as the working fluid in their experimental study. Approximately 700 W cooling was achieved with the boiler operating at 120°C, the condenser at 28°C and the evaporator at 10°C. A COP<sub>o</sub> of 0.544 was demonstrated. The ECS COP<sub>o</sub> is dependent on the boiler and evaporator temperatures and is independent of the condenser temperature up to some critical value. This critical condenser temperature results in a critical ejector pressure ratio ( $\phi^*$ ), above which the ejector cannot function as the entrainment ratio ( $\omega$ ) and the COP<sub>o</sub> quickly reduce to zero. For low  $\phi$ , the flow through the ejector primary nozzle becomes under-expanded and a free expansion wave in the mixing chamber limits secondary entrainment. An increased boiler temperature therefore requires an increased condenser critical temperature to maintain the critical driving pressure ratio ( $\phi^*$ ) across the ejector. This is an attractive result for applications where the sink is



operated at an elevated temperature. If the geometry of the ejector were to be variable, it would enable variable critical operating points ( $\varphi^*$ ).

Sun [29] analyzed the effect of variable ejector geometries on the performance of an ECS. The author also concluded that the geometry of the ejector should ideally be variable in order to provide constant cooling capacity at various boiler, evaporator and condenser operating temperatures. A decrease in boiler temperature or an increase in condenser temperature requires comparably larger ejector nozzle and diffuser geometries to maintain critical operation at  $\varphi^*$ .

Meyer *et al.* [27] demonstrated an open-loop steam-jet ECS. Various ejector nozzle diameters ranging from 1.5 mm to 3.5 mm were investigated with a fixed mixing section diameter of 18 mm. The optimal primary nozzle exit position (*NXP*) was experimentally determined to be -5 mm. A  $COP_o$  of 0.253 was achieved using an ejector with a primary nozzle throat diameter of 3.5 mm, a boiler temperature of 95°C, an evaporator temperature of 10°C and a water cooled condenser temperature of 22.6°C. It is evident that the ECS performance is largely dependent on the boiler and condenser operating temperatures, as well as the ejector geometry.

Chunnanond *et al.* [30] experimentally investigated the pressure profile along the ejector axis. The results confirmed that a pressure ratio ( $\varphi$ ) above some critical point ( $\varphi^*$ ) results in unchoked flow. Superheating the vapor at the primary inlet offers no performance advantage other than preventing the condensation of a wet fluid (see schematic in Figure A.5, Appendix A). Increasing the primary nozzle exit position (*NXP*) from the mixing chamber improves the entrainment ratio ( $\omega$ ) and the  $COP_o$ .

Using steam as the working fluid is environmentally friendly but does limit the evaporator operating temperature to above the freezing point of water. Cizungu *et al.* [31] investigated modern environmentally friendly refrigerants including R-123, R-134a, R-152a and R-717 for use in an ECS to provide sub-zero cooling. Khalil *et al.* [32] conducted a theoretical study on an ECS using R-134a as the working fluid. In order for the evaporator to operate at 10°C, the boilers were maintained between 64°C and 74°C with a condensing temperature of 35°C. This temperature range is appropriate for low-grade solar or waste heat sources. Increased boiler temperatures result in improved ejector performance. Huang *et al.* [33] investigated an ECS using R-141b that achieved a  $COP_o$  of 0.5 with a generator temperature of 90°C, condenser temperature of 28°C and an evaporator temperature of 8°C. Using a solar thermal source of 700 W/m<sup>2</sup> the  $COP_o$  was reduced to 0.22. Roman *et al.* [34] investigated an ECS employing a variety of two-phase working fluids. Performance improved with an increase in boiler

temperature and a decrease in condenser temperature. The ejector geometry is specifically designed for a given fluid and only one steady state critical operating point. Literature pertaining to the intricacies of ejector design is presented in section 6.1.

### iii) Novel ECS

The circulation pump used in the conventional ECS renders it mechanically unreliable and expensive for application on spacecraft. The development of a pump-free ECS is an attractive concept that few researchers have investigated.

Nguyen *et al.* [35] developed a pump-free gravity assisted ECS where the low pressure side (condenser) is elevated to 7 m. This provided the gravity head necessary to return the working fluid to the high pressure boiler. Such a system is unsuitable for micro-gravity applications. Huang *et al.* [36] and Wang *et al.* [37] investigated an ECS that is driven by a thermal pump with no circulation pump required in the loop (Figure 2.16). The thermal pump is conceptually similar to the PTL where two vapor generators, or boilers, are cyclically pulsed to drive the flow of refrigerant around the loop. This design has the same gravity dependant limitation as that Nguyen *et al.* [35]. The condenser is elevated to 1.8 m for the gravity head to assist with flow back to the generators. The lower liquid receiver tanks are intermittently cooled to depressurize the vapor generators in order to receive liquid from the condenser during the liquid intake phase. The cooling jackets are deactivated during the pressurizing and pulsing phases of the generators. This concept is more complex than the PRS, requires excess power consumption and cannot function in a gravity-free environment.

The solar integrated thermal management and power (SITMAP) cycle was proposed by Nord *et al.* [38] and further investigated by Kandil *et al.* [25] (Figure 2.17). It was developed for spacecraft applications and combines a thermal management and power producing system resulting in significant weight savings. Nitrogen gas is superheated by waste heat or solar thermal energy to drive a turbine, which produces electrical power to drive a pump or other electrical equipment. An ejector compresses the flow rather than a conventional compressor in the cooling part of the cycle. The SITMAP system was further investigated by Zheng and Weng [39] who simulated the cycle performance. An evaporating temperature of 280K is achievable with a 395K generating and 290K condensing temperature.

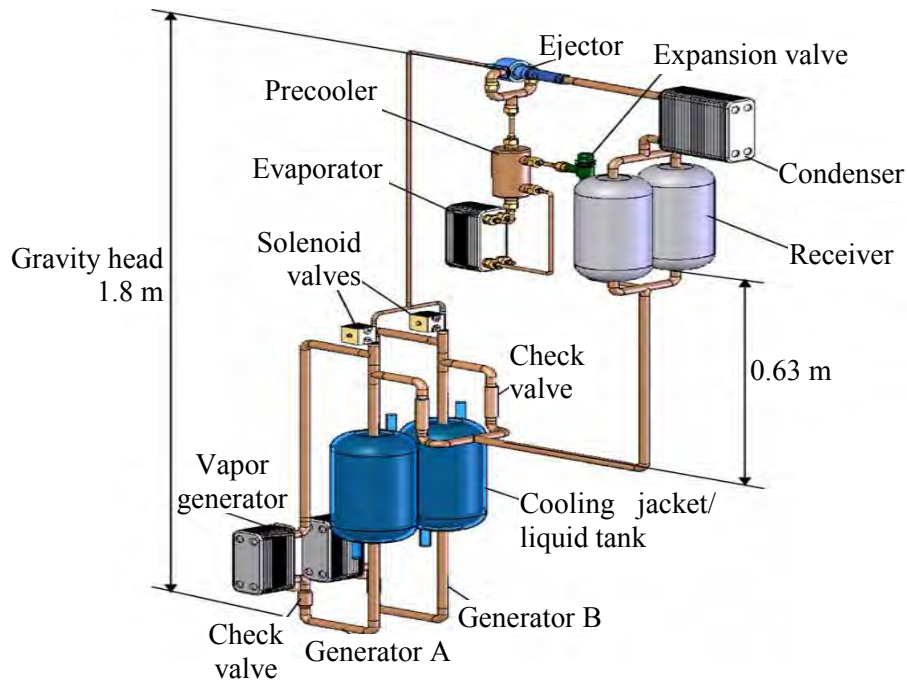


**Figure 2.16** Thermally pumped ECS investigated by Huang *et al.* [36]. The system relies on a 1.8 m gravity head and intermittent cooling of the generator tanks.

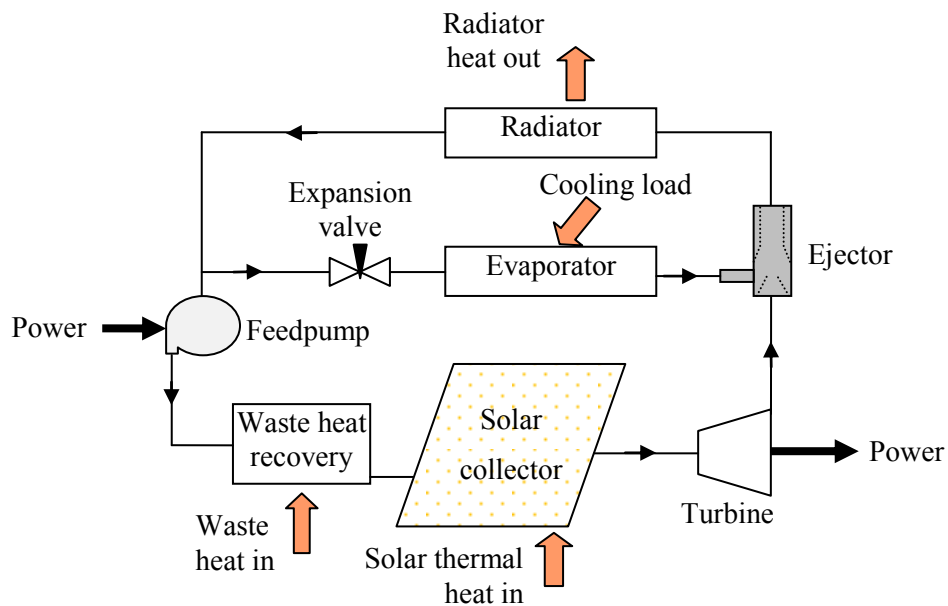


**Figure 2.17** Solar integrated thermal management and power (SITMAP) system [25].

### 2.7.3 PRS concept development

The PRS proposed by Brooks *et al.* [5] is a two-phase, active cooling system which combines the technologies of the SITMAP ECS and the PTL. Replacing the SITMAP pump-turbine combination with a pair of PTL constant volume boilers results in a pump-free refrigeration

system that can be powered by solar or waste heat sources. Whereas earlier work conducted at UKZN focused solely on the design of a PTL [21,4], this research also aims to test the PRS concept.

A schematic of the PRS is shown in Figure 2.18. The thermodynamic cycle is shown in the T-s diagram, in Figure 2.19. Refrigerant is pressurized in the isochoric process 4-6 (constant volume) in the isolated boiler. At  $\Delta P_{set}$  the refrigerant is pulsed out of the boiler and directed through the ejector cooling loop. The low pressure flow through the ejector entrains refrigerant from the evaporator, and compresses it to the condenser pressure. Flow in the LRL is split such that a portion of it expands in the cooling loop to provide refrigeration, and a portion is injected into the alternate low pressure boiler.

Brooks *et al.* [5] highlight the challenges regarding the design of the ejector with the aid of a computational analysis. Preliminary experimental work and CFD modeling indicated that entrainment is possible using an ejector driven by pulsatile flow [5]. The present effort therefore focuses on the design and optimization of an ejector to cope with transient flow. The design and analysis of an appropriate ejector for use in such a system is addressed. Following this, a full prototype of the ejector-based refrigeration system is constructed and tested.

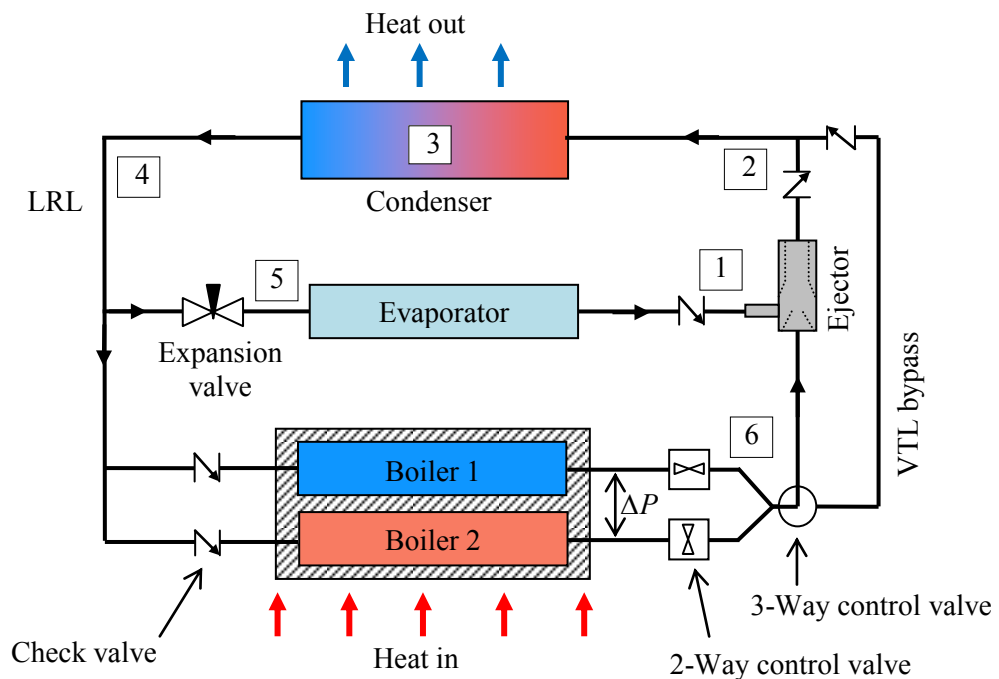


**Figure 2.18** Schematic of PRS. Pulses from the PTL boilers are directed through the ejector cooling loop.

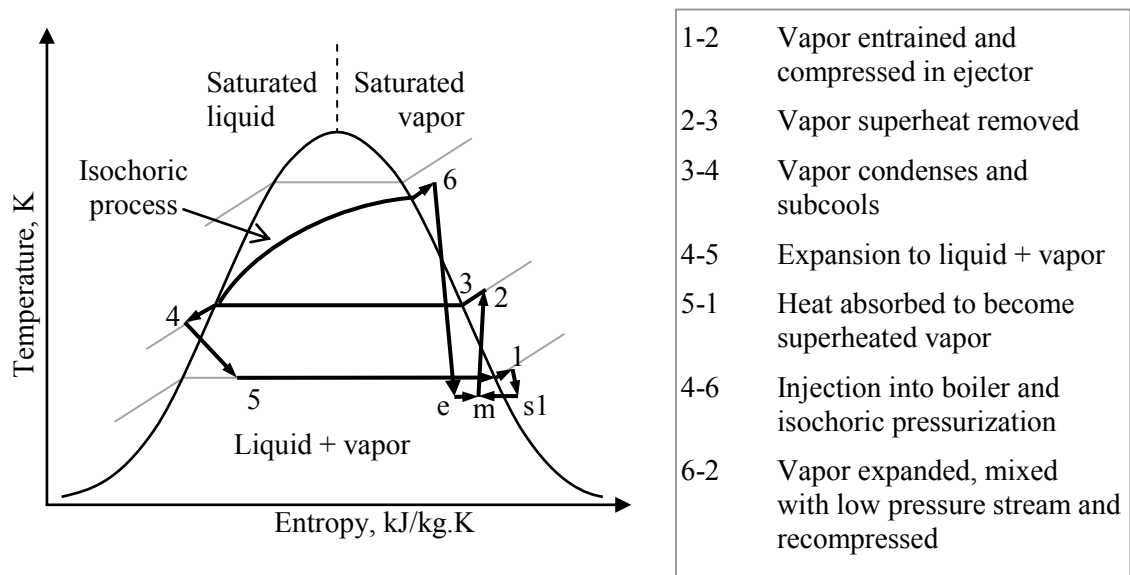


**Figure 2.19** Temperature - Entropy diagram for the PRS.

Eliminating the pump improves reliability and results in power and mass savings, which is attractive for spacecraft applications. In addition, the PRS would provide an energy-conscious alternative to terrestrial vapor-compression refrigeration.

#### 2.7.4 PRS for terrestrial applications

The PRS does not require power intensive rotating equipment and can be powered by waste heat or solar thermal energy. It is therefore well-suited to rural areas without access to grid electricity and can offset power consumption in urban areas. An alternative technology that has found successful application terrestrially is the adsorption refrigerator. Although it is power-free and heat-driven, it suffers from a poor  $COP_o$  in the range of 0.1 to 0.5 [40].

Sustainable technologies have become more prevalent as the world endeavors to rely less on fossil fuels and reduce carbon emissions. It is estimated that 15% of electricity consumption worldwide is used for refrigeration and air conditioning processes [22]. South Africa, the largest greenhouse gas producer in Africa, signed the Kyoto Protocol in 2002 [41], yet coal-fired power stations account for 95% of the country's domestic power production [42]. Implementing sustainable energy systems is necessary to preserve resources and reduce harmful emissions.

Cooling systems are most desirable in mid-latitude sunny regions where a plentiful supply of solar radiation can be exploited. The use of solar energy makes particular sense as it is the most abundant source of renewable energy available, at approximately  $1.08 \times 10^{14}$  kW worldwide [43]. As cooling demands increase with intensity of solar radiation, the excess heat may be exploited to power cooling systems.

In off-grid areas, a flat plate, evacuated tube or concentrating solar collector can be coupled to the PRS to provide a renewable heat source at high temperatures. Novel solar collectors such as the rear focusing ring array concentrator and fiber optic transmission system developed by Mouzouris *et al.* [44] can be used to channel heat to a point of application. Waste heat is a common by-product in industrial processes and can be recovered utilized to drive the PRS. Using waste heat or solar thermal energy to provide refrigeration would reduce power consumption, help conserve fossil fuel resources and improve living conditions for communities in remote, off-grid regions of the world, particularly in developing nations such as South Africa.

### 3 PULSE THERMAL LOOP DESIGN

This chapter details the design and selection of various components required for a PTL engineering prototype. The completed system is photographed in Figure 3.1. The physical and geometric properties of this PTL are compared with previous versions in Table A.2, Appendix A. The design considerations for the boilers and the condenser include the prospect of using them in the proposed PRS, as described in Chapter 6.

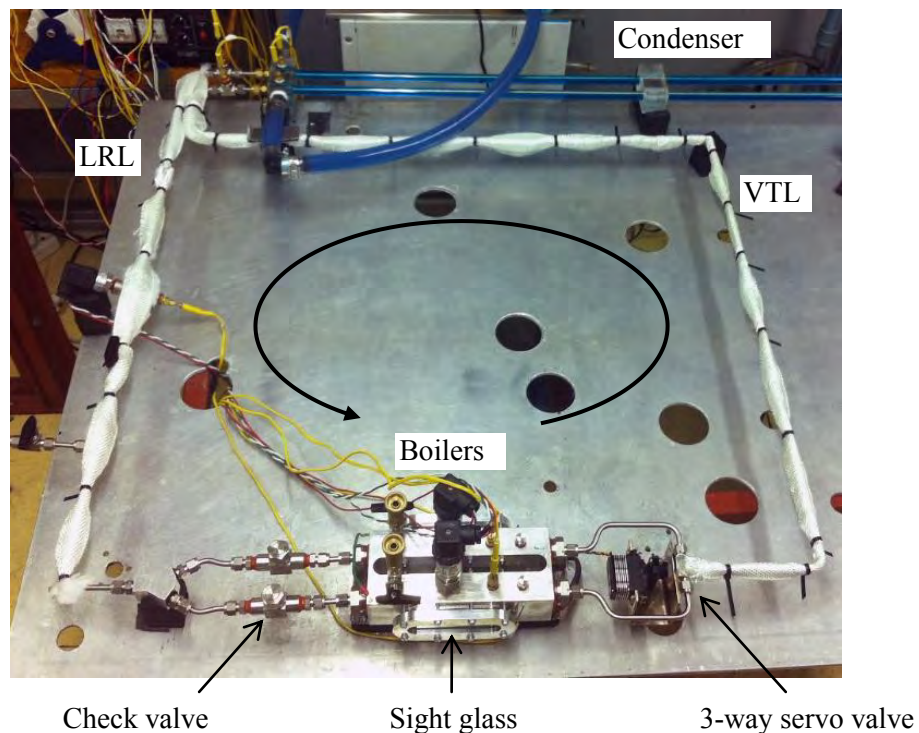


**Figure 3.1** The assembled PTL including thermally coupled boilers, a VTL, a condenser, and a LRL. Flow in an anti-clockwise direction is controlled through the use of check valves and a 3-way servo valve. Two VTL lengths were investigated.

#### 3.1 PTL design

The PTL design requirements were obtained from the literature and evaluated using a modified version of the quality function development (QFD) technique, in Table A.3 and Table A.4, Appendix A.

Important design requirements identified include ensuring a leak-free system that is fitted with sufficient instrumentation and provision of a custom software application to control the valves and log experimental data. Variable boiler heater power ( $Q$ ) and  $\Delta P$  control are ranked as the

most important requirements in the design of the PTL. These are the independent (controllable) variables. Testing  $Q$  and  $\Delta P_{set}$  affects the dependant variables which include the pulse frequency ( $f$ ) and the system temperatures.

The main PTL design features are summarized as follows:

### **i) Performance**

The boiler block is manufactured from aluminum 6082-T6 having a conductivity of 180 W/m.K. The design includes two 500 W electrical heaters to simulate a waste heat source and instrumentation to enable performance evaluation and comparison with previous PTLs. Multiple valves control the flow of refrigerant around the loop. This includes a custom servo-actuated 3-way ball valve. The PTL is designed to achieve a large driving pressure differential ( $\Delta P$ ) which would benefit the operation of the PRS. A sight glass installed at each boiler chamber permits visualization of the injection, boiling and flow of refrigerant during testing. Custom control software was developed, which logs experimental data to a spreadsheet file.

### **ii) Geometry and assembly**

The PTL is compact in design to minimize weight as this is an essential requirement for spacecraft components. This also reduces the thermal inertia, and hence the cool-off periods between experiments. The transfer lines are constructed of 1/4" stainless steel tubes to ensure compatibility with the available equipment. The PTL design makes use of modular components including quick connect fittings that enable system reconfiguration and testing of the PRS. The system is assembled in the horizontal plane to minimize gravitational effects. Volume ratios reported in the literature are used to ensure operational success and to enable direct comparison with earlier systems.

### **iii) Safety**

The PTL operates at temperatures of up to 100°C and pressures of up to 25 bar. For this reason adequate design safety factors ( $SF$ ) are applied and pressure relief valves and software fail-safes are considered. Leaks are avoided as exposure to the working fluid may have adverse effects on the operators. Tapered national pipe thread (NPT) and compression fittings are used throughout as they provide a pressure tight seal. A laminated glass pane shields the operators from the experiment.



### 3.2 Refrigerant selection

There are four groups of refrigerants including chlorofluorocarbons (CFCs including R-12 and R-114), hydrochlorofluorocarbons (HCFCs including R-22, R-123 and R-142b), hydrofluorocarbons (HFCs including R-134a and R-152a) and additional refrigerants such as water (R-718b) and ammonia (R-717). CFCs and HCFCs are being phased out due to the Montreal Protocol. Various refrigerants and their properties are compared in Table A.5, Appendix A.

The chosen refrigerant must be chemically stable, non-toxic, non-explosive, non-corrosive and environmentally friendly. Some refrigerants are now prohibited due to their ozone depleting potential (ODP) and global warming potential (GWP) [22]. This includes R-11, R-12, and R-113. Refrigerant thermophysical properties include the boiling temperature at 1 bar, boiling pressure at 100°C, molecular mass and the latent heat of vaporization. The fluid pressure at the boiler temperature should not be too high in order to avoid heavy construction of the pressure vessel and instrumentation. Satoh *et al.* [45] showed that a larger molecular weight is beneficial in an ejector cycle as this can result in an increased entrainment ratio and compression ratio. A fluid with an increased latent heat of vaporization is able to provide greater heat transfer capability. Water is a possible working fluid, however, it reacts with 304 and 316 stainless steel in some aerospace applications [6], and is limited to applications above freezing point. Ammonia is an attractive refrigerant with a large latent heat of vaporization, but is highly toxic and corrosive [6]. Methanol works well with stainless steel but reacts with aluminum [6].

Refrigerant R-134a was selected to enable the direct comparison of the results in this work with that of Weislogel and Bacich [16] and Brooks *et al.* [4]. It is well suited to the expected operating temperatures and pressures. It has a low boiling point of -26.1°C at standard pressure and an acceptable pressure of 39.72 bar at 100°C. It has a favorable latent heat of vaporization of 190.9 kJ/kg and molecular mass of 102.3 g/mol. The only disadvantage is that it is classified as a wet vapor refrigerant where its saturated vapor curve on the T-s diagram has a negative slope (Figure A.1, Appendix A). When the fluid undergoes expansion, as in the case of an ejector nozzle, it passes through the two-phase region and condensed droplets form in the vapor flow. The vapor may be superheated prior to expansion to avoid condensation [46].

### 3.3 Boiler design

The complete PTL boiler assembly is shown in Figure 3.2. It incorporates cartridge heater elements, sight glass windows and threaded ports for pressure transducers, thermocouples and

refrigerant charging valves. The block was machined from a 215 mm x 100 mm x 75 mm billet of aluminum 6082-T6. The design drawings are provided in Figures C.3 and C.4, Appendix C. The boiler chambers each have a capacity of 81.2 cm<sup>3</sup>. Two 12 mm diameter through holes directly beneath the boiler chamber locate the 500 W electric cartridge heaters. Thermal inertia is minimized by removing unnecessary material. Leaks are minimized by using compatible sight glass gaskets (grafoil or non-asbestos) and ensuring that the cover plate bolts are tightened to the correct torque. Flow control valves are located at the boiler inlet and outlet ports.

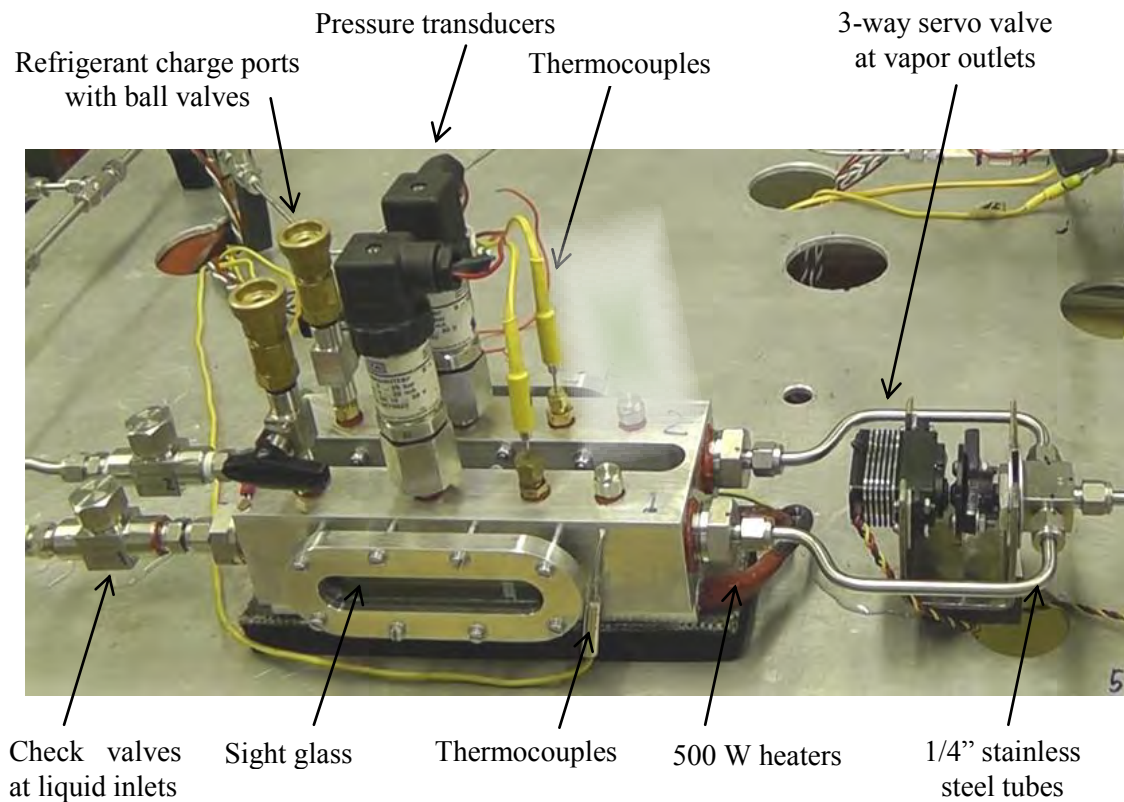


**Figure 3.2** Complete PTL boiler section including valves and instrumentation.

### 3.3.1 Boiler block material

Four materials were considered for the manufacture of the boiler block, including aluminum 6082-T6, copper, brass and 316 stainless steel (Table A.6, Appendix A). Aluminum 6082-T6 was selected for its superior thermal qualities and low cost. It has a density of 2700 kg/m<sup>3</sup>, specific heat of 0.903 kJ/kg.K and a thermal conductivity of 180 W/m.K. These properties result in a light weight design with excellent heat transfer performance.

The minimum wall thickness ( $t$ ) of aluminum 6082-T6 for the boiler is calculated according to the requirements of a thin walled pressure vessel using the hoop stress method, Equation 3.1

[47] (Appendix B.1). For an internal radius ( $r$ ) of 11 mm, a maximum pressure ( $P$ ) of 25 bar and a yield stress ( $\sigma_y$ ) of 250 MPa, a minimum wall thickness of 0.11 mm is calculated. The wall thickness safety factor ( $SF$ ) of the boiler block design exceeds 10.

$$t_{min} = (P \times r) / \sigma_y \quad (3.1)$$

### 3.3.2 Sight glass window

Two sight glass window options were considered for incorporation into the boiler design (Figure 3.3). The threaded end cap incorporating a fused sight glass was used in a previous PTL [21]. It enabled visual confirmation of refrigerant injection but it was difficult to see boiling taking place. Large borosilicate gauge glass windows [48] were selected as they provide a clearer view of the injection, boiling and pulsing process. The glass was installed using a bolted cover plate and a gasket material.



**Figure 3.3** Sight glass windows (a) threaded end cap, and (b) flat gauge glass

The gauge glass  $SF$  is calculated using Equation 3.2 [49], (Appendix B.1). For a modulus of rupture,  $M$ , (or MOR strength) of 16.55 MPa [50], an internal pressure ( $P$ ) of 25 bar, a thickness ( $t$ ) of 17 mm, and an unsupported area ( $A$ ) of 2.5 in<sup>2</sup>, an  $SF$  of 3.9 is calculated.

$$SF = (3.48 \times M \times t^2) / P \times A \quad (3.2)$$

The boiler sight glass bolts were appropriately tightened to avoid leaks or tensile failure under loading. The applicable theory is detailed in Figure B.1, Appendix B.1. The tightening force ( $Fi$ ), tightening torque ( $Ti$ ) and  $SF$  of the sight glass bolts are calculated using Equations 3.3 to 3.5 [51]. SAE Class 4.8 (M4) steel bolts were selected for the design, having a proof stress of 310 MPa. Each bolt is tightened to the calculated torque of 2 N.m. A bolt  $SF$  of 5.14 is calculated.

$$F_i = 0.9 \times A_{bolt} \times \sigma_y \quad (3.3)$$

$$T_i = 0.2 \times F_i \times D_{bolt} \quad (3.4)$$

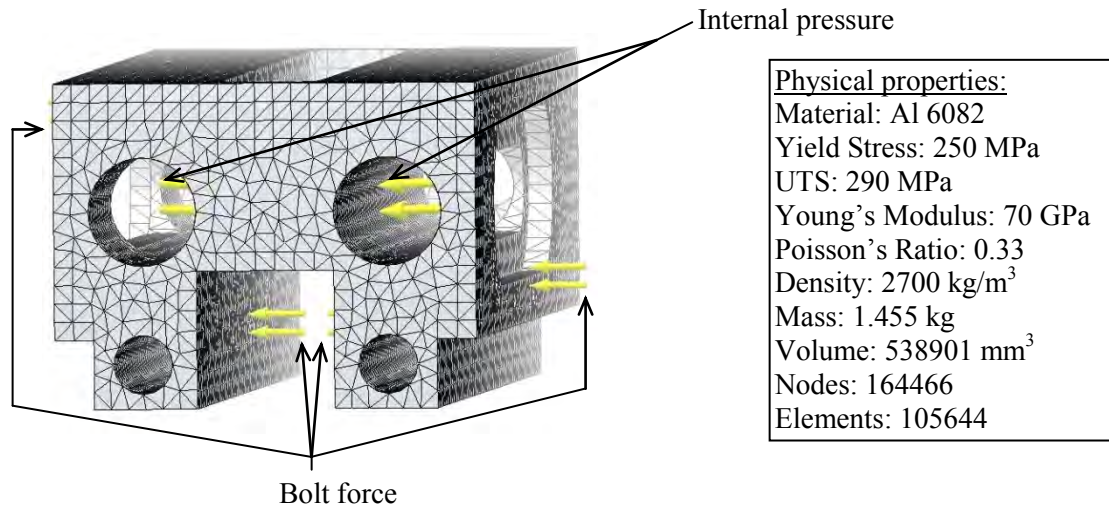
$$SF = \sigma_y / \sigma_{bolt} \quad (3.5)$$

### 3.3.3 Boiler stress computational analysis

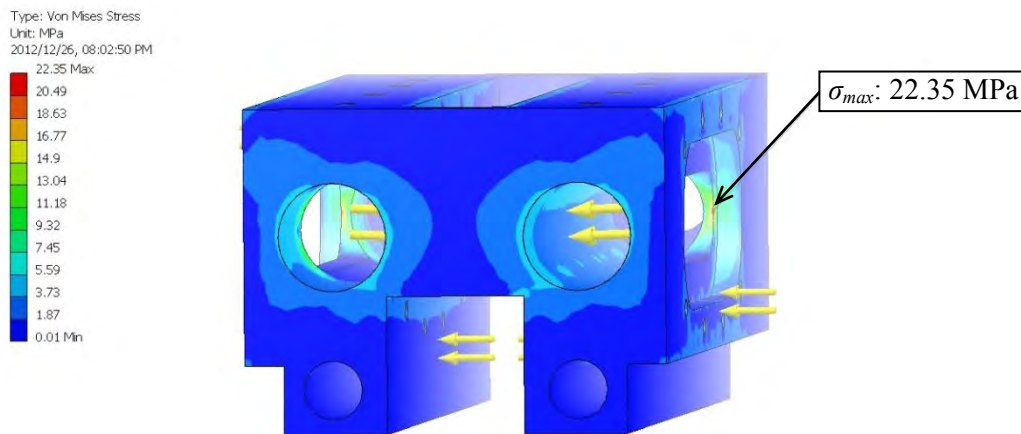
A simplified finite element analysis (FEA) was carried out on the boiler block in Autodesk Inventor. This investigated the maximum stress and deformation of the block under the maximum loading conditions. The mesh of the boilers is shown in Figure 3.4 containing 164466 nodes with 105644 elements. An internal pressure of 25 bar is applied and the compressive bolt force from the 8 sight glass bolts is approximated as a uniform load of 9800 N on each side of each chamber (calculated in Appendix B.1). The analysis does not take into account the local stress points at the nut washer/boiler interface, or corners.

Figure 3.5 shows the Von Mises Stress contours for the given loading conditions. The maximum stresses occur at the inner diameter of the boiler chambers and decrease with an increase in distance away from the pressurised chamber. A maximum stress ( $\sigma_{max}$ ) of 22.35 MPa occurs at the sight glass cavity minimum wall thickness, which is 2 mm. A cross-section drawing indicating the minimum wall thickness is shown in Figure C.2, Appendix C. The stress profile is compared with the ultimate tensile stress (UTS) of 290 MPa to give the  $SF$  contour plot in Figure 3.6. The minimum  $SF$  is 11.18. Figure 3.7 shows the exaggerated deformation of the boiler block due to the loading conditions. A maximum displacement of 0.0025 mm occurs at the maximum stress points.

The results indicate a robust boiler design when considering the loading conditions, and the various  $SF$  including that of the material, the bolts and the sight glass. The design is limited to the  $SF$  of the sight glass itself, which is 3.9.



**Figure 3.4** Mesh applied to boiler block before simulation. Arrows indicate the applied bolt forces and the internal pressures.



**Figure 3.5** Von Mises analysis of boiler block showing a maximum stress of 22.35 MPa, at the minimum cross-section.

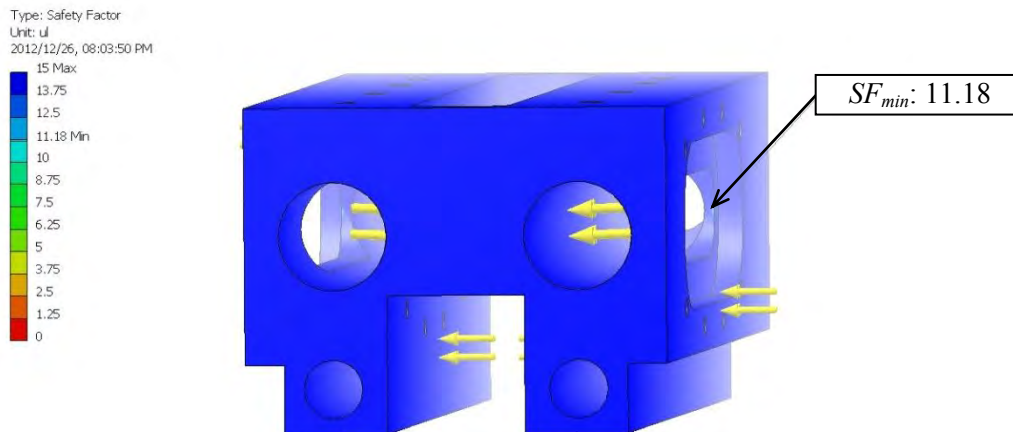


**Figure 3.6** Safety Factor contour plot of the boiler block showing a minimum of 11.18.

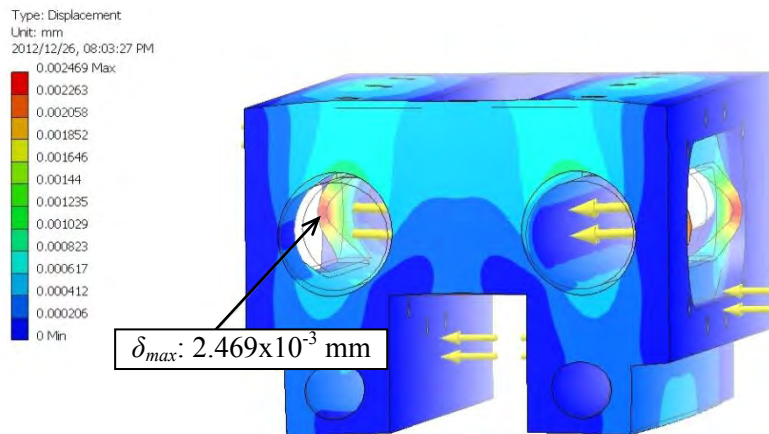


**Figure 3.7** Displacement analysis of the boiler block showing a maximum of 0.0025 mm

### 3.3.4 Boiler valves and instrumentation

The complete boiler design includes check valves at the inlets and flow control valves at the outlets to control the flow (pulses) of refrigerant around the loop. Refrigerant charge valves and instrumentation including pressure transducers and thermocouples are located at each boiler.

#### i) Check valves at boiler inlets

One-way check valves at the boiler inlets ensure flow in one direction and isolates the pressurizing boiler. Various valve types were considered including the spring loaded poppet check valve and the lift check valve (Figure 3.8). These open when the upstream pressure is greater than the downstream pressure by a set value. The set cracking pressure can be specified from 0.3 bar to 1.8 bar [52,53].

The poppet check valve operates with a spring operated poppet that seals against an O-ring when closed. Forward flow has a flow coefficient ( $C_v$ ) of 0.47 [52]. The O-ring material can be specified as either Buna-N or FKM. These materials react with fluorocarbons such as R-134a, and swell over time, permitting leakages. The lift check valve, although gravity dependant since it has to be orientated vertically, operates with no springs or elastomers [53]. Forward flow lifts the weighted poppet opening the valve with a  $C_v$  of 0.3. Reverse flow seats the poppet against the orifice with a metal-to-metal seal. As gravity dependency is not of major concern during this prototype phase, such a valve was selected to enable robust experimentation and counter the leaks that were present in the previous setup [21].



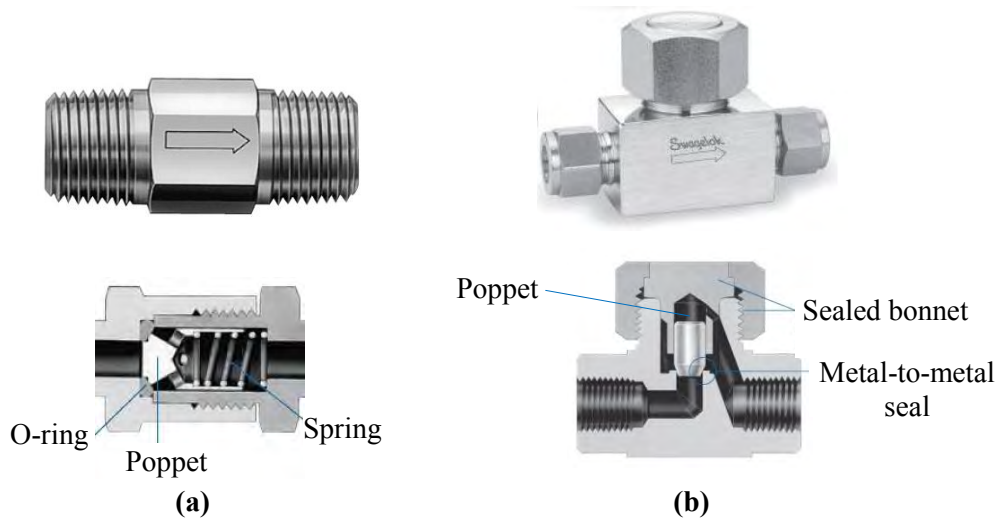


**Figure 3.8** (a) Poppet check valve and, (b) lift check valve [52,53]

## ii) Outlet servo valve

Active control of the fluid pulses using timed valves is necessary for operation of the PTL. A custom servo-controlled 3-way ball valve is implemented in the current control scheme rather than the solenoid valves that were used in the previous system [21]. This is to prevent the internal leaks that were reported. A 3-way valve and its function are shown in Figure 3.9. As an alternative, a commercial system could make use of a passive valve (for example a 3-way diaphragm-operated valve with hysteresis [16]) which is preset to a specific  $\Delta P_{set}$ .



**Figure 3.9** 3-Way valve operation [54]

The valve selected for the PTL has 1/4" compression fittings at its inlets and makes use of an optional UHMPWE packing material with ethylene propylene O-rings [54]. The optional packing material results in a lower starting torque of 2.6 N.m compared to 3.7 N.m for the standard PTFE packing material [55]. This reduces the load on the servo that actuates it, resulting in a faster actuation speed. The valve has a  $C_v$  of 0.9.

A servo with the highest possible torque and speed rating was sourced, namely the Hitec HS-7980 TH servo [56] (Table A.8, Appendix A). At 7.4 Volts it can actuate the output shaft up to a speed of 0.17 s/60° with a maximum stall torque of 4.31 N.m.

The servo is attached to the 3-way valve using a bracket (Figure 3.10) that is manufactured from a stainless steel sheet, cut to the correct profile and bent into a U-shape. The servo is controlled using a LabVIEW application with pulse width modulation (PWM).

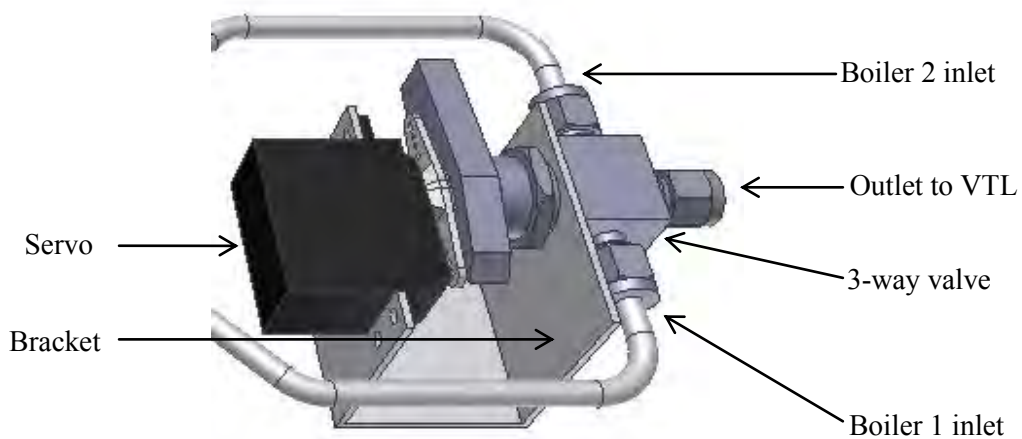


**Figure 3.10** 3-Way servo valve assembly

### iii) Pressure relief valves

Pressure relief valves are required on pressure vessels for safety purposes. They are principally similar to poppet check valves, in that they only allow flow in one direction when a set cracking pressure is reached. The cracking pressure is set by the spring tension of the valve to a desired safety limit. If the pressure inside the chamber exceeds this limit, the valve is operated.

A previous PTL included these valves at the boiler chambers [21]. The valves were prone to premature failure and were not dependable. Such valves are not incorporated into the current design and a level of safety is designed into the custom software instead. When a set pressure or temperature limit is reached, the software cuts the power to the boiler heaters, reducing the pressure and temperature of the working fluid.

### iv) Charge port valves

The charge ports located on each boiler chamber are used to fill the system with refrigerant. The charge port assembly includes a two-way ball valve and a Swagelok QC series quick connect



body (female) [57]. The QC body enables the connection to the charging cylinder which has a QC stem (male). Both the stem and the body include shut-off valves that are closed when decoupled. The ball valves on either side of the quick connects are required to control the flow of refrigerant when the quick connects are engaged.

#### v) Instrumentation

A pressure transducer and two thermocouples are installed at each boiler chamber for data acquisition. Two WIKA S-10 pressure transducers are utilized to provide absolute pressure readings from 0 bar to 25 bar. Four Type-K thermocouples provide temperature measurement of the boiler block material and the vapor inside the boiler chamber. The interface between the instrumentation and the LabVIEW control system is described in Chapter 4.

### 3.4 Refrigerant charging cylinder

A charging cylinder provides an easy, accurate and safe method filling the PTL or PRS with a set mass of refrigerant (Figure 3.11). It is comprised of off-the-shelf components including a 75 cm<sup>3</sup> cylinder, a pressure gauge, a Type-K thermocouple, a two-way ball valve, a quick connect (QC) stem for easy attachment to the PTL boilers, and a Schrader valve for connecting to the refrigerant supply cylinder. The design is easy to operate and enables accurate recording of the mass of refrigerant that enters the system.

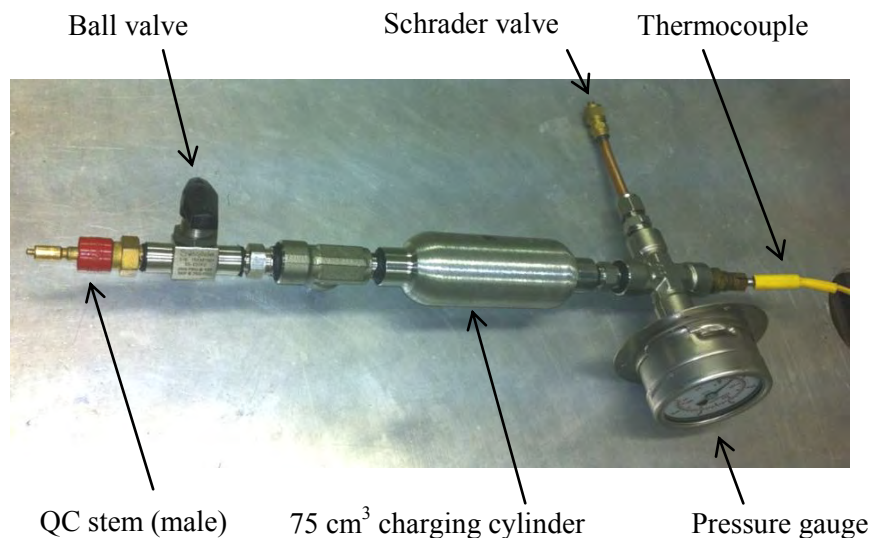


**Figure 3.11** Refrigerant charging cylinder includes a pressure gauge and a thermocouple. It allows for accurate measurement of the mass of refrigerant with which the system is charged.

### 3.5 Condenser design

During operation of the PTL a heat exchanger removes thermal energy from the working fluid that is pulsed through the lines, and represents the radiator on a spacecraft TMS. The heat exchanger maintains the  $\Delta P$  between the boilers and the condenser. Variable condenser temperature control is therefore a functional requirement. Different types of heat exchangers can be employed including concentric tube, shell-and-tube (serpentine), and crossflow arrangements [6]. For the heat transfer rate required here (with a maximum of 1 kW) the concentric tube, or double pipe heat exchanger is adequate. A concentric tube heat exchanger was designed using a simplified analytical model and is constructed from stainless steel and extruded transparent acrylic tubes.

#### 3.5.1 Application of concentric tube heat exchanger theory

A simple double pipe heat exchanger consists of two concentric pipes. One fluid flows through the inside of the smaller pipe while the other fluid flows in the annular region between the two pipes. The two fluids can either move in the same direction (parallel) or in opposite directions (counter flow) as shown in Figure 3.12. Both flow arrangements can be achieved using the same apparatus. The parallel flow arrangement in Figure 3.12 (a) is characterized by an initially large temperature difference between the two fluids, which approaches zero with an increase in length along the condenser axis. The outlet temperature of the cold fluid,  $T_{c,o}$ , cannot exceed the outlet temperature of the hot fluid,  $T_{h,o}$ . For the counter flow arrangement in Figure 3.12 (b), the fluids enter at opposite ends, flow in opposite directions and exit at opposite ends. The temperature of the cold fluid at the outlet,  $T_{c,o}$ , can exceed the temperature of the hot fluid at the outlet,  $T_{h,o}$ .

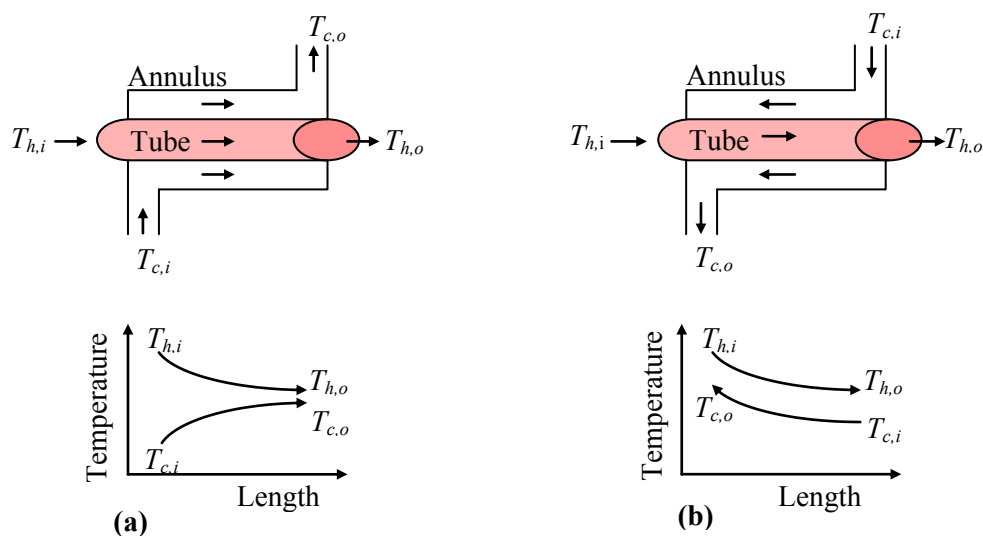


**Figure 3.12** A double pipe heat exchanger setup in (a) parallel flow and (b) counter flow arrangement with the corresponding temperature profile plots [47,58]

An in-depth two-phase condensation model was beyond the scope of this work and the focus here was to develop an approximate design, based on the overall heat transfer required of the heat exchanger. The heat transfer ( $q$ ) in a concentric tube annulus (Figure 3.13) is governed by Newton's law of cooling, Equation 3.6. This is manipulated to give the length ( $L$ ) of the condenser in Equation 3.7. The overall heat-transfer coefficient ( $U$ ) is the thermal resistance to heat transfer between two fluids, separated by a solid wall, through convection and conduction. It can be calculated using Equation 3.8. The convection terms ( $h_h$  and  $h_c$ ) apply to the inner and outer surfaces of the inner tube. The conduction term is for a plain cylindrical wall and cannot be neglected in this analysis due to the significant relative wall thickness of the 1/4" tubes (0.9 mm). By convention, the working fluid is routed through the inner tube if it has a lesser mass flow rate than the cooling fluid [47]. The overall heat transfer is usually governed by the outer surface area of the inner tube [58]. By substituting the surface areas and cancelling terms, the overall heat transfer coefficient can be found explicitly using Equation 3.9. The logarithmic mean temperature difference ( $\Delta T_{lm}$ ) for counter-flow and parallel-flow arrangements is given by Equation 3.10. For the same set of inlet and outlet temperatures,  $\Delta T_{lm}$  for counter-flow exceeds that of the parallel-flow arrangement. The counter flow arrangement was selected as it results in a more compact heat exchanger [47,58].

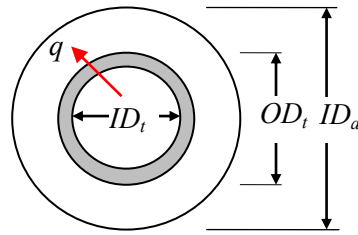


**Figure 3.13** Concentric tube annulus showing inner and outer tube diameters

$$q = UA\Delta T_{lm} \quad (3.6)$$

$$L = q / (U\Delta T_{lm}\pi OD_t) \quad (3.7)$$

$$1/UA = 1/h_i A_i + \frac{\ln\left(\frac{OD_t}{ID_t}\right)}{2\pi k L} + 1/h_o A_o \quad (3.8)$$

$$U_o = \left[ OD_t/h_h ID_t + 1/h_c + \frac{\ln\left(\frac{OD_t}{ID_t}\right) OD_t}{2k} \right]^{-1} \quad (3.9)$$

$$\Delta T_{lm} = \begin{cases} (T_{h,i} - T_{c,o}) - (T_{h,o} - T_{c,i}) / \ln \left( \frac{T_{h,i} - T_{c,o}}{T_{h,o} - T_{c,i}} \right) \dots \text{Counter flow} \\ (T_{h,i} - T_{c,i}) - (T_{h,o} - T_{c,o}) / \ln \left( \frac{T_{h,i} - T_{c,i}}{T_{h,o} - T_{c,o}} \right) \dots \text{Parallel flow} \end{cases} \quad (3.10)$$

The fluid properties in Equations 3.11 to 3.17 are evaluated at the mean temperature for the cold and hot fluids, where  $T_m = 0.5*(T_{in} + T_{out})$ . The energy balance for the concentric tube is based on a constant surface temperature on the tube side, determined by the cooling fluid, with an insulated (adiabatic) shell [58]. The hot fluid in the tube is therefore cooled to the temperature of the cold fluid with a heat capacity rate,  $C_{min}$ , defined in Equation 3.12. The maximum heat transfer calculated in Equation 3.12 is derived from the steady flow energy equation. The convection coefficients ( $h_h$  and  $h_c$ ) in Equation 3.9 are calculated using Equation 3.13. The anticipated lower convection coefficient of the hot fluid controls the rate of heat transfer between the two fluids. A low flow velocity results in a longer condenser length requirement. Also, because the convection coefficient of the cold fluid is much larger than that of the hot fluid, the temperature of the tube wall will follow closely that of the cold fluid [47]. For the flow inside the tube, the inner diameter,  $ID_t$ , is used. The hydraulic diameter ( $D_h$ ) for annulus flow is calculated using Equation 3.14, where  $A_c$  and  $P_w$  are the flow cross-section area and the wetted perimeter, respectively.

$$C_{min} = \dot{m}_h C_{p,h} \quad (3.11)$$

$$q_{max} = C_{min}(T_{h,i} - T_{c,i}) \quad (3.12)$$

$$h = Nu k / D \quad (3.13)$$

$$D = \begin{cases} ID_t & \dots \text{Tube flow} \\ D_h = 4A_c / P_w \equiv (ID_a - OD_t) & \dots \text{Annulus flow} \end{cases} \quad (3.14)$$

The convection coefficient in Equation 3.13 requires the calculation of both the Reynolds numbers ( $Re$ ) and Nusselt numbers ( $Nu$ ) for tube and annulus flow, using Equations 3.15 and 3.16 respectively [47].  $Nu$  is constant for laminar flow in a pipe ( $Re < 2300$ ) but varies for laminar flow in an annulus. The power equation for laminar annulus flow is a curve fit approximation of tabulated values for flow in a circular tube annulus, with one surface at constant temperature and the other insulated (Figure A.2, Appendix A). For transitional and turbulent flow ( $Re > 2300$ ) the Gnielinski correlation gives less than 10% error when compared to the simpler Dittus-Boelter equation, which can give as much as 25% error [47]. To make use

of the Gnielinski correlation, the friction factor is first computed either through the Moody diagram or using the correlation developed by Petukhov, Equation 3.17 [47]. The velocity of flow in the annulus is calculated from continuity, in Equation 3.18. The economic velocity of water is in the range of 1.4 m/s to 2.8 m/s [58].

$$Re = \begin{cases} 4\dot{m}/\pi ID_t \mu & \dots \text{Tube flow} \\ 4\dot{m}/\pi(ID_a - OD_t)\mu & \dots \text{Annulus flow} \end{cases} \quad (3.15)$$

$$Nu = \begin{cases} 3.66 & \dots \text{Tube flow, } Re < 2300 \\ 4.4438(OD_t/ID_a)^{-0.43} & \dots \text{Annulus flow, } Re < 2300 \\ (f/8)(Re - 1000)Pr / \sqrt{1.07 + 12.7(f/8)^{1/2}(Pr^{2/3} - 1)} & \dots Re > 2300 \end{cases} \quad (3.16)$$

$$f = (0.79 \ln(Re) - 1.64)^{-2} \quad \dots Re > 10^4 \quad (3.17)$$

$$V = \dot{m} / [\rho\pi(ID_a^2 - OD_t^2)/4] \quad (3.18)$$

### 3.5.2 Condenser analytical model

Equations 3.6 to 3.18 are coded in MATLAB to investigate the size of the condenser required. The script file is supplied in Appendix F.1. The pseudo-code flow chart in Figure 3.14 describes the analytical procedure. The model investigates a range of annulus diameters resulting in different annulus flow velocities and lengths required to meet a set of operating conditions.

The following assumptions are made to simplify the model:

- 1) The overall heat transfer coefficient is constant over the length of the heat exchanger
- 2) Fluid properties in Equations 3.11 to 3.17 are evaluated at the average saturation temperature.
- 3) The fluid properties are constant steady state
- 4) Phase change is not considered
- 5) Potential energy affects are negligible
- 6) No heat loss to the surroundings

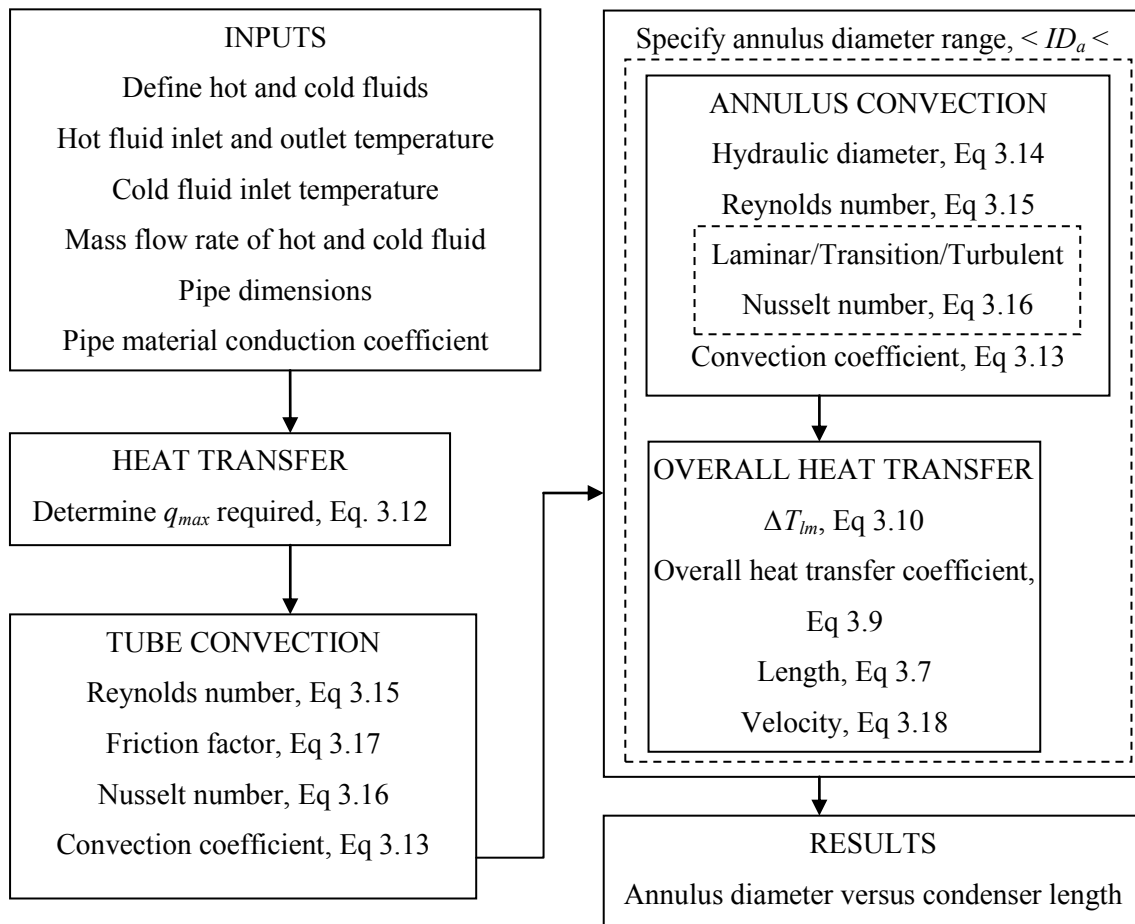


**Figure 3.14** Pseudo-code flow chart for the analytical model of the PTL condenser.

### 3.5.3 Condenser model results

Three coolants were considered for the condenser, including water, a glycol-water mixture of 50:50 and a glycol-water mixture of 30:70. The inputs to the model anticipate the nominal operating temperatures and flow rates of the PTL, as given in Table 3.1. The mass flow rate and operating temperatures of the refrigerant (hot side) are known from previous PTL experiments [59]. Refrigerant flows through the condenser tube (which is a 1/4" tube with 4.55 mm ID) at 5 g/s, entering it at 60°C and condensing to 20°C. The temperature of the condenser coolant is set at 15°C [2]. A range of annulus diameters (larger than the tube diameter) is also specified. For the experimental prototype, a chiller is used with a centrifugal pump providing an approximately steady flow rate of 110 g/s.

**Table 3.1** User defined parameters for the condenser design and selected results. [59]

<b>Design inputs</b>	Refrigerant (hot side)	R-134a
	Refrigerant inlet temperature	60.0°C
	Refrigerant inlet quality	1.00
	Refrigerant outlet temperature	20.0°C
	Refrigerant mass flow rate	5 g/s
	Coolant (cold side)	Water or ethylene glycol-water mixture
	Coolant inlet temperature	15.0°C
	Coolant inlet quality	0
	Coolant mass flow rate	110 g/s
	Tube material conductivity	316 stainless steel, $k_{ss} = 16.30$ W/m.K
	Tube outer diameter, $OD_t$	1/4" $\approx$ 6.35 mm
	Tube inner diameter, $ID_t$	4.55 mm
	Annulus diameter range, $ID_a$	6.5 mm $< ID_a <$ 80 mm
<b>Results</b>	Maximum heat transfer	257.47 W
	Annulus fluid outlet temperature	15.63°C
	Tube fluid Reynolds number	113091.20

The results are presented in Figures 3.15 to 3.17. Similar design graphs can be generated for different steady flow rates, operating temperatures and tube materials. For this case, a total heat transfer of 257.5 W is calculated. Referring to Figure 3.15, water has a lower viscosity than the glycol-water mixtures which results in a larger Reynolds number, larger Nusselt number and an improved heat transfer coefficient. Figure 3.16 shows that this results in a smaller condenser length requirement for a given annulus diameter. An increased glycol percentage in the glycol-water solution increases the viscosity resulting in a reduced Reynolds number, smaller Nusselt number, poorer heat transfer coefficient and an increased condenser length requirement for a given annulus diameter.

The 30% glycol-water offers an acceptable condenser size whilst enabling operation at below freezing temperatures. Figure 3.17 shows the relationship between the coolant flow velocity and the annulus diameter. Continuity requires a reduced flow velocity for increased annulus diameters. The three profiles are similar due to the three fluids having similar saturated liquid densities.

A 14 mm ID annulus diameter was selected for the design, giving a flow velocity of 0.9 m/s (Figure 3.17). From Figure 3.16 the condenser length is 2.35 m. The use of copper tubing was

also investigated as copper is 25 times more conductive than stainless steel. It was found that this would only result in a 51 mm (or 2.2%) reduction in the condenser length for the selected fluid and annulus diameter. This is due to the conduction term of Equation 3.9 having a relatively small impact on the overall heat transfer coefficient in comparison to the convection terms.

This condenser may be used for other fluids including water and glycol-water of 0% to 30% glycol concentration. The lower viscosity of these fluids will result in the condenser being over-designed and will enable subcooling. Conversely, a slight increase in the condenser length will enable subcooling of the 30:70 glycol-water.

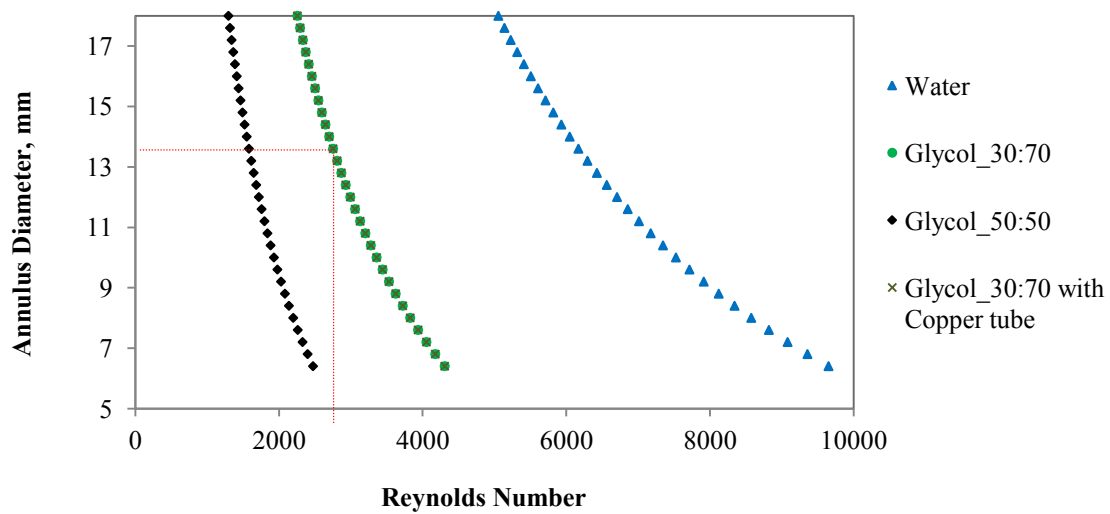


**Figure 3.15** Condenser annulus diameter vs. Reynolds number. Increased fluid viscosity results in a lower Reynolds number.

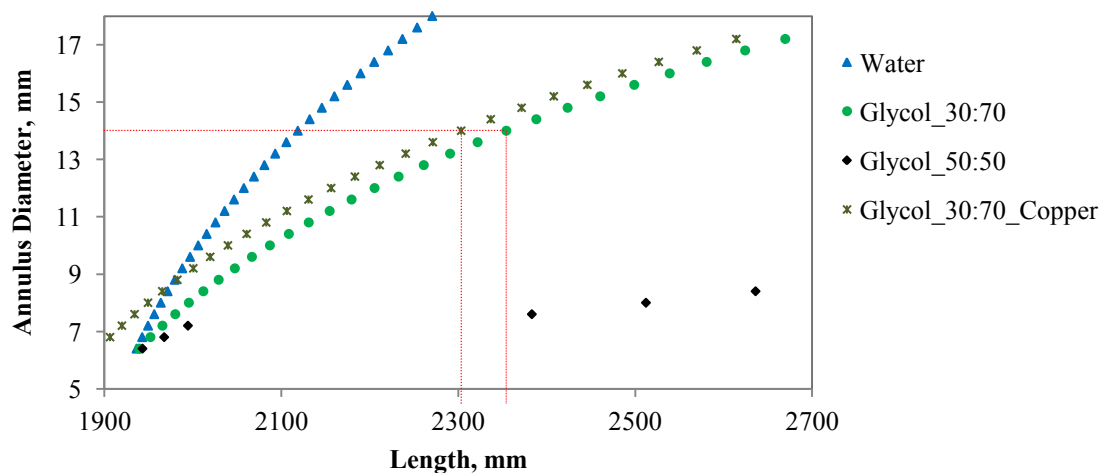


**Figure 3.16** Condenser annulus diameter vs. condenser length. Increased fluid viscosity results in a longer condenser length requirement.



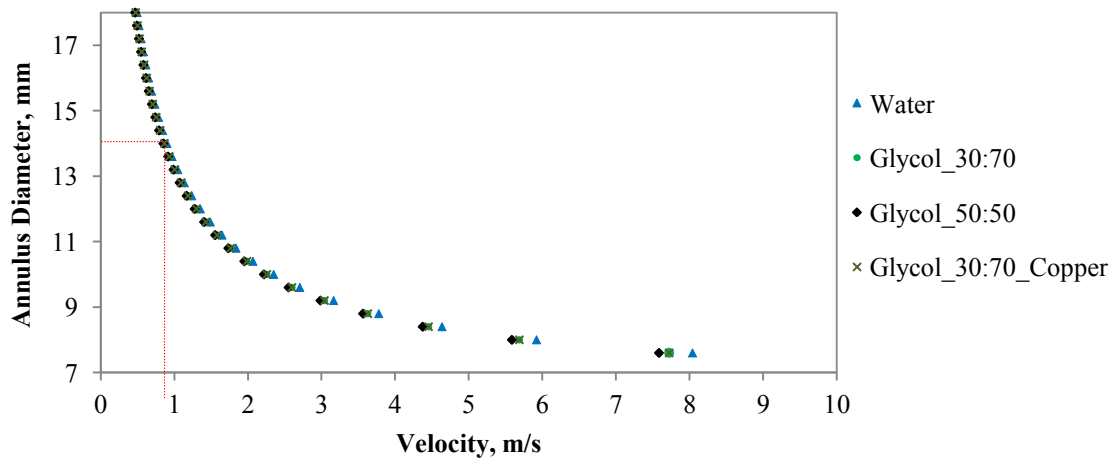


**Figure 3.17** Condenser annulus diameter vs. annulus flow velocity. The velocity profiles are similar due to the different fluids having similar saturated liquid densities.

### 3.5.4 Final condenser design

The design is presented in Figure 3.18. The concentric tubes consist of 1/4" stainless steel inner tubes and 14 mm ID extruded acrylic outer tubes. The 30:70 glycol-water coolant enters and exits the annulus via the inlet manifold. Refrigerant vapor is supplied to the inner tube and exits as subcooled liquid. Thermocouples measure the temperature of both fluids at the inlets and outlets. The manifolds are connected using two 14 mm ID (by 16 mm OD) tubes with a total length of 2354 mm.

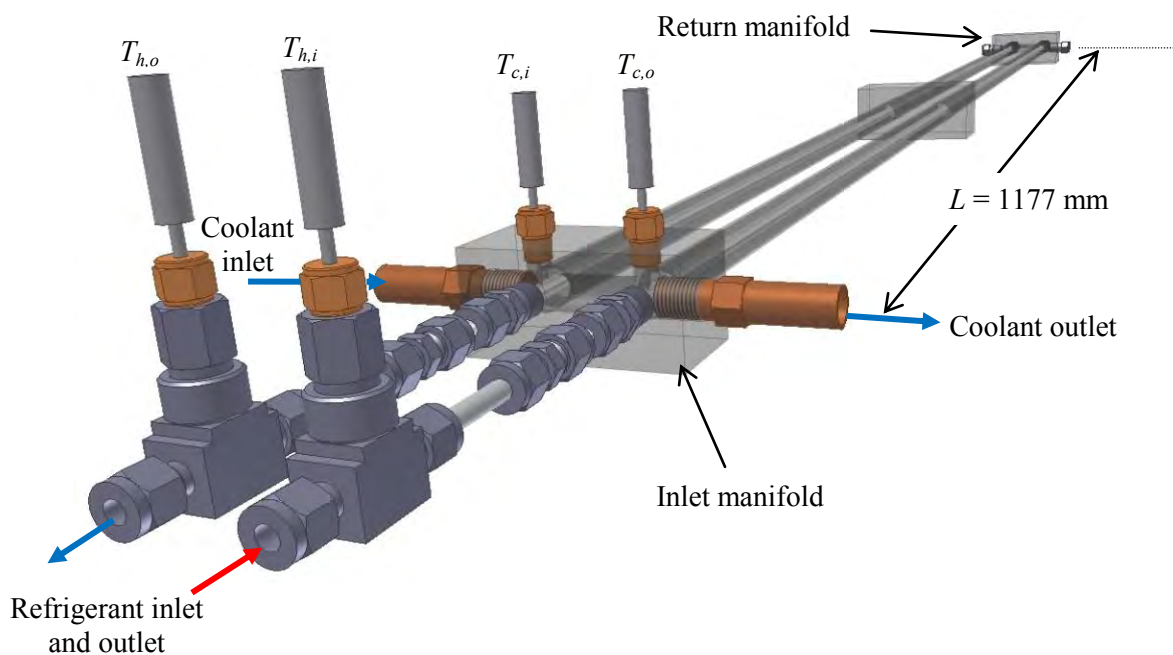


**Figure 3.18** Concentric tube counter-flow condenser design.

### 3.5.5 Condenser assembly

The manufactured condenser is shown in Figure 3.19. The annulus tubes and the manifolds are made from acrylic. The required holes are drilled into the manifolds and the ports tapped with 1/8", 1/4" and 1/2" NPT threads. Two 16 mm holes on each manifold locate the annulus tubes. The tubes are glued into place using chloroform. Four Type-K thermocouples are installed at the fluid inlets and outlets. The fittings are assembled with silicon to eliminate potential leaks. The alternate condenser temperature symbols used in the control software are shown in the figure.

The manufactured condenser length of 2632 mm is 25% longer than the calculated design length. This provides a margin of safety which enables the condenser to perform under varied operating conditions. The condenser tube volume is 42.82 cm<sup>3</sup>.

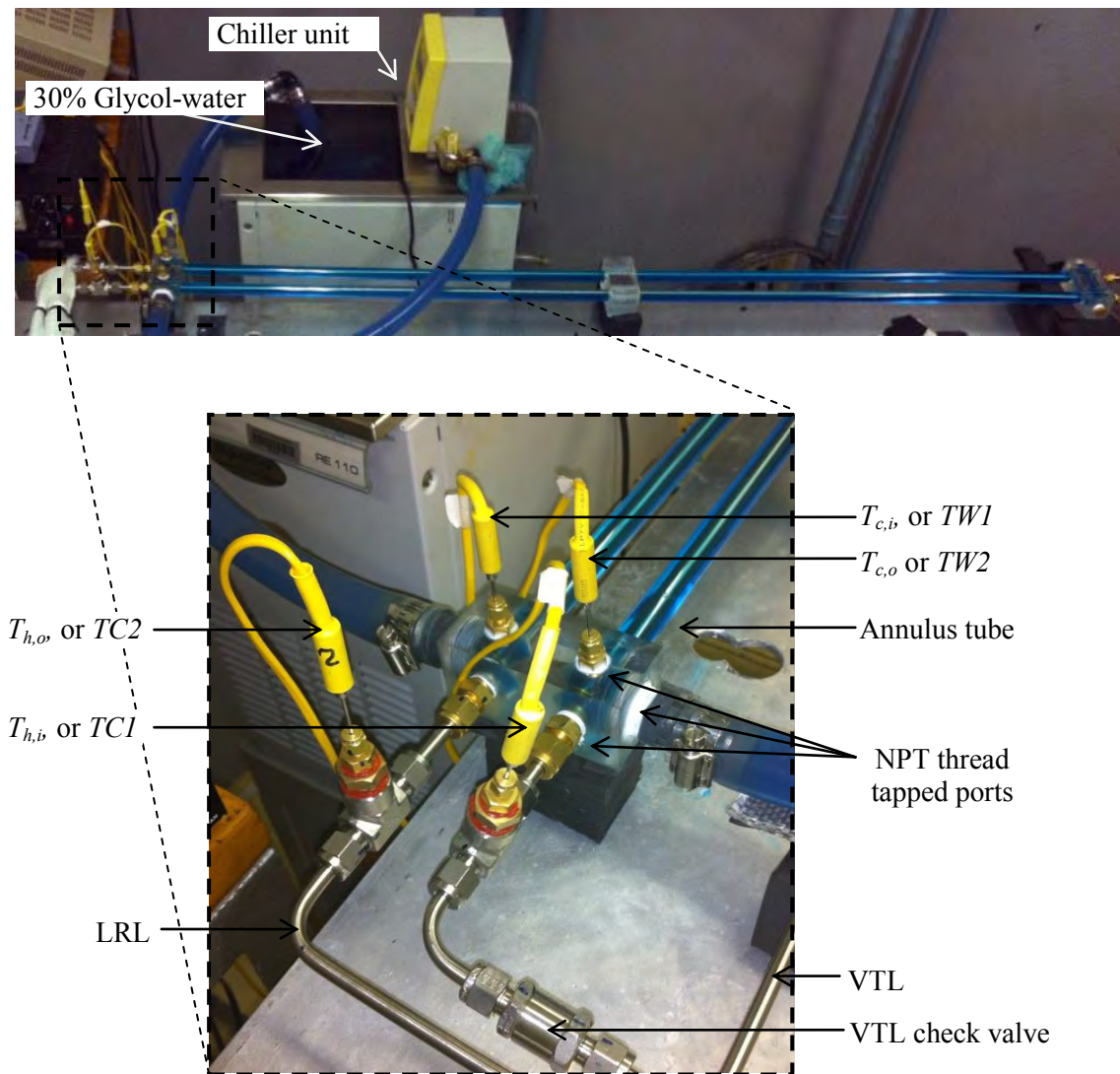


**Figure 3.19** Concentric tube condenser inlet manifold with the hot and cold fluid inlet and exit thermocouples and the VTL check valve.

The coolant is supplied using a LAUDA chiller unit with variable temperature control. The temperature can be adjusted from -30°C to +90°C when using a 30% glycol-water mixture.

### 3.6 Adiabatic transfer lines (VTL and LRL)

The volumes of the remaining system components depend on the boiler volume, and the refrigerant charge mass. A correctly sized VTL, condenser and LRL ensures that there is enough system volume for the boiler pulses to expand and condense into. The guideline volumes of these components are calculated in Table 3.2, using the volume ratios reported by Weislogel and Bacich [16]. This assumes that the system is initially charged with a vapor fraction of 60% to 80% at 6 bar and 20°C. The volume of the condenser in Figure 3.19 is 42.83 cm<sup>3</sup> which is 14.9% smaller than the recommended volume of 50.3 cm<sup>3</sup>. The adiabatic VTL and LRL volumes can be adjusted to achieve the desired overall volume ratio of 1.4.

**Table 3.2** System component guideline volumes based on reported ratios.

	Volume [16], cm <sup>3</sup>	Volume ratio, (Component volume/boiler volume)	PTL and PRS recommended volume, cm <sup>3</sup>
<b>Boiler</b>	44.8	1.00	81.2
<b>VTL</b>	19.7	0.4	35.7
<b>Condenser</b>	27.8	0.6	50.3
<b>LRL</b>	14.9	0.3	26.8
<b>VTL + condenser + LRL</b>	62.4	1.4	113.1

The VTL and LRL plumbing consists of 1/4" transport tubes, valves and fittings. Stainless steel is selected for its compatibility with the instrumentation and fittings. The recommended volumes of the VTL and LRL are 35.7 cm<sup>3</sup> and 26.8 cm<sup>3</sup> respectively. The thermodynamic process should ideally be adiabatic if the VTL and LRL are well insulated, as shown in Figure 3.1.

The VTL consists of simple 90° tube bends. Flow constrictions are minimized to reduce the head losses associated with the high flow velocity. A poppet check valve with a cracking pressure of 0.023 bar (1/3 psi) is installed in the VTL just before the condenser, as shown in Figure 3.19. This ensures that the VTL does not receive backflow of liquid refrigerant from the condenser during low pulse frequency operation. Two VTL lengths are investigated having volumes of 31 cm<sup>3</sup> and 52.5 cm<sup>3</sup>.

The LRL consists of tube bends, a cross fitting with instrumentation, a ball valve, a vent port, and a flow splitting manifold, shown in Figure 3.20. The LRL can be outfitted with more

components as the low flow velocity will result in a relatively small head loss. The stainless steel cross fitting is fitted with a WIKA A-10 pressure transducer and a Type-K thermocouple. This is included in the LRL to aid in determining system leaks. The ball valve is used to isolate the boilers from the loop during leak tests. The vent port enables the connection of a vacuum pump to the loop. This is necessary to evacuate non-condensable gases before charging with refrigerant. The vent port is also used to discharge refrigerant from the system. The flow split manifold simply splits the liquid flow going to the two check valves at the boiler inlets.

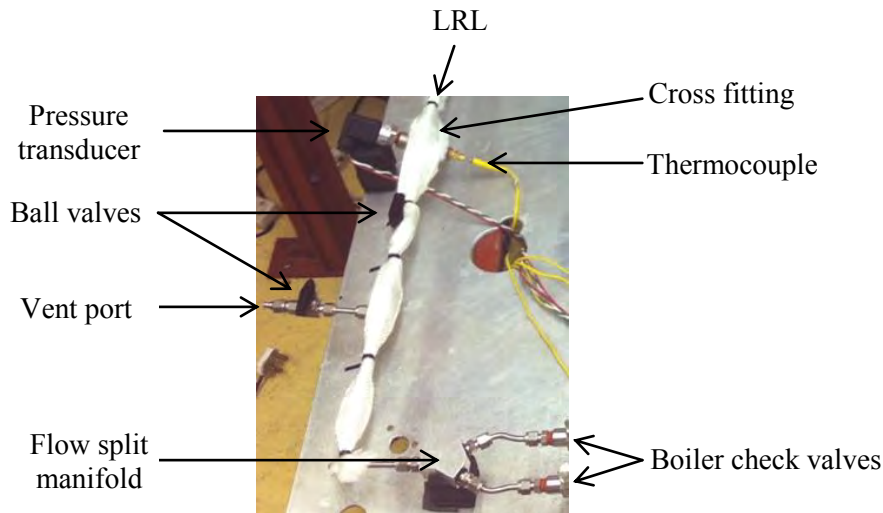


**Figure 3.20** LRL components including necessary valves and instrumentation.

### 3.7 System head losses

The flow of refrigerant through the system's tubing passes through a variety of bends, valves and fittings, or is subjected to abrupt changes in the flow area, which results in flow separation and losses. The system head loss is calculated to work out the minimum pumping pressure required for PTL operation.

The losses include both minor and major losses. Major losses are due to fluid friction with the tube walls and the minor losses are due to flow constrictions. Minor losses arise from flow separation around the corners and swirling secondary flows (caused by centripetal acceleration) [6].

The head loss calculations are included in Appendix B.2 and assume incompressible steady flow. It is assumed that the system is charged such that the VTL and the first half of the condenser contain saturated vapor, and the latter half of the condenser and the LRL contain saturated liquid. The solution is therefore split into two parts; i) the pressure losses in the vapor section, and ii) the pressure losses in the liquid section.

The velocity is calculated from the assumed flow rate of 5 g/s, for the vapor and the liquid portions, using Equation 3.19. The Reynolds number ( $Re$ ) can then be calculated from Equation 3.20. The friction factor ( $f$ ) is found using the Moody Diagram [58] with the Reynolds number and the relative roughness ( $\epsilon/D$ ) of the tube. The total head loss is given by Equation 3.21. The major head loss ( $h_f$ ) due to static head and fluid friction in the transport tubing is calculated using Equation 3.22 where  $L$  and  $D$  are the length and diameter of the pipe, respectively. The PTL is constructed in the horizontal plane therefore has zero static head. The minor head losses are calculated using Equation 3.23, where  $K$  is the sum of the loss coefficients. The head losses can be converted to absolute pressure values using Equation 3.24.

$$V = \dot{m} / \rho A \quad (3.19)$$

$$Re = \rho V D / \mu \quad (3.20)$$

$$h_T = h_f + h_{lm} \quad (3.21)$$

$$h_f = f L V^2 / 2 D g \quad (3.22)$$

$$h_{lm} = K V^2 / 2 \quad (3.23)$$

$$P = \rho g h \quad (3.24)$$

The total head loss amounts to 46.6 m (R-134a) for the vapor section and 0.71 m (R-134a) for the liquid section. The largest contributing loss is the minor losses in the VTL, which amounts to 36 m, or 0.29 bar. The head losses result in a total pressure loss of 0.45 bar. This result does not take into account the losses caused by the multiple changes in flow area due to the fittings used. The significance of this result is that the driving  $\Delta P_{set}$  must be greater than 0.5 bar in order for the PTL to pump refrigerant around the loop.

### 3.8 Final assembly

The final assembly is shown in Figure 3.1. The boiler sub-assembly is connected to the condenser sub-assembly using transport tubing and the various fittings and valves. A second variant of the PTL was also investigated which has a longer VTL. To minimize gravity effects the system is assembled in the horizontal plane. It is thermally isolated from the aluminum table by elevating it at various points using EPDM (ethylene propylene diene monomer) sponge. The adiabatic transport tubes (VTL and LRL) are covered with multilayer insulation. Without such insulation, the VTL and LRL are prone to heat exchange with the ambient air which could affect steady state results, especially at low pulse frequencies.

### **3.9 Instrumentation uncertainty**

The system includes 9 type-K thermocouples which have an uncertainty of  $\pm 0.2^{\circ}\text{C}$ . This is less than 1% for temperatures above  $20^{\circ}\text{C}$ . Two Wika S-10 pressure transducers are installed at the boilers having a maximum uncertainty of  $\pm 0.5\%$  with a response time of 1 ms [60]. One Wika A-10 pressure transducer is installed in the LRL having a maximum uncertainty of  $\pm 1\%$  and a response time of 4 ms [61]. A water pump is used for the glycol-water coolant. The mass flow rate is estimated at 0.1 kg/s.

## 4 CONTROL SYSTEM

The PTL and the PRS are controlled using National Instruments (NI) hardware and a custom-written NI LabVIEW application. This is implemented in a single package to enable efficient use of time and resources available as the hardware is common to both systems. The setup shown in Figure 4.1 includes a computer with NI LabVIEW (Laboratory virtual instrumentation engineering workbench) software, power supplies, instrumentation and NI hardware. The software monitors pressures and temperatures at key locations around the loop. Driving pressure differential, or  $\Delta P$ , control logic is implemented. One or both 3-way servo valves are actuated, depending on the flow configuration. The valve at the outlet of the boilers actuates when a set pressure differential,  $\Delta P_{sets}$  is reached to pulse refrigerant around the loop.

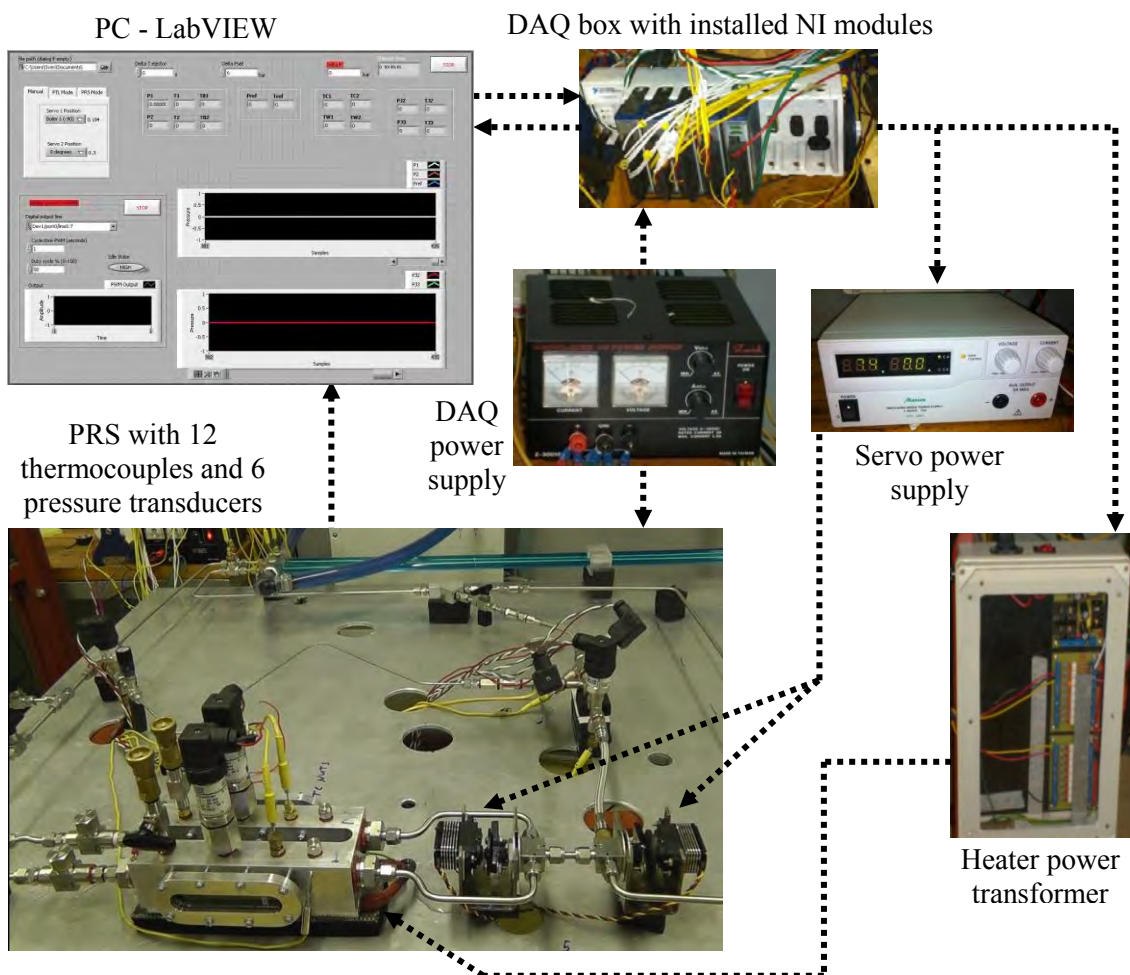


**Figure 4.1** Control hardware for PRS experimental prototype.

### 4.1 $\Delta P$ control features

$\Delta P$  control is the most reliable of the PTL control options. This was investigated and confirmed

by Brooks *et al.* [4] and Weislogel *et al.* [2]. In this scheme, the boiler pressures ( $P1$  and  $P2$ ) are measured once per loop iteration and the absolute difference,  $|\Delta P|$ , is calculated and compared with a set value,  $\Delta P_{set}$ . One pressure transducer measures the building pressure of the isolated boiler whilst the other measures the pressure of the pulsed boiler, which is in communication with the condenser and depressurizing. The software actuates the servo valves when  $|\Delta P| > \Delta P_{set}$ .

NI LabVIEW is a graphical programming language used for data acquisition and automated control. The feed-back data flow environment enables a loop-based control scheme. A custom virtual instrument (VI) is developed with a simple graphical user interface (GUI). The GUI is shown in Figure D.1, Appendix D, and displays the real-time system pressures and temperatures. It enables system parameters such as  $\Delta P_{set}$ ,  $Q$  and valve position to be changed on demand during manual as well as automated operation. The experimental data are recorded to a spreadsheet file for data analysis.

A fast sampling rate of 10 Hz captures finite changes in pressure and temperature. This enables investigation of the transient conditions at the ejector, in the PRS. Fail-safes are incorporated into the VI logic by limiting the maximum temperature and absolute pressure to 100°C and 25 bar, respectively.

## 4.2 $\Delta P$ control logic

The various instruments used in the PTL and the PRS are shown in Figure 4.2. The instruments' specifications are detailed in Table A.11 Appendix A. The basic  $\Delta P$  control logic used for actuating the servos is described with the aid of Figure 4.3. Three operating modes are selectable on the GUI with tabbed-control. A limited description of the VI components is provided in Appendix D.

The operating modes include:

### A. Manual operation

Valves can be actuated on demand for charging and pre-conditioning the system.

### B. PTL operation

This enables the autonomous operation of the PTL.

- i) Valve 1 remains at -90° throughout test
- ii) Monitor pressures and check for  $|\Delta P| > \Delta P_{set}$

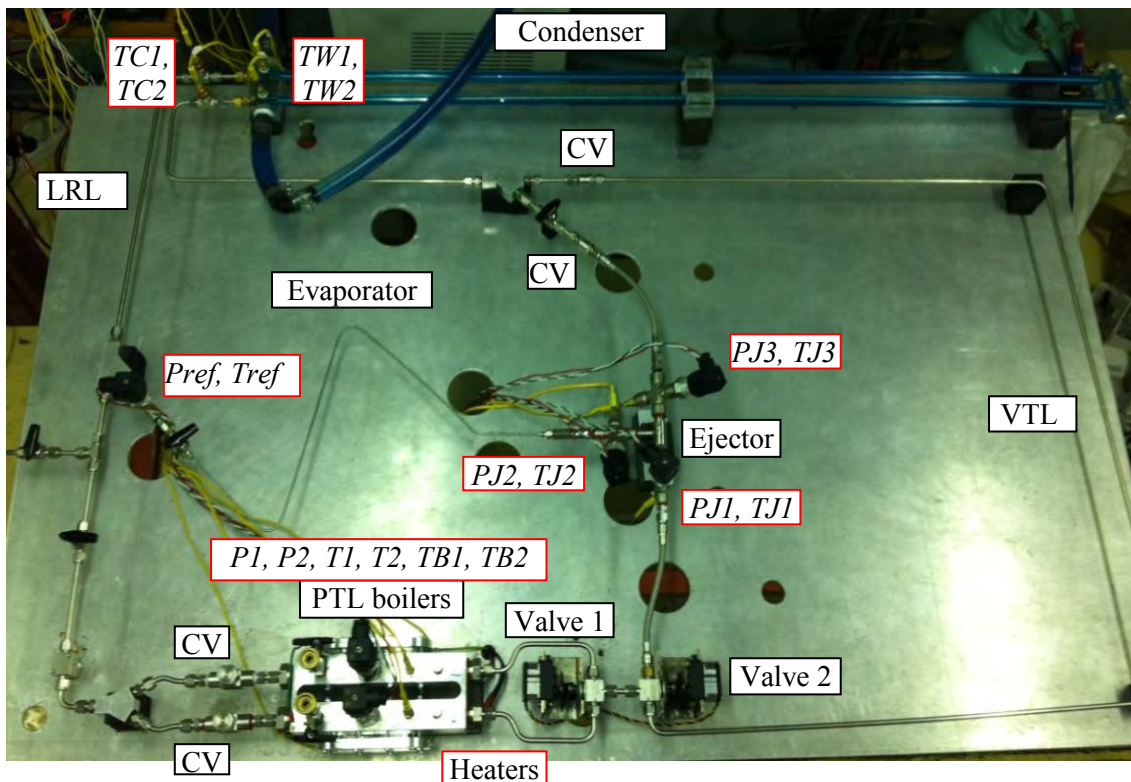


- iii) Valve 1 moves from  $\pm 90^\circ$  to  $\pm 90^\circ$ , sending a pulse of refrigerant through the VTL
- iv) Wait for  $|\Delta P| > \Delta P_{set}$ , and repeat from step ii.

C. PRS operation – Variant I

This enables autonomous operation of the PRS using a second valve.

- i) Monitors pressures and checks for  $|\Delta P| > \Delta P_{set}$
- ii) Valve 2 moves to  $+90^\circ$
- iii) Valve 1 moves from  $\pm 90^\circ$  to  $\pm 90^\circ$ , sending a portion or all of the pulse of refrigerant to the cooling loop
- iv) Wait  $\Delta t_{ejector}$  after valve 1 has moved. This depends on the portion of the pulse required to drive the ejector
- v) Valve 2 moves to  $-90^\circ$  (if required), sending the remainder of the pulse of refrigerant around the PTL bypass in an effort to minimize non-isentropic losses at the ejector
- vi) Wait for  $|\Delta P| > \Delta P_{set}$ , and repeat from step ii.



CV: Check valve      P: Pressure transducer      T: Thermocouple

**Figure 4.2** Instrument locations for the PTL and PRS. Other variants were investigated incorporating the same instruments.

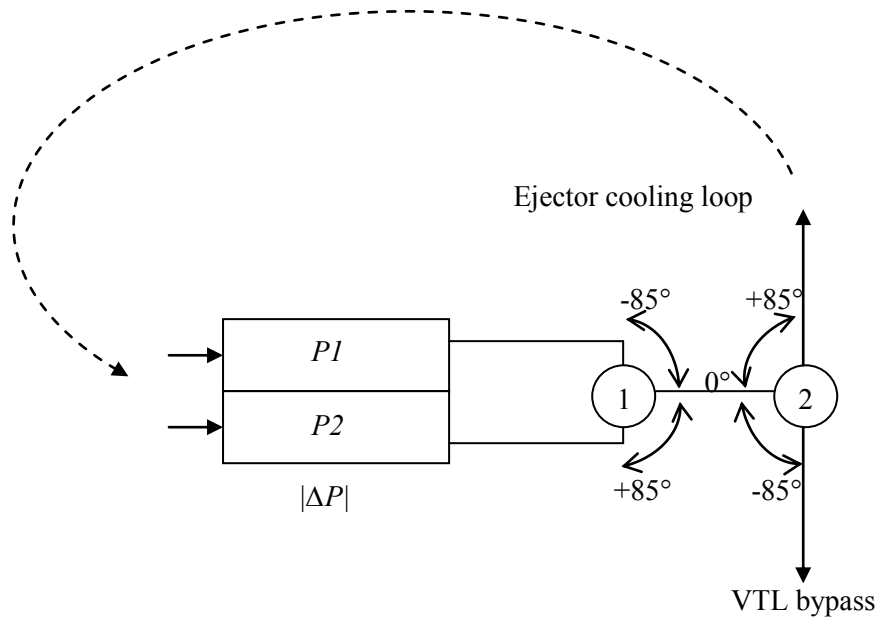


**Figure 4.3** Schematic of  $\Delta P$  control logic for manual, PTL and PRS operation.

### 4.3 Servo control with PWM

The servos and the heaters are controlled with pulse width modulation (PWM). The average power of a signal is controlled by altering the duty cycle of a fixed frequency pulse train, shown in Figure 4.4. The duty cycle is the ratio of the time for which the signal is high to the pulse period. For a pulse frequency of 100 Hz, the period ( $1/f$ ) is 10 ms. A standard servo's neutral position occurs when the signal is high for 1.5 ms. This translates to a 15% duty cycle for the given frequency. If the frequency is doubled, the duty cycle doubles to 30%. The increased 'on' time relative to the pulse period, improves the power output. The servos are duty cycled at 200 Hz in the application.

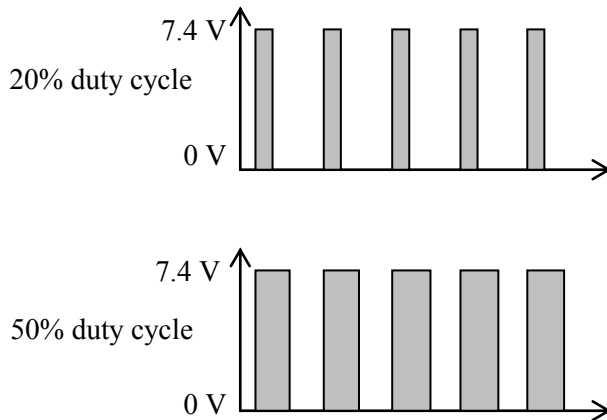


**Figure 4.4** PWM signals with different duty cycles.

The NI 9474 digital output module includes two digital counters. These are used to generate the PWM signals for the two servos. A pull down resistor (of 10 k $\Omega$ ) is required to ground the floating signal (when the signal is in the ‘off’ state).

#### **4.4 Heater power control with PWM**

Due to the hardware limitation of only having two counters available (which are used for the servos), the heaters’ PWM is generated in software with a loop controlled Boolean signal generator. The Boolean signal consists of a string of 1s and 0s representing the duty cycle. The signal is sent to the transformer box, which powers the two 500 W heaters when the signal is high (1s). A 10% duty cycle results in 100 W heat input at the boilers.

#### **4.5 Hardware**

The hardware includes an NI cDAQ chassis, five modules, two power supplies, a transformer box, and the instrumentation.

##### **4.5.1 Power supply**

Two separate power supplies are required in the current configuration. One power supply powers the pressure transducers whilst the other powers the servos. The servo power supply has a current limiting feature which is set to 7 Amps to prevent overloading them. A transformer provides the heaters with 230 V AC when it receives a positive signal from heater the output module. The power supplies are connected to a common ground.

##### **4.5.2 DAQ chassis and modules**

A compact cDAQ 9172 chassis is used to interface the input/output modules with the computer via USB 2.0 interface. The chassis has 8 slots available of which 5 are utilized in the current application. The modules include:

- 1) NI 9211
  - 4 channel thermocouple input module
  - 24 bit resolution
  - $\pm 80$  mV inputs
- 2) NI 9203
  - 8 channel analog input module (for the pressure transducers)
  - 16 bit resolution
  - $\pm 20$  mA

3) NI 9474

- 8 channel digital output (for heater and servo control)
- 5 V to 30 V signal generation
- 2 counters

### 4.5.3 Instrumentation

Twelve Type-K thermocouples and six pressure transducers are installed in the system. The transducers are Wika S-10 and Wika A-10 units, each of which converts the pressure into a 4 mA to 20 mA electrical signal. The signal is then converted back into a pressure reading using Equations 4.1 and 4.2, where  $I$  is the current in Amps. The Wika S-10 and A-10 models measure absolute pressure in the range of 1 bar to 25 bar and 0 bar to 24 bar, respectively.

$$P = 1562.5 \times I - 5.25 \dots \text{Wika S-10} \quad (4.1)$$

$$P = 1562.5 \times I - 6.25 \dots \text{Wika A-10} \quad (4.2)$$

## 4.6 Summary

A LabVIEW application enables efficient control over both the PTL and the PRS variants. The VI (described in D.3) includes tabbed control for selecting manual, PTL auto or PRS auto control. The application monitors the temperatures and pressures, and actuates the valves when  $\Delta P_{set}$  is reached. The data are logged to a spreadsheet file for post processing the results. Fail-safes are integrated into the logic to ensure safety of the equipment and the operators.

## 5 PULSE THERMAL LOOP PERFORMANCE

This phase of the research involved validating the PTL concept experimentally for a range of operating conditions. This includes investigating the system performance for a range of driving pressure differentials ( $\Delta P_{set}$ ) and power inputs ( $Q$ ). The experimental data are analyzed presenting nominal and off-nominal operation.

### 5.1 Experimental procedure

The experimental procedures include evacuating the system, charging it with refrigerant, pre-start up, starting, steady state and shut down.

#### 5.1.1 Evacuating procedure

A vacuum pump is connected to the vent port in the LRL to put the loop under a vacuum and remove non-condensable gases. The pressure is lowered to approximately 0.05 bar and the system is monitored for leaks.

#### 5.1.2 Charging procedure

Before charging the system with refrigerant, an acceptable charge mass is calculated to achieve the desired mass distribution around the loop during operation. Figure 5.1 is adapted from Weislogel and Bacich [16] and illustrates the mass distribution of the vapor and liquid in the loop, just prior to a pulse occurring. Under normal operating conditions it is assumed that the open (depressurized) boiler, the VTL and half the condenser contains slightly superheated vapor at 8 bar just prior to a pulse. The second half of the condenser and the LRL contain saturated liquid at 8 bar. Lastly, the sealed boiler contains 20% saturated liquid and 80% saturated vapor at 14 bar. A charge mass of 80.9 g is calculated for these conditions in Appendix B.3.

The calculated charge mass of 80.9 g gives a system vapor fraction ( $x$ ) of 76% at 20°C, in Equation 5.1. This falls within the recommended range of 60% to 80%. The PTL is able to operate with an increased charge mass (i.e. a lower vapor fraction), however, an increase in refrigerant mass results in increased system pressures for a given heat input and condenser temperature.

$$m_{T\ system} / V_T = \rho_l - x\rho_l + x\rho_v \quad (5.1)$$

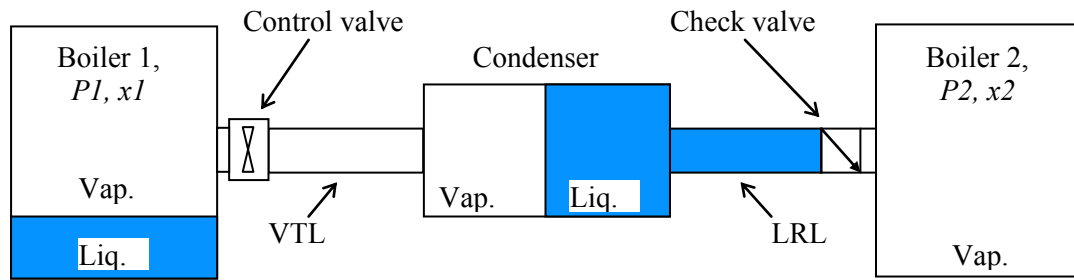


**Figure 5.1** Schematic of refrigerant mass distribution before a 16 bar pulse with a  $\Delta P_{set}$  of 8 bar. [16]

After leak testing, both the loop and the charging cylinder are evacuated. The empty mass of the charging cylinder is recorded using a digital scale accurate to 0.1 g. The charging cylinder is cooled using ice to lower the pressure in the vessel. It is then connected to an R-134a supply line via the Schrader valve and filled with liquid refrigerant. The cylinder is warmed up to ambient conditions, whilst the boiler block is cooled using ice packs. The total mass of the full charging cylinder is recorded to note the amount of refrigerant it contains. The cylinder connects to the boiler block using quick connects, as shown in Figure 5.2. The two-way valve on either side of the quick connects controls the flow of refrigerant into the boiler chamber (Figure 5.3). One boiler chamber filled with saturated liquid at 20°C contains an approximate mass of 102 g. After discharge, the empty cylinder mass is recorded to note the mass of refrigerant transferred to the system. This process is repeated until the system is adequately charged.

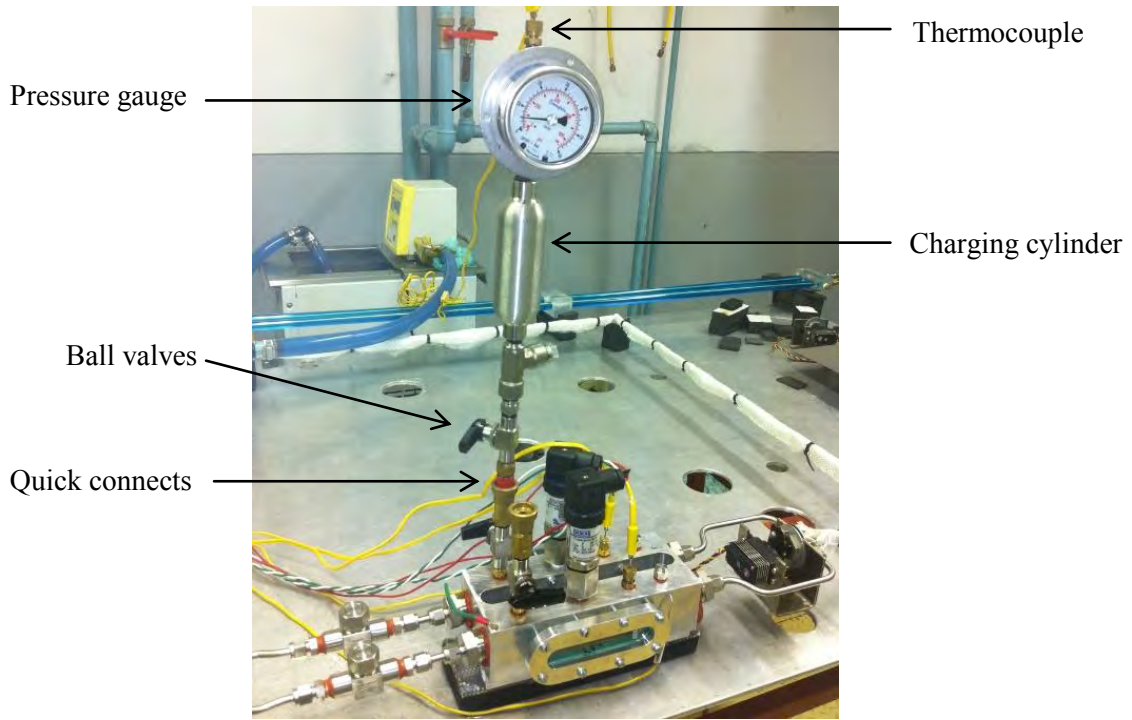


**Figure 5.2** Charging cylinder connected to the boiler using quick connects. The ball valves are opened to fill the boilers with refrigerant.

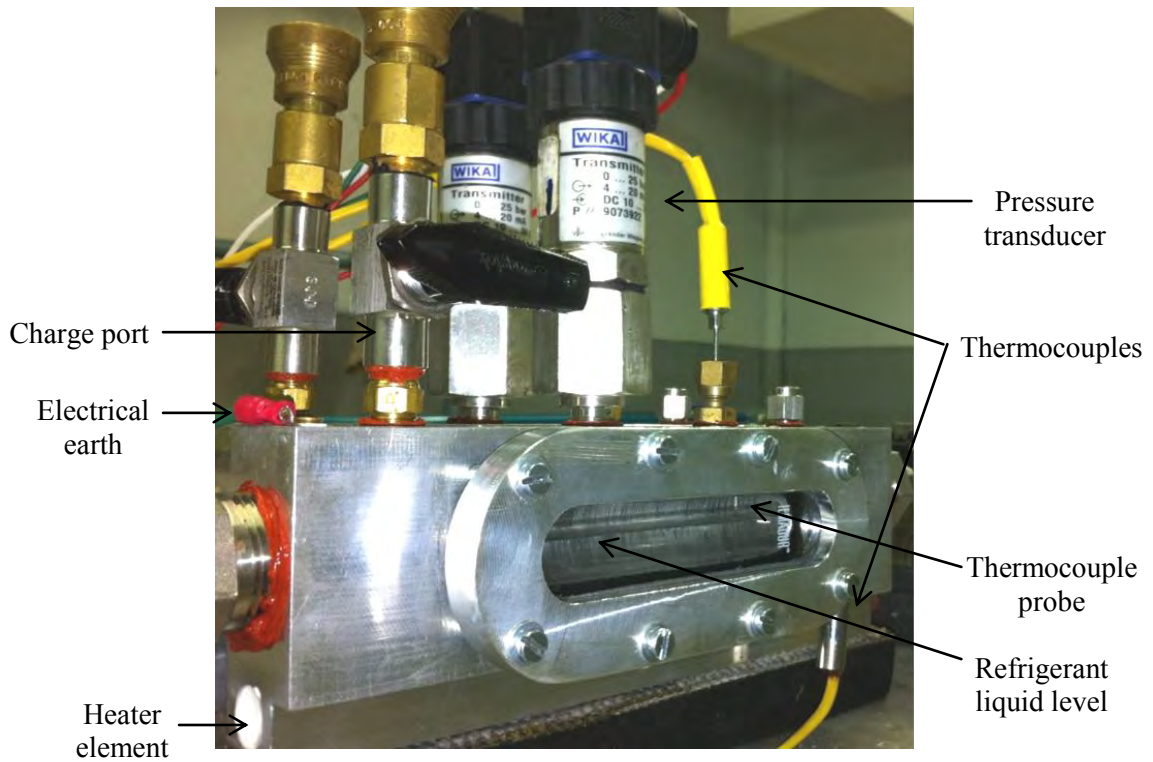


**Figure 5.3** Boiler liquid level viewed through the sight glass.

### 5.1.3 Start-up procedure

Once the system is charged with an adequate mass of refrigerant ( $0.6 < x < 0.8$ ), certain pre-conditioning steps are followed to ensure an appropriate refrigerant mass distribution in the loop before start-up:

1. The loop is pre-conditioned such that at least one boiler contains the required refrigerant level (approximately 20% full).
2. If a boiler contains more than 20% liquid refrigerant, heat is applied and some of the mass is directed into the loop. This ensures that there is enough condensed fluid in the LRL to be injected into the lower pressure boiler after the first pulse. The loop is pre-conditioned through controlling the evaporator and condenser temperatures.
3. The condenser coolant temperature ( $TWI$ ) is set, along with the power input ( $Q$ ), and  $\Delta P_{set}$ .
4. If both boilers contain an adequate amount of refrigerant, the operator has two options to achieve the required  $\Delta P_{set}$ :
  - a. Allow one boiler to communicate with the condenser during start-up allowing the mass of refrigerant to evaporate, migrate to, and condense in the condenser. This will ensure that there is liquid present in the LRL before the first pulse occurs. The alternate boiler is isolated and increasing in pressure until  $\Delta P_{set}$  is reached to initiate valve toggling.
  - b. Allow both boilers to be isolated from the condenser and increasing in pressure during start-up. This gives the operator redundancy in case one of the boilers' valves leak during start-up. If no internal leakage occurs, the first of the two pulses can take place at some intermediate pressure value. The alternate boiler continues to increase in pressure until  $\Delta P_{set}$  is reached to initiate valve toggling.
5. Prior to the first pulse, the VTL is externally heated. This minimizes premature condensation during the first few pulses. The system can be started without this pre-conditioning step.
6. Ice is placed at the boiler inlet check valves during start-up to prevent heat creep and ensure that liquid (not vapor) refrigerant is available for injection. The system can be started without this pre-conditioning step.



### 5.1.4 Steady-state operation

A settling time of up to 10 min is allowed after a system variable is changed. This ensures that steady state is reached and provides the necessary data to enable higher level analysis of the results.

### 5.1.5 Shut-down procedure

The use of a routine shut-down procedure prevents damage to equipment and facilitates the subsequent start-up. This includes:

1. Switching to manual control
2. Turning off the heater power whilst monitoring the temperature and pressure
3. Turning off the coolant fluid flowing through the condenser

## 5.2 Experimental results

The PTL was successfully demonstrated 22 times during this phase of the research. The longest unbroken run lasted a total of 7 hours and 19 minutes. These results support the notion that the PTL has good potential for deployment as a thermal management system in the power range from 200 W to 800 W.

The response of the system to changes in four variables, namely,  $\Delta P_{set}$ , heater power ( $Q$ ), condenser temperature ( $TWI$ ), and refrigerant charge vapor fraction ( $x$ ), was investigated. The primary independent variables included  $\Delta P_{set}$  and  $Q$ . During operation, one variable was changed systematically whilst the others were kept constant. Refrigerant charge mass and condenser temperature were kept constant.

### 5.2.1 PTL - ideal start-up

For a PTL that has been previously charged, operated, and shut down under normal conditions, no pre-conditioning of the loop is required. The loop starts by simply turning on the heater power if at least one of the boilers contains an appropriate mass of refrigerant.

Figure 5.4 illustrates that start-up is often characterized by an initial temperature overshoot, especially for starting at increased  $\Delta P_{set}$ .  $P1$  and  $P2$  represent the absolute pressure inside the two boiler chambers whilst  $TB1$  and  $TB2$  represent the boiler block temperatures. In this test, the system was charged with 115 g of R-134a (65% vapor at 20°C). Power was supplied to the boilers at 800 W simulating a waste heat load, and the condenser was set to 20°C. PTL operation was initiated at 320 s reducing the boiler temperature from 80°C to a steady 53°C

within 200 s. The average pressure in the boilers reduced from 17 bar to 12.5 bar. The graph illustrates the importance of having a TMS for controlling the temperature of sensitive electronics. If there was no TMS in place, the block temperature would rapidly have reached 100°C.

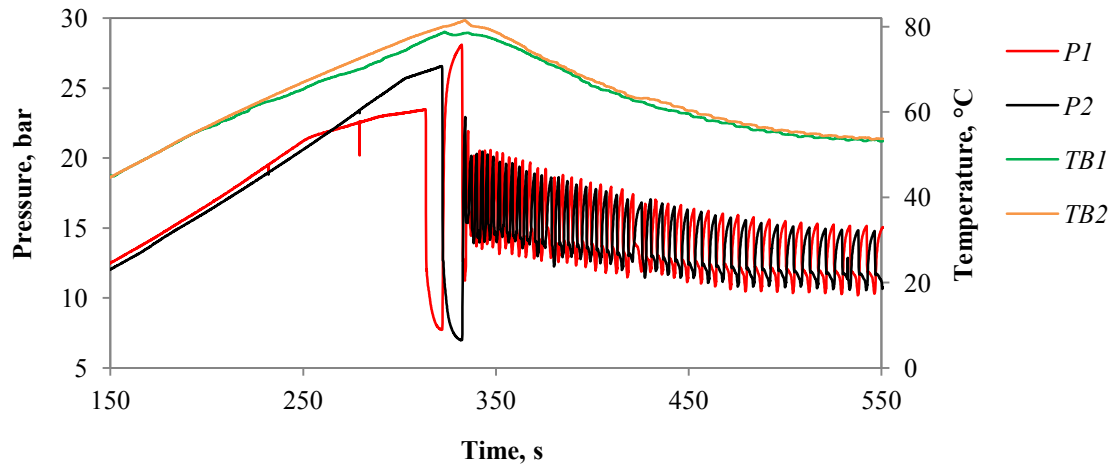


**Figure 5.4** Ideal PTL start-up pressure and temperature response. Short VTL with  $x = 0.65$ ,  $Q = 500$  W and  $TWI = 20^\circ\text{C}$ . After initiating pulses with a  $\Delta P_{set}$  of 4 bar, the average boiler pressure reduced from 24 bar to 12.5 bar, and temperature reduced from  $80^\circ\text{C}$  to  $54^\circ\text{C}$ .

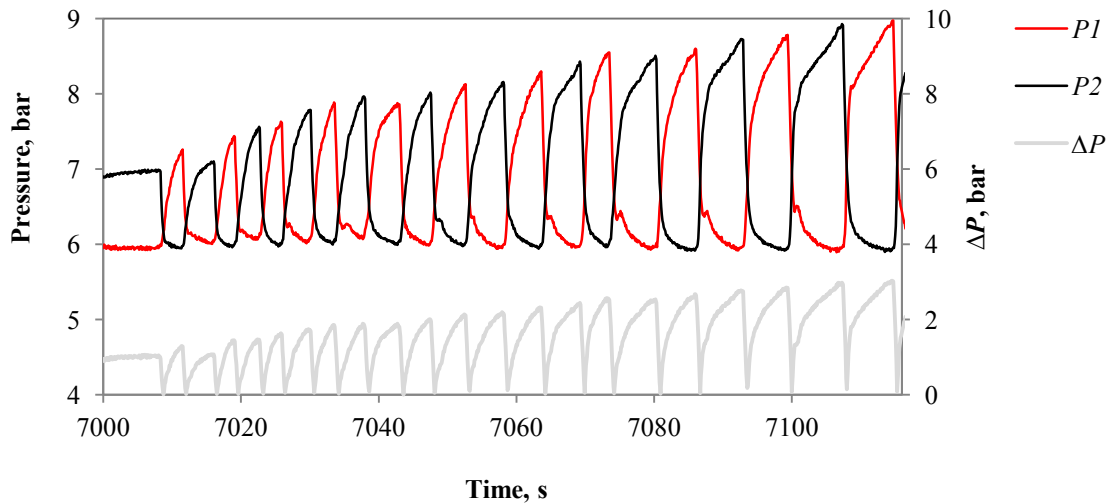
### 5.2.2 PTL - non-ideal start-up

Off-nominal start-up or even failure of the loop occurs if the refrigerant mass and distribution is not ideal. In this way the PTL is similar to a CPL or LHP, which are sensitive to wick liquid levels at start-up.

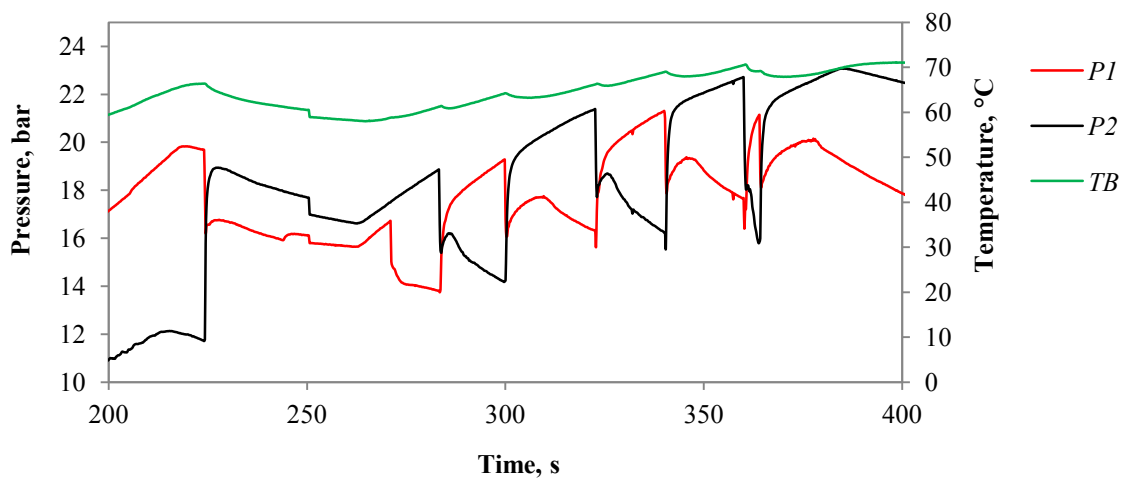
A low refrigerant mass in the boilers at start-up can result from improper shut-down or internal valve leaks. The loop can however be started by forcing the pulses at low to progressively larger  $\Delta P_{set}$  (from as low as 1 bar). This can be seen in Figure 5.5 where the boilers initially contained very little mass and could not pressurize. The  $\Delta P_{set}$  was incrementally increased from 1 bar to 3 bar and slowly more mass was circulated which allowed for the boiler pressures to increase, enabling increasingly larger  $\Delta P_{set}$ . This flexibility in starting is advantageous compared to CPL and LHP systems.

Figure 5.6 shows the result of the PTL being over-charged with 170 g of refrigerant, or 52% vapor. Heat was supplied to the boilers at 500 W and the condenser was set to  $15^\circ\text{C}$ . The pressure history indicates that the  $\Delta P$  is highly pressure limited, relying more on the pressurizing boiler to increase  $\Delta P$  since the emitted pulse cannot exchange heat with the

condenser. This is due to the condenser being flooded with excess refrigerant. The average boiler pressure ( $P$ ) and temperature ( $TB$ ) continue to increase and the test is aborted. Photographs of this experiment are provided in Figure E.2, Appendix E, and video footage is provided in Appendix G.3.



**Figure 5.5** PTL start-up from a low  $\Delta P_{set}$  of 1 bar.



**Figure 5.6** PTL start-up with high charge mass. Large VTL with  $x = 0.52$ ,  $Q = 500$  W and  $TWI = 15^\circ\text{C}$ . The system pressure increases, and the test is aborted.

Figure 5.7 shows the result of an under-charged PTL with 80 g of R-134a, or 79% vapor. Heat was supplied to the boilers at 300 W and the condenser was set to  $15^\circ\text{C}$ . The pressure history indicates that the  $\Delta P$  is both condenser and pressure limited. Since the system is under-charged, the pulsed refrigerant tends to collect in the condenser which is approximately  $5^\circ\text{C}$  colder than the ambient LRL. A pulse results in a small amount of refrigerant vapor in the LRL being injected into the lower pressure boiler. Subsequently, the boilers cannot pressurize and increase

in temperature since evaporative cooling is limited. The condenser cannot depressurize any further than the saturated temperature limit. The average boiler temperature ( $TB$ ) continues to increase and the test is aborted.

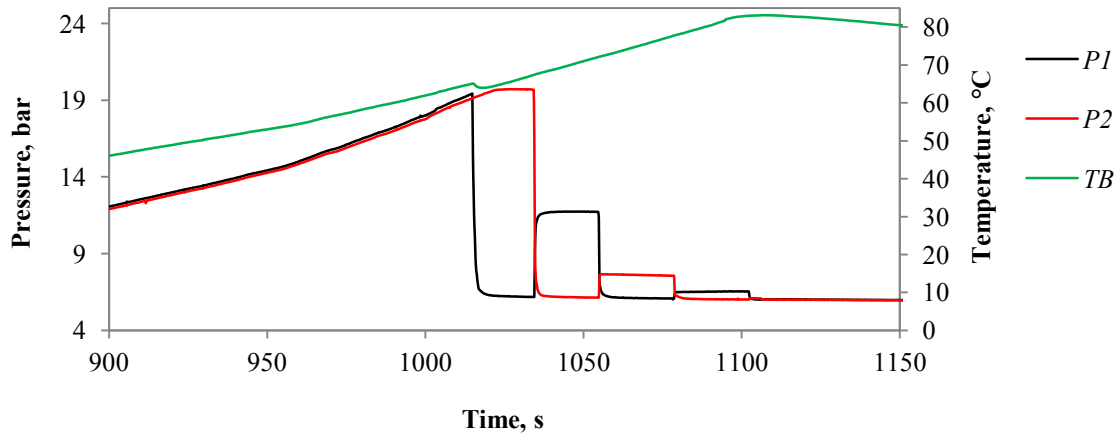


**Figure 5.7** PTL start-up with low charge mass. Large VTL with  $x = 0.79$ ,  $Q = 300$  W and  $TWI = 15^\circ\text{C}$ . The boiler temperature increases, and the test is aborted.

### 5.2.3 PTL – asymmetric operation

The PTL operated asymmetrically in a number of experiments. Symmetric operation is characterized by approximately isothermal boilers which pressurize and depressurize at approximately the same rate to reach similar maximum and minimum pressures. Approximately equal amounts of refrigerant are injected into each boiler with each pulse. Asymmetric operation is characterized by each boiler operating between different maximum and minimum pressures with the refrigerant mass unevenly distributed around the loop. One boiler consistently receives a different mass of refrigerant to the other.

The three primary causes of asymmetric pulsing include:

1. Uneven heating of the boilers  
This can occur for thermally decoupled boilers which are exposed to different heat sources. This was not the case with the current set-up.
2. Step changes in the operating conditions  
The working fluid can be unevenly distributed due to transient changes in  $\Delta P_{set}$  or  $Q$  during testing. A larger increment (or step change) in  $\Delta P_{set}$ , affects the subsequent mass injection into the alternate boiler. As the alternate boiler receives more mass than the one that preceded it, it cools and takes longer to pressurize. This could be the cause of the uneven mass distribution seen in Figure 5.8.

### 3. Incorrectly calibrated check valves

An incorrectly calibrated boiler inlet check valve will require a different cracking pressure in order for it to operate, and may close prematurely. In this case, one of the boilers is consistently charged with a lesser mass of refrigerant. The data indicate that the asymmetry experienced in this study is unbiased therefore check valve calibration is unlikely to be the cause.

Figure 5.8 shows the effects of asymmetric operation. For a constant  $Q$  of 400 W, and  $\Delta P_{set}$  ranging from 3 bar to 9 bar, the pressure histories for the two boilers ( $P1$  and  $P2$ ) occur between different maximum and minimum pressures. A closer view of the pressure history from 1860 s to 2100 s is shown. Boiler 1 initially operates at approximately 6°C higher temperature than boiler 2. The trend indicates that boiler 1 is initially pulse limited where it is under mass and relies on  $P1$  to increase in order to generate the  $\Delta P$ . The pressure oscillates between 6.5 bar and 13.5 bar. Boiler 2 pressurizing is initially condenser limited where it is over mass and relies on  $P1$  to decrease in order to generate the  $\Delta P$ . The pressure oscillates between 8.6 bar and 11.5 bar.

A level of feedback control can mitigate asymmetric operation and improve system performance. The  $\Delta P_{set}$  in this test was intermittently decreased from 5 bar to 4 bar during  $P1$  pressurizing, for three pulses occurring at 1930 s, 1970 s and 2000 s. This results in a weaker pulse which forces a reduced amount of refrigerant into the alternate lower pressure boiler ( $P2$ ).  $TB2$  starts to increase whilst  $TB1$  starts to decrease, since boiler 1 receives comparably more refrigerant. The process can be repeated until the temperatures converge and the pulses become more symmetrical. The pulsing is notably more symmetric after 3100 s, where the two boiler temperatures have equalized.

Feedback control was manual in this study, however it could be implemented in software to ensure a greater level of control. This would enable software to monitor which boiler is operating at a lower pressure and temperature, and then intervene to force a particular boiler to pulse at a different  $\Delta P_{set}$  in an effort to distribute the refrigerant more evenly between the boilers. This opens up an interesting new avenue of research related to PTL operation and control.

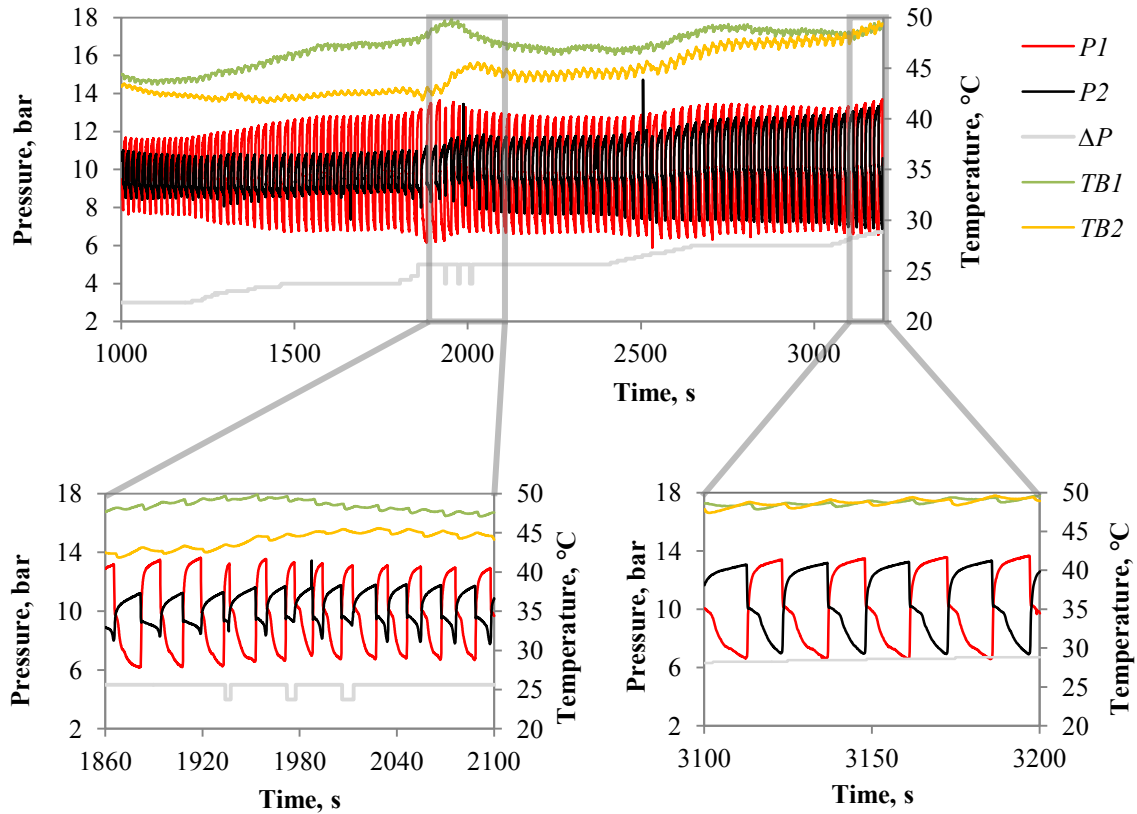


**Figure 5.8** Asymmetric pulsing. Small VTL with  $x = 0.65$ ,  $Q = 400$  W and  $TWI = 20^\circ\text{C}$ . The macro view shows the temperature and pressure response to  $\Delta P$  feedback control. The boiler containing the lesser mass ( $P1$ ) is intermittently pulsed at a lower  $\Delta P_{set}$  forcing less R-134a into the alternate boiler ( $P2$ ). Operation becomes more symmetric.

#### 5.2.4 PTL – varied $\Delta P_{set}$

The pressure and temperature history of a typical experiment is provided in Figure 5.9 to enable a macro description of the effect of  $\Delta P_{set}$  on the boiler temperature ( $TB$ ) and the pulse frequency ( $f$ ). The pulse frequency ( $f$ ) is defined as the number of pulses achieved by the two boilers per second (Hz), Equation 5.2.

$$f = \frac{\text{no. pulses}}{\text{time}} \quad (5.2)$$

In this test, the PTL had a large VTL of  $52.5 \text{ cm}^3$  installed. It was charged with 64% vapor at  $20^\circ\text{C}$ , the heater power ( $Q$ ) was set to 500 W and the condenser coolant temperature ( $TWI$ ) was maintained at  $15^\circ\text{C}$ . During  $\Delta P_{set}$  transients, the loop responded naturally by adjusting the block temperature ( $TB$ ) and the pulse frequency ( $f$ ). Adequate time was allowed between steps in  $\Delta P_{set}$  for  $TB$  to stabilize. In Figure 5.9, as  $\Delta P_{set}$  is reduced from 10 bar to 4 bar, the mean boiler

pressure decreases from 12 bar to 9 bar,  $TB$  decreases from 61°C to 45°C and the pulse frequency ( $f$ ) increases from 0.108 Hz to 0.252 Hz. The results indicate that a certain  $\Delta P_{set}$  can be specified to maintain  $TB$  at a desired value.

A set of data plots are shown for this test in Figure 5.10 (a) and (b), where 50 seconds of data are displayed for  $\Delta P_{set}$  of 10 bar and 4 bar, respectively. Referring to Figure 5.10 (a), the refrigerant injection, pressurizing and pulsing process is indicated on the vapor temperature history trend ( $TI$ ) for boiler 1, whose pressure history is marked in red. At steady states the vapor temperature ( $TI$ ) fluctuations are as high as  $\pm 4^\circ\text{C}$ , whilst the block remains at an approximately constant temperature ( $TBI$ ). A typical mass injection, pressurizing and pulsing process is photographed in Figure E.1, Appendix E. Experimental video footage is also provided in Appendix G.1 and G.2.

Vapor temperature inside boiler 1 ( $TI$ ) varies by up to 13°C for a  $\Delta P_{set}$  of 10 bar and up to 5°C for a  $\Delta P_{set}$  of 4 bar. The block temperature ( $TBI$ ) is approximately isothermal for both  $\Delta P_{set}$  values and only varies by  $\pm 1^\circ\text{C}$  for a given steady state  $\Delta P_{set}$ . There is noticeably less temperature fluctuation at lower  $\Delta P_{set}$ . The PTL therefore enables an almost isothermal heat sink temperature ( $TB$ ), even though it is an oscillatory cycle.

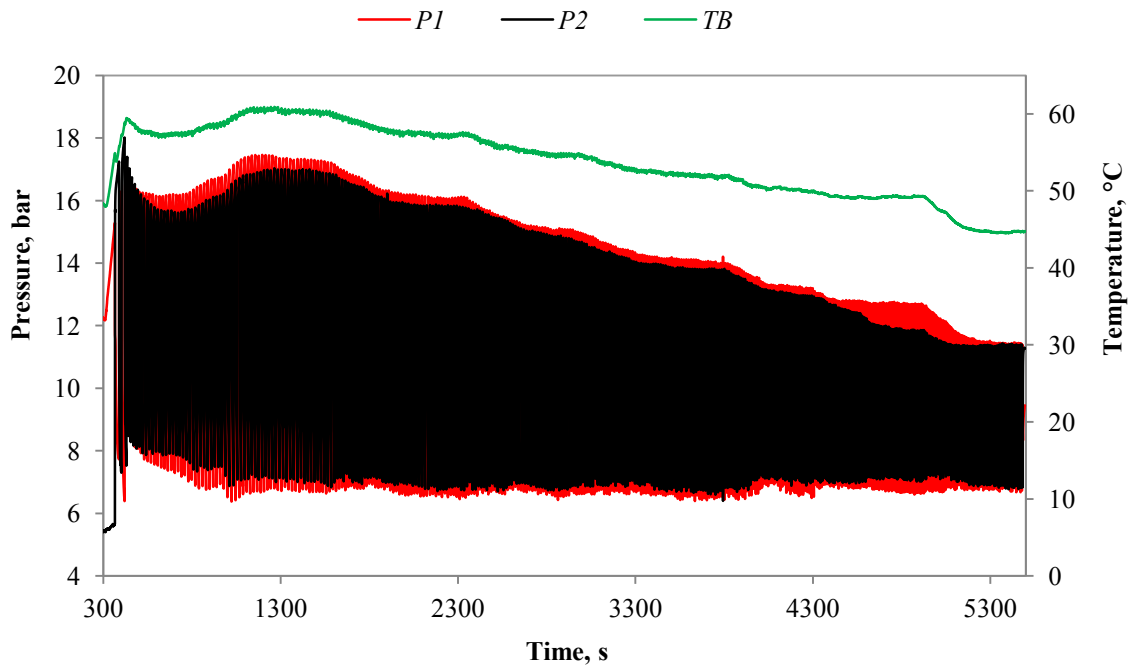
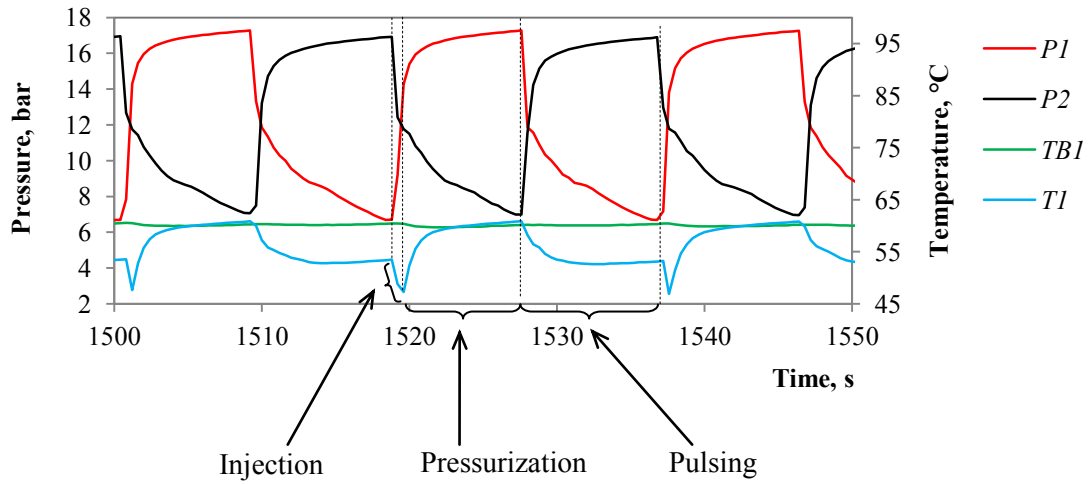
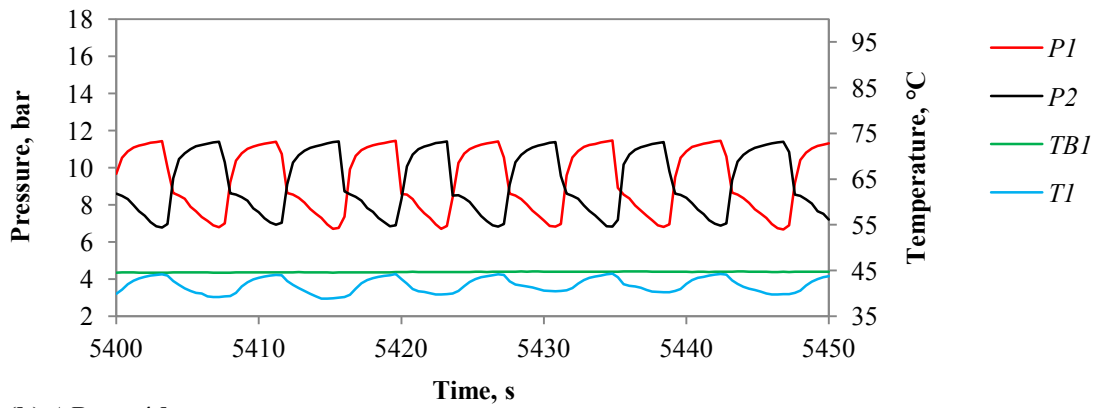


**Figure 5.9** Typical pressure and temperature history as a function of  $\Delta P$  control. Large VTL with  $x = 0.64$ ,  $Q = 500$  W and  $TWI = 15^\circ\text{C}$ . Although pulse detail is lost, the macro view highlights how the boiler temperature reduces from 60°C to 45°C with a reduction in  $\Delta P_{set}$  from 10 bar to 4 bar.



(a)  $\Delta P_{set} = 10$  bar



(b)  $\Delta P_{set} = 4$  bar

**Figure 5.10** Frequency and temperature response to  $\Delta P_{set}$ . Large VTL with  $x = 0.64$ ,  $Q = 500$  W and  $TWI = 15^\circ\text{C}$ . (a)  $\Delta P_{set} = 10$  bar, (b)  $\Delta P_{set} = 4$  bar.

The relationship between  $\Delta P_{set}$ ,  $f$ , and  $TB$  is presented in Figure 5.11. An increase in  $\Delta P_{set}$  from 5 bar to 10 bar results in a reduced  $f$  from 0.25 Hz to 0.11 Hz and an increased  $TB$  from  $46^\circ\text{C}$  to  $60^\circ\text{C}$ . The relationships are approximately linear. Visual inspection of the liquid injection at the sight glass confirms that less mass is injected with a decrease in  $\Delta P_{set}$ . It is assumed that the overall circulation rate remains approximately the same (at 5 g/s) due to the increased  $f$ . Slight asymmetry during steady pulsing is present in this test.



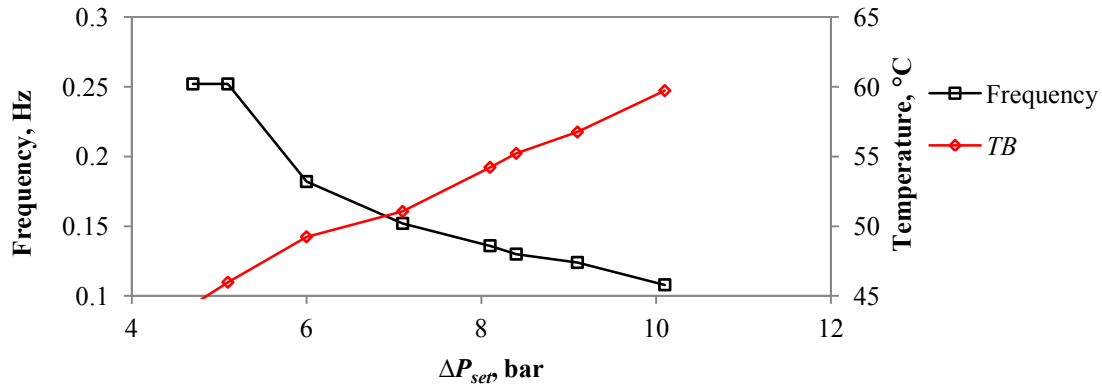


**Figure 5.11**  $\Delta P_{set}$  vs.  $f$  and  $TB$ . Large VTL with  $x = 63.72\%$ ,  $Q = 500$  W and  $TWI = 15^\circ\text{C}$ .

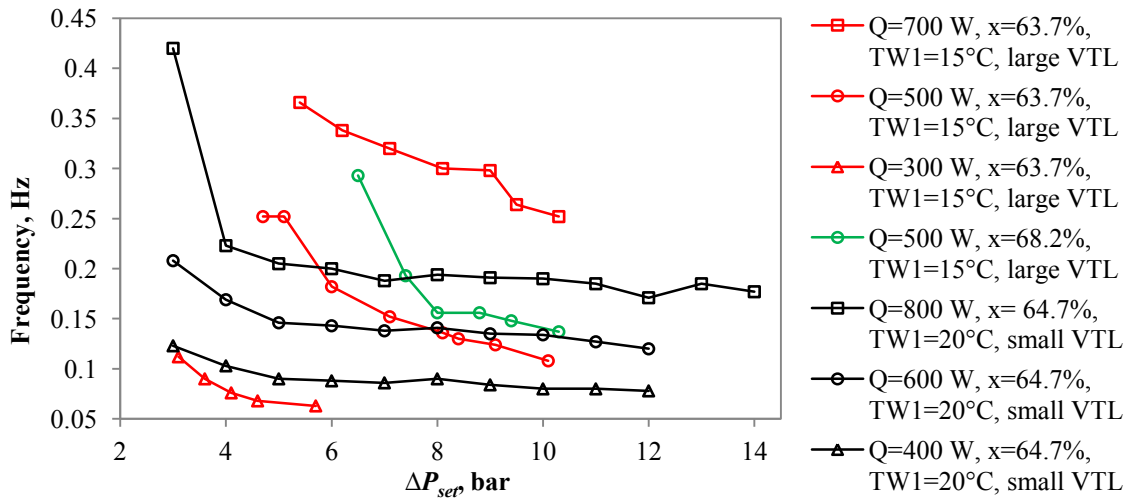
Numerous tests were carried out with two experimental setups including a small VTL and a large VTL. Different power inputs ( $Q$ ) and driving pressure differentials ( $\Delta P_{set}$ ) were investigated resulting in the performance map of Figure 5.12. A range of  $\Delta P_{set}$  from 3 bar to 12 bar result in  $f$  ranging from 0.05 Hz to 0.42 Hz. The results marked in red were obtained for a PTL that had a large VTL of  $52.5\text{ cm}^3$  and which was charged with 64% vapor. The condenser temperature was set to  $15^\circ\text{C}$ . To aid in this discussion, this is termed the reference set of results.

The results marked in green were obtained for the same experimental setup as the reference, except that a lower refrigerant charge mass (or increased  $x$ ) was used. Less refrigerant results in increased  $f$  and decreased operating temperatures, for a given  $\Delta P_{set}$  at a constant  $Q$  of 500 W.

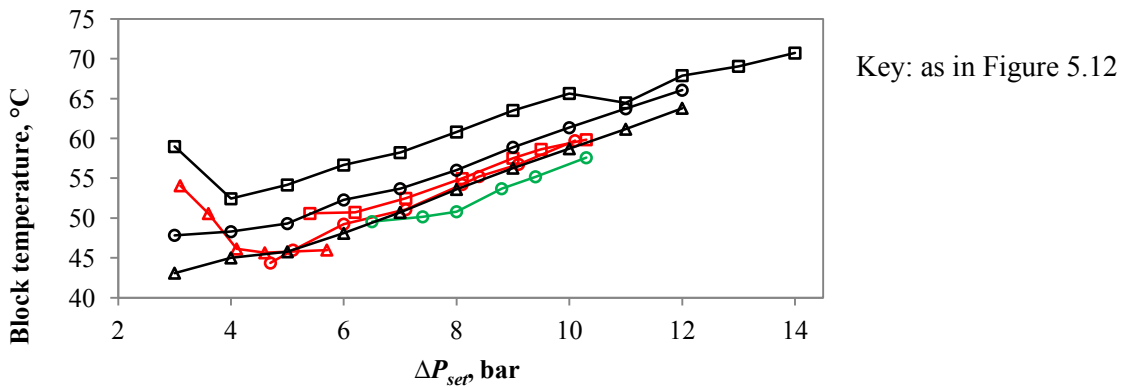
The results marked in black were obtained for a PTL that had a smaller VTL in comparison to the reference (of  $31\text{ cm}^3$ ), and which was charged with a similar vapor quality of 64.7%. The condenser was operated at a temperature of  $20^\circ\text{C}$ . In comparison to the reference, the results follow a flatter trend. This is due to the smaller VTL which provides less volume for a pulse to expand and condense into. The pulse becomes condenser limited as the condenser now has a larger liquid fraction which effectively reduces the available condenser area. The  $f$  remains low at reduced  $\Delta P_{set}$  as the depressurizing boiler takes longer to reduce in pressure in comparison to the reference. The results indicate that a larger VTL has a similar effect on  $f$  as a lower charge mass (or increased  $x$ ) does, which confirms the findings of Weislogel and Bacich. [16].

Figure 5.13 illustrates the effect of varying  $\Delta P_{set}$  on the boiler block temperature ( $TB$ ).  $TB$  generally increases with an increase in  $\Delta P_{set}$ , even though more mass is injected per pulse. This is due to the reduced  $f$  seen in Figure 5.12. Reduced  $f$  allows more time for  $TB$  to increase in-between pulses. The PTL's average heat transfer is approximately independent of  $\Delta P_{set}$ , shown in Figure 5.14. The average heat transfer at the condenser is approximately 55% that of the

power input at the boilers (from Equation 3.12, Appendix B.4), due to heat loss to the environment and pressure dissipated in overcoming the system head.



**Figure 5.12** Frequency vs.  $\Delta P_{set}$  for a range of heat inputs, charge mass and VTL size.



**Figure 5.13** Block temperature vs.  $\Delta P_{set}$  for a range of heat inputs, charge mass and VTL size.

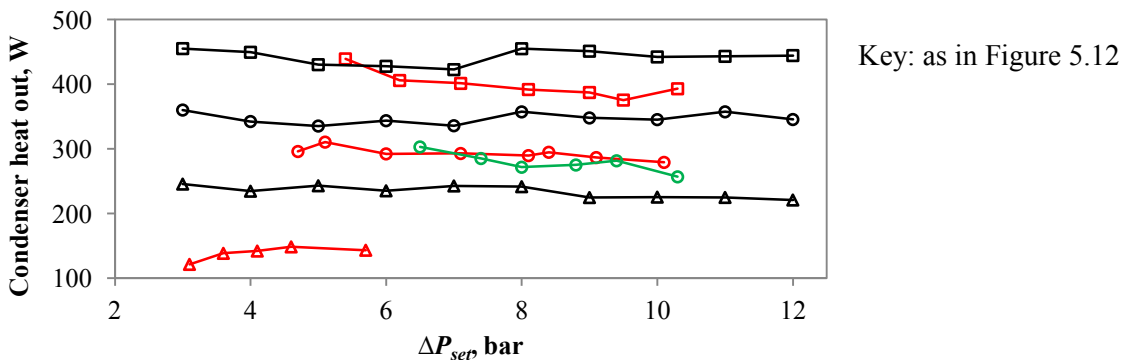


**Figure 5.14** Average condenser heat transfer vs.  $\Delta P_{set}$  for a range of heat inputs, charge mass and VTL size.

The results obtained are compared with various PTL performance curves generated by Weislogel and Bacich [16,2] and Brooks *et al.* [4], in Figure 5.15 and Figure 5.16. The figures represent a complete operating window, or map, for the different PTL configurations tested. PTL operation is bounded by the dashed lines representing the circulation limit (above), pulse limit (on the left and right) and the heat leak limit (below). As an operating point changes from inside the window to outside the window, steady states become difficult to achieve. Another limit not described here is the refrigerant charge mass limit.

The pulse limit on the left of Figure 5.15 is due to a low  $\Delta P_{set}$  that is unable to overcome the system head losses resulting in less mass injection per pulse. Lesser mass injection increases the operating temperature ( $TB$ ) and frequency ( $f$ ). For a reduced  $\Delta P_{set}$  the  $f$  increases (Figure 5.15) and  $TB$  decreases (Figure 5.16). The performance of the PTL in this study was limited to the servo valve frequency which operated at a maximum of 0.42 Hz. This prevented investigation at  $\Delta P_{set}$  below 3 bar since higher frequencies were required. The pulse limit on the right is due to insufficient mass in the boiler which therefore cannot pressurize to meet the required  $\Delta P_{set}$ .

The circulation limit is the maximum circulation rate that can be achieved for a given PTL and working fluid. The working fluid is limited by its critical heat flux capacity. The limit can be increased by improving heat transfer at the boilers, reducing flow resistances, and increasing  $\Delta P_{set}$ .

The heat leak limit occurs at low  $f$  operation which results in heat creep from the boilers into the LRL. Refrigerant upstream of the one-way check valve is preheated to a vapor resulting in decreased mass injection. The pressurizing boiler subsequently contains insufficient mass and cannot pressurize to meet the required  $\Delta P_{set}$ .  $TB$  also increases as less heat is removed from the boilers.

A small heater could be integrated in the commercial PTL application to avoid the system from shutting down when the heat load is not providing sufficient thermal energy. This would prevent the operating point from passing through the heat leak limit (by increasing  $f$ ) or the right hand pulse limit (by increasing the  $\Delta P_{set}$ ). When the heat load drops below a threshold value, for instance 100 W, the auxiliary heater could be activated to provide an additional 100 W, to maintain an adequate  $\Delta P_{set}$ . The PTL would then be classified as an active system due to the electrical energy required to power the heaters. This is common practice with other passive systems such as LHPs and CPLs, in order to provide reliable operation. These results highlight an important design requirement for the pulse refrigeration system (PRS) since the  $\Delta P_{set}$  must be maintained to drive the ejector.

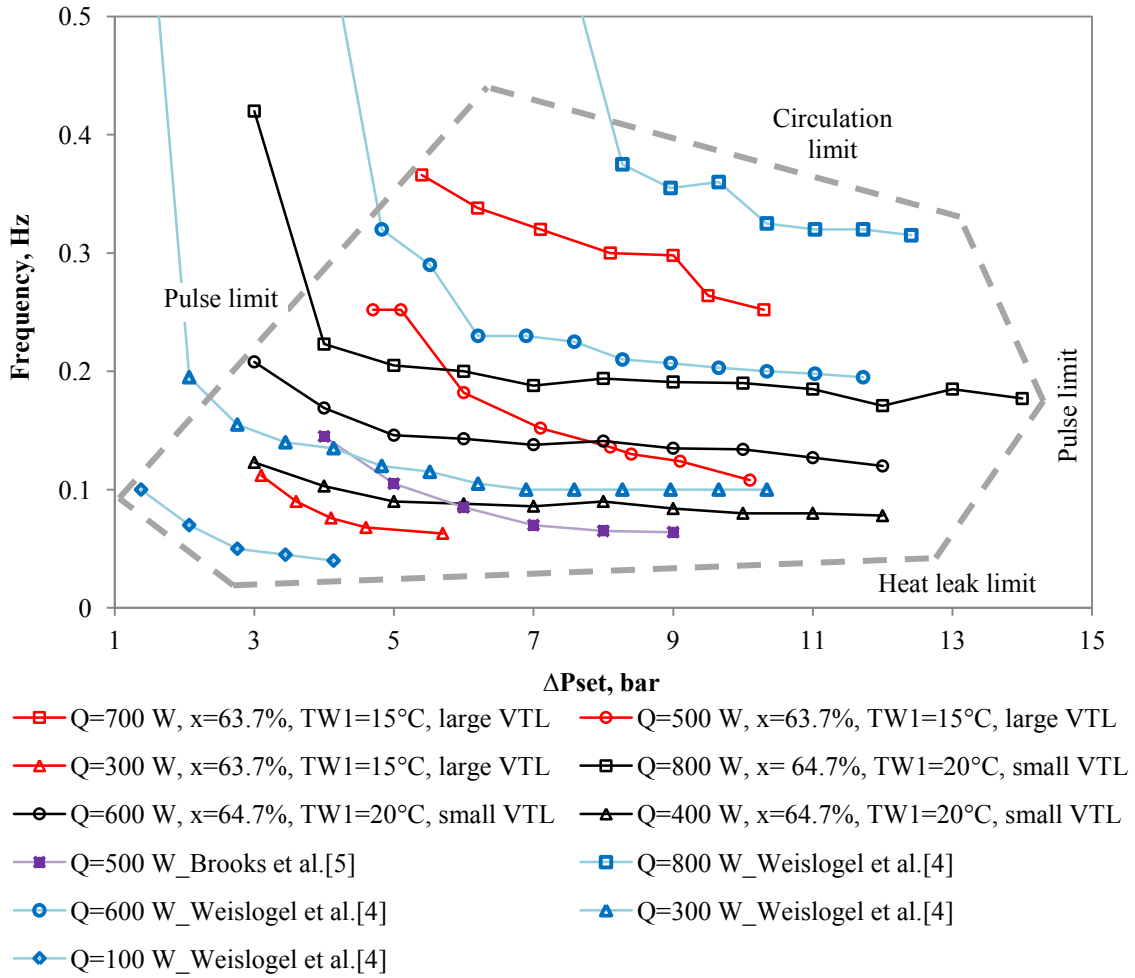


**Figure 5.15** Frequency vs.  $\Delta P_{set}$  performance map including results from the literature [16,4]. The operating envelope is indicated by the dashed lines and can be used to design a PTL for a particular application. Increased  $Q$  improves the circulation limit, the pulse limit and  $f$ .

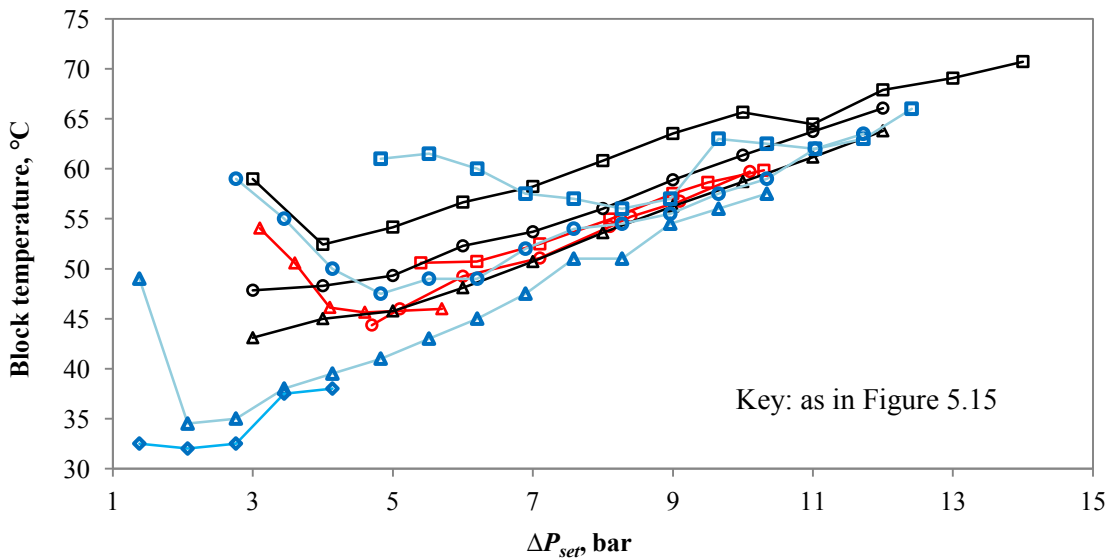


**Figure 5.16**  $T_B$  vs.  $\Delta P_{set}$  performance map including results from the literature [16].

### 5.2.5 PTL – varied heater power input

Table 5.1 provides the average and local heat flux values applicable to this work. The average heat flux ( $q''_{ave}$ ) is computed using the total surface area inside the boiler for different heater power inputs. The total surface area is approximated as the circumference of the boiler chamber multiplied by the length, giving  $138.2 \text{ cm}^2$ . Experimentally, the boilers are partially filled with liquid (to approximately 20%). The local heat flux ( $q''_{local}$ ) was calculated by Weislogel *et al.* [2] using the wetted surface area and compared with the critical heat flux limit of  $43 \text{ W/cm}^2$  to determine the maximum heat that can be supplied to the boilers. The local heat flux calculated here ( $29 \text{ W/cm}^2$  for  $800 \text{ W}$  power input) approaches that of the theoretical heat flux limit. The maximum heat transfer achievable with the current boiler design is  $1189 \text{ W}$ . Modification of the boiler design to include a greater wetted surface area, would result in the lowering of  $q''_{local}$ , which would enable operation at increased power inputs.

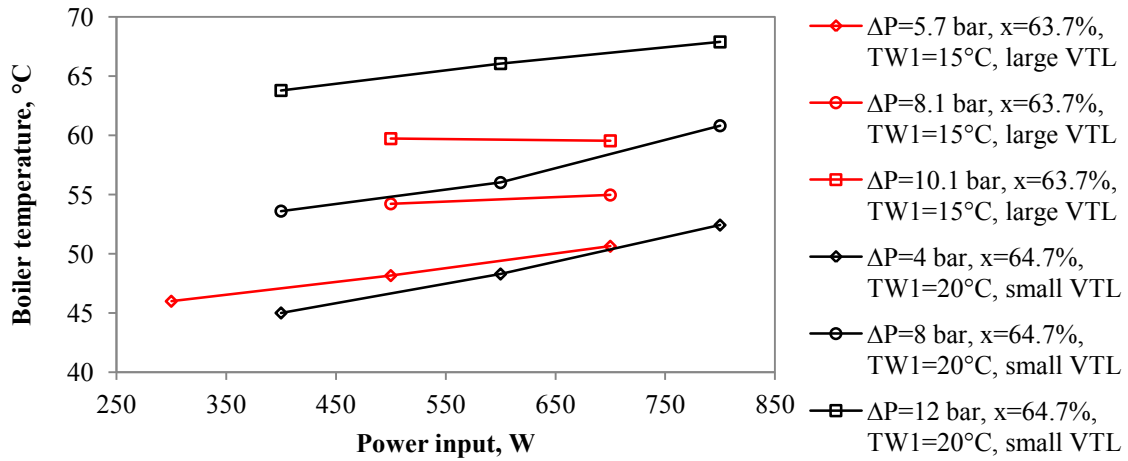
**Table 5.1** Average and local heat flux compared with the theoretical maximum

Power, W	$A_{total}$ , $\text{cm}^2$	$A_{wetted}$ , $\text{cm}^2$	$q''_{ave}$ , $\text{W/cm}^2$	$q''_{local}$ , $\text{W/cm}^2$
200.0	138.2	27.7	1.5	7.2
800.0	138.2	27.7	5.8	29.0
1189.0	138.2	27.7	8.6	43.0 (theoretical limit, Zuber Eq. [47])

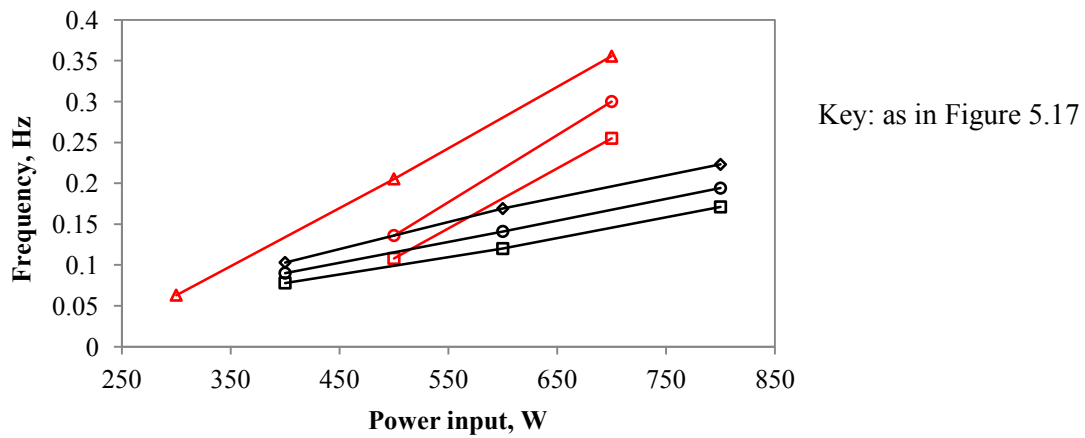
Power input ( $Q$ ) versus the average boiler temperature ( $TB$ ) for two experimental setups (small VTL and large VTL) is graphed in Figure 5.17. The graph indicates that  $TB$  only varies by a maximum of  $7.4^\circ\text{C}$  for the given  $Q$  range. A PTL with a larger VTL offers improved isothermal operation (constant  $TB$ ) for a given  $\Delta P_{set}$  and varying  $Q$ . This is indicated by the red curves varying less in temperature than the black curves. Furthermore, the boiler temperature is less affected by increasing  $Q$  than it is by increasing  $\Delta P_{set}$ . Referring to the PTL with the larger VTL (in red), increasing  $\Delta P_{set}$  from  $5.7 \text{ bar}$  to  $10.1 \text{ bar}$  whilst supplying  $Q$  at  $500 \text{ W}$  results in a  $TB$  increase of  $11.5^\circ\text{C}$ . In contrast, increasing  $Q$  from  $300 \text{ W}$  to  $700 \text{ W}$ , whilst maintaining  $\Delta P_{set}$  at  $5.7 \text{ bar}$ , results in an increase in  $TB$  of  $2.3^\circ\text{C}$ . This is due to  $f$  adjusting to the heat load, as shown in Figure 5.18, where  $f$  is directly proportional to  $Q$ . The frequency for the PTL with a smaller VTL is less dependent on  $Q$ .

Figure 5.19 shows that the average heat transfer at the condenser (Appendix B.4) is directly proportional to the power input at the boilers ( $Q$ ) and approximately independent of  $\Delta P_{set}$ . The PTL is able to maintain the heat transfer from a load, independent of  $\Delta P_{set}$ . The frequency simply adjusts to maintain the required heat transfer from the source to the sink. For application

as a TMS, a temperature sensitive device generating variable heat loads can be maintained at an approximately isothermal (constant) temperature by keeping  $\Delta P_{set}$  constant. The condenser effectiveness is calculated as 0.98 for the case where  $Q$  was 500 W and  $\Delta P_{set}$  was 10.1 bar.



**Figure 5.17** Power input ( $Q$ ) vs. boiler temperature ( $TB$ ) for varied  $\Delta P_{set}$ .



**Figure 5.18** Power input ( $Q$ ) vs. pulse frequency ( $f$ ) for varied  $\Delta P_{set}$ .

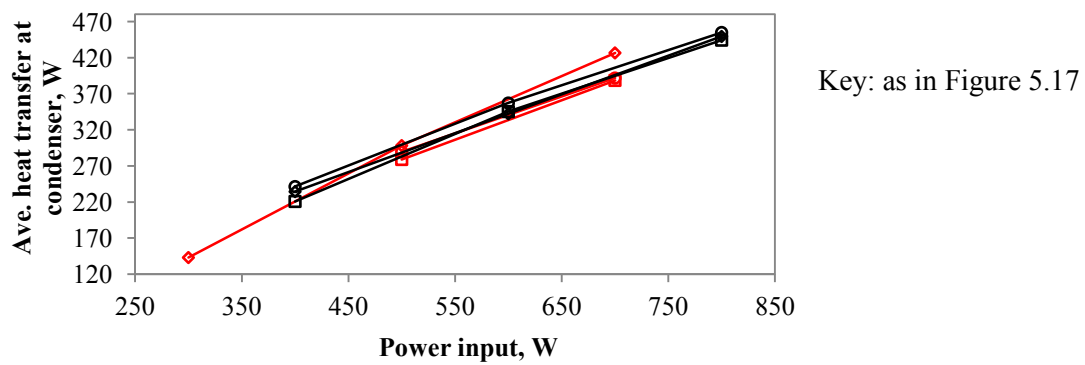


**Figure 5.19** Power input ( $Q$ ) vs. average condenser heat transfer for varied  $\Delta P_{set}$ .

### 5.3 Summary

The PTL design considerations included incorporating the components into the design of the PRS prototype. The components are modular and can be reconfigured by simply interchanging fittings, valves and transport tubing. The boilers manufactured here are at least twice as large as previous versions developed by Brooks *et al.* [4] and du Clou *et al.*[21]. This increases the pump capacity, or circulation limit, available for the PTL and the PRS, with increased  $\Delta P_{set}$ . The custom condenser enables accurate temperature control and the instrumentation permits calculation of heat transfer.

Refrigerant R-134a was chosen as the working fluid for the PTL and the PRS. It is well suited to the expected operating pressures and temperatures, and enables cooling at below freezing temperatures in the PRS evaporator section. The only negative aspect of R-134a is that it is classified as a wet fluid. Expansion at the ejector inlet nozzle in the PRS may produce suspended liquid droplets that can affect performance.

PTL performance was experimentally investigated for a range of driving pressures ( $\Delta P_{set}$ ) and power inputs ( $Q$ ). The increased boiler capacity improved PTL operation for increased  $Q$  and  $\Delta P_{set}$  up to 800 W and 14 bar, respectively. A maximum local heat flux of 28.9 W/cm<sup>2</sup> was demonstrated. For a constant  $Q$ , a decreased  $\Delta P_{set}$  results in an increased pulse frequency ( $f$ ) and a reduced boiler temperature ( $TB$ ). For a constant  $\Delta P_{set}$ , increased  $Q$  results in an increased  $f$  and an approximately isothermal  $TB$ . Also, a smaller VTL enables operation at increased  $\Delta P_{set}$  and decreased  $f$  for a given  $Q$ , but with an increased  $TB$ . A smaller VTL requires a reduced charge mass to prevent condenser limited operation.

The PRS in Chapter 6 must operate near the right hand pulse limit and the circulation limit identified in Figure 5.15 to benefit from the increased  $\Delta P$  and  $f$ . Increased  $Q$  provides a degree of superheat which prevents condensation in the ejector during expansion. A high  $\Delta P_{set}$  is also necessary to drive the PRS ejector. The  $\Delta P_{set}$  can initially be as high as 12 bar and reduce to 0 bar within a few seconds. Due to the highly transient nature of the pulses, careful consideration of the ejector design and predicting its performance is necessary. This is carried out using two one-dimensional analytical models.

## 6 PULSE REFRIGERATION SYSTEM PROTOTYPE

The objective of this chapter, which is an extended version of a paper by du Clou *et al.* [59], is to develop the PRS prototype (Figure 2.18, repeated below). The PRS is an evolution of the PTL that incorporates a novel ejector-based pump-free cooling loop. It is driven by waste heat or solar thermal energy, can operate independently of gravity, and is suitable for both terrestrial and space application. A cooling effect is derived by supplying the primary inlet to an ejector with unsteady pressure pulses from the PTL boilers. Flow through the ejector is intended to entrain and raise the pressure of the refrigerant from the cooling loop evaporator, thereby replacing the compressor required in conventional VCR.

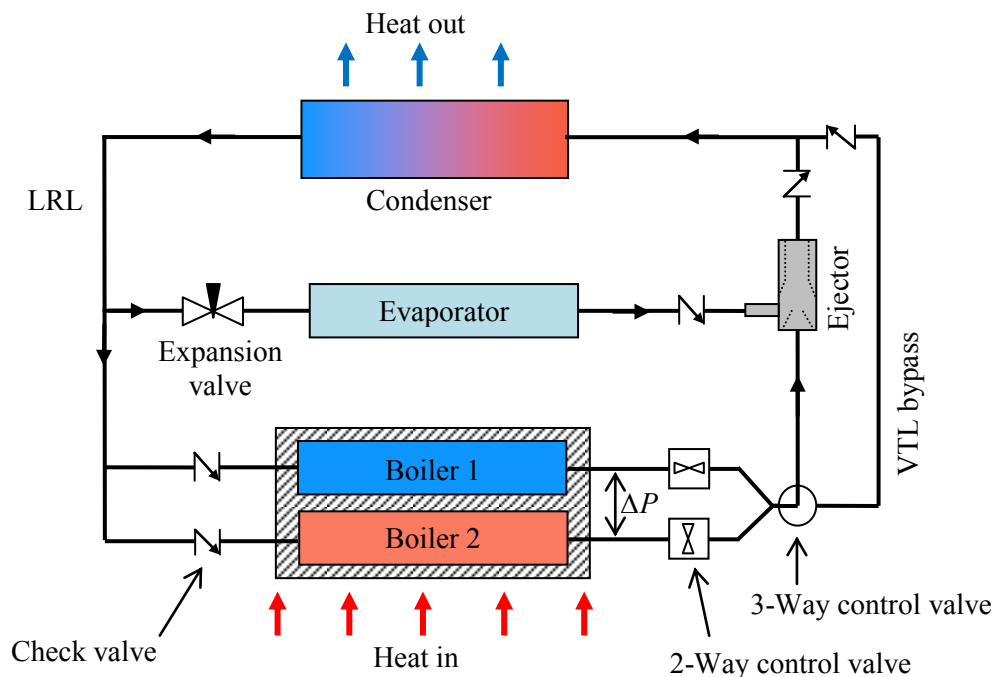


**Figure 2.18** Schematic of PRS variant I. Pulses from the PTL boilers are directed through the ejector cooling loop.

The transient application results in the ejector underperforming for most of the pulse. Simple ejector design and performance analysis models were developed as part of the primary research goals, to characterize the ejector's operation in the PRS (Appendix F). The design code permits optimization of the ejector geometry for steady flow conditions, whereas the performance code permits investigation of the ejector geometry for unsteady, two-phase flow applications. The performance code is a significant component of this work as it provides a simple method of mapping the quasi-steady ejector operating modes, through the transient flow regime. The two models are implemented in MATLAB, and account for homogeneous two-phase flow by incorporating NIST REFPROP real vapor data subroutines (they do not rely on isentropic gas relations). The models are validated with experimental data from the literature.



A prototype of the ejector-based PRS was constructed, incorporating the components from the PTL. Additional components include the ejector and the evaporator branch with an expansion valve and the associated instruments. Two configurations of the same device were experimentally tested to investigate the concept.

## 6.1 Ejector theory

An ejector is a mechanically simple mixing device that has no moving parts, which provides compression to a secondary stream and is analyzed using compressible flow theory. A few common applications include producing a vacuum, emptying storage tanks, and thermo-compressors that are used to raise the pressure of a secondary lower pressure stream. Benefits of the ejector include simple construction, ease of installation, no moving parts, no maintenance and a long operational life. The primary disadvantage is that the fixed geometry does not allow for variation in the operating parameters.

The ejector depicted in Figure 6.1 is comprised of four sections: the converging-diverging (CD) nozzle at the primary inlet, the suction chamber housing the secondary inlet, the constant-area mixing chamber and the recovery diffuser. During steady operation, the primary flow expands and accelerates through the CD nozzle to reach supersonic velocity (from  $p0$  to  $e$ ). The supersonic low pressure flow at the outlet of the nozzle (from  $e$  to  $l$ ) entrains a secondary flow (from  $s0$  to  $s1$ ), which is at some intermediate pressure. The flows mix depending on the mixing theory, and a normal shock wave forms in the constant area chamber resulting in pressure recovery. Further pressure is recovered in the diffuser (from  $2$  to  $c$ ) due to compression. The design of the inlet CD nozzle strongly influences the performance of the ejector.

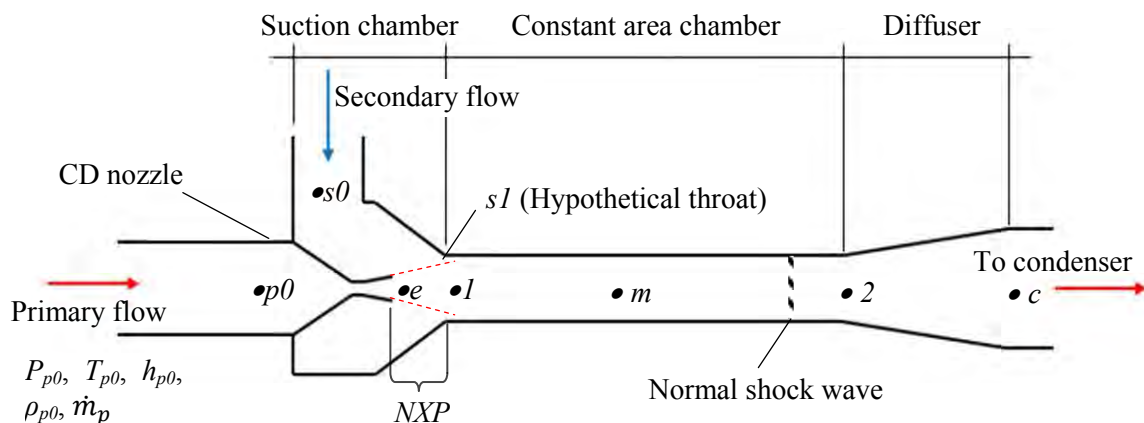


**Figure 6.1** Ejector schematic. The primary flow expands in the CD nozzle and entrains a secondary flow. Pressure is recovered with a normal shock wave during steady operation. [59]

The two primary geometric design ratios include the nozzle area ratio ( $A_e/A_t$ ) and the ejector area ratio ( $A_m/A_t$ ), where  $A_e$  is the CD nozzle exit area,  $A_t$  is the CD nozzle throat area and  $A_m$  is the ejector mixing chamber area. The ejector is classified using three performance ratios including the entrainment ratio ( $\omega$ ), the compression ratio ( $\psi$ ) and the driving pressure ratio ( $\varphi$ ), which are described in Equations 6.1 to 6.3. The entrainment ratio ( $\omega$ ) is the ratio of the ejector secondary mass flow rate to the motive mass flow rate. The ejector compression ratio ( $\psi$ ) is the ratio of the downstream pressure (at the condenser) to the secondary inlet's stagnation pressure,  $P_{s0}$  (at the evaporator). The driving pressure ratio ( $\varphi$ ) is the ratio of the condenser pressure to the stagnation pressure ( $P_{p0}$ ) at the ejector's primary inlet. Note that  $P_{p0}$  is analogous to the boiler pressure that feeds the ejector ( $P1$  or  $P2$ ).

$$\omega = \dot{m}_s / \dot{m}_p \quad (6.1)$$

$$\psi = P_c / P_{s0} \quad (6.2)$$

$$\varphi = P_c / P_{p0} \quad (6.3)$$

The ejector operating modes are identified in Figure 6.2 and are dependent on the operating driving pressure ratio ( $\varphi$ ). During critical mode operation, the condenser back pressure is sufficiently low (or the driving pressure is sufficiently high) resulting in both the primary and secondary ejector streams being choked (Fabri choking) [62]. This results in a constant maximum entrainment ratio ( $\omega$ ). If  $\varphi$  is increased beyond a critical point,  $\varphi^*$ , (by increasing the condenser pressure or decreasing the primary inlet pressure) the ejector enters the subcritical mode of operation. The normal shock wave regresses along the constant area chamber into the mixing chamber, and into the CD nozzle. The secondary fluid becomes unchoked, reducing  $\omega$ . Entrainment continues to decrease as  $\varphi$  approaches unity, where back-flow may occur.

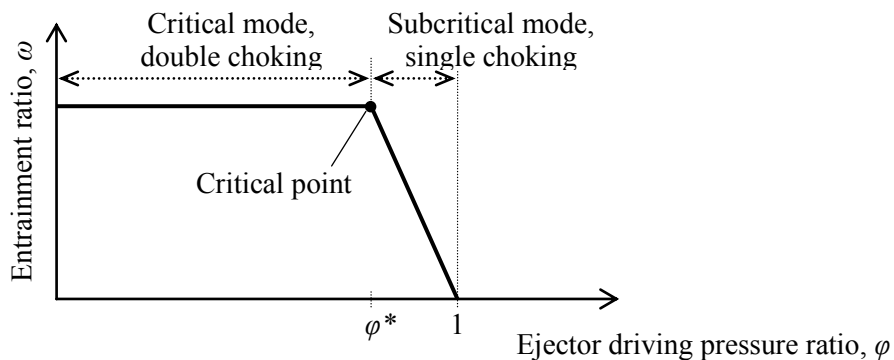


**Figure 6.2** Ejector operating modes dependant on the driving pressure ratio,  $\varphi$ . [63]

In a PRS with a large enough feed boiler, the flow through a relatively small ejector would be considered steady. However, the PRS has a finite volume boiler and condenser of  $81.2 \text{ cm}^3$  and

42.8 cm<sup>3</sup>, respectively. The ejector is therefore subject to a transient, blow-down effect characterized by an initially strong but decaying pressure pulse. Figure 6.3 shows such a PTL pulse, that decays from 18.5 bar to a condenser pressure of 7.2 bar ( $\Delta P_{set} = 11.3$  bar).  $P_2$  resembles the pressure at the primary inlet to the ejector,  $P_{p0}$ , and  $P_c$  is the downstream pressure at the condenser. The ejector pressure ratio ( $\varphi$ ) is seen to increase from 0.38 to unity within 2 s, as the pulse expands and condenses. This transient process limits entrainment at the ejector secondary inlet to a finite period at the start of the pulse.

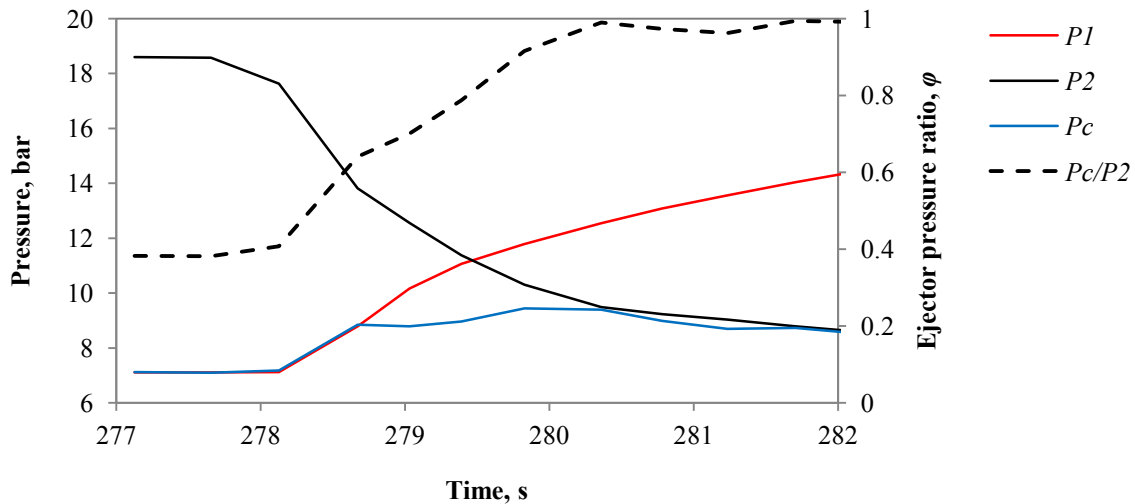


**Figure 6.3** PTL pulse showing anticipated ejector driving pressure ratio ( $\varphi$ ) increasing to unity within 2 s as the pulse pressure ( $P_2$ ) falls to meet the lower condenser pressure ( $P_c$ ).

## 6.2 Ejector literature

The design of ejectors for various ECS is widely reported with different theories of operation. A comparison of ejectors designed and tested by various researchers is presented in Table A.10 of Appendix A. These ejectors were designed for and investigated under steady flow conditions.

Although much research has been carried out on ejectors analytically [38,63,31,64,29,65,46,66,67,25], computationally [68,69,27,70] and experimentally [71,36,27], there is still not a well defined method to design such a device for operation under transient conditions (as is expected with the PRS), especially where two-phase flow is involved. Mostly, the research focuses on single and two-phase ejectors under steady state operating conditions. Bartosiewicz *et al.* [69] concluded that a one-dimensional ejector model cannot accurately predict the performance at subcritical operating modes. This is due to the one-dimensional ejector models being constrained by the requirement of having the normal shock wave locate itself in the constant area section. CFD models are not limited by this constraint. A number of authors including Bartosiewicz *et al.* [69] and Park *et al.* [70] have used CFD models to predict

ejector performance during off-design operation, where the shock wave regresses into the ejector suction chamber.

It is evident that ejector performance is vital to the functioning of the PRS proposed here, and is the limiting component in the system design. In this work, two analytical ejector models are developed that i) compute the required ejector geometry for steady state operation and, ii) predict the performance of the ejector during quasi-steady transients. The second model is a first step towards modeling ejector transient performance using a one-dimensional approach.

### 6.2.1 Nozzle

The nozzle at the inlet to the ejector enables expansion of the motive flow, converting enthalpy into kinetic energy. For a real (compressible) fluid, a converging-diverging (CD) nozzle enables supersonic flow as the motive fluid is able to expand and accelerate further in the diverging portion of the nozzle.

Variable ejector nozzle back pressure ratio ( $P_R$ ) has received little attention in the literature as it is not an important design feature for ejectors operating in the fully developed flow regime. In this study the  $P_R$  is a critical parameter and is defined as the ratio of the CD nozzle back pressure ( $P_1$ ) to the primary stagnation inlet pressure ( $P_{p0}$ ) (Equation 6.4). For a given nozzle area ratio ( $A_e/A_t$ ), the  $P_R$  determines the ejector operating modes. Note that the ejector pressure ratio ( $\varphi$ ) resembles the pressure ratio across the entire ejector whilst  $P_R$  resembles the pressure ratio across the CD nozzle. A nozzle that is perfectly expanded results in ejector critical mode operation.

$$P_R = P_1/P_{p0} \quad (6.4)$$

$$\text{where, } P_{p0} \equiv P1$$

A key geometric parameter for an ejector is the CD nozzle exit to throat area ratio ( $A_e/A_t$ ). Selvaraju *et al.* [72] and Sankarlal *et al.* [73] designed miniature ejectors for an ECS having an  $A_e/A_t$  of 2.6. This is comparable with most of the literature which give area ratios between 2.5 and 3.9 [63,71,31,74,26,68,72,73,75,76]. Zhu *et al.* [74] investigated the nozzle diverging angle and the nozzle exit position ( $NXP$ ) using computational fluid dynamics (CFD). The CD nozzle diverging angle must increase with an increase in driving pressure ( $P1$ ). The  $NXP$  is not only proportional to the diameter of the constant area section ( $D_m$ ) but must also increase with a rise in  $P1$  to maintain adequate performance. Small diverging angles are important in controlling the rate of expansion and preventing flow separation. Common diverging angles are between 4° and

10° [66,72,68,27,30]. The *NXP* (shown in Figure 6.1), provides the best performance when it is located at a distance of 1.5 to 3.4 times the diameter of the constant area section ( $D_m$ ) before the inlet of the constant area section [74,68,71,63]. Some analytical models have incorporated nozzle isentropic efficiencies which are in the range of 0.8 to 1.0 [31,26,63,72,29,76,77].

### Nozzle operating modes

The CD nozzle critical modes are depicted in Figure 6.4 as a function of the  $P_R$ . (The CD nozzle critical modes should not be confused with the ejector critical mode of operation in Figure 6.2). In conventional nozzle theory flow is induced by decreasing the  $P_R$  by way of reducing the back pressure ( $P_t$ ) at the nozzle exit. For application in a PRS ejector, the CD nozzle  $P_R$  is affected by the ejector driving pressure ratio ( $\varphi$ ). It is therefore subject to changes in both the supply pressure ( $P_{p0}$ ) at the boilers and the back pressure ( $P_c$ ) at the condenser.

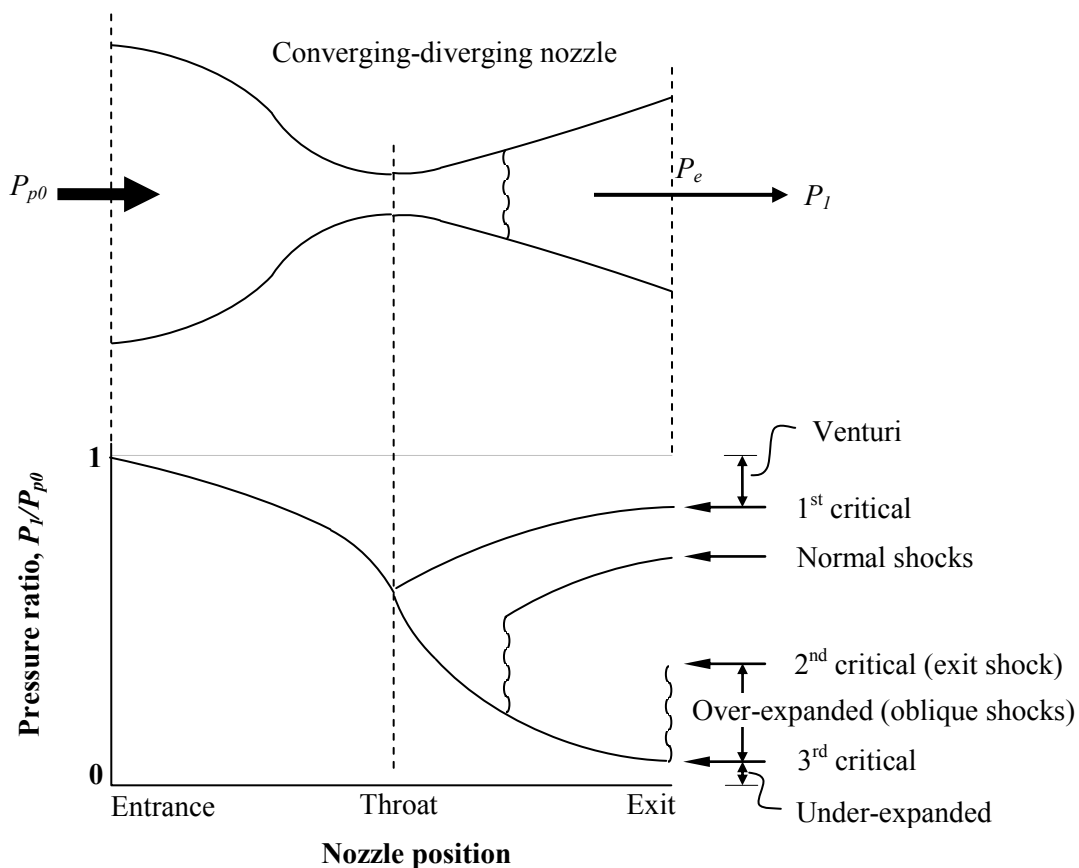


**Figure 6.4** Compressible flow theory for converging-diverging nozzle showing critical operating modes [78]

For a  $P_R$  less than the third critical point ( $P_R < 3^{\text{rd}}$  critical), where  $P_e > P_t$ , the nozzle flow is under-expanded. This may result in the free expansion wave blocking the secondary inlet to the

ejector. A slight increase in the  $P_R$  from the third critical point ( $3^{\text{rd}} < P_R < 2^{\text{nd}}$  critical) results in the flow being over-expanded ( $P_e < P_l$ ) with a complex series of supersonic wave motions, or non-isentropic oblique shocks. The oblique shocks occur outside the nozzle and are weaker than normal shocks. The angle of the shock adjusts to produce the required pressure rise to meet  $P_l$ . The resulting flow is still supersonic if the oblique shocks are weak. Stronger oblique shocks induce mixing layer separation resulting in loss of energy and a marked pressure increase [69].

For a CD nozzle operating at its second critical point, a normal shock is located at the exit plane resulting in a pressure increase that is precisely required to meet the back pressure ( $P_l$ ). This is the strongest type of shock that could occur during the transient operation, and must be avoided. For a  $P_R$  in-between the first and second critical point ( $1^{\text{st}} < P_R < 2^{\text{nd}}$  critical) the normal shock locates itself inside the diverging section such that the pressure change before the shock, across the shock and downstream of the shock results in the exit pressure ( $P_e$ ) being equal to the back pressure ( $P_l$ ). The first critical point represents flow that is choked at the throat with a Mach number of one, and is subsonic for both the converging and diverging sections. Any  $P_R$  above the first critical point ( $P_R > 1^{\text{st}}$  critical) results in reduced mass flow rate and subsonic flow throughout the CD nozzle.

For the PRS, the flow through the ejector nozzle should be perfectly expanded to the  $3^{\text{rd}}$  critical point to achieve the best performance, minimizing the non-isentropic shocks. Due to the transient ejector driving pressure ratio ( $\varphi$ ) shown in Figure 6.3, the ejector in the PRS will only function at its critical mode for a finite period, at the start of each pulse. Ideally, a variable geometry nozzle would enable optimal operation during blow-down. This was reported by Eames *et al.* [28]. As  $\varphi$  increases to unity, the CD nozzle exit diameter can be reduced to maintain supersonic low pressure flow at the outlet whilst avoiding non-isentropic shock waves. However, a fixed geometry nozzle is selected for the PRS due to the small scale manufacturing limitations required of a laboratory scale ejector.

### **6.2.2 Suction chamber**

The one-dimensional approach to ejector design assumes that the secondary inlet feeds the ejector axisymmetrically around the entire circumference. This assumption may lead to an over prediction of the entrainment ratio ( $\omega$ ). Common isentropic mixing efficiencies range from 0.85 to 0.95 [31,63,72,77].

There are two theories that can be applied to the mixing of the primary and secondary streams:

**i) Constant pressure mixing**

Constant pressure mixing theory was developed by Keenan *et al.* [79] and is more common in the literature. This theory assumes that the primary and secondary fluids expand to the same pressure and mix before entering the constant area section. The authors developed a one-dimensional model incorporating this theory and applying the conservation of mass, energy, and momentum as well as ideal gas assumptions. Eames *et al.* [26] and Huang *et al.* [63] modified the one-dimensional ejector model developed by Keenan *et al.* [79] to include isentropic efficiencies. These models, however, rely on ideal gas relations and cannot account for two-phase flow.

**ii) Constant area mixing**

Fabri and Siestrunk [62] theorized that a fictitious secondary throat is formed between the primary core flow and the converging channel of the ejector housing (shown in Figure 6.1). The secondary flow expands, without mixing, along the fictitious duct to reach sonic velocity, resulting in the double choking condition. Munday and Bagster [80], Kandil *et al.* [25] and various other researchers have developed one-dimensional models incorporating Fabri choking theory. The model developed by Kandil *et al.* [25] accounts for real vapor data, but does not consider isentropic efficiencies.

### **6.2.3 Constant area chamber**

The design of the constant area chamber depends on three key ratios ( $A_m/A_t$ ,  $L_m/D_m$  and  $NXP/D_m$ ). The area ratio of the mixing chamber to the nozzle throat ( $A_m/A_t$ ) commonly ranges from 4 to 11.5 [63,66,74,73,70,68,72,81,76]. For optimal mixing of the two fluids to occur, the length to diameter ratio of the mixing chamber ( $L_m/D_m$ ) is commonly 10 [66,72,73,70]. During critical operation a normal shock wave forms towards the end of the constant area section resulting in pressure recovery. Mixing chamber isentropic efficiencies can range from 0.8 to 1.0 [26,63].

### **6.2.4 Diffuser**

Pressure increases at constant entropy in the diffuser due to the increasing cross-sectional area. The diffusing angle commonly ranges from 6.3° to 9.4° [63,72,76]. The diffuser isentropic efficiency commonly ranges from 0.8 to 1.0 [31,26,63,72,29,76].

### 6.3 Governing equations of the ejector analytical model

The design and performance of the ejector is addressed through the development of an analytical computational model consisting of two parts; a design code (Appendix F.2) and a performance analysis code (Appendix F.3). The codes are implemented in MATLAB R2006b [82] with real vapor data sub-routines from NIST REFPROP V7.0. [83]. The software is used to investigate the relationship between the ejector's geometry, operating conditions and the performance under two-phase, transient flow conditions, as encountered in the pump-free PRS.

The fluid properties are iteratively calculated at various locations along the ejector axis using compressible flow theory with the conservation of mass, energy, and momentum described by Equations 6.5 to 6.7 [23]. These solve for the one-dimensional geometric profile of the ejector. The energy equation includes an isentropic efficiency term,  $\eta_{is}$ , to account for friction losses.

$$\dot{m} = \rho AV \quad (\text{continuity}) \quad (6.5)$$

$$h_0 = h + \frac{1}{2\eta_{is}} V^2 \quad (\text{energy}) \quad (6.6)$$

$$PA = \dot{m}V \quad (\text{momentum}) \quad (6.7)$$

The sonic velocity ( $a$ ) and Mach number ( $M$ ) for a real gas are calculated using Equations 6.8 and Equation 6.9. The flow area and diameter are calculated using Equations 6.10 and 6.11.

$$a = \sqrt{(\Delta P / \Delta \rho)_s} \quad (6.8)$$

$$M = V/a \quad (6.9)$$

$$A = \dot{m}/(\rho V) \quad (6.10)$$

$$D = \sqrt{4A/\pi} \quad (6.11)$$

The velocity of the mixed flow,  $V_m$ , is calculated by combining the momentum of the two streams in Equation 6.12 [26], where  $V_p$  and  $V_s$  are the flow velocities of the primary and secondary fluid, and  $\dot{m}_p$  and  $\dot{m}_s$  are their respective mass flow rates. The mass flow rate of the mixed fluid,  $\dot{m}_m$ , is obtained from Equation 6.1.



$$V_m = (\dot{m}_p V_p + \dot{m}_s V_s) / \dot{m}_m \quad (6.12)$$

If the mixed flow Mach number is greater than unity, the pressure after the shock wave ( $P_y$ ) is iterated until the calculated density after the shock ( $\rho_y$ ) equals the look up density [25,38,84]. The flow velocity after the shock ( $V_y$ ) is calculated from the conservation of mass and momentum for the iterated pressure ( $P_y$ ), in Equation 6.13, where  $P_m$  and  $\rho_m$  are the pressure and density of the mixed flow before the shock. The enthalpy after the shock ( $h_y$ ) is calculated in Equation 6.14. Conservation of mass across the shock, which occurs at constant area, gives the calculated density after the shock, Equation 6.15. The calculated density is then compared to the look-up density (obtained from REFPROP using the iterated pressure and the calculated enthalpy). The solution converges when the look-up density is less than the calculated density.

$$V_y = (P_m + \rho_m V_m^2 - P_y) / \rho_m V_m \quad (6.13)$$

$$h_{y \text{ calculated}} = h_m + 1/2 V_m^2 - 1/2 V_y^2 \quad (6.14)$$

$$\rho_{y \text{ calculated}} = \rho_m V_m / V_y \quad (6.15)$$

The following assumptions apply to both models [78]:

1. For steady flow, the fluid properties are constant across the cross-section at any given x-coordinate.
2. Certain fluids (like R-134a) condense when they expand due to the isentropic curve crossing through saturated vapor line into the two-phase region of the pressure-enthalpy diagram. The resulting mixture quality is high,  $x > 0.95$ , which gives a low liquid volume fraction. Under these conditions it is reasonable to assume that the two phase mixture is homogeneous with no slip between phases. The pressure and temperature of the vapor and liquid fractions are equal.
3. To account for non-ideal losses due to friction and mixing, isentropic efficiency coefficients are included in the code. When set to 1, adiabatic flow is assumed everywhere except across shocks where there is an entropy rise.
4. The thickness of the shock is negligible.
5. Kinetic energy at the primary and secondary reservoir is negligible (at stagnation).
6. The mixing of the primary and secondary streams is assumed to occur at constant pressure after the secondary stream has expanded to the hypothetical throat.
7. Flow separation from the boundary is ignored, assuming small angles and polished

surfaces.

8. The ejector walls are adiabatic.

#### 6.4 Steady-state ejector design model

The design code permits optimization of the ejector geometry for a given set of steady flow conditions. The model geometry is optimized by using both the constant pressure mixing theory developed by Keenan *et al.* [79] and the Fabri choking theory developed by Fabri and Siestrunk [62]. The model is validated against numerical and experimental results from the literature.

A number of one-dimensional analytical models have been developed with the purpose of comparing different refrigerants, and to investigate the design of ejectors for different operating conditions [26,29,63,84,38,80,64]. The model developed here, generates the optimum ejector geometry given a required entrainment ratio and steady operating inputs at the primary and secondary inlets. A user defined nozzle back pressure ratio,  $P_R$ , is imposed and the model assumes that the inlet nozzle operates at this critical point, where  $P_e = P_I$ . The pseudo-code solution flow chart is provided in Figure 6.5. Routine application of the governing equations, with real vapor data from NIST REFPROP, solves the flow at each point along the ejector axis. The normal shock wave is captured by iteratively increasing the pressure across the shock, and finding the local fluid properties using the conservation of mass and momentum for the control volume surrounding the shock, until the calculated density after the shock is equal to or greater than the reference density.

One input variable ( $P_{p0}$ ,  $P_{s0}$ ,  $P_c$ ,  $x_0$ ,  $x_s$ , or  $\dot{m}$ ) can be varied while keeping the others constant to obtain a range of design graphs. The primary independent variable in the PRS is  $\Delta P_{set}$ , therefore the primary ejector variable investigated is  $P_{po}$ . The design is completed by selecting suitable lengths or converging diverging angles from the literature. A list of published ejector geometric profiles, including the angles, is provided in Table A.10, Appendix A.

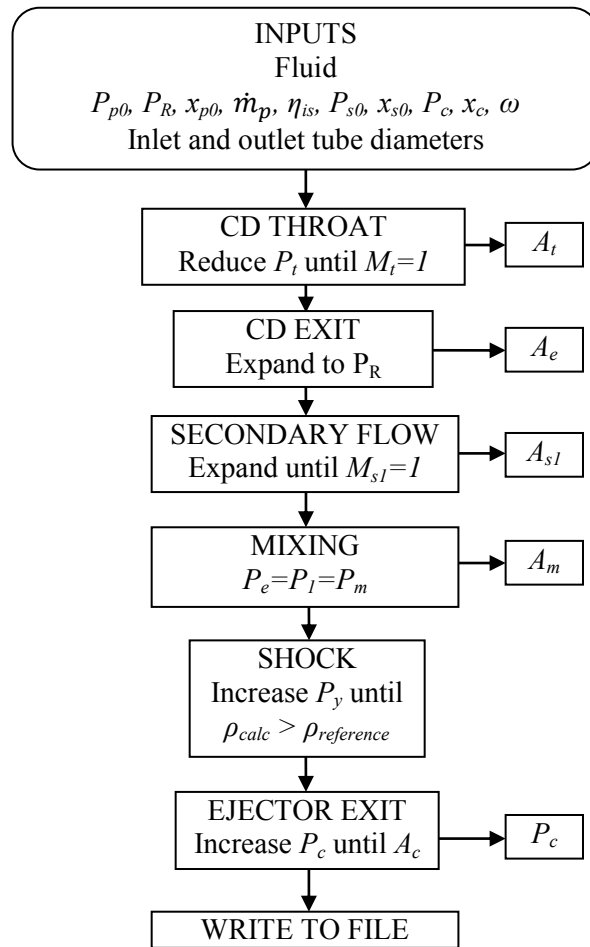


**Figure 6.5** Pseudo-code flow chart for the ejector design model. [78]

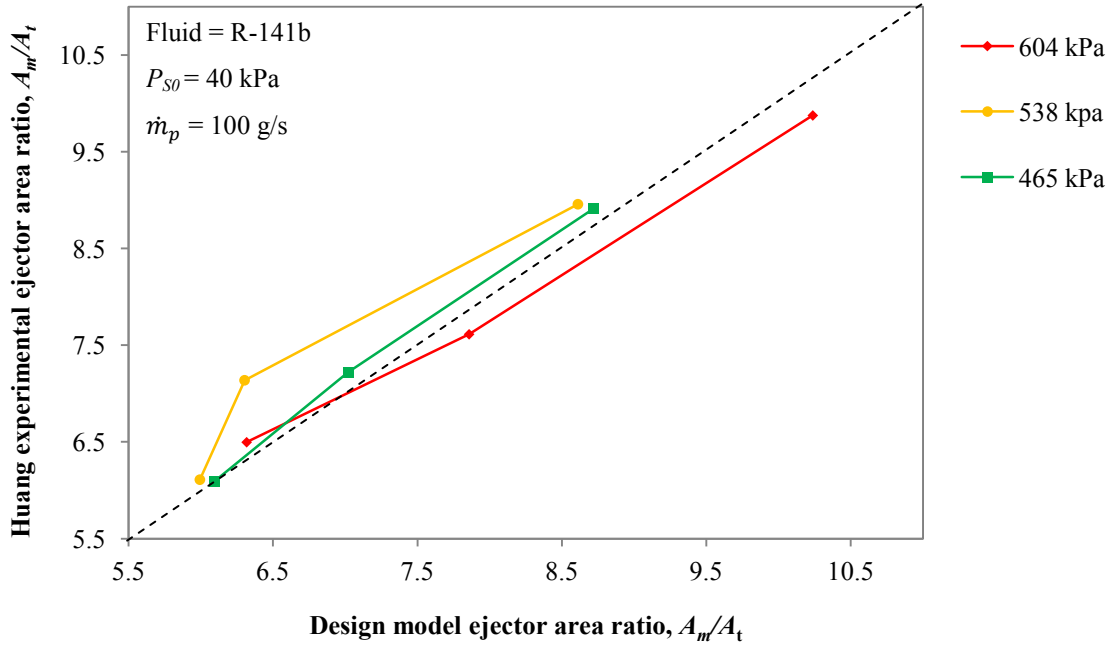
### 6.4.1 Design model validation

In an effort to validate the two-phase ejector model, its output was compared with experimental and analytical data from Huang *et al.* [63]. To this end, refrigerant R-141b was selected as the working fluid and optimal ejector area ratios ( $A_m/A_t$ ) were determined by varying the operating pressure and entrainment ratio ( $\omega$ ). The results were then compared on a series of 45° plots to assess deviation from the output of Huang *et al.* [63]. Three generator pressures ( $P_{p0}$ ) including 400 kPa, 465 kPa, and 537 kPa (saturated vapor) were investigated, each with varied  $\omega$ .

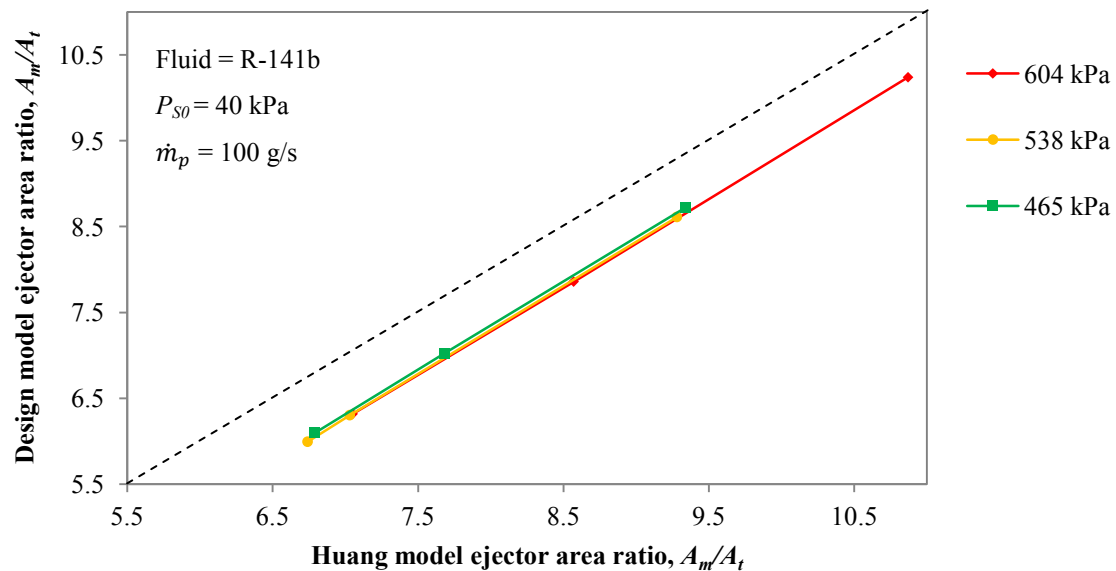
Figure 6.6 graphs the modeled area ratios against the experimental area ratios of Huang *et al.* [63]. The distribution of data about the diagonal suggests that the model developed here closely follows the output of Huang *et al.* [63] with a mean error of 6%.

Figure 6.7 graphs the modeled area ratios against the analytical results of the model developed by Huang *et al.* [63], where the fluid properties are solved using the isentropic relations rather

than the governing equations. A systematic error of 8.5% is seen in the figure and may be attributed to this model not including an empirical loss coefficient. The results also confirm that the ejector area ratio is proportional to the entrainment ratio.



**Figure 6.6** The design model area ratios are compared to the experimental results of Huang *et al.* [63]. The model shows good agreement with the experimental results.



**Figure 6.7** The design model area ratio results are compared with the results from the model developed by Huang *et al.* [63]. The models are directly proportional but are offset by a constant term.

### 6.4.2 Design model results

The design of a suitable ejector for application in the PRS is investigated using the design model. The results are presented in Figures 6.8 to 6.9, where R-134a is selected for the analysis. The boiler pressure that feeds the primary inlet to the ejector is varied from 18 bar to 10 bar. The ejector operates with a secondary inlet pressure of 4 bar, a primary mass flow rate of 5 g/s, an entrainment ratio ( $\omega$ ) of 0.2 and a CD nozzle back pressure ratio ( $P_R$ ) of 0.1. The tube diameters upstream and downstream of the ejector are constrained by the PRS transport lines which are 1/4" (4.55 mm *ID*) at the primary inlet and exit, and 1/8" (1.8 mm *ID*) at the secondary inlet.

Figure 6.8 illustrates the ejector geometry required for different supply pressures, whilst maintaining a fixed  $P_R$  and  $\omega$ . The results indicate that an increased supply pressure requires a smaller ejector to expand the working fluid to the required  $P_R$ . In other words, a decreased  $\phi$  will result in under-expanded flow for a fixed CD nozzle and  $P_R$ .

Referring to the 18 bar results (red trace) in Figure 6.9, the cross section diameter at different axial locations along the ejector is plotted against the static pressure at that location. The working fluid initially expands from the 4.5 mm inlet to the 0.92 mm throat to reach sonic velocity. The flow continues to expand to the CD nozzle exit with a diameter of 1.51 mm. The secondary flow is entrained by the low pressure region and is choked by the hypothetical throat that is formed between the core flow and the ejector wall. The primary and secondary flow then mix at constant pressure and the diameter of the flow increases to 1.76 mm. A shock wave in the constant area section (shown by vertical lines in the plot) raises the pressure of the working fluid. The diameter increases to the 4.5 mm diffuser outlet, resulting in further pressure recovery. For a decreased supply pressure of 14 bar (yellow trace), the ejector CD nozzle throat, exit and mixing chamber diameters must increase by 13.6%, 12.6% and 9.5% respectively, in order to maintain the required nozzle back pressure ratio ( $P_R$ ), entrainment ratio ( $\omega$ ) and mass flow rate ( $\dot{m}_p$ ).

Figure 6.10 illustrates the static pressure and the Mach number contour along the ejector axis. The normal shock is evident at position 3 along the horizontal axis, indicated by the step increase in static pressure with a decrease in Mach number. The straight line plots in Figure 6.9 and Figure 6.10 are due to the limited sample points solved by the model; realistically the pressure and Mach number plots follow a curve.

Similar design graphs can be generated by keeping the feed pressure constant and varying other

independent variables including  $P_{s0}$ ,  $P_c$ ,  $x_0$ ,  $x_s$ , or  $\dot{m}_p$ . A selected geometry in Figure 6.8 is analyzed using the ejector performance model in section 6.5.2, where it is supplied with a transient pressure resembling a pulse from one of the PTL boiler chambers. The model simulates the operating modes of the CD nozzle at the inlet to the ejector enabling the prediction of the ejector performance.

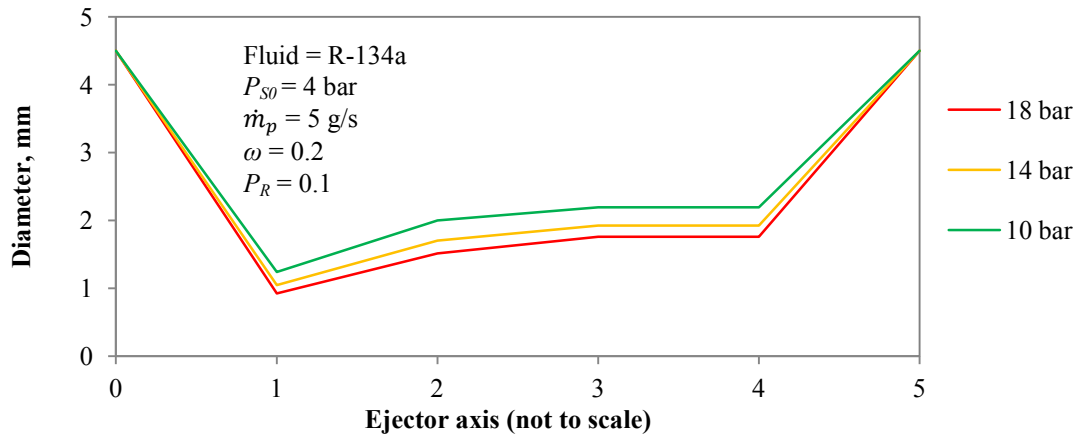


**Figure 6.8** Ejector geometry designs for a range of steady inlet stagnation pressures. [78]

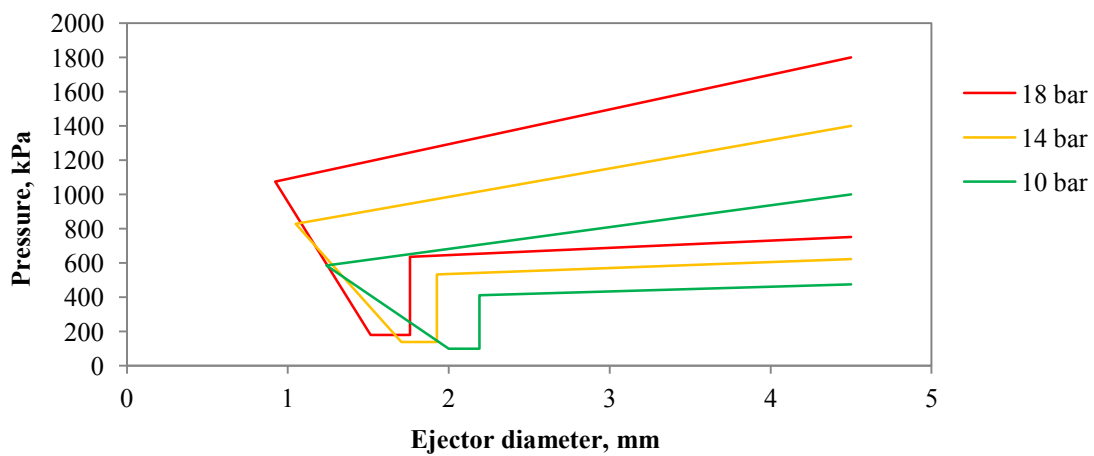


**Figure 6.9** Static pressure plot at different cross-section locations (diameter) along the ejector axis. The vertical lines represent normal shock waves in the constant area section. (100 kPa = 1 bar). [78]

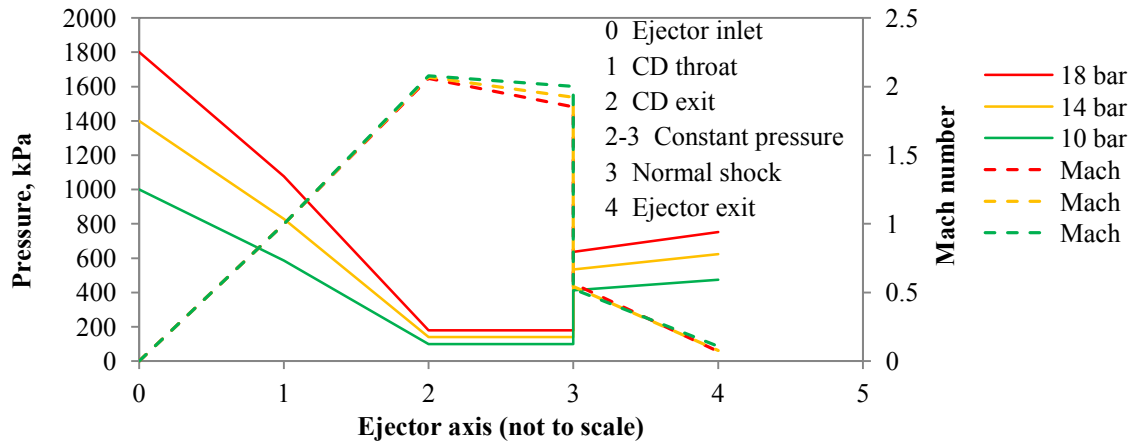


**Figure 6.10** Static pressure and Mach number profiles along the ejector axis (100 kPa = 1 bar) for varied input stagnation pressure. [78]

### 6.5 Transient ejector nozzle performance model

The performance analysis code (in Appendix F.3) permits investigation of an ejector's CD nozzle with unsteady, two phase flow. It predicts the ejector nozzle operating modes and the type and location of the non-isentropic shock waves. It can be used as a tool in predicting if (and when) ejector entrainment is achieved. A quasi-steady approach is followed to map the performance of the device through the transient flow regime. This model is unique in being able to solve for the transient operating modes of the CD nozzle at the ejector inlet which enables interpretation of the ejector operating modes from the Mach number and pressure profiles. To the author's knowledge, there is no analytical model available for analyzing the ejector performance in a transient blow-down application. The oblique shocks are characterized by a complex series of supersonic wave motions that cannot be modeled using one-dimensional theory, although the occurrence and duration of the oblique shocks can be predicted.

The code is implemented using the logic diagram in Figure 6.11. It solves for the operating modes of a given ejector nozzle that is fed by a depressurizing boiler, initially containing a fixed mass. The unsteady flow is assumed to be quasi-steady with the instantaneous flow properties being a function of time. At each incremental time step, a fixed mass of refrigerant leaves the boiler resulting in a decrease in feed pressure, temperature and density. The CD nozzle operating modes are solved to investigate the occurrence of non-isentropic oblique and normal shock waves. Although the boiler block in a PRS would operate at an approximately constant temperature, the rapid blow-down reduces the pressure of the refrigerant inside the vessel faster than thermal conduction and convection from the block to the refrigerant can take place. Therefore the boundary for boiler control volume is considered to be adiabatic, and the

refrigerant depressurizes isentropically.

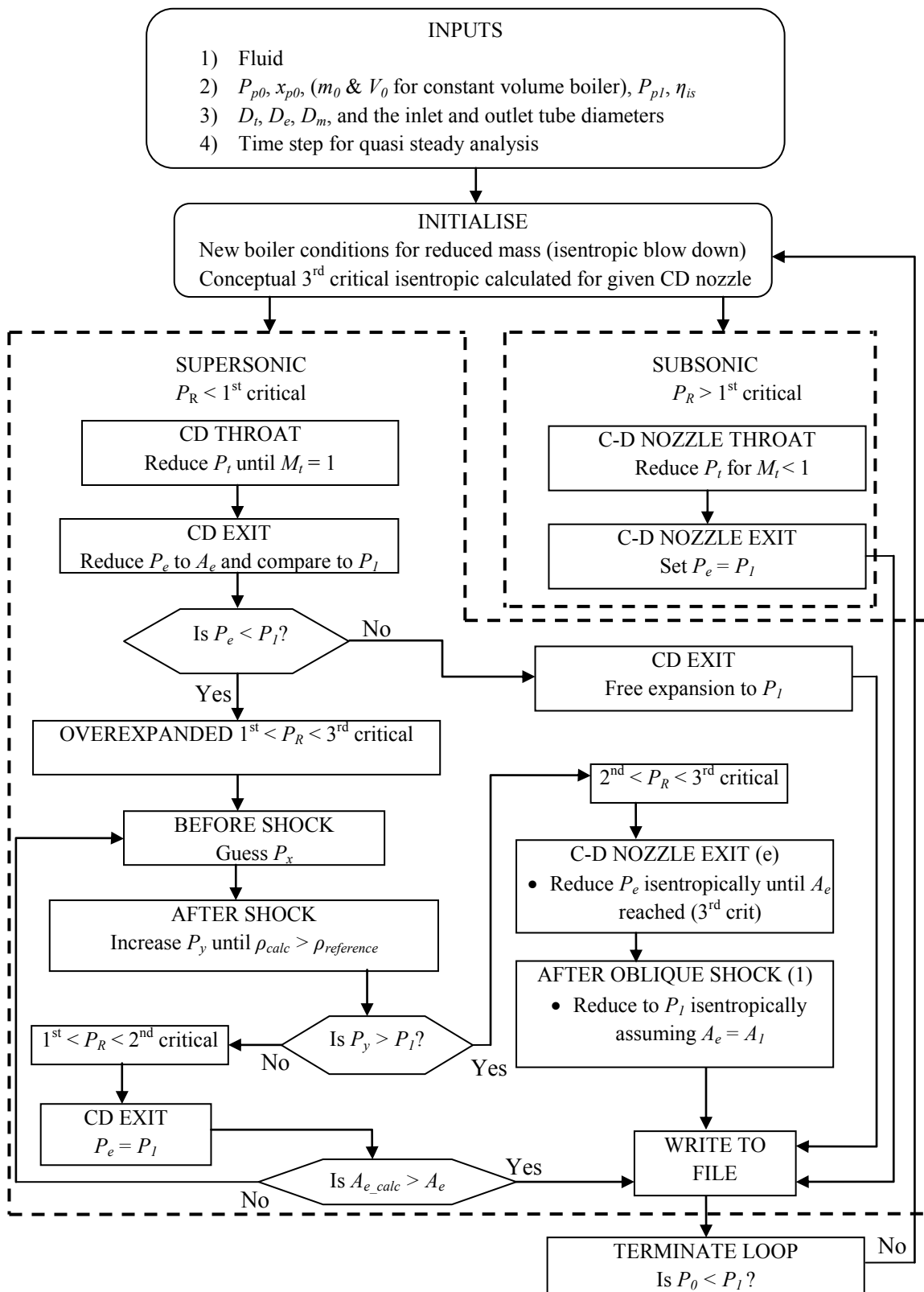


**Figure 6.11** Transient performance logic flow chart for the analysis of unsteady flow through an ejector CD nozzle. [78]



### 6.5.1 Transient model validation

The accuracy of the code was compared with an ideal gas model, using Equations 6.16 to 6.24, where  $k$  is the ratio of specific heats ( $C_p/C_v$ ), and nitrogen as the working fluid. The ideal solution was compared with the real solution, which makes use of Equations 6.5 to 6.15.

$$P = P_0 / [1 + ((k - 1)/2)M^2]^{k/(k-1)} \quad (6.16)$$

$$\rho = \rho_0 / [1 + ((k - 1)/2)M^2]^{1/(k-1)} \quad (6.17)$$

$$T = T_0 / [1 + ((k - 1)/2)M^2] \quad (6.18)$$

$$A = (A_t/M) [(1 + ((k - 1)/2)M^2) / ((k + 1)/2)]^{(k+1)/(2(k-1))} \quad (6.19)$$

$$\dot{m}_{choked} = A_t P_0 \sqrt{(k/RT_0)} (2/(k + 1))^{(k+1)/(2(k-1))} \quad (6.20)$$

$$M_y = \sqrt{(M_x^2 + 2/(k - 1)) / ((2k/(k - 1))M_x^2 - 1)} \quad (6.21)$$

$$P_y = P_x [M_x^2 (2k/(k + 1)) - (k - 1)/(k + 1)] \quad (6.22)$$

$$\rho_y = \rho_x [(((k + 1)/2)M_x^2) / (1 + ((k - 1)/2)M_x^2)] \quad (6.23)$$

$$P_{0y} = P_0 \left[ \frac{(((k+1)/2)M_x^2 / (1 + ((k-1)/2)M_x^2))^{k/(k-1)}}{(((2k/(k+1))M_x^2 - (k-1)/(k+1))^{1/(k-1)}} \right] \quad (6.24)$$

Figures 6.12, 6.13 and 6.14 compare the real to the ideal results for the case where a 100 cm<sup>3</sup> boiler containing 8 g of pressurized nitrogen ( $x \approx 1$ ) is expanded through a CD nozzle, having a 0.8 mm throat and 1.6 mm exit diameter. The back pressure for the CD nozzle is set at 40 kPa to simulate the required ejector suction pressure. The figures show that the output pressures, Mach number and the mass flow rate converge to similar results. The error ranges from 1.3% to 12%. The isentropic free expansion wave for under-expanded flow and oblique shocks for over-expanded flow downstream of the CD nozzle cannot be modeled accurately using one-dimensional theory, but the analysis does predict when they occur.

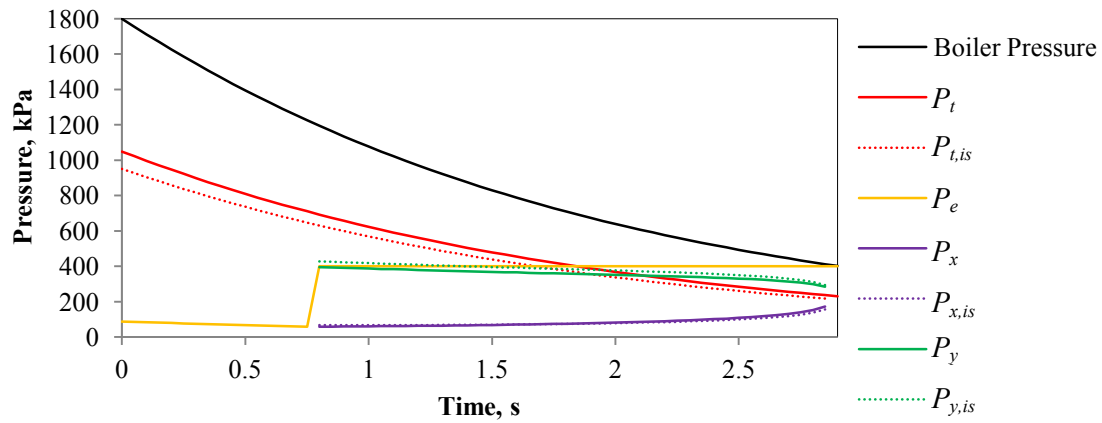


**Figure 6.12** Static pressure at different nozzle locations during transient blow-down. The real gas solution (solid lines) is compared with the ideal gas solution (dotted lines) from Equations 6.16 and 6.22. The error ranges from 3.0% to 12%. [78]

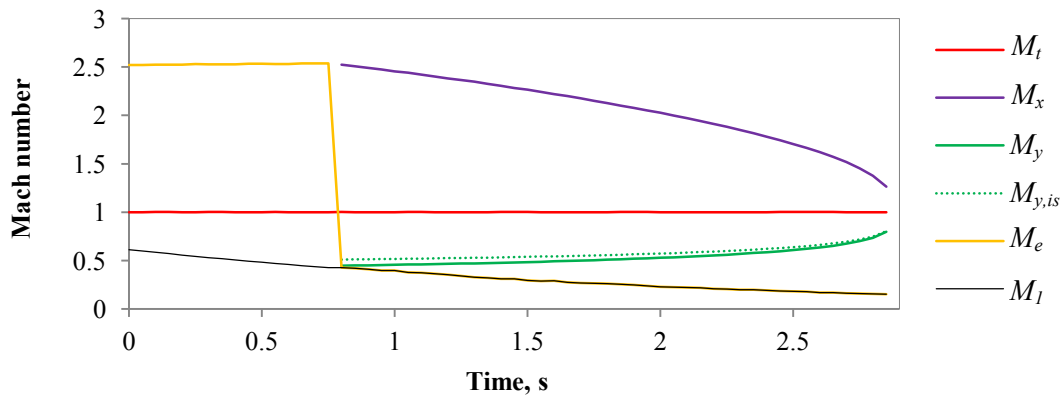


**Figure 6.13** Mach number for different nozzle locations during the transient blow-down. The real gas solution (solid line) is compared with the ideal gas solution (dotted line) from Equation 6.17. The error reduces from 12% to 1%. [78]

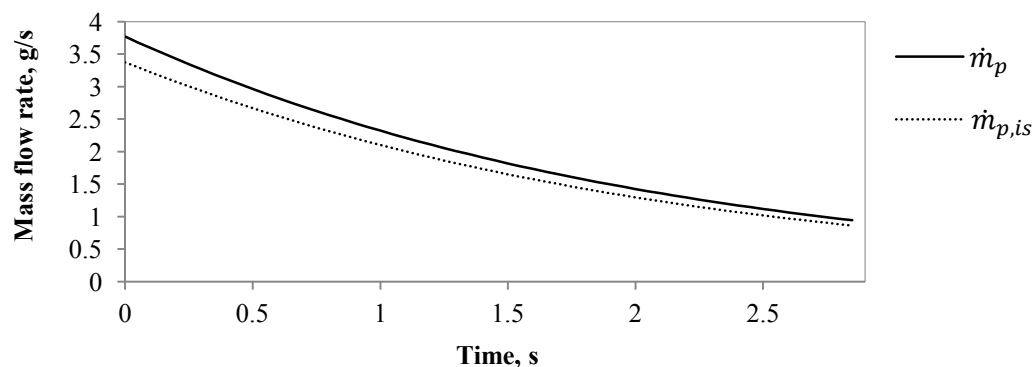


**Figure 6.14** Choked mass flow rate reduces as the boiler empties. The real gas solution (solid line) is compared with the ideal gas solution (dotted line) from Equation 6.20. The error reduces from 11% to 1%. [78]

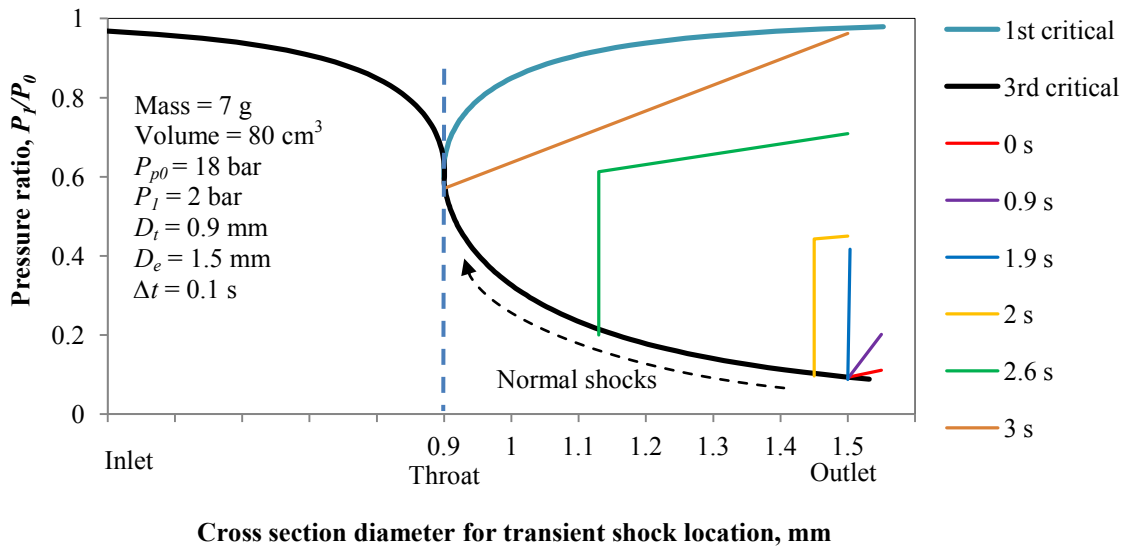
## 6.5.2 Transient model results

The transient model enables investigation of the dynamic behavior of an ejector's CD nozzle subject to a blow-down operation. The one-dimensional model focuses on the inlet nozzle since it is the most important part in an ejector. The under-expanded free expansion wave and the over-expanded shock train cannot be captured using one-dimensional theory, but the analysis gives a good indication of the flow dynamics involved. The presence of shocks greatly reduces the motive flow velocity, and increases the pressure. For an ejector to provide maximum entrainment, the CD nozzle must fully expand the flow and avoid oblique and normal shocks that produce entropy.

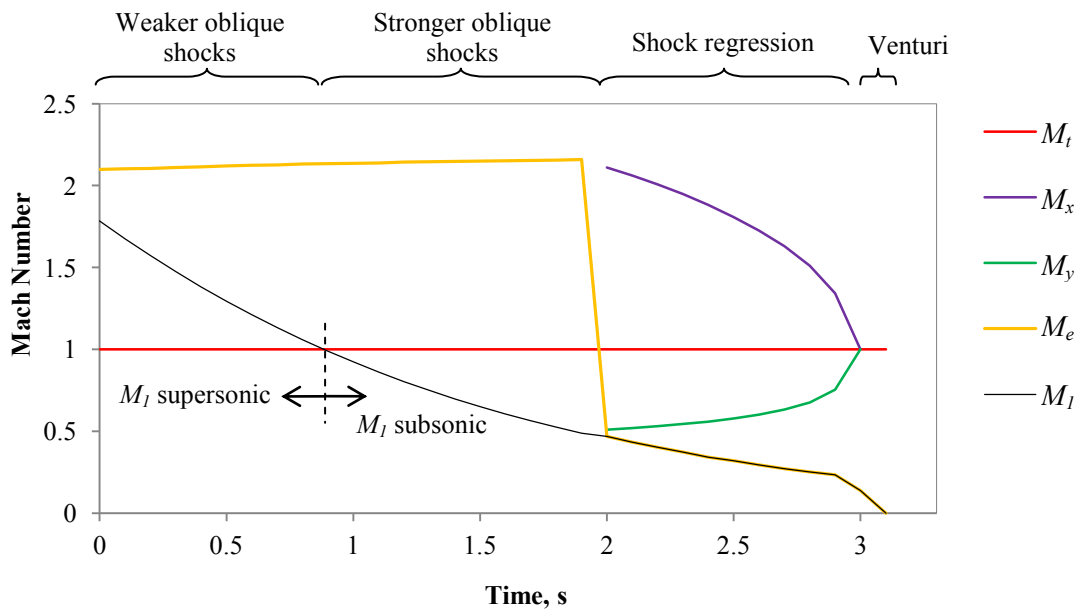
The results presented here pertain to the ejector geometry that is required for the 18 bar pulse ( $\Delta P_{set} = 8$  bar) in Figure 6.8. The CD nozzle geometry has a 0.9 mm throat with a 1.5 mm exit diameter. An 80 cm<sup>3</sup> PTL boiler was simulated containing 7 grams of R-134a pressurised to 18 bar and exhausted through the CD nozzle. The results show the ejector operating modes and shock locations with respect to time. The back pressure ( $P_i$ ) downstream of the CD nozzle is set to 2 bar.

Figure 6.15 graphs the operating modes during the transient blow-down; note the similarity to Figure 6.4. The quasi-steady approach tracks the shock location as it moves up the nozzle towards the throat. The straight line plots after the shocks are due to the limited sample points solved by the model; realistically, these should form a curve. In this case, it is evident that the flow is never perfectly expanded as it is initially over-expanded, with an increasing pressure ratio as the pulse dissipates. The cross-section diameter at the shock can be read off the x-axis. At 2.6 seconds (green trace) the normal shock is located at the 1.13 mm cross-section, approximately half way inside the nozzle. The oblique shocks (red and purple trace) are a schematic representation of the flow because of one-dimensional flow assumptions.

The Mach numbers at the throat, before the shock, after the shock, at the exit, and downstream of the CD nozzle are plotted in Figure 6.16, for the 3 second pulse. The flow downstream of the CD nozzle ( $M_i$ ) remains supersonic for 0.9 seconds (29% of the blow-down) with weak oblique shocks which may still result in secondary entrainment. After 0.9 seconds, progressively stronger oblique shocks occur reducing the downstream Mach number. This is followed by normal shock waves inside the CD nozzle from 1.9 seconds, limiting secondary entrainment.



**Figure 6.15** Operating modes of a CD nozzle (0.9 mm to 1.4 mm) during 3 second blow-down, indicating transient oblique and normal shocks. [59]



**Figure 6.16** Mach number at different locations in the CD nozzle in response to the 3 second transient blow-down. [59]

### 6.5.3 Optimizing ejector geometry

To maximize secondary entrainment, the velocity of flow out of the motive nozzle into the suction chamber must remain supersonic for an appreciable amount of time, thereby reducing the period in which non-isentropic shocks occur. Using the operating conditions that were modeled in Figure 6.15, the ejector CD nozzle geometry was varied to investigate the effect on the downstream Mach number,  $M_l$ . By reducing the CD nozzle outlet diameter to less than the

steady state design condition of 1.5 mm, the flow is expected to initially be below the third critical point (under-expanded). This ensures that the design condition is met at some time during the blow-down where the nozzle flow is perfectly expanded to the third critical pressure ratio.

Figure 6.17 shows the Mach number profiles for different CD nozzle outlet geometries subjected to the same blow-down conditions. As the outlet diameter is reduced, the period of downstream supersonic flow increases (period where  $M_1 > M_t$ ). For a converging only nozzle, free expansion from the nozzle exit to the downstream pressure occurs. The free expansion wave may block the flow of secondary fluid altogether which must be avoided. Rather than allow the flow to expand freely, the diverging section controls the rate of expansion and directs the flow downstream. A total of six exit diameters were investigated for the current flow conditions, ranging from 0.9 mm to 1.4 mm. The resulting periods of supersonic and subsonic flow are plotted in Figure 6.18. The best design choice would be that corresponding to Figure 6.17 (b). An exit diameter of 1.1 mm results in the critical pressure ratio being reached at 1 second, with supersonic flow lasting up to 1.7 seconds. The remaining 1.2 seconds of blow-down is subsonic and is associated with losses due to oblique and normal shocks.

The operating modes of the designed nozzle are plotted in Figure 6.19. The results are similar to Figure 6.15 except that the smaller exit diameter of 1.1 mm results in a reduced period of non-isentropic shocks. An animation of the transient operating modes is included in Appendix F. The flow is initially under-expanded for 1 second, at which point it passes through the third critical design condition. Progressively stronger oblique shocks occur from 1 second to 2.5 seconds, followed by normal shocks that regress up the nozzle.

Provided that the control scheme is sufficiently adept, the pulse can be directed through a bypass loop for the latter portion of the blow-down, avoiding the ejector and the losses associated with it.

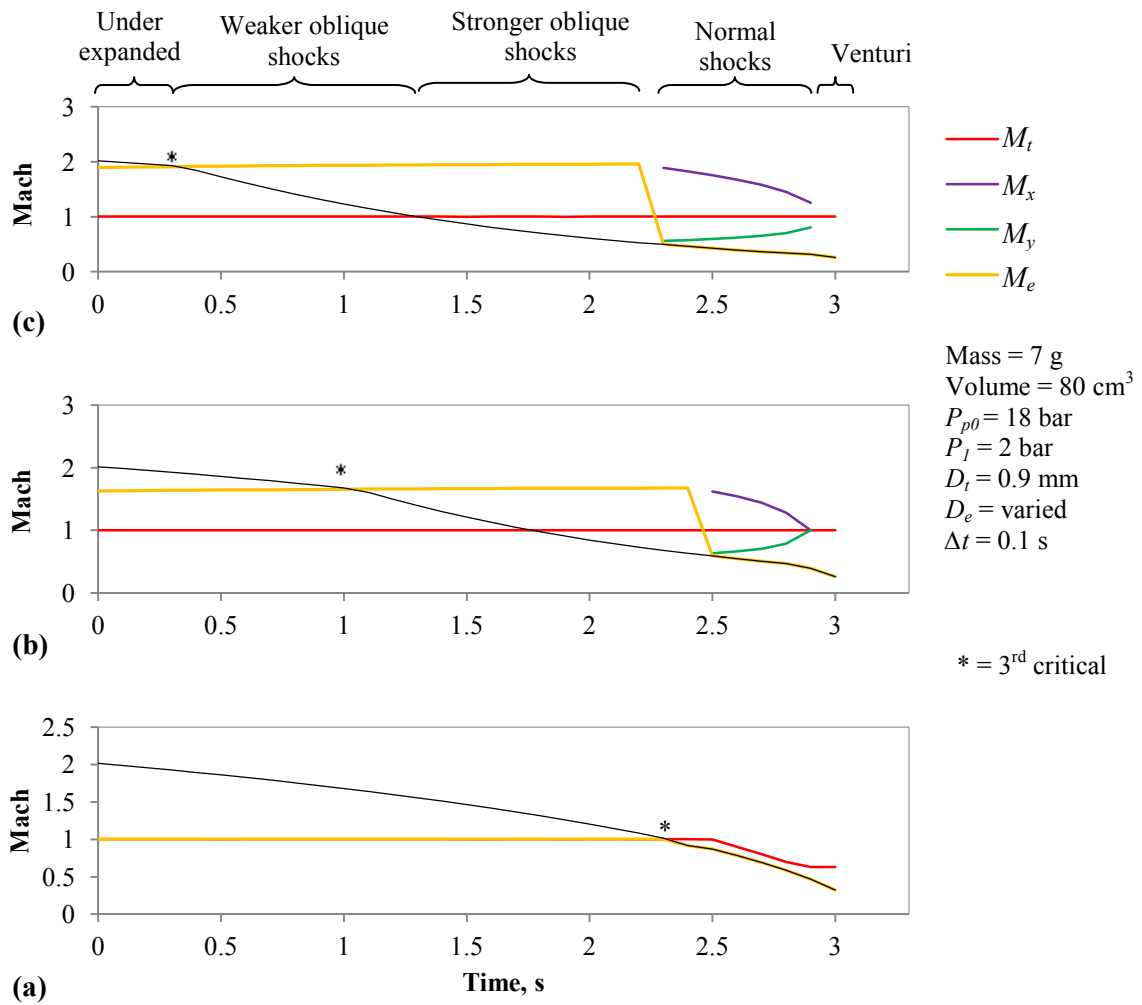


**Figure 6.17** Mach number profiles for different ejector nozzle geometries (a)  $D_e = 0.9$  mm, (b)  $D_e = 1.1$  mm, and (c)  $D_e = 1.3$  mm. [59]

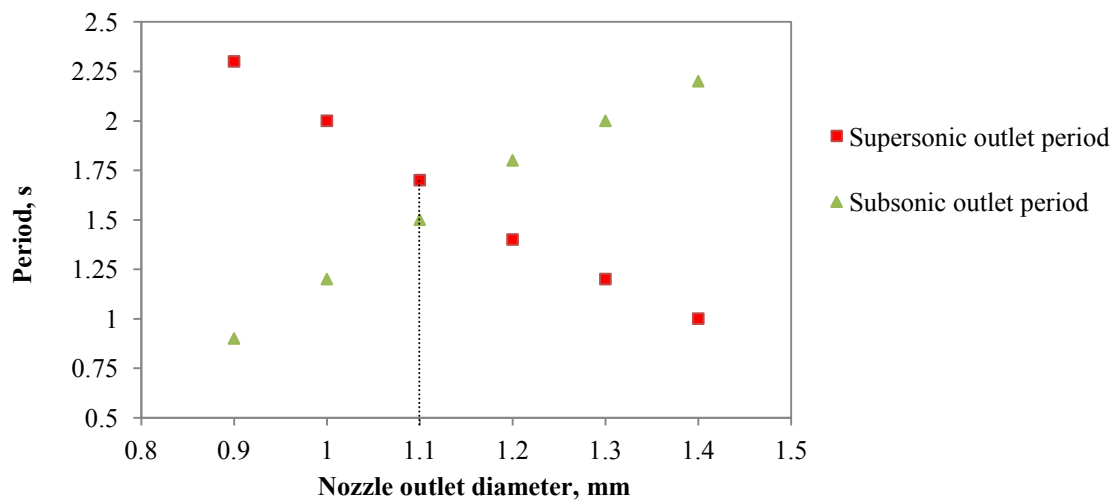


**Figure 6.18** Periods of supersonic and subsonic flow for different CD nozzle exit diameters, and constant throat diameter of 0.9 mm.

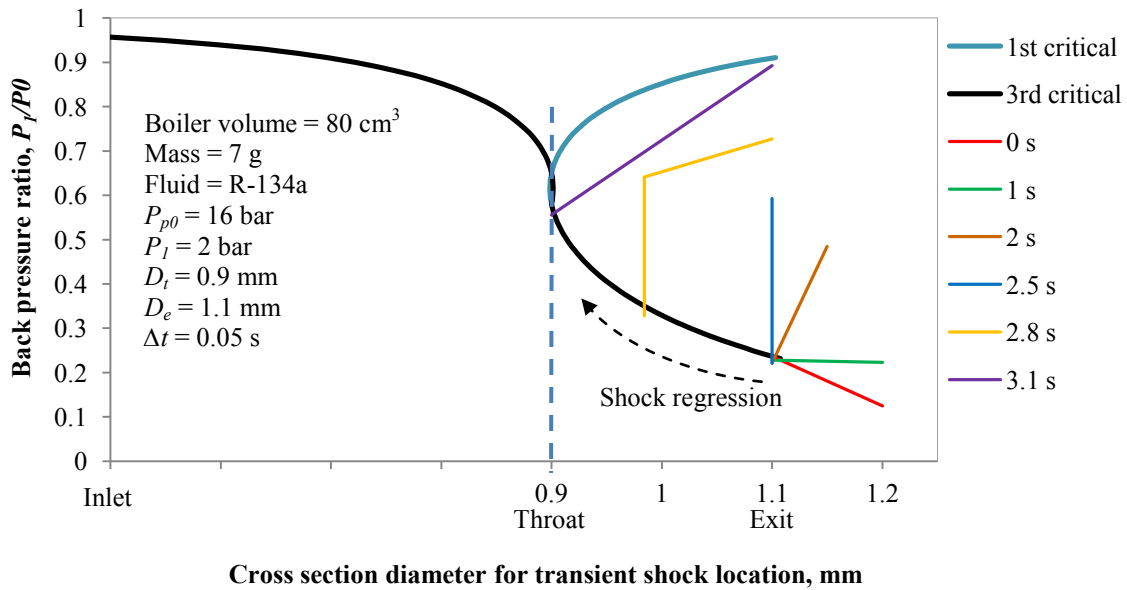


**Figure 6.19** Operating modes of a CD nozzle (0.9 mm to 1.1 mm) during 3.1 second blow-down, indicating transient oblique and normal shocks.

## 6.6 PRS components

The PRS was assembled from the components used in the PTL. Additional components include an ejector, expansion valve, evaporator tube, check valve, additional pressure transducers, thermocouples and an additional 3-way servo valve. The small volume of the tube has a negligible affect the refrigerant charge mass. Individual control of both 3-way valves is provided on the graphical user interface (GUI) of the custom NI LabVIEW control application, described in Chapter 5.

### 6.6.1 Expansion valve

The expansion valve provides a pressure drop of up to 6.8 bar across it, expanding the fluid into the evaporator. The evaporator is a simple 1/8" stainless steel tube that connects the LRL to the secondary inlet of the ejector, Figure 6.20. A small expansion valve was selected having 1/8" tube ports and a vernier scale.

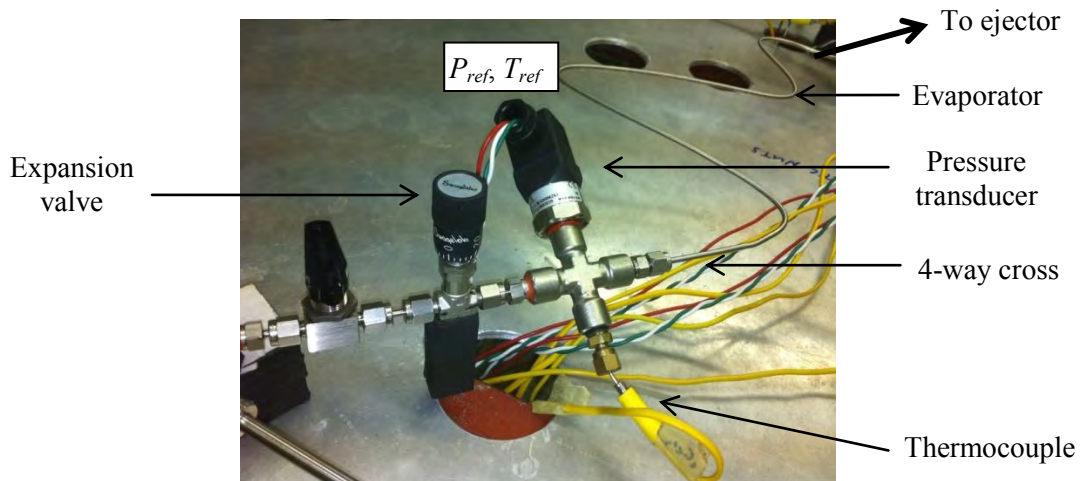


**Figure 6.20** Expansion valve and evaporator tube in the ejector cooling loop.

### 6.6.2 The ejector

A custom ejector was designed (Figures C.9 and C.10, Appendix C) but not employed in the PRS. Three commercial ejectors were available with nozzle throat diameters of 2.4 mm, 1.5 mm and 0.8 mm. The smallest ejector with a 0.8 mm throat diameter was installed in the PRS, Figure 6.21. This ejector is similar to the design requirement of having a 0.9 mm throat. During operation, valves are toggled such that refrigerant is pulsed through the ejector to entrain and compress refrigerant from the cooling loop evaporator.

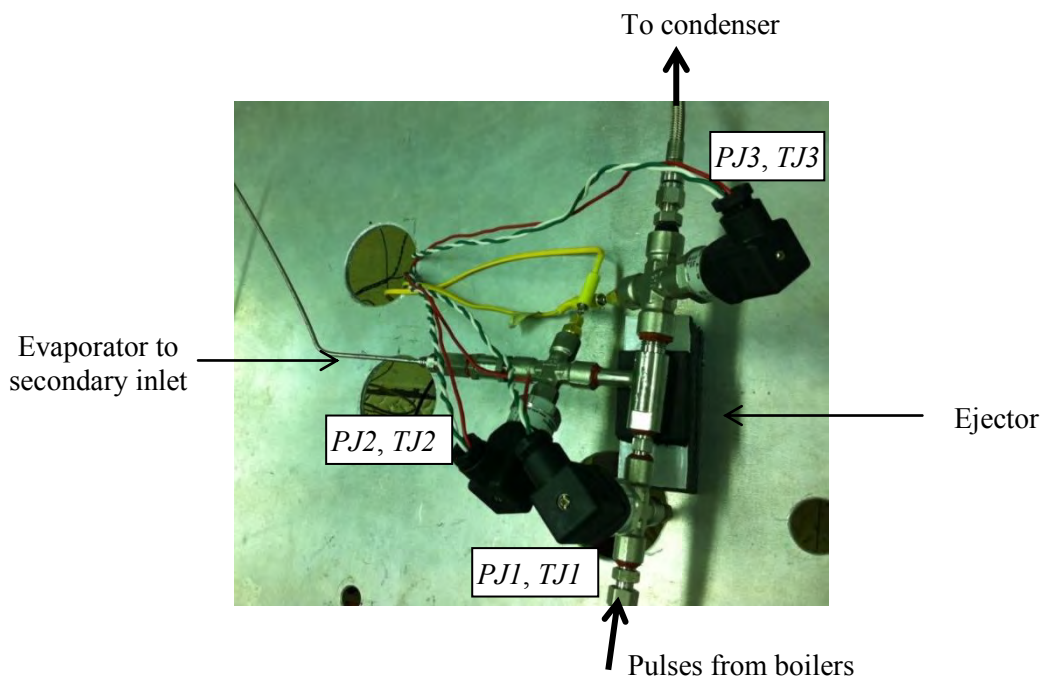


**Figure 6.21** Ejector installed with pressure transducers and thermocouples



## 6.7 PRS variants

### i) Variant I

The PRS was configured such that two variants could be tested. Variant I (shown schematically in Figure 2.18) is photographed in Figure 6.22. It enables operation of the PTL when the ejector cooling loop is bypassed. Two valves at the outlet of the boilers are actuated to pulse refrigerant either through the VTL bypass or through the ejector cooling loop. Ideally, the automated control scheme operates the second valve such that the ejector functions for the first portion of the pulse exploiting the high pressure ratio across it. When the boiler pressure falls below a predetermined value, the valves toggle such that the flow bypasses the ejector. This avoids the non-isentropic losses associated with the shocks that occur in an ejector at low  $\Delta P$ . This method of operation requires a low pulse frequency ( $f$ ) to enable time for the servo-valves to actuate. The servos that actuate the valves are rated at  $0.17 \text{ s}/60^\circ$  therefore they require at least  $0.26 \text{ s}$  to travel  $90^\circ$ . Considering the torque required for actuating the valves, the servo's speed is further decreased. Closer examination of the PTL performance map reveals that a PTL operating near the right pulse limit would provide increased  $\Delta P$  at low  $f$ .

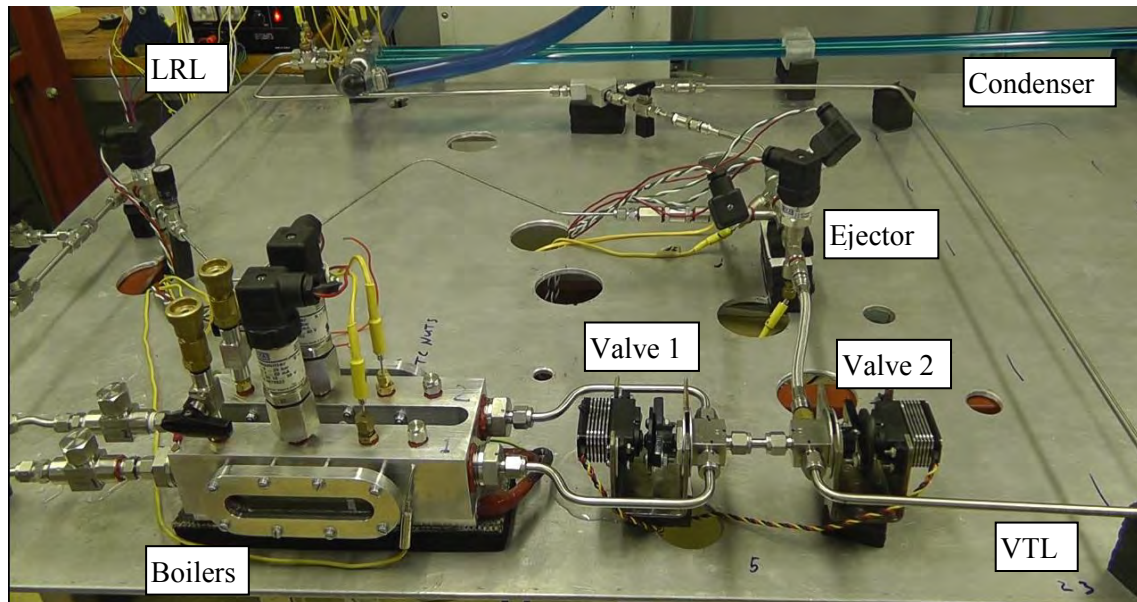


**Figure 6.22** PRS variant I integrates a VTL bypass which enables normal PTL operation. Valve 2 is actuated to direct pulses of refrigerant through the ejector cooling loop during PRS operation.

## ii) Variant II

Variant II (shown schematically in Figure 6.23) photographed in Figure 6.24 is simpler in design and does not include a VTL bypass. The second 3-way valve is located in the LRL to direct refrigerant either to the boilers or to the evaporator. Ideally, the evaporator section is closed off during pulsing to maximize the flow to the boilers. This allows for the maximum amount of refrigerant to be circulated back to the boilers, maintaining steady operation. The valve is actuated in-between pulses to replenish the liquid refrigerant upstream of the expansion valve. The ensuing pulse is intended to entrain refrigerant out of the evaporator lowering the temperature and pressure.

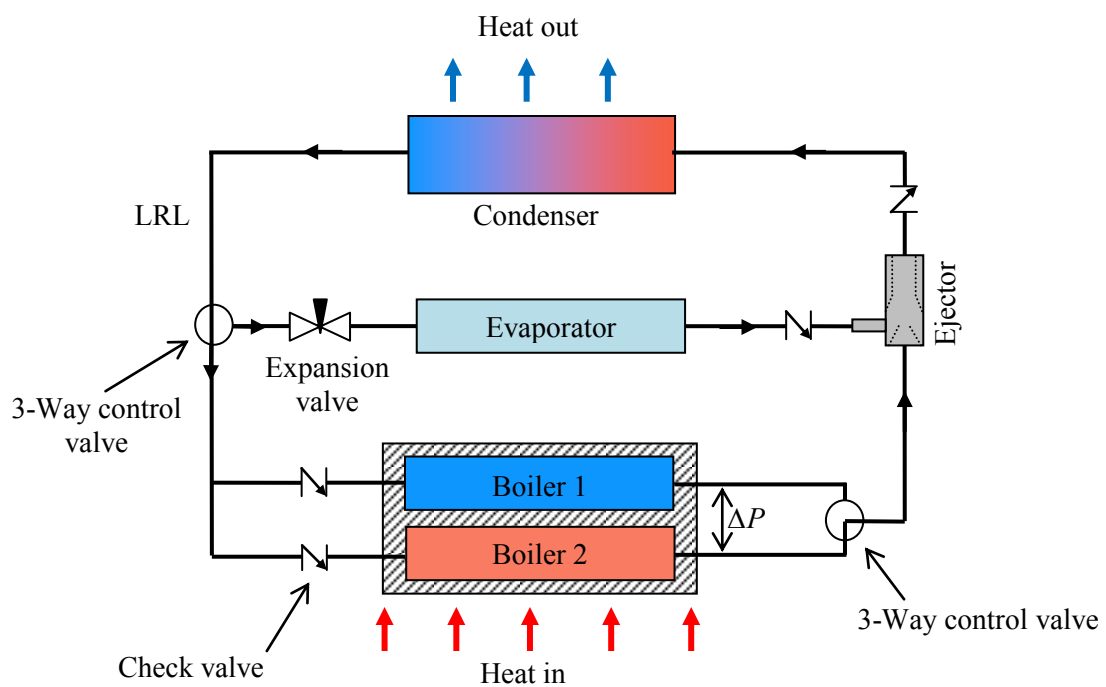


**Figure 6.23** Schematic of PRS variant II. The second 3-way valve is located in the LRL.

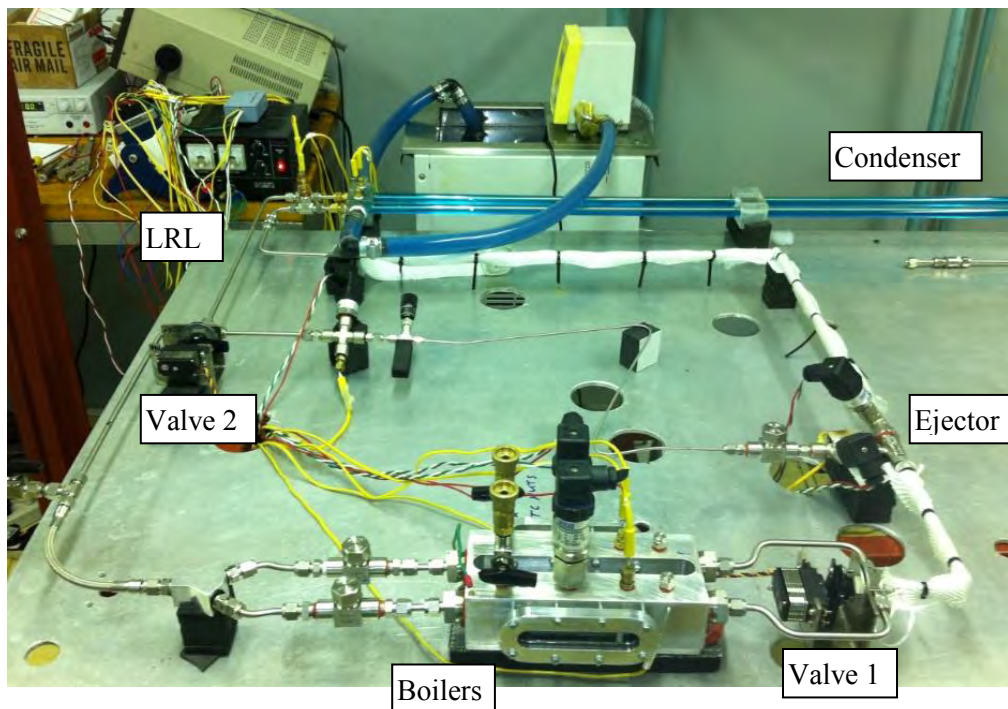


**Figure 6.24** PRS variant II includes a 3-way valve in the LRL and no VTL bypass loop.

## 6.8 PRS experimental results

A number of experiments were carried out in an effort to validate the PRS concept. This included different system configurations (variants I and II), valve operation, heat input and  $\Delta P_{set}$ . Although no cooling effect was achieved, promising results were obtained. Automated operation of the second 3-way servo valve could not be carried out (in both variants) due to the unpredictable pulsing of the boilers. The second valve, whether installed in the VTL for variant I or the LRL for variant II, was configured manually depending on PTL or PRS operation.

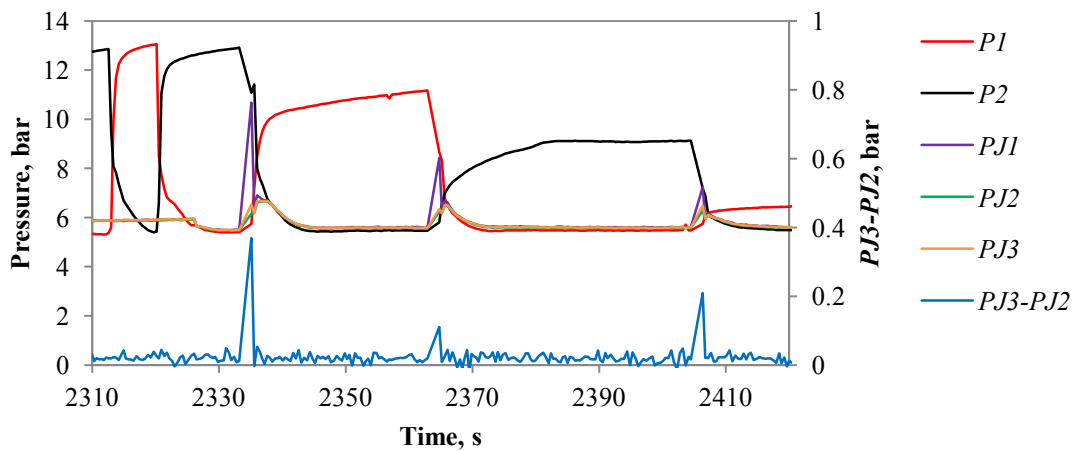
### 6.8.1 Unsteady PRS operation

Figure 6.25 shows the pressure history for an experiment where variant I operated in PTL mode with a steady state  $\Delta P_{set}$  of 7.5 bar, until 2335 s. The system was charged with  $x = 67\%$  vapor, heat was supplied at 300 W and the condenser was set to 15°C. At 2335 s the valves were configured such that the pulses were directed through the ejector cooling loop. The absolute pressure measured at the ejector inlets ( $P_{J1}$ ,  $P_{J2}$ ,  $P_{J3}$ ) was initially 5.5 bar. At the start of the pulse  $P_{J1}$  increases to 10.6 bar. This is 2.4 bar less than  $P_2$ , and is due to the expansion process lowering the pressure. Ideally, the ejector should be placed as close to the boiler exit as possible to exploit the high  $\Delta P$ , and improve the ejector back pressure ratio ( $\phi$ ). This also reduces the

chance of two-phase flow developing in the ejector. Within three pulses the system stalled because the boilers were unable to pump sufficient refrigerant through the condenser to the alternate boiler.

In Figure 6.26 variant I is close to stalling at 2700 s, operating with a reduced  $\Delta P_{set}$  and increasing  $TB$ . The operation was switched over to PTL mode where the pulses were diverted through the VTL at 4220 s. The temperatures and pressures quickly stabilized. This highlights the robust operation of the PTL where the  $\Delta P_{set}$  was raised from 0.6 bar to 8 bar and  $TB$  reduced by 13°C within 50 s.

An attempt to start the variant II is shown in Figure 6.27. The system was charged with  $x = 68\%$  vapor, which was insufficient. The pressure trend mimicked that of the trend seen in Figure 5.7, displaying both pressure and condenser limited operation. This indicates a low charge mass, or large vapor fraction. A PRS clearly requires more refrigerant in the loop in comparison to a PTL. Increased charge mass reduces the head loss associated with the vapor section, but can result in increased system pressure.



**Figure 6.25** PRS variant I where operation is switched from PTL to PRS mode.  $Q = 300$  W,  $x = 0.67$ ,  $TWI = 15^\circ\text{C}$ . The system stalls within 3 pulses. The trend indicates a low charge mass. The initial pulse with  $\Delta P_{set} = 7.5$  bar provides compression ( $PJ3-PJ2$ ) to the secondary inlet of 0.4 bar.

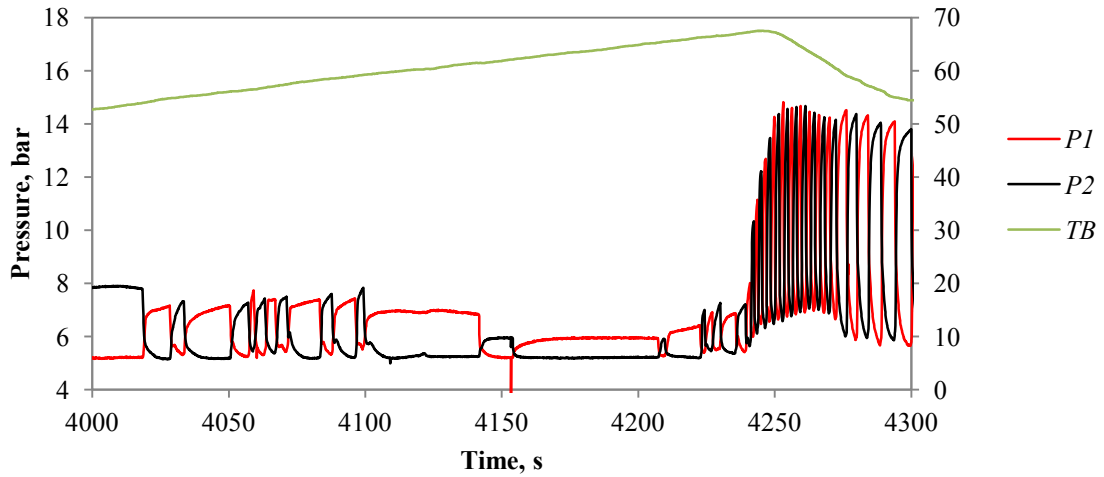


**Figure 6.26** PRS variant I, operating with unsteady pulses and decreasing  $\Delta P_{set}$ , increasing in temperature and about to stall. Pulses are diverted through the VTL bypass at 4220 s to reduce boiler block temperature. This highlights the importance of having a bypass loop in the PRS.

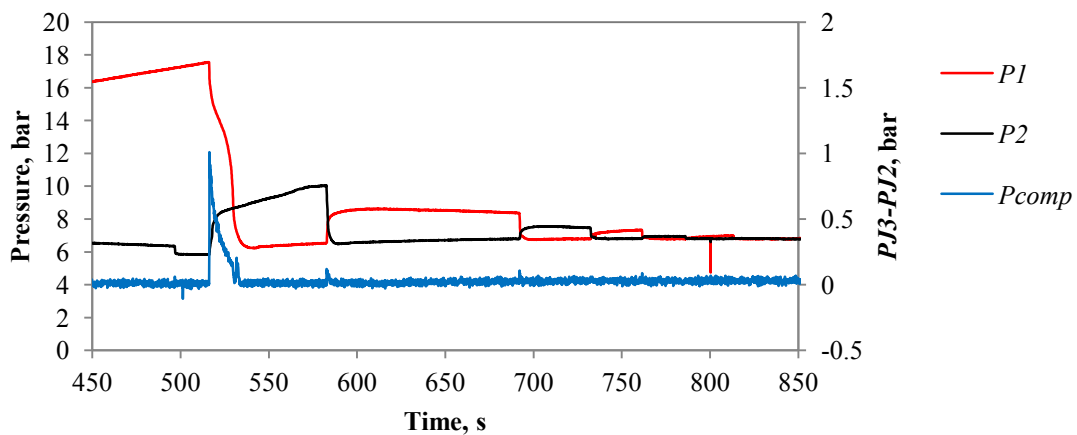


**Figure 6.27** PRS variant II operation with  $x = 0.68$ . The system is both condenser and pressure limited, indicating a low charge mass. The initial pulse with  $\Delta P_{set} = 11.5$  bar results in 1 bar compression ( $PJ3-PJ2$ ) of the secondary stream.

### 6.8.2 Steady PRS operation

Due to the increased capacity of the current boiler design, and the simpler construction of variant II, the system was able to circulate refrigerant without stalling. This was the first demonstration of a PRS that was able to sustain steady pulsing, although the refrigeration effect could not be achieved.

The PRS was frequently characterized by steady but asymmetric pulsing. The system was unable to provide cooling and could be described as a PTL with a flow constrictor. Figure 6.28

presents the maximum steady-state compression that was achieved for variant II. A  $\Delta P_{set}$  of 11 bar resulted in a maximum compression of 0.73 bar. Compression increases with an increase in  $\Delta P_{set}$ , which is also evident in Figure 6.29. The average  $\Delta P$  is 4.2 bar and the slightly stronger pulses result in improved compression.

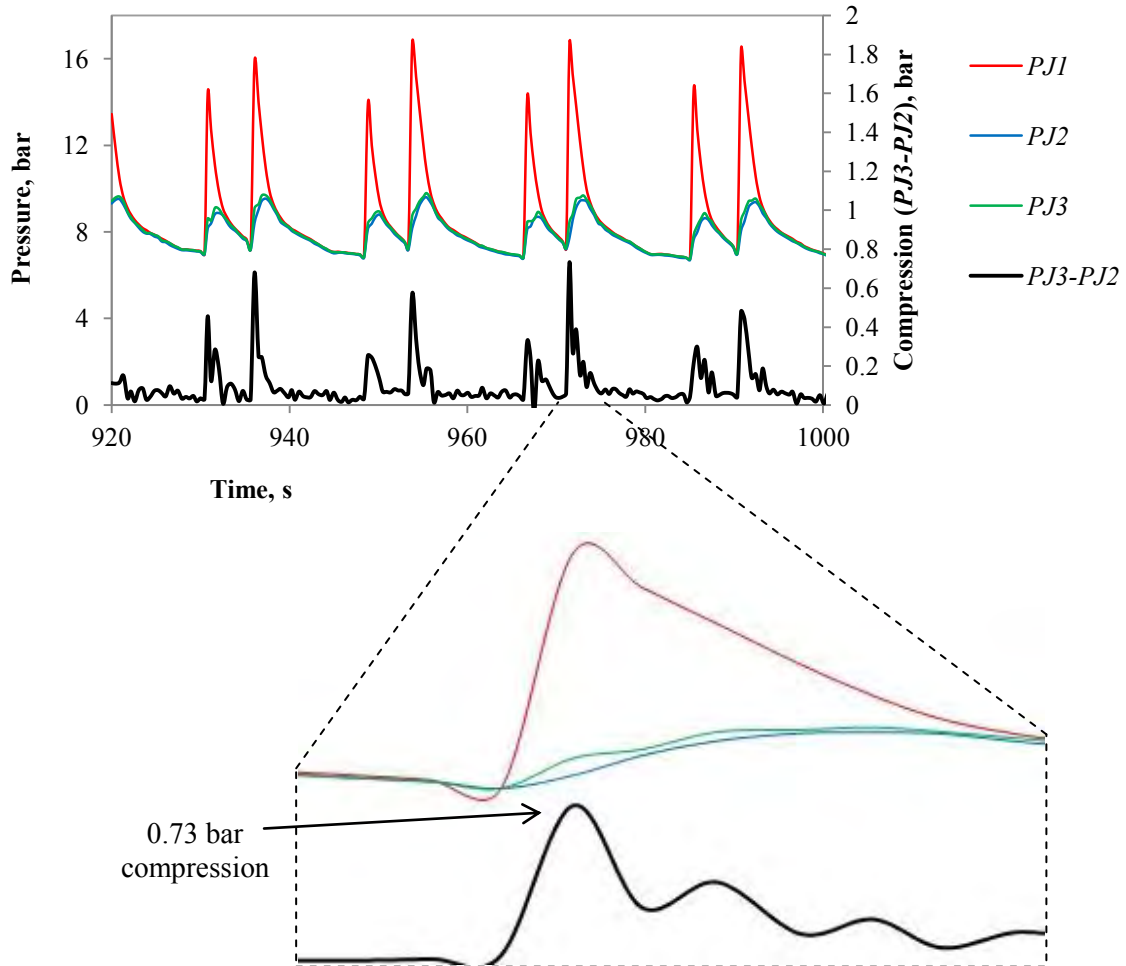


**Figure 6.28** Steady (asymmetric) operation of variant II results in asymmetric compression of the secondary inlet to the ejector.  $\Delta P_{set} = 9$  bar to 11 bar,  $x = 55\%$ ,  $TWI = 15^\circ\text{C}$

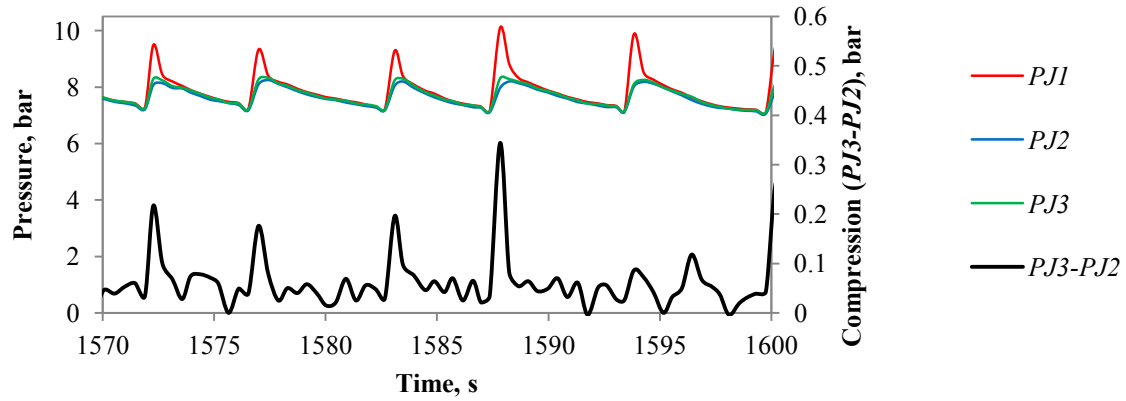


**Figure 6.29** Low  $\Delta P$  pulsing through ejector of variant II results in uneven compression.  $\Delta P_{set} = 4.2$  bar,  $x = 55\%$ ,  $TWI = 15^\circ\text{C}$

Extended duration experiments lasted up to 6 hours, but symmetric pulsing was difficult to achieve. The limited data obtained in testing at steady-state conditions enabled the generation of the performance curves shown in Figures 6.30 and 6.31. The  $\Delta P_{set}$  vs.  $f$  map in Figure 6.30 resembles that of a conventional PTL where  $\Delta P_{set}$  is inversely proportional to  $f$ . The performance curve generated for test 1 (Variant I with integrated PTL and PRS) is noticeably different to the two curves generated for test 2 (variant II – simple PRS). Variant II has substantially less fittings in the VTL, which enables improved circulation of refrigerant with increased  $f$ . Two PTL curves are superimposed to aid in the comparison. Variant II generates similar performance curves to a PTL at approximately half the operating power. The PRS requires more refrigerant (or reduced  $x$ ).

Figure 6.31 provides the compression curves for the experiments. An increased  $\Delta P_{set}$  provides increased compression of the fluid at the secondary inlet to the ejector. Variant II was unable to maintain steady states at  $\Delta P_{set}$  above 6 bar.

Although the PRS did not function in refrigeration mode, the reaction of the ejector to the flow pulses as shown in Figure 6.28 and 6.29 is encouraging, and suggests that the PRS concept may well function as expected with additional modifications.



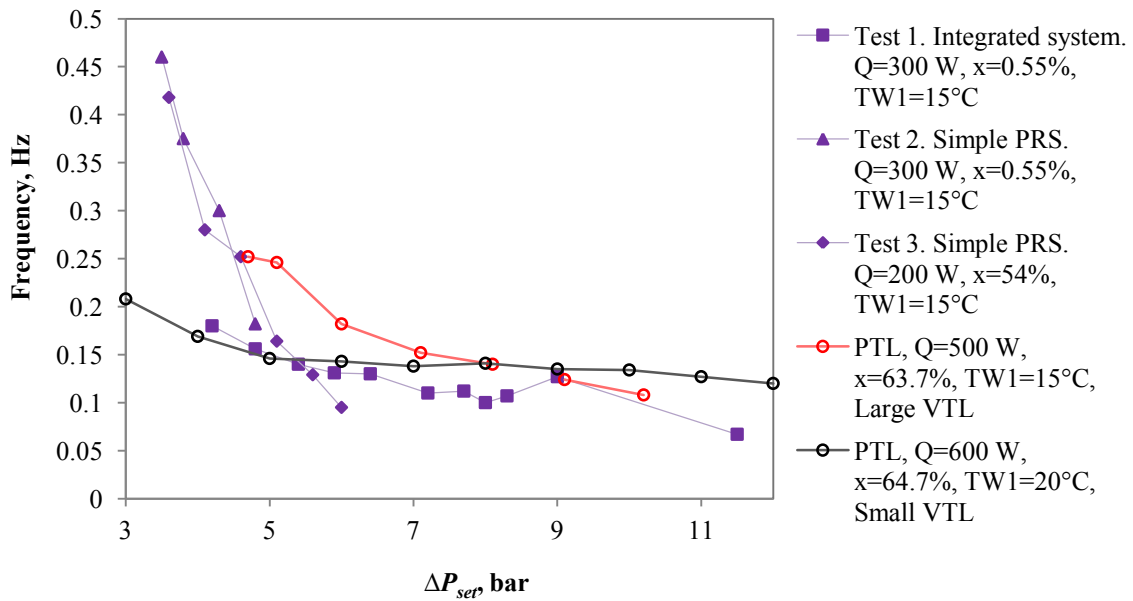


**Figure 6.30**  $\Delta P_{set}$  vs. Frequency for three PRS tests. Two PTL curves are superimposed for comparison. The inversely proportional relationship is characteristic of a PTL pumped system.

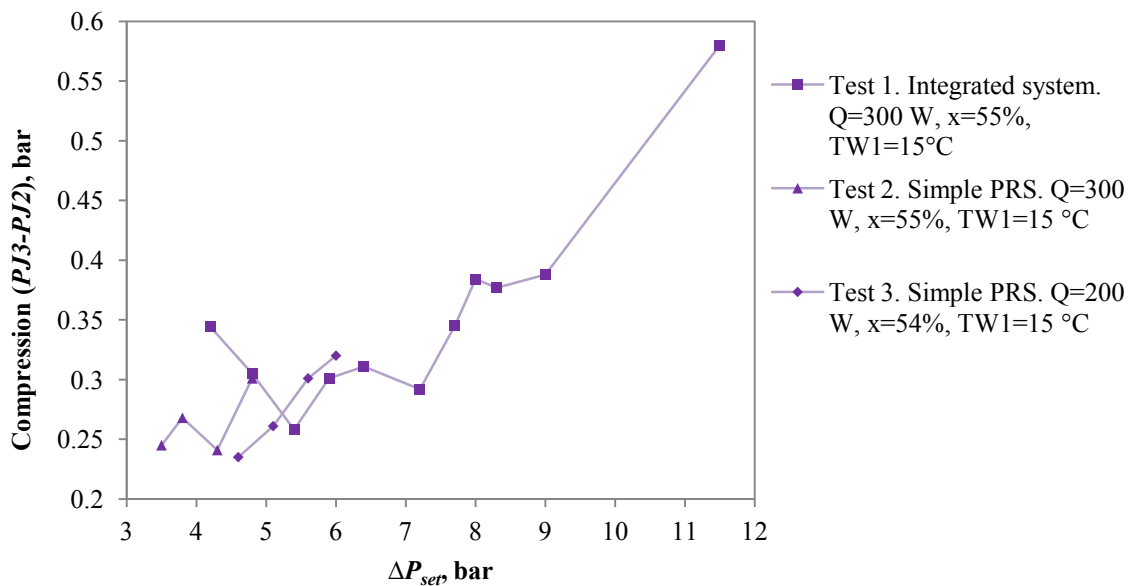


**Figure 6.31**  $\Delta P_{set}$  vs. Compression achieved by the ejector. Compression increases with  $\Delta P_{set}$ .

## 6.9 Summary

Two variants of the prototype ejector-based PRS were tested. The PRS was assembled using the PTL boilers, condenser and the components required in the ejector cooling loop.

The ejector in the cooling part of the cycle was driven by the PTL boilers and was therefore exposed to transient pulses of refrigerant. The design of an appropriate ejector was investigated



through the development of two analytical ejector models. The design code was used to prescribe an appropriate ejector geometry for steady-state flow conditions. The geometry was then investigated using the transient performance analysis model.

For both PRS variants investigated, the highest compression achieved was 0.73 bar (this was from a  $\Delta P_{set}$  of 11 bar) and the system was unable to achieve refrigeration. Although the integration of an ejector with a PTL was demonstrated, the rapid decrease in  $\Delta P$  and the poor circulation rate through the cooling loop resulted in little to no entrainment ( $\omega$ ) at the ejector. The transient model of the ejector indicated that performance would improve with the incorporation of a custom made ejector that has a smaller nozzle exit diameter. The smaller exit diameter would result in the flow initially being under-expanded, and therefore pass through the third critical point of operation, to achieve a maximum entrainment of 0.2, for a finite period.

It is probable that the ejector pressure ratio ( $\phi$ ) increases to unity much faster than what is predicted by the transient model. The transient model does not take into account the increasing back pressure at the condenser, in response to Boyle's Law. A modification to the code is required to enable improved performance prediction.

A scaled up PRS using a similar sized ejector would result in a longer transient blow down with a more appreciable portion of entrainment. This may offer the best approach for successfully transforming the PTL into a pump-free refrigeration device.

## 7 CONCLUSION

Two thermal management systems were investigated for terrestrial and space applications. The pulse thermal loop (PTL) is a lightweight, semi-passive cooling system. During operation, it provides approximately isothermal two-phase cooling of heat-generating equipment, without a circulation pump. High heat transfer capability and long transport distances make the PTL more attractive than passive heat pipes (CPLs and LHPs). In comparison to pumped cycles, the PTL is able to provide power-free operation with similar driving pressures.

The PTL tested in this study included two thermally coupled boilers incorporating pressure transducers and thermocouples. The boilers were at least two times larger than previous versions and featured 115 mm long sight glass windows. The loop made use of modular components that enabled rapid system reconfiguration. A concentric tube heat exchanger was designed and constructed from extruded transparent acrylic tubes. A custom servo-controlled 3-way ball valve was designed and implemented in the control scheme.

A PTL performance map was generated and compared with the literature. Ideal and non-ideal start-up conditions were investigated (including under and over-charge mass) as well as operation at low  $\Delta P_{set}$ . A smaller pressure differential and an increased pulse frequency results in improved heat transfer at the boilers. Feedback control theory can be implemented in software to ensure a greater level of control, reduce asymmetrical behavior, and improve reliability. The PTL responds well to  $\Delta P_{set}$  ranging from 3 bar to 12 bar and varied heater inputs ranging from 100 W to 800 W. The corresponding local heat flux density (in terms of wetted area) ranged from 7.2 W/cm<sup>2</sup> to 28.9 W/cm<sup>2</sup>. Boiler vapor temperature fluctuations were typically  $\pm 4^\circ\text{C}$ . Increased pulse frequencies result in less vapor temperature fluctuation at the boilers. The PTL can operate at  $\Delta P_{set}$  below 3 bar, but this is typically associated with a high pulse frequency ( $f$ ). The servo valves used in this study were limited to a maximum of 0.5 Hz. System failure occurred on three occasions due to the 3-way servo valves malfunctioning, therefore reliability must be addressed. Solenoid valves would be better suited to increased pulse frequencies at lower  $\Delta P_{set}$ . The results indicate that a temperature sensitive device generating variable heat loads can be maintained at an approximately isothermal (constant) temperature by keeping  $\Delta P_{set}$  constant. The pulse frequency self adjusts to the required heat transfer.

The PTL was transformed into a PRS where the boilers and condenser operated as a heat pump. It was intended to provide power-free cooling without a pump or compressor in the loop. This was not demonstrated. The high driving pressures developed at the boilers were supplied to the

ejector with the aim of entraining and compressing a secondary stream. The PRS essentially functioned as a PTL with a flow restrictor in the VTL, providing isothermal cooling of the boiler block. Operation of the PRS was, however, more erratic and asymmetrical than the PTL.

The PRS performance was dependent on the functioning of the ejector. A design code was developed which determined the required ejector geometry for operation under steady state conditions. A quasi-steady two-phase performance code was also developed to analyze the dynamic behavior of the ejector performance in response to a transient pressure wave from the boilers. This was the first such predictive tool of its kind.

A smaller nozzle diverging exit diameter results in a longer period of supersonic downstream flow and fewer shock waves. Designed correctly, an ejector that operates in a transient system can provide entrainment for a finite period. A commercial ejector was selected for incorporation in the design of the pulse refrigeration system, and although the prototype was unable to provide cooling, the ejector did provide some compression to the secondary stream.

The PTL and the PRS are similar systems and experimental data demonstrates that the PTL offers potential for use in future spacecraft thermal control: it is robust, provides high heat transfer rates at high heat flux density, performs under a range of operating conditions, can be made passive using diaphragm valves, is flexible in design, and provides reduction in radiator weight due to the two-phase heat transfer. The ejector-based pulse refrigeration system (PRS) does not require a circulation pump and would be suitable for terrestrial and space (gravity-free) applications. Further analysis of the transient PRS is necessary in order to effect successful operation.

Numerous factors have been identified which should be investigated to improve the performance of the PTL, and to demonstrate the PRS. An improved boiler design could enhance the liquid contact area which would provide increased heat transfer at higher heat flux densities. This would improve the limits of the operating window in Figure 5.15. A power-free diaphragm valve should be investigated for use in the PTL to demonstrate absolute semi-passive operation. Such a valve must be validated for high  $\Delta P$  operation. PTL configurations with more than two boilers should also be investigated.

The control algorithm can be improved on by adding  $\Delta P$  feed-back control. This will enhance steady operation by avoiding asymmetrical pressure trends. The application would monitor the maximum and minimum pressures achieved at each boiler to determine which is pressure or

condenser limited (during pressurization). The condenser limited boiler is typically cooler and can be intermittently pulsed at a higher  $\Delta P_{set}$  to force more mass into the pulse limited boiler, which will reduce its temperature and pressure.

Alternative working fluids with significantly different latent heat of vaporization can be investigated. A dry refrigerant should improve the performance of the ejector in the proposed PRS. A small heater could also be added upstream of the ejector to investigate superheating the flow before expansion, thereby avoiding two-phase flow. A large condenser, which pressurizes less during blow-down through the ejector, should be investigated for the PRS. This will improve the ejector pressure ratio,  $\phi$ . The design of a larger boiler would also improve the blow-down period through the ejector.

The ejector transient model can be improved on by including the pressurization of the condenser due to Boyle's Law. This would provide improved performance prediction of the transient blow-down. Also, one-dimensional empirical correlations of the oblique shocks (Fanno and Rayleigh lines) should be investigated and included in the transient model.

## REFERENCES

- [1] Gilmore, D.G., Hardt, B.E., Prager, R.C., Grob, E.W., Ousley, W. *Space Mission Analysis and Design*. Edited by W.J. Larson, Wertz, J.R. 3<sup>rd</sup> ed: Microcosm Press and Kluwer Academic Publishers, 2005.
- [2] Weislogel, M.M., Hitch, B., and Bacich, M.A. "High performance oscillatory heat transport system." In *37<sup>th</sup> Fluid Dynamics Conference and Exhibit*. Portland, Oregon: American Institute of Aeronautics and Astronautics, 2004.
- [3] Weislogel, M.M., "A high performance heat pipe," National Aeronautics and Space Administration SBIR 1998 Phase I, 1998.
- [4] Brooks, M.J., Nortje, L.C., Lear, W.E., and Sherif, S.A. "Parametric control of a two-phase thermal management system for space applications." In *ASME Summer Heat Transfer Conference*, Pg. 464-70. Jacksonville, Florida, USA, 2008.
- [5] Brooks, M.J., du Clou, S., Mhlongo, M., Olivier, J.P., Lear, W.E., and Sherif, S.A. "Pulse-driven refrigeration: Progresses and challenges." In *7<sup>th</sup> International Energy Conversion Engineering Conference (IECEC)*. Denver, CO: AIAA, 2009.
- [6] *Spacecraft Thermal Control Handbook*. Edited by D.G. Gilmore. 2<sup>nd</sup> ed. El Segundo: The Aerospace Corporation, 2002.
- [7] Zak, A., Simplest Satellite, [http://www.russianspaceweb.com/sputnik\\_design.html](http://www.russianspaceweb.com/sputnik_design.html), 19 November 2012
- [8] Mitchell, D.P., Sputnik-3, [http://www.mentallandscape.com/S\\_Sputnik3.htm](http://www.mentallandscape.com/S_Sputnik3.htm), 19 Nov 2012
- [9] Freeman, R., An Overview of Explorer 1, <http://www.helium.com/items/1621289-an-overview-of-explorer-1>, 19 November 2012
- [10] Gemini Technical Description <http://www.astronautix.com/articles/gemtion.htm>, 26 November 2012
- [11] Kohlhase, C., Peterson, C.E., The Cassini Mission to Saturn and Titan  
<http://www.esa.int/esapub/bulletin/bullet92/b92kohlh.htm>, 27 November 2012
- [12] Birur, G.C., and Bhandari, P., "Mars pathfinder active heat rejection system: successful flight demonstration of a mechanically pumped cooling loop," JPL, California Institute of Technology, Pasadena, 1997.
- [13] Price, S., Phillips, T., and Knier, G., Staying cool on the ISS,  
[http://science.nasa.gov/science-news/science-at-nasa/2001/ast21mar\\_1/](http://science.nasa.gov/science-news/science-at-nasa/2001/ast21mar_1/), 11 January 2013

- [14] Malik, T., FAQ: International Space Station Cooling System Pump Failure, <http://www.space.com/8900-faq-international-space-station-cooling-system-pump-failure.html>, 11 January 2013
- [15] Griffin, M.D., French, J.R. *Space Vehicle Design*. 2<sup>nd</sup> ed: American Institute of Aeronautics and Astronautics, 2004.
- [16] Weislogel, M.M., and Bacich, M.A. "A high performance semi-passive cooling system: The Pulse Thermal Loop." In *ASME Heat Transfer/Fluids Engineering Summer Conference*, 145-54. Charlotte, North Carolina, USA, 2004.
- [17] Hanford, A.J., and Ewert, M.K., "Advanced Active Thermal Control Systems," National Aeronautics and Space Administration, Centre for AeroSpace Information, Elkrige, Washington, 1996.
- [18] Weislogel, M.M. "Passive oscillatory heat transport systems." In *Space Technology and Applications International Forum-STAIF, American Institute of Physics Conference*, edited by M.S. El-Genk, pp. 241-49. Albuquerque, NM, 2002.
- [19] TDA Research, <http://www.tda.com/Research/research.htm>, 05 December 2012
- [20] Weislogel, M.M., "An advance passive non-capillary microscale cooling cycle," TDA Research, Wheat Ridge, CO, 2004.
- [21] du Clou, S., Mhlongo, M., Sukhmandan, K., and Valentim, D. "Design and construction of a pulse refrigeration system for use in terrestrial and space-based thermal management systems." University of KwaZulu-Natal, 2008.
- [22] Abdulateef, J.M., Sopian, K., Alghoul, M.A., and Sulaiman, M.Y., "Review on solar-driven ejector refrigeration technologies," *Renewable and Sustainable Energy Reviews*, vol.13, no.6-7, 2008, pp.1338-49.
- [23] Moran, M.J., and Shapiro, H.N. *Fundamentals of Engineering Thermodynamics*. 5<sup>th</sup> ed. Chichester: John Wiley & Sons, Inc., 2006.
- [24] Anderson, E.A. *Thermodynamics*. Boston, MA: PWS Publishing, 1994.
- [25] Kandil, S.M., Lear, W.E., and Sherif, S.A., "Performance of a jet-pumped cryogenic refrigeration system," *Journal of Propulsion and Power*, vol.20, no.6, 2004, pp.1018-25.
- [26] Eames, I.W., Aphornratana, S., and Haider, H., "A theoretical and experimental study of a small-scale steam jet refrigerator," *International Journal of Refrigeration*, vol.18, no.6, 1995, pp.378-86.
- [27] Meyer, A.J., Harms, T.M., and Dobson, R.T., "Steam jet ejector cooling powered by waste or solar heat," *Renewable Energy*, vol.34, no.1, 2009, pp.297-306.

- [28] Eames, I.W., Aphornratana, S., and Sun, D.-W., "The jet-pump cycle—A low cost refrigerator option powered by waste heat," *Heat Recovery Systems and CHP*, vol.15, no.8, 1995, pp.711-21.
- [29] Sun, D.-W., "Variable geometry ejectors and their applications in ejector refrigeration systems," *Energy*, vol.21, no.10, 1996, pp.919-29.
- [30] Chunnanond, K., and Aphornratana, S., "An experimental investigation of a steam ejector refrigerator: the analysis of the pressure profile along the ejector," *Applied Thermal Engineering*, vol.24, no.2-3, 2004, pp.311-22.
- [31] Cizungu, K., Mani, A., and Groll, M., "Performance comparison of vapour jet refrigeration system with environment friendly working fluids," *Applied Thermal Engineering*, vol.21, no.5, 2001, pp.585-98.
- [32] Khalil, A., Fatouh, M., and Elgandy, E., "Ejector design and theoretical study of R134a ejector refrigeration cycle," *International Journal of Refrigeration*, vol.34, no.7, 2011, pp.1684-98.
- [33] Huang, B.J., Chang, J.M., Petrenko, V.A., and Zhuk, K.B., "A solar ejector cooling system using refrigerant R141b," *Solar Energy*, vol.64, no.4-6, 1998, pp.223-26.
- [34] Roman, R., and Hernandez, J.I., "Performance of ejector cooling systems using low ecological impact refrigerants," *International Journal of Refrigeration*, vol.34, no.7, 2011, pp.1707-16.
- [35] Nguyen, V.M., Riffat, S.B., and Doherty, P.S., "Development of a solar-powered passive ejector cooling system," *Applied Thermal Engineering*, vol.21, no.2, 2001, pp.157-68.
- [36] Huang, B.J., Hu, S.S., and Lee, S.H., "Development of an ejector cooling system with thermal pumping effect," *International Journal of Refrigeration*, vol.29, no.3, 2006, pp.476-84.
- [37] Wang, J.H., Wu, J.H., Hu, S.S., and Huang, B.J., "Performance of ejector cooling system with thermal pumping effect using R141b and R365mfc," *Applied Thermal Engineering*, vol.29, no.10, 2009, pp.1904-12.
- [38] Nord, J.W., Lear, W.E., and Sherif, S.A., "Analysis of heat-driven jet-pumped cooling system for space thermal management," *Journal of Propulsion and Power*, vol.17, no.3, 2001, pp.566-70.
- [39] Zheng, B., and Weng, Y.W., "A combined power and ejector refrigeration cycle for low temperature heat sources," *Solar Energy*, vol.84, no.5, 2010, pp.784-91.
- [40] Wang, R.Z., and Oliveira, R.G., "Adsorption refrigeration--An efficient way to make good

- use of waste heat and solar energy," *Progress in Energy and Combustion Science*, vol.32, no.4, 2006, pp.424-58.
- [41] Kyoto Protocol, United Nations Framework Convention on Climate Change,  
<http://www.unfccc.int>, 25 May 2010
- [42] Krupa, J., and Burch, S., "A new energy future for South Africa: The political ecology of South African renewable energy," *Energy Policy*, vol.39, no.10, 2011, pp.6254-61.
- [43] Thirugnanasambandam, M., Iniyan, S., and Goic, R., "A review of solar thermal technologies," *Renewable and Sustainable Energy Reviews*, vol.14, no.1, 2010, pp.312-22.
- [44] Mouzouris, M., and Brooks, M.J. "Nonimaging solar thermal collector for high temperature terrestrial and space applications." In *SPIE Optics and Photonics*. San Diego, CA, 2009.
- [45] Satoh, D., Tanaka, S., Yoshida, K., and Esashi, M., "Micro-ejector to supply fuel-air mixture to a micro-combustor," *Sensors and Actuators A: Physical*, vol.119, no.2, 2005, pp.528-36.
- [46] Aidoun, Z., and Ouzzane, M., "The effect of operating conditions on the performance of a supersonic ejector for refrigeration," *International Journal of Refrigeration*, vol.27, no.8, 2004, pp.974-84.
- [47] Incropera, F.P., Dewitt, D.P., Bergman, T.L., Lavine, A.S. *Fundamentals of Heat and Mass Transfer*. 6<sup>th</sup> ed. New Jersey: John Wiley & Sons, Inc, 2007.
- [48] Flat Gauge Glass - Reflex & Transparent,  
[http://www.johnernst.com/glass\\_gaskets\\_p44.html](http://www.johnernst.com/glass_gaskets_p44.html), 13 September 2011
- [49] Technical Glass Products,  
[http://www.technicalglass.com/downloads/TGP\\_2010\\_Catalog.pdf](http://www.technicalglass.com/downloads/TGP_2010_Catalog.pdf), 15 August 2011
- [50] BK-7 Borosilicate Crown Glass, [http://www.internationalcrystal.net/optics\\_03.htm](http://www.internationalcrystal.net/optics_03.htm), 24 December 2012
- [51] Juvinall, R.C., and Marshek, K.m. *Fundamentals of Machine Component Design*. 4<sup>th</sup> ed. New York: John Wiley and Sons, 2006.
- [52] Check Valves, <http://www.swagelok.com/downloads/WebCatalogs/EN/MS-01-176.pdf>, 5 November 2011
- [53] Lift Check Valves, <http://www.swagelok.com/downloads/WebCatalogs/EN/MS-01-98.pdf>, 5 November 2011
- [54] One-Piece Instrumentation Ball Valves,  
<http://www.swagelok.com/downloads/WebCatalogs/EN/ms-02-331.pdf>, 26 December 2012



- [55] Actuated Ball Valve Selection Guide,  
<http://www.swagelok.com/downloads/WebCatalogs/EN/MS-02-136.PDF>, 26 December 2012
- [56] HS-7980TH Servo, [http://www.servocity.com/html/hs-7980th\\_servo.html](http://www.servocity.com/html/hs-7980th_servo.html), , 25 April 2012
- [57] Quick-Connects, <http://www.swagelok.com/downloads/WebCatalogs/EN/MS-01-138.pdf>,  
 26 December 2012
- [58] Janna, W.S. *Design of Fluid Thermal Systems*. 3<sup>rd</sup> ed. Stamford: Global Engineering, 2011.
- [59] du Clou, S., Brooks, M.J., Lear, W.E., Sherif, S.A., and Khalil, E.E. "Pulsed ejector cooling system." In *10th International Energy Conversion Engineering Conference (IECEC)*. Atlanta, Georgia: AIAA, 2012.
- [60] High-quality pressure transmitter for general industrial applications Model S-10,  
[http://www.wika.co.za/upload/DS\\_PE8101\\_GB\\_1392.pdf](http://www.wika.co.za/upload/DS_PE8101_GB_1392.pdf), 18 December 2012
- [61] Pressure transmitter for general industrial applications Model A-10,  
[http://www.wika.co.za/upload/DS\\_PE8160\\_GB\\_1631.pdf](http://www.wika.co.za/upload/DS_PE8160_GB_1631.pdf), 18 December 2012
- [62] Fabri, J., and Siestrunck, R. "Supersonic air ejectors." In *Advances in Applied Mechanics*, edited by H.L. Dryden, and von Kármán, T.H., 1-34: Elsevier, 1958.
- [63] Huang, B.J., Chang, J.M., Wang, C.P., and Petrenko, V.A., "A 1-D analysis of ejector performance," *International Journal of Refrigeration*, vol.22, no.5, 1999, pp.354-64.
- [64] Ouzzane, M., and Aidoun, Z., "Model development and numerical procedure for detailed ejector analysis and design," *Applied Thermal Engineering*, vol.23, no.18, 2003, pp.2337-51.
- [65] Kairouani, L., Elakhdar, M., Nehdi, E., and Bouaziz, N., "Use of ejectors in a multi-evaporator refrigeration system for performance enhancement," *International Journal of Refrigeration*, vol.32, no.6, 2009, pp.1173-85.
- [66] Cizungu, K., Groll, M., and Ling, Z.G., "Modeling and optimization of two-phase ejectors for cooling systems," *Applied Thermal Engineering*, vol.25, no.13, 2005, pp.1979-94.
- [67] Fairuzov, Y.V., and Bredikhin, V.V., "Two-phase cooling system with a jet pump for spacecraft," *Journal of Thermophysics and Heat Transfer*, vol.9, no.2, 1995, pp.285-91.
- [68] Rusly, E., Aye, L., Charters, W.W.S., and Ooi, A., "CFD analysis of ejector in a combined ejector cooling system," *International Journal of Refrigeration*, vol.28, no.7, 2005, pp.1092-101.
- [69] Bartosiewicz, Y., Aidoun, Z., and Mercadier, Y., "Numerical assessment of ejector

- operation for refrigeration applications based on CFD," *Applied Thermal Engineering*, vol.26, no.5–6, 2006, pp.604-12.
- [70] Park, B.H., Lim, J.H., and Yoon, W., "Fluid dynamics in starting and terminating transients of zero-secondary flow ejector," *International Journal of Heat and Fluid Flow*, vol.29, no.1, 2008, pp.327-39.
- [71] Huang, B.J., and Chang, J.M., "Empirical correlation for ejector design," *International Journal of Refrigeration*, vol.22, no.5, 1999, pp.379-88.
- [72] Selvaraju, A., and Mani, A., "Experimental investigation on R134a vapour ejector refrigeration system," *International Journal of Refrigeration*, vol.29, no.7, 2006, pp.1160-66.
- [73] Sankarlal, T., and Mani, A., "Experimental investigations on ejector refrigeration system with ammonia," *Renewable Energy*, vol.32, no.8, 2007, pp.1403-13.
- [74] Zhu, Y., Cai, W., Wen, C., and Li, Y., "Numerical investigation of geometry parameters for design of high performance ejectors," *Applied Thermal Engineering*, vol.29, no.5-6, 2009, pp.898-905.
- [75] Chaiwongsa, P., and Wongwises, S., "Effect of throat diameters of the ejector on the performance of the refrigeration cycle using a two-phase ejector as an expansion device," *International Journal of Refrigeration*, vol.30, no.4, 2007, pp.601-08.
- [76] Yapıcı, R., and Ersoy, H.K., "Performance characteristics of the ejector refrigeration system based on the constant area ejector flow model," *Energy Conversion and Management*, vol.46, no.18-19, 2005, pp.3117-35.
- [77] Zhu, Y., Cai, W., Wen, C., and Li, Y., "Shock circle model for ejector performance evaluation," *Energy Conversion and Management*, vol.48, no.9, 2007, pp.2533-41.
- [78] du Clou, S., Brooks, M.J., Lear, W.E., Sherif, S.A., and Khalil, E.E. "An ejector transient performance model for application in a pulse refrigeration system." In *9<sup>th</sup> International Energy Conversion Engineering Conference (IECEC)*. San Diego, CA: AIAA, 2011.
- [79] Keenan, J.H., Neumann, E.P., and Lustwerk, F., "Investigation of ejector design by analysis and experiment," *ASME Journal of Applied Mechanics*, vol.72 1950, pp.299 - 309.
- [80] Munday, J.T., and Bagster, D.F., "A new ejector theory applied to steam jet refrigeration," *Ind. Engng Chem., Process Des. Dev.*, vol.16, no.4, 1977, pp.442-49.
- [81] Yadav, R.L., and Patwardhan, A.W., "Design aspects of ejectors: Effects of suction chamber geometry," *Chemical Engineering Science*, vol.63, no.15, 2008, pp.3886-97.
- [82] MATLAB. *version 7.3.0.267 (R2006b)*. Natick, MA: The MathWorks Inc, 2006.

- [83] Lemmon, E.W., Huber, M.L., McLinden, M.O. NIST Standard Reference Database 23: Reference Fluid Thermodynamic and Transport Properties-REFPROP, Version 7.0., National Institute of Standards and Technology, Standard Reference Data Program, Gaithersburg, 2010
- [84] Sherif, S.A., Lear, W.E., Steadham, J.M., Hunt, P.L., and Holladay, J.B., "Analysis and modeling of a two-phase jet pump of a thermal management system for aerospace applications," *International Journal of Mechanical Sciences*, vol.42, no.2, 2000, pp.185-98.
- [85] Extruded Alloys and Tempers,  
[http://www.google.co.za/url?sa=t&rct=j&q=al%206082%20specific%20heat&source=web&cd=5&ved=0CEwQFjAE&url=http%3A%2F%2Fwww.cosmosaluminium.gr%2Findex.php%2Fel%2Fcomponent%2Fdocman%2Fdoc\\_download%2F1--&ei=00jXUMbWAtGKhQf1yoCwBA&usg=AFQjCNF3p0-Zp-q-uAEB7kbEHkm2Tf5F\\_Q](http://www.google.co.za/url?sa=t&rct=j&q=al%206082%20specific%20heat&source=web&cd=5&ved=0CEwQFjAE&url=http%3A%2F%2Fwww.cosmosaluminium.gr%2Findex.php%2Fel%2Fcomponent%2Fdocman%2Fdoc_download%2F1--&ei=00jXUMbWAtGKhQf1yoCwBA&usg=AFQjCNF3p0-Zp-q-uAEB7kbEHkm2Tf5F_Q),  
23 December 2012
- [86] AISI Type 316L Stainless Steel, annealed plate,  
<http://asm.matweb.com/search/SpecificMaterial.asp?bassnum=MQ316L>, 23 December 2012

## **APPENDIX**

### **A. TABLES**

**Table A.1** Comparison of various thermal management technologies for space applications

	High driving pressure	Gravity independence	High heat flux	Multiple evaporators	Zero power consumption	Active cooling	Comments
Heat pipe							Limited transport length, low pressure pumping, limited heat flux
LHP/CPL							Limited transport length, low pressure pumping and, limited heat flux
Single-phase pumped loop							Long transport distances, high pressure pumping, high heat flux and convective cooling, can operate in adverse gravity environments, and requires electrical power for pump
Two-phase pumped loop or ECS							Long transport distances, high pressure pumping, high heat flux and evaporative cooling, normally gravity dependant, cools to below condenser temperature, and requires electrical power for pump
PTL							Long transport distances, high pressure pumping, moderate heat flux and evaporative cooling, can operate in adverse gravity environments and competes with pumped cycles requiring no pump
PRS							Long transport distances, high pressure pumping, high heat flux and evaporative cooling, can operate in adverse gravity environments, cools to below condenser temperature, and competes with pumped cycles requiring no pump

\* white – no relationship, light grey – light relationship, light blue – moderate relationship and dark blue – strong relationship

**Table A.2** Comparison of different PTL designs

	Weislogel 1998 [3] 1 of 4	Weislogel 1998 [3] 2 of 4	Weislogel <i>et al.</i> 2004 [2,16]	Brooks <i>et al.</i> 2007 [4]	Brooks <i>et al.</i> 2008 [5]	Current PTL
<b>Working fluid</b>	R-134a	R-134a	R-134a, R-10a, ammonia	R-134a	R-134a	R-134a
<b>Volumes (cm<sup>3</sup>)</b>	Boiler: 98 (x2), Condenser: 60, VTL+LRL: 64, Total: 320 cm <sup>3</sup>	Boiler: 90 (x2), Condenser: 34, VTL+LRL: 69, Total: 283 cm <sup>3</sup>	Boiler: 44.8 (x2), Condenser: 27.8, VTL: 19.7, LRL: 14.9, Total: 152 cm <sup>3</sup>	Boiler: 31.5 (x2), Condenser: 39.2, VTL: 27.7, LRL: 21, Total: 159.9 cm <sup>3</sup>	Boiler: 36 (x2), Condenser: 40.7, VTL: 26, LRL: 24.4, Total: 163.1 cm <sup>3</sup>	Boiler: 81.2 (x2), Condenser: 42.8, VTL: 31, LRL: 23.4, Total: 265.2 cm <sup>3</sup>
<b>Charge level vapor quality</b>	$V_{\text{vapor}}/V_{\text{total}}$ : 0.6 to 0.746 @ 20°C	$V_{\text{vapor}}/V_{\text{total}}$ : 0.6 to 0.746 @ 20°C	$V_{\text{vapor}}/V_{\text{total}}$ : 0.594- 0.807 @ 20°C	Refrigerant mass of 80 to 120 g	Refrigerant mass of 80 to 120 g	$V_{\text{vapor}}/V_{\text{total}}$ : 0.632 – 0.687 @ 20°C
<b>Transport tubing (condenser + VTL + LRL)</b>	4.82 mm ID, 6.98 m long	4.82 mm ID, 5.82 m long	4.82 mm ID, 3.3 m long	4.55 mm ID, 2.4 m + 1.7 m + 1.29 m = 5.4 m	4.55 mm ID, 2.5 m + 1.6 m + 1.5 m = 5.6 m	4.55 mm ID, 5.98 m long
<b><math>(V_{\text{tubes}})/V_{\text{boiler}}</math></b>	2.27	1.14	1.4	2.44	2.53	1.16
<b>Boiler type</b>	Two thermally uncoupled 7/8" ID x 254 mm long copper cylinders. 5 x 750 W band heaters per boiler	Two thermally coupled 3/4" ID x 318 mm long copper cylinders. 5 x 750 W band heaters for both boilers	Two thermally coupled 12.7 mm ID x 305 mm long copper block, heated by a single cartridge heater.	Two thermally uncoupled 15 mm ID, 2 x 500 W cartridge heaters	Two thermally coupled 14 mm ID x 236 long, 2 x 500 W cartridge heaters	Two thermally coupled 22 mm ID x 200 mm long copper cylinders. Sight glass. 2 x 500 W cartridge heaters
<b>Condenser type</b>	Counter-flow concentric tube, water at 15 °C	Counter-flow concentric tube, water at 15 °C	Serpentine, counter- flow, water cooled at 20 °C	Counter-flow, water cooled at 20 °C, 0.16625 kg/s	Counter-flow, water cooled at 20 °C, 0.16625 kg/s	Counter-flow concentric tube, glycol-water at 15 °C and 20 °C, 0.1 kg/s
<b><math>Q</math> range (W)</b>	400 to 2100	400 to 900	25 to 1200	400 to 800	80 to 150	100 to 800
<b><math>\Delta P</math> range (bar)</b>	1 to 12.4	1 to 8.2	0.5 to 16.5	4 to 8	3 to 8	0.5 to 12
<b>Instrumentation</b>	Type-K thermocouples, validyne pressure transducers, 3-way solenoid valves	Type-K thermocouples, validyne pressure transducers, 3-way solenoid valves	Type-K thermocouples, validyne pressure transducers, 3-way solenoid valves	Type-K thermocouples, Wika S-10 and A-10 pressure transducers, 2-way solenoid valves	Type-K thermocouples, Wika S-10 and A-10 pressure transducers, 2-way solenoid valves	Type-K thermocouples, Wika S-10 and A-10 pressure transducers, 2-way servo valves

**Table A.3** Pair-wise comparison of the project requirements giving relative importance

Design requirements		1	2	3	4	5	6	7	8	9	10	11	12	Totals	Ranking (%)
1	High heat transfer		0	0	0	0	1	0	1	0	1	0	1	4	5.4
2	High $\Delta P$	1		1	0	1	1	0	1	0	1	0	1	7	9.5
3	Prevent asymmetry	1	0		0	1	1	1	1	0	1	0	1	7	9.5
4	No leaks	1	1	1		1	1	1	1	0	1	0	1	9	12.2
5	Material compatibility	1	0	0	0		1	0	1	0	0	0	1	4	5.4
6	Modular components	0	0	0	0	0		0	0	0	1	0	1	4	5.4
7	Maintain volume ratios	1	1	0	0	1	1		1	0	0	0	1	7	9.5
8	Sight glass	0	0	0	0	0	1	0		0	1	0	1	4	5.4
9	Instrumentation	1	1	1	1	1	1	1	1		1	1	1	11	14.8
10	Custom software	1	0	0	0	1	0	1	0	0		0	1	4	5.4
11	Data logging	1	1	1	1	1	1	1	1	0	1		1	11	14.8
12	Gravity free operation	0	0	0	0	0	0	0	0	0	0	0		2	2.7
<b>TOTALS</b>														74	100

**Table A.4** Quality Function Development technique for ranking engineering requirements

Functional requirements / Design requirements	Variable heater power	High boiler conductivity	$\Delta P$ control	Variable pulse frequency	Variable condenser Temperature	Workshop capability	Instrument range	Instrument calibration	Fast sample rate	Fluid compatibility	Quick connects and compression fittings	PRS ejector analysis and design	Relative importance (%)
High heat transfer	3	9	9	9	3		1	1		9		9	5.4
High $\Delta P$	9	3	9	9	9		9	1	3	9	3	9	9.5
Prevent asymmetry	3	9	9	3	1		1	3	3				9.5
No leaks						9				9	9		12.2
Material compatibility	9	9			1	3				9	3		5.4
Modular components	3				3	9	3	1		1	9		5.4
Maintain PTL volume ratios						3				1		1	9.5
Sight glass	3					9				1			5.4
Instrumentation	9	3	9	3	9		9	9	9	3		9	14.8
Custom software	9		9	3	3		3		9			3	5.4
Data logging	1		1	1	1		3	9	9			3	14.8
Gravity free operation			9		9		3						2.7
Specification or limit	< 1000 W	> 100 W/m.K	< 25 bar	< 1 Hz	> -10°C		< 25 bar or 100°C	< 1%	10 Hz				
Score * (Importance % x relationship)	407.8	255.6	440.5	238	305.1	251.7	318.5	315.2	372	357.2	203.1	337.4	
Rank	2	9	1	11	8	10	6	7	3	4	12	5	
<b>Relationship score:</b> 9 - Strong relationship 3 - Moderate relationship 1 - Weak relationship				The scoring takes into account the weighted importance of the project requirements, from Table A.3.									



**Table A.5** Refrigerant comparison [22,83]

	<b>R-134a</b>	<b>R-123</b>	<b>R-141b</b>	<b>R142b</b>	<b>R12</b>	<b>R-152a</b>	<b>Ammonia (R-717)</b>	<b>Water (R-718b)</b>
<b>Composition</b>	HFC	HCFC	HCFC	HCFC	CFC	HFC	NH <sub>3</sub>	H <sub>2</sub> O
<b>Wet/Dry</b>	wet	dry	dry	wet	wet	wet	wet	wet
<b>Boiling point at 1bar (°C)</b>	-26.36	27.46	31.69	-9.43	-30.06	-24.32	-33.60	99.60
<b>Pressure at 100 °C (bar)</b>	39.72	7.86	6.77	20.84	33.40	35.05	6.26	1.01
<b>Molecular mass (g/mol)</b>	102.03	152.93	116.95	100.5	120.91	66.05	17.03	18.02
<b>Latent heat at boiling (kJ/kg)</b>	217.16 (at -26.36°C)	170.34 (at 27.46°C)	223.08 (at -31.69°C)	222.27 (at -9.43°C)	166.20 (at -30°C)	330.18 (at -24.32°C)	1370.30 (at -33.6°C)	2256.40 (at 100°C)
<b>GWP, ODP</b>	0.26, 0.02	0.02, 0.016	0.15, 0.15	0.36, 0.06	3.00, 0.90	2.80, 0	0, 0	0, 0
<b>Compatibility (materials)</b>	Reacts with FKM, Viton, Kelrez, Fluorel, Kel-F	-	Reacts with FKM, Viton, Buthyl	May react with aluminum	Reacts with FKM, Viton, Buthyl, PTFE, PCTFE, silicon, EPDM	Reacts with FKM, Viton, Buthyl, PCTFE	Toxic, corrosive (Brass, Copper)	-

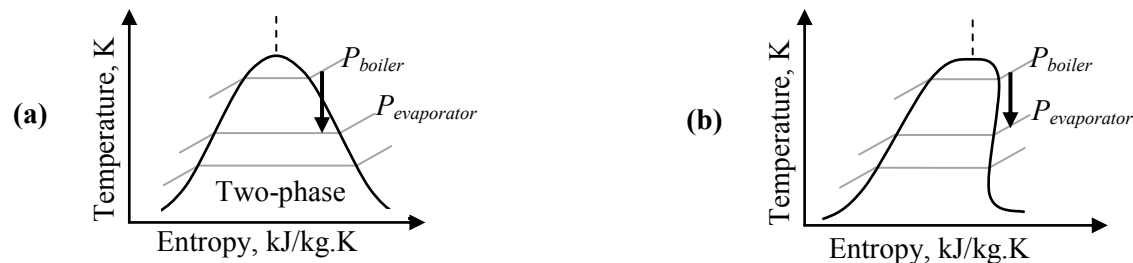


**Figure A.1** Temperature vs. Entropy schematics for (a) a wet vapor refrigerant, and (b) a dry vapor refrigerant. A wet vapor refrigerant has a negative slope saturated vapor line. As it undergoes isentropic expansion, it passes through the two-phase region and condensed bubbles form in the vapor flow. The vapor may be superheated to avoid this. A dry vapor refrigerant has a positive slope saturated vapor line. It remains a superheated vapor during expansion.

**Table A.6** Specifications of candidate materials for boiler block

	<b>Al 6082 (T6) [85]</b>	<b>Cu [23]</b>	<b>SS 316 [86]</b>	<b>Brass [23]</b>
<b>Melt point, K</b>	585°C	1358	1400	900
<b>Density (<math>\rho</math>), kg/m<sup>3</sup></b>	2700	8930	7978	8470
<b>Specific heat (<math>C_p</math>), J/kg.K</b>	896	385	500	369
<b>Thermal conductivity (<math>k</math>), W/m.K</b>	180.0	401.0	16.3	116.0
<b>Youngs Modulus, GPa</b>	70	117.5	193	109.6
<b>Thermal expansion, K<sup>-1</sup></b>	23.4x10 <sup>-6</sup>			
<b>Poisson's ratio</b>	0.33	0.345		0.331
<b>Yield or Proof Stress, MPa</b>	250	330	250	103.4
<b>Tensile strength (<math>UTS</math>), MPa</b>	290	380	565	275

**Table A.7** 3-Way valve specifications [54,55]

	<b>SS-43GXES4</b>
<b>Tube fitting size, inch</b>	1/4
<b>Packing</b>	UHMWPE
<b>O-rings</b>	Ethylene Propylene
<b>Starting torque required, N.m</b>	2.6
<b>Reactivity with R-134a</b>	No
<b>Flow coefficient (<math>C_v</math>) for <math>\Delta P = 6.8</math> bar</b>	0.9

**Table A.8** Servo specifications (HS-7980 TH Monster Torque) [56]

	<b>At 6.0 Volt</b>	<b>At 7.4 Volt</b>
<b>Operating speed at no load, s/60°</b>	0.21	0.17
<b>Stall torque, N.m</b>	3.53	4.31
<b>Motor type</b>	Coreless carbon brush	
<b>Temperature range, °C</b>	-20 to 60	
<b>Gear material</b>	Titanium	
<b>Dimensions, mm</b>	43.8 x 22.4 x 40	
<b>Weight, g</b>	78.2	

**Table A.9** Tabulated Nusselt numbers for laminar flow in an annulus [47]

$OD_i/ID_a$	0.05	0.1	0.25	0.5	1
$Nu$	17.46	11.56	7.37	5.74	4.76

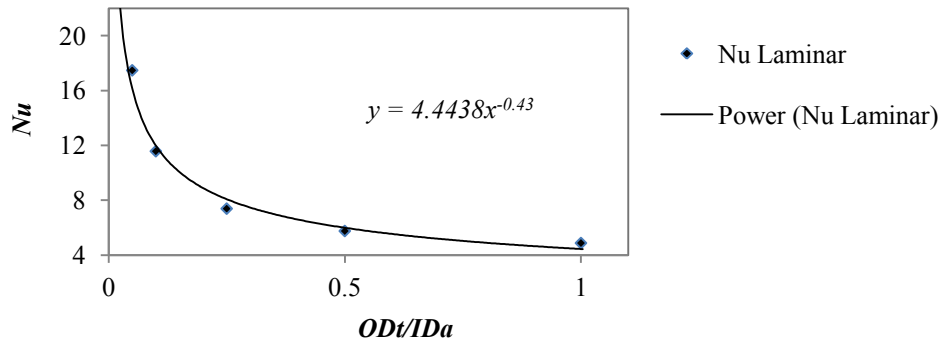


**Figure A.2** Nusselt number for laminar flow tabulated values curve fit approximation, gives Equation 3.16.

**Table A.10** Comparison of ejector geometries from the literature

Literature	Code	$D_t$ (mm)	$D_e$ (mm)	$A_e/A_t$	Nozzle converging angle	Nozzle diverging angle	$NXP$ (mm)	Chamber Inlet Angle	$D_m$ (mm)	$A_m/A_t$	$L_m/D_m$	$NXP/D_m$	Chamber diffusing angle
<b>Huang <i>et al.</i> [63]</b>	AA	2.64	4.50	2.91				22°	6.70	6.441		1.50	9.41°
	AB							30°	6.98	6.99			
	AC							23°	7.60	8.29			
	AD							22°	8.10	9.41			
	AG							30°	7.34	7.73			
	EG	2.82	5.10	3.27				30°	7.34	6.77			
	EC							23°	7.60	7.26			
	ED							22°	8.10	8.25			
	EE							23°	8.54	9.17			
	EF							23°	8.84	9.83			
EH							28°	9.20	10.64				
<b>Selvaraju and Mani [72]</b>		0.50	0.80	2.56		10°		34°	1.40	7.84	10 - 12		6.4°
		0.80	1.30	2.641					1.90	5.64	8 - 10		6.3°
		1.00	1.60	2.56					2, 2.9	4.00, 8.41	10 - 12		6.3°, 6.4°
<b>Cizungu <i>et al.</i> [31]</b>				3.06	20°	4°	12 to 24			4, 5.76, 7.84	10.00		3°
<b>Rusly <i>et al.</i> [68]</b>		2.64	4.50	2.89		3.5°		5°	7.12	7.27	5.00	1.50	3.5°
<b>Sankarlal and Mani [73]</b>		0.50	0.80	2.56				34.5°	1.40	7.84	8.21		
		0.80	1.30	2.64				34.5°	1.90	5.67	8.52		
		1.00	1.70	2.89				34.5°	2.00	4.00	8.60		
<b>Yapici and Ersoy [76]</b>		2.85	5.60	3.86		5°			9.00			0.5 – 2.0	5°
<b>Meyer <i>et al.</i> [27]</b>		2.50	8.00	10.24		10°	5		18.00	51.80			
		3.00	12.00	16.00					18.00	36.00			
		3.50	14.00	16.00					18.00	26.40			

$D_t$  – Nozzle throat diameter,

$D_e$  – Nozzle exit diameter,

$D_m$  – Mixing chamber diameter,

Angles measured from the horizontal plane,

$NXP$  – Distance from nozzle exit to constant area mixing chamber

**Table A.11** Control hardware specifications

	<b>Pressure transducer</b>		<b>Thermocouple</b>	<b>Servo</b>	<b>Heater</b>
<b>Model</b>	Wika-S10	Wika-A10	Type-K	Hitec HS 9800	-
<b>Quantity</b>	2	4	12	2	2
<b>Connection</b>	BSP thread	BSP thread	1/8" compression	-	-
<b>Input</b>	10 V to 30 V DC	10 V to 30 V DC	-	7.4 V DC (limited to 7 Amp)	230 V AC
<b>Output</b>	4 mA to 20 mA	4 mA to 20 mA	0 mV to 50 mV	4.1 N.m	-
<b>Range</b>	0 bar to 25 bar	-1 to 24 bar	0°C to 1260°C	-180° to +180°	0 W to 500 W

## B. CALCULATIONS

### B.1. Boiler design

#### B.1.1. Minimum wall thickness

$$t_{min} = (P \times r) / \sigma_y \dots \text{Hoop stress (or circumferential shear stress) [47]} \quad (3.1)$$

Where  $P$  is the maximum operating pressure (25 bar),  $r$  is the internal radius (11 mm) and  $\sigma_y$  is the yield strength of aluminum 6082-T6 (250 MPa).

$$\therefore t_{min} = (25 \times 10^5 \times 11 \times 10^{-3}) / 250 \times 10^6$$

$$\underline{t_{min} = 0.11 \text{ mm}}$$

Comment: The minimum thickness used in the design of the boilers was 2 mm (Figure C3). Therefore, the resulting  $SF$  is greater than 10.

#### B.1.2. Borosilicate gauge glass safety factor

$$SF = (3.48 \times M \times t^2) / PA \quad (\text{Imperial units}) [49] \quad (3.2)$$

Where,

$M = 2400 \text{ psi}$  [50],  $t = 17 \text{ mm}$  [48],  $P = 25 \text{ bar} = 362.59 \text{ psi}$ , and

$A$  is the unsupported area calculated from the dimensions given in Figure C.3.

$$A = l \times b + \pi D^2 / 4 = 80 \times 18 + \pi(18)^2 / 4$$

$$A = 1694.5 \text{ mm}^2 = 2.626 \text{ in}^2$$

$$\therefore SF = \left( 3.48 \times 2400 \times \left( \frac{17}{25.40} \right)^2 \right) / 362.59 \times 2.626$$

$$\underline{SF = 3.93}$$

### B.1.3. Sight glass bolt tightening torque and safety factor

Soft clamped members with rigid bolt theory (Figure B.1) is used to calculate

- the tightening force,  $F_i$
- the tightening torque,  $T_i$  and,
- The Safety Factor,  $SF$

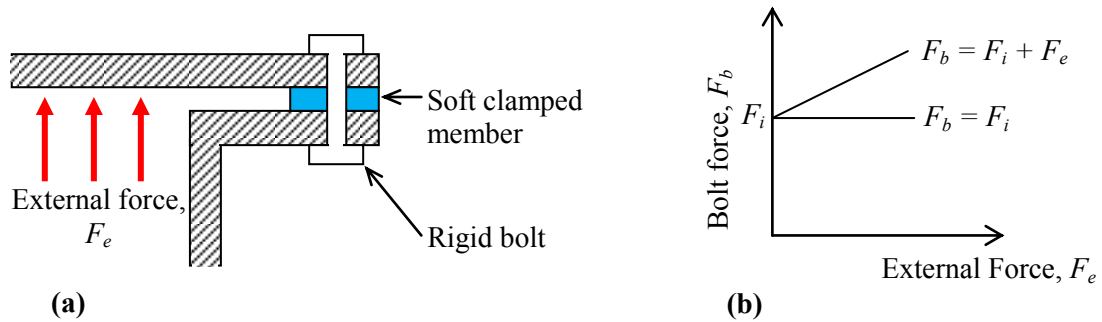


**Figure B.1** (a) Soft clamped members with a rigid bolt, and (b) bolt force diagram used to calculate initial tightening force ( $F_i$ ). [51]

#### a) Tightening force

$$F_i = 0.9 \times A_{bolt} \times \sigma_y \quad [51] \quad (3.3)$$

Where,

An M4 bolt is investigated having a yield/proof stress of  $\sigma_y = 310 \text{ MPa}$  [51] and cross section area of  $A_{bolt} = 8.78 \text{ mm}^2$  [51]

$$\therefore F_i = 0.90 \times 8.78 \times 310$$

$$\underline{F_i = 2449.62 \text{ N}}$$

#### b) Tightening torque

$$T_i = 0.2 \times F_i \times D_{bolt} \quad [51] \quad (3.4)$$

$$T_i = 0.20 \times 2449.62 \times 4$$

$$\underline{T_i = 1959.7 \text{ N.mm}}$$

### c) Safety Factor

The safety factor is calculated for the maximum load per bolt (8 bolts per sight glass)

$$SF = \sigma_y / \sigma_{bolt} \quad (3.5)$$

Where,

$$F_e = (P_{max} \times A) / 8$$

The chamber has a maximum internal pressure of  $P_{max} = 25$  bar and, unsupported area of  $A = 1694.5 \text{ mm}^2$

$$\therefore F_e = (2.5 \times 1694.5 / 8)$$

$$F_e = 529.53 \text{ N}$$

And,

$$\sigma_{bolt} = F_e / A_{bolt}$$

$$\sigma_{bolt} = 529.53 / 8.78$$

$$\sigma_{bolt} = 60.31 \text{ MPa}$$

$$\therefore SF = 310 / 60.31$$

$$\underline{SF = 5.14}$$

#### B.1.4. Total boiler volume

The total boiler volume includes the chamber, sight glass cavity, and the tube volumes at the inlet and exit to the boiler up to the valves. The cut-away boiler cross-section including the sight glass cavity and relative dimensions is shown in Figure B.2. The cavity length is 200 mm and the tube lengths at the inlet and exit to the boilers are 90 mm and 180 mm, respectively.



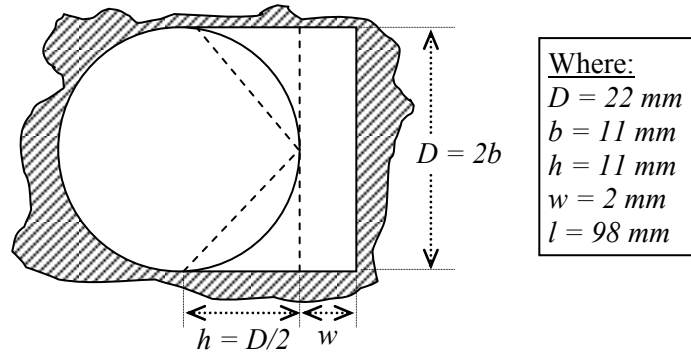


**Figure B.2** Cut-away cross-section of boiler chamber showing sight glass cavity detail.

$$V_{boiler} = V_{chamber} + V_{cavity} + V_{tubes}$$

Where,

$$V_{cavity} = \left[ (w \times b) + 2 \times \frac{2}{3} \left( \frac{1}{2} \times b \times h \right) \right] \times l_{cavity}$$

$$V_{cavity} = \left[ (2 \times 9) + 2 \times \frac{2}{3} \left( \frac{1}{2} \times 9 \times 9 \right) \right] \times 98$$

$$V_{cavity} = 7056 \text{ mm}^3$$

$$V_{boiler} = \left( \frac{\pi D_{chamber}^2}{4} \times l_{boiler} \right) + V_{cavity} + \left( \frac{\pi D_{tubes}^2}{4} \times l_{tubes} \right)$$

$$V_{boiler} = \left( \pi \times 22^2 / 4 \times 200 \right) + 7056 + \left( \pi \times 4.55^2 / 4 \times (90 + 180) \right)$$

$$V_{boiler} = 76026.54 + 756 + 4390.12$$

$$V_{boiler} = 81172.66 \text{ mm}^3 = \underline{81.2 \text{ cm}^3}$$

### B.1.5. Transport tube safety factor by Hoop Stress method

$$t_{min} = (P \times r) / \sigma_y \dots \text{Hoop stress (or circumferential shear stress) [47]} \quad (3.1)$$

Where  $P$  is the maximum operating pressure (25 bar),  $r$  is the internal radius (2.28 mm) and  $\sigma_y$  is the yield strength of 316 stainless steel (250 MPa).

$$\therefore t_{min} = (25 \times 10^5 \times 2.28 \times 10^{-3}) / 250 \times 10^6$$

$$\underline{t_{min} = 22.8 \times 10^{-6} \text{ mm}}$$

Comment: The 1/4" tube wall thickness is 0.9 mm. This results in a large  $SF$  greater than 10000.

## B.2. System head loss

The system head loss is calculated for the vapor and liquid portions separately in part (a) and part (b).

Assumptions:

- The system is charged with enough refrigerant such that half the condenser and the LRL contain saturated liquid refrigerant. The other half of the condenser and the VTL contain saturated vapor.
- An average flow rate of 5 g/s
- An average system pressure of 16 bar is assumed for saturated liquid and vapor states.

Stainless steel properties:  $C = 0.0021$

For a 1/4" tube:  $\epsilon/D = 0.00046$  and  $A = 16.26 \text{ mm}^2$

### PART A: Calculate losses for vapor portion only

R-134a vapor properties at 16 bar:  $\mu_v = 13.433 \text{ } \mu\text{Pa}\cdot\text{s}$   $\rho_v = 82.464 \text{ kg/m}^3$ ,

$$V = \dot{m} / \rho A \quad (3.19)$$

$$V = 5 \times 10^{-3} / 82.464 \times 16.26 \times 10^{-6}$$

$$V = 3.73 \text{ m/s}$$

$$Re = \rho V D / \mu \quad (3.20)$$

$$Re = 82.464 \times 3.729 \times 4.55 \times 10^{-3} / 13.433 \times 10^{-6}$$

$$Re = 1.04 \times 10^5$$

From Moody diagram,  $f = 0.021$  [58]

$$h_f = f L V^2 / 2 D g \quad (3.22)$$

$$\text{Where } L = L_{VTL} + \frac{1}{2} L_{\text{condenser}} = 1905 + \frac{1}{2} 2634 = 3222 \text{ mm}$$

$$h_f = 0.021 \times 3.222 \times 3.729^2 / 2 \times 4.55 \times 10^{-3} \times 9.81$$

$$\underline{h_f = 10.54 \text{ m}}$$

$$P_f = \rho g h_f$$

$$P_f = 82.464 \times 9.81 \times 10.54$$

$$P_f = 8526.1 \text{ Pa} = \underline{0.085 \text{ bar}}$$

**Table B.1** List of fittings and loss coefficients in vapor portion. [6,58]

Fitting	Amount	Loss coefficient, $K$	$\Sigma K$
Pipe entrance	1	0.50	0.30
90° bend	8	0.31	2.48
Check valve	1	Le/D=100	-
T-joint in-line flow	1	0.30	0.30
<b><math>\Sigma K</math></b>			<b>3.08</b>

$$h_{lm} = KV^2/2 \quad (3.23)$$

$$h_{lm} = 3.08 \times 3.729^2/2$$

$$h_{lm} = 21.41 \text{ m}$$

Loss due to the check valve is calculated from:

$$h_{lm} = f \times L_e/D \times V^2/2$$

$$h_{lm} = 0.021 \times 100 \times 3.729^2/2$$

$$h_{lm} = 14.6 \text{ m}$$

$$\Sigma h_{lm} = 21.41 + 14.6 = \underline{36 \text{ m}}$$

$$P_{lm} = \rho g h_f \quad (3.24)$$

$$P_{lm} = 82.464 \times 9.81 \times 36.01$$

$$P_{lm} = 29131.08 \text{ Pa} = \underline{0.291 \text{ bar}}$$

### PART B: Calculate losses for liquid portion only

R-134a liquid properties at 16 bar:  $\mu_l = 127.31 \mu\text{Pa}\cdot\text{s}$  and  $\rho_l = 1063.7 \text{ kg/m}^3$

$$V = \dot{m}/\rho A \quad (3.19)$$

$$V = 5.0 \times 10^{-3} / (1063.7 \times 16.26 \times 10^{-6})$$

$$V = 0.29 \text{ m/s}$$

$$Re = \rho V D / \mu \quad (3.20)$$

$$Re = 1063.7 \times 0.289 \times 4.55 \times 10^{-3} / 127.31 \times 10^{-6}$$

$$Re = 1.1 \times 10^4$$

From Moody diagram,  $f = 0.034$  [58]

$$h_f = f LV^2 / 2Dg \quad (3.22)$$

$$\text{Where } L = L_{LRL} + \frac{1}{2} L_{condenser} = 1440 + \frac{1}{2} 2634 = 2757 \text{ mm}$$

$$h_f = 0.034 \times 2.757 \times 0.289^2 / 2 \times 4.55 \times 10^{-3} \times 9.81$$

$$\underline{h_f = 0.0877 \text{ m}}$$

$$P_f = \rho g h_f \quad (3.24)$$

$$P_f = 1063.7 \times 9.81 \times 0.0877$$

$$P_f = 915 \text{ Pa} = \underline{0.009 \text{ bar}}$$

**Table B.2** List of fittings and loss coefficients in liquid portion. [58,6]

Fitting	Amount	Loss coefficient, $K$	$\Sigma K$
Pipe exit	1	0.922	0.50
90° bend	5	0.31	1.55
Lift check valve	1	12.00	12.00
T-joint in-line flow	2	0.30	0.60
Cross in-line flow	1	0.30	0.30
Ball valve (open)	1	0.05	0.05
<b><math>\Sigma K</math></b>			<b>15</b>

$$h_{lm} = KV^2 / 2 \quad (3.23)$$

$$h_{lm} = 15 \times 0.289^2 / 2$$

$$\underline{h_{lm} = 0.626 \text{ m}}$$

$$P_{lm} = \rho g h_f \quad (3.24)$$

$$P_{lm} = 1063.7 \times 9.81 \times 0.6264$$

$$P_{lm} = 6536.42 \text{ Pa} = \underline{0.065 \text{ bar}}$$

$$\therefore \Sigma P_{losses} = (P_f + P_{lm})_{vap} + (P_f + P_{lm})_{liq}$$

$$\Sigma P_{losses} = (0.085 + 0.291) + (0.009 + 0.065)$$

$$\underline{\Sigma P_{losses} = 0.45 \text{ bar}}$$

### B.3. System charge mass

An adequate system charge mass is calculated according to **Figure 5.1**, assuming that the following mass distribution is present before a boiler is pulsed:

- 1) Half the condenser and the LRL contain saturated liquid at 8 bar.
- 2) The VTL and half the condenser contain saturated vapor at 8 bar.
- 3) The pressurizing boiler contains 20% saturated liquid and 80% saturated vapor at 16 bar.

R-134 properties:	At 16 bar	$\rho_v = 82.464 \text{ kg/m}^3$	$\rho_l = 1063.7 \text{ kg/m}^3$
	At 8 bar	$\rho_v = 39.025 \text{ kg/m}^3$	$\rho_l = 1182.2 \text{ kg/m}^3$

#### Vapor mass calculations:

- a) Empty boiler at 8 bar

$$m = \rho_v \times V_{boiler}$$

$$m = 39.025 \times 81.2 \times 10^{-6}$$

$$m = 3.2 \text{ g}$$

- b) VTL at 8 bar

$$m = \rho_v \times V_{VTL}$$

$$m = 39.025 \times 31 \times 10^{-6}$$

$$m = 1.2 \text{ g}$$

- c)  $\frac{1}{2}$  condenser at 8 bar

$$m = \rho_v \times V_{0.5(\text{condenser})}$$

$$m = 39.025 \times 21.4 \times 10^{-6}$$

$$m = 0.8 \text{ g}$$

- d) 80% of pressurizing boiler at 16 bar

$$m = \rho_v \times V_{0.8(\text{boiler})}$$

$$m = 82.464 \times 0.8 \times 81.2 \times 10^{-6}$$

$$m = 5.4 \text{ g}$$

$$m_{T \text{ vapor}} = 3.2 + 1.2 + 0.8 + 5.4$$

$$\underline{m_{T \text{ vapor}} = 10.6 \text{ g}}$$

**Liquid mass calculations:**

a)  $\frac{1}{2}$  condenser at 8 bar

$$m = \rho_l \times V_{0.5(\text{condenser})}$$

$$m = 1182.2 \times 21.4 \times 10^{-6}$$

$$m = 25.3 \text{ g}$$

b) LRL at 8 bar

$$m = \rho_l \times V_{LRL}$$

$$m = 1182.2 \times 23.4 \times 10^{-6}$$

$$m = 27.7 \text{ g}$$

c) 20% of pressurizing boiler at 16 bar

$$m = \rho_l \times V_{0.2(\text{boiler})}$$

$$m = 1063.7 \times 0.2 \times 81.2 \times 10^{-6}$$

$$m = 17.3 \text{ g}$$

$$m_{T\text{liquid}} = 25.3 + 27.7 + 17.3$$

$$\underline{m_{T\text{liquid}} = 70.3 \text{ g}}$$

**Total charge mass required to meet the operating condition:**

$$m_{T\text{system}} = 70.3 + 10.6$$

$$\underline{m_{T\text{system}} = 80.9 \text{ g}}$$

**System mass fraction:**

The total system mass fraction at 20°C can be calculated from,

$$m_{T\text{system}}/V_T = \rho_l - x\rho_l + x\rho_v$$

Where the saturated properties of R-134a at 20°C are:  $\rho_v = 27.763 \text{ kg/m}^3$ ,

$$\rho_l = 1225.4 \text{ kg/m}^3$$

$$\therefore 80.9 \times 10^{-3} / 259.6 \times 10^{-6} = 1225.4 - x(1225.4 - 27.763)$$

$$\therefore x = 0.763 \approx \underline{76\%}$$

Comment: This falls between the recommended values of 60% to 80%, in Table A.2.

#### B.4. Condenser performance

An example calculation of the average heat transfer at the condenser is provided here.

For 500 W heat input, a  $\Delta P_{set}$  of 10 bar,  $TWI$  of 15°C.

The heat transfer at the condenser is calculated from Equation 3.12

$$q_c = \dot{m}_c C_{p,c} (T_{c,o} - T_{c,i})_{ave}$$

Where,  $\dot{m}_{water-glycol} = 0.102$  kg/s (assumed minimum mass flow rate)

$C_{p,c} = 3698$  J/kg.K (for 30:70 glycol-water at 15°C)

$$\Delta T_{ave} = \left[ \frac{\sum_{L3752}^{L4002} TC2}{251} - \frac{\sum_{K3752}^{K4002} TC1}{251} \right], \text{ where } T_{c,i} = TW1 \text{ and } T_{c,o} = TW2 \text{ (from experimental results)}$$

$$\Delta T_{ave} = 0.742^\circ\text{C}$$

$$\therefore \underline{q = 279.04 \text{ W}}$$

The average mass flow rate of the refrigerant can be calculated from the heat transfer rate,

$$\dot{m}_{R134a} = \frac{q}{(C_{p,h} \times (T_{h,o} - T_{h,i})_{ave})}$$

Where,  $C_{p,h} = 1043.8$  J/kg.K for R-134a vapor flow

$$\Delta T_{ave} = \left[ \frac{\sum_{I3752}^{I4002} TH2}{251} - \frac{\sum_{J3752}^{J4002} TH1}{251} \right], \text{ where } T_{h,i} = TH1 \text{ and } T_{h,o} = TH2$$

$$\dot{m}_{R134a} = 279.04 / (1043.8 \times 26.96)$$

$$\underline{\dot{m}_{R134a} = 9.9 \text{ g/s}}$$

Comment: This result assumes a constant vapor  $C_p$ -value to give an approximated mass flow rate. The results could be analyzed to consider the condensation taking place at the condenser

but would be beyond the scope of this work.

### B.5. Effectiveness NTU method

$$C_{min} = \dot{m}_{R134a} \times c_{p,h} = 10.3 \text{ J/s}$$

$$C_{max} = \dot{m}_{coolant} \times c_{p,c} = 377.2 \text{ J/s}$$

$$\therefore q_{max} = C_{min}(T_{h,i} - T_{c,i}) = 10.3 \times (38.34 - 15.01)$$

$$q_{max} = 240.2 \text{ J/kg}$$

#### Effectiveness

$$\begin{aligned} \varepsilon &= q/q_{max} = C_h(T_{h,i} - T_{h,o})/q_{max} \\ &= 10.3(38.34 - 15.58)/240.2 \end{aligned}$$

$$\underline{\varepsilon = 0.98}$$

#### Heat transfer rate

$$q = \varepsilon C_{min}(T_{h,i} - T_{c,i}) = 0.98 \times 10.3(38.34 - 15.58)$$

$$\underline{q = 229.74 \text{ W}}$$

Note that this should be similar to the heat transfer rate calculated in B.4

#### Number of Transfer Units

$$C_r = \frac{C_{min}}{C_{max}} = \frac{10.3}{377.2} = \underline{27.3 \times 10^{-3}}$$

For  $C_r < 1$ ,

$$NTU = \frac{1}{C_r - 1} \ln \left( \frac{\varepsilon - 1}{\varepsilon C_r - 1} \right) =$$

$$\left( \frac{1}{[27.3 \times 10^{-3} - 1]} \right) \times \ln \left( \frac{(0.98 - 1)}{[0.98 \times (27.3 \times 10^{-3}) - 1]} \right)$$

$$\underline{NTU = 4}$$



## C. DRAWINGS

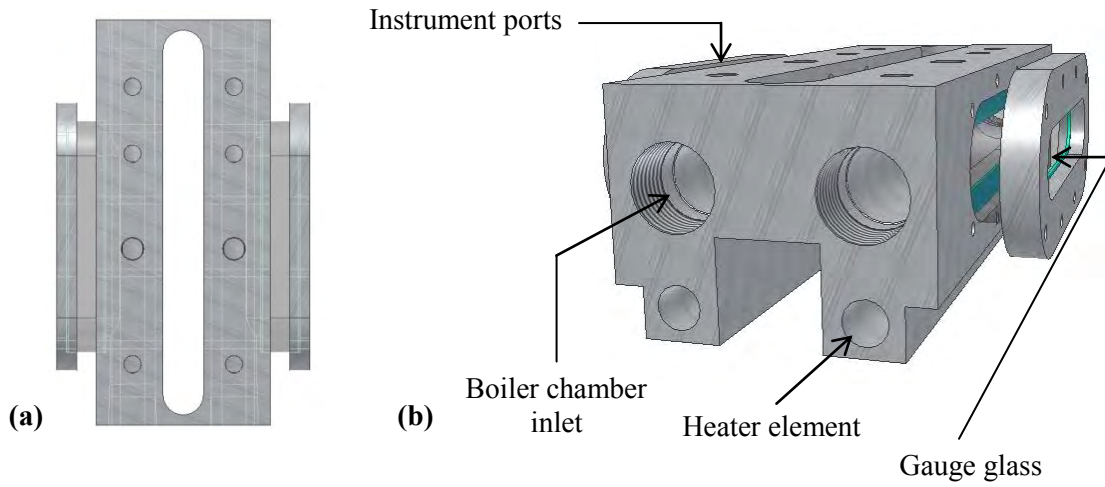


**Figure C.1** Boiler block design (a) top view and (b) isometric view

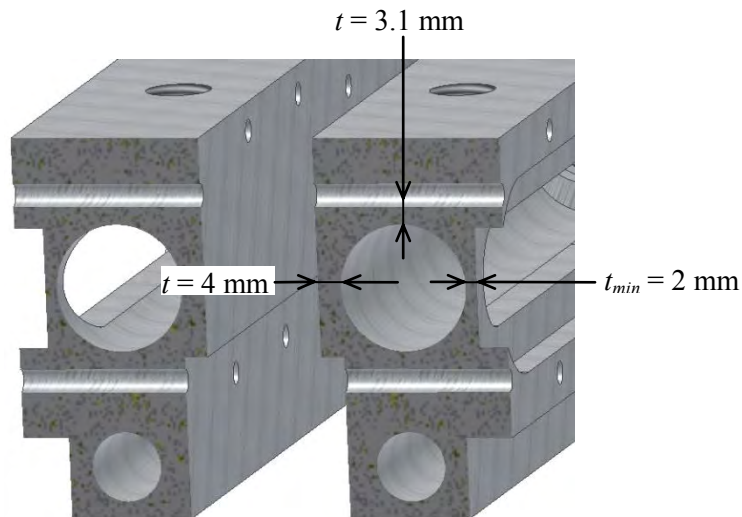


**Figure C.2** Cross-sectioned isometric view of the boilers showing the minimum thickness where the maximum stress occurs

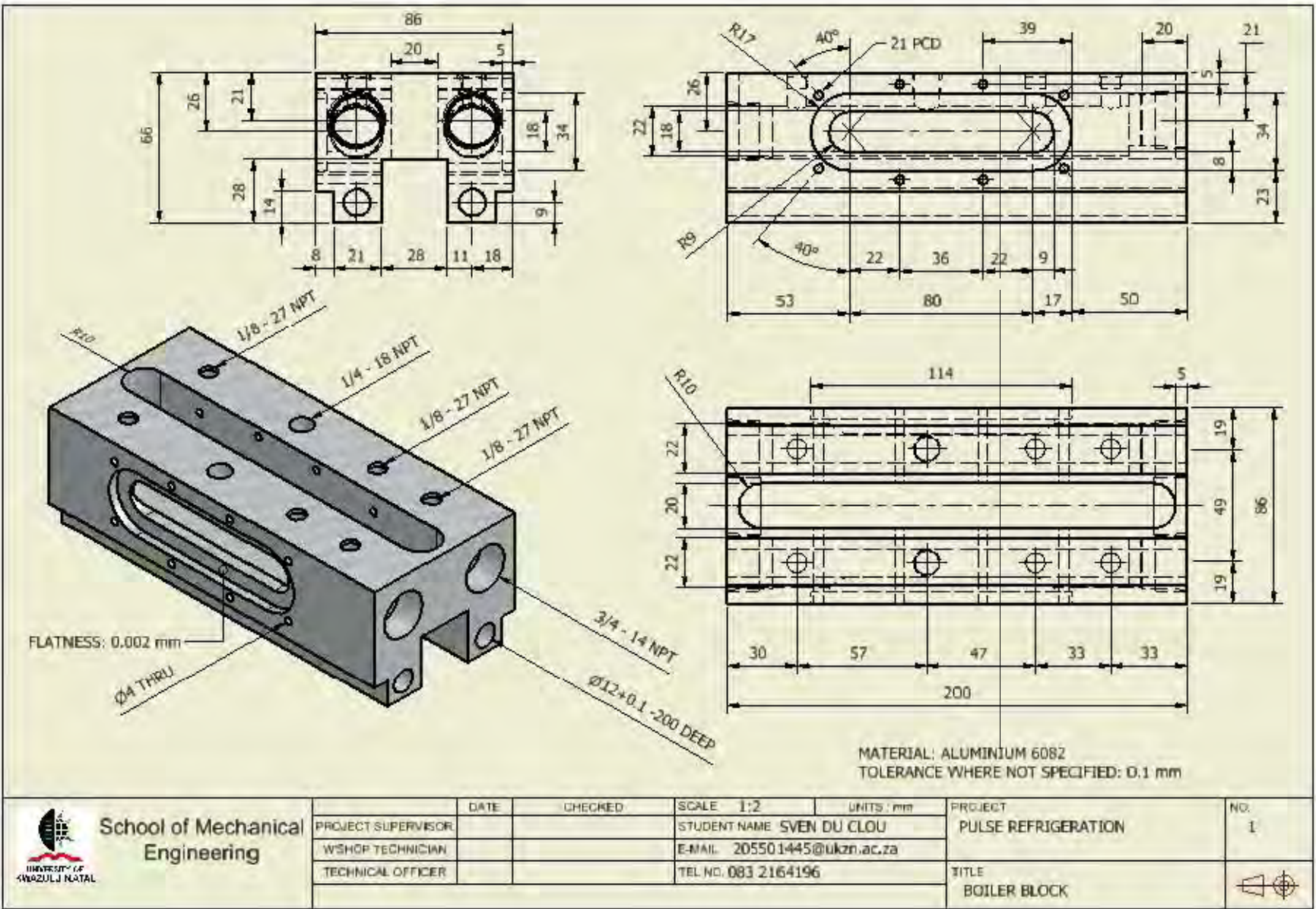




Figure C.3 Boiler block machine drawing

 <b>School of Mechanical Engineering</b>	PROJECT SUPERVISOR	DATE	CHECKED	SCALE 1:2	UNITS : mm	PROJECT	NO.
	WSHOP TECHNICIAN			STUDENT NAME SVEN DU CLOU		PULSE REFRIGERATION	1
	TECHNICAL OFFICER			E-MAIL: 205501445@ukzn.ac.za			
				TEL NO. 083 2164196		TITLE	
						BOILER BLOCK	



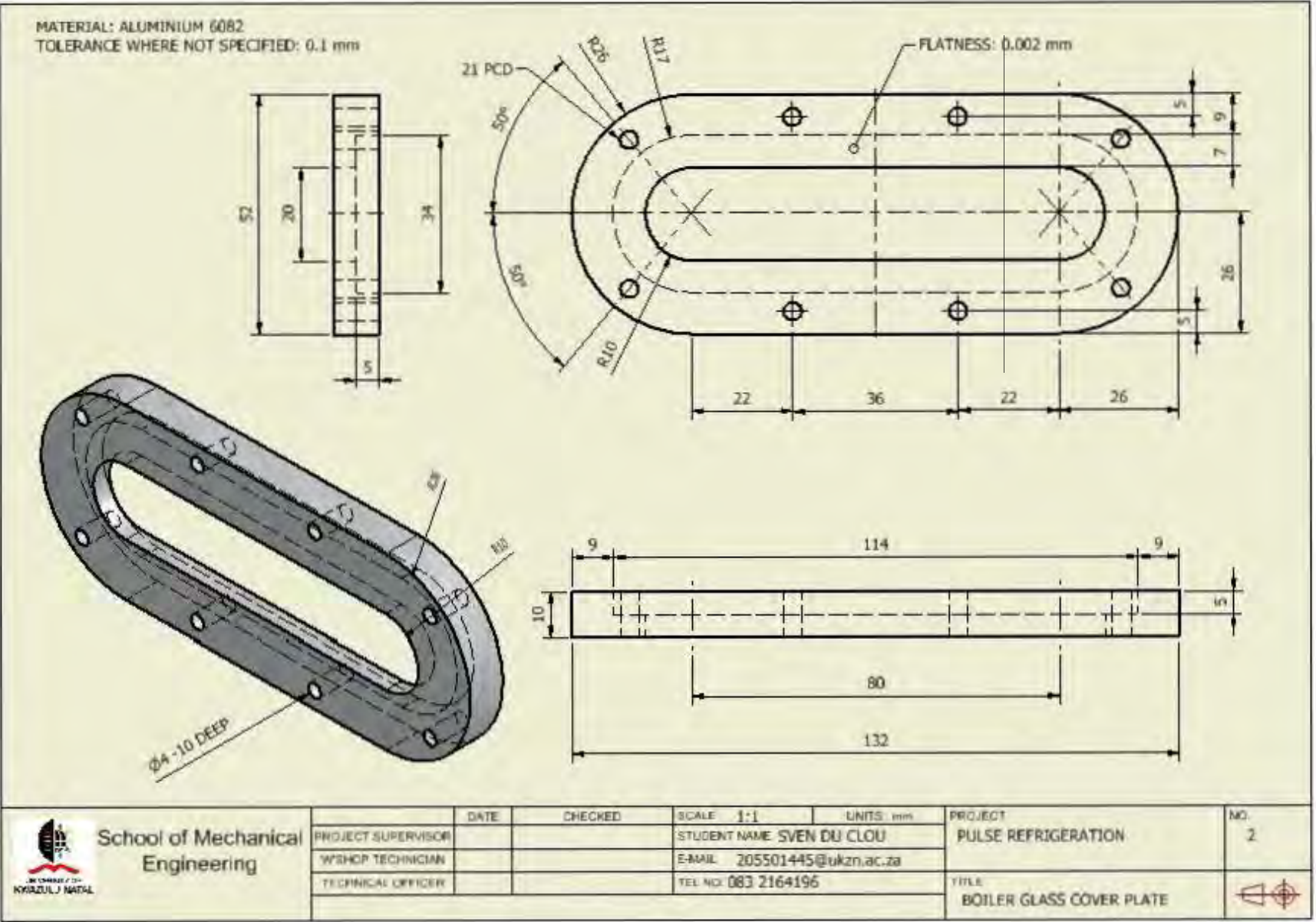
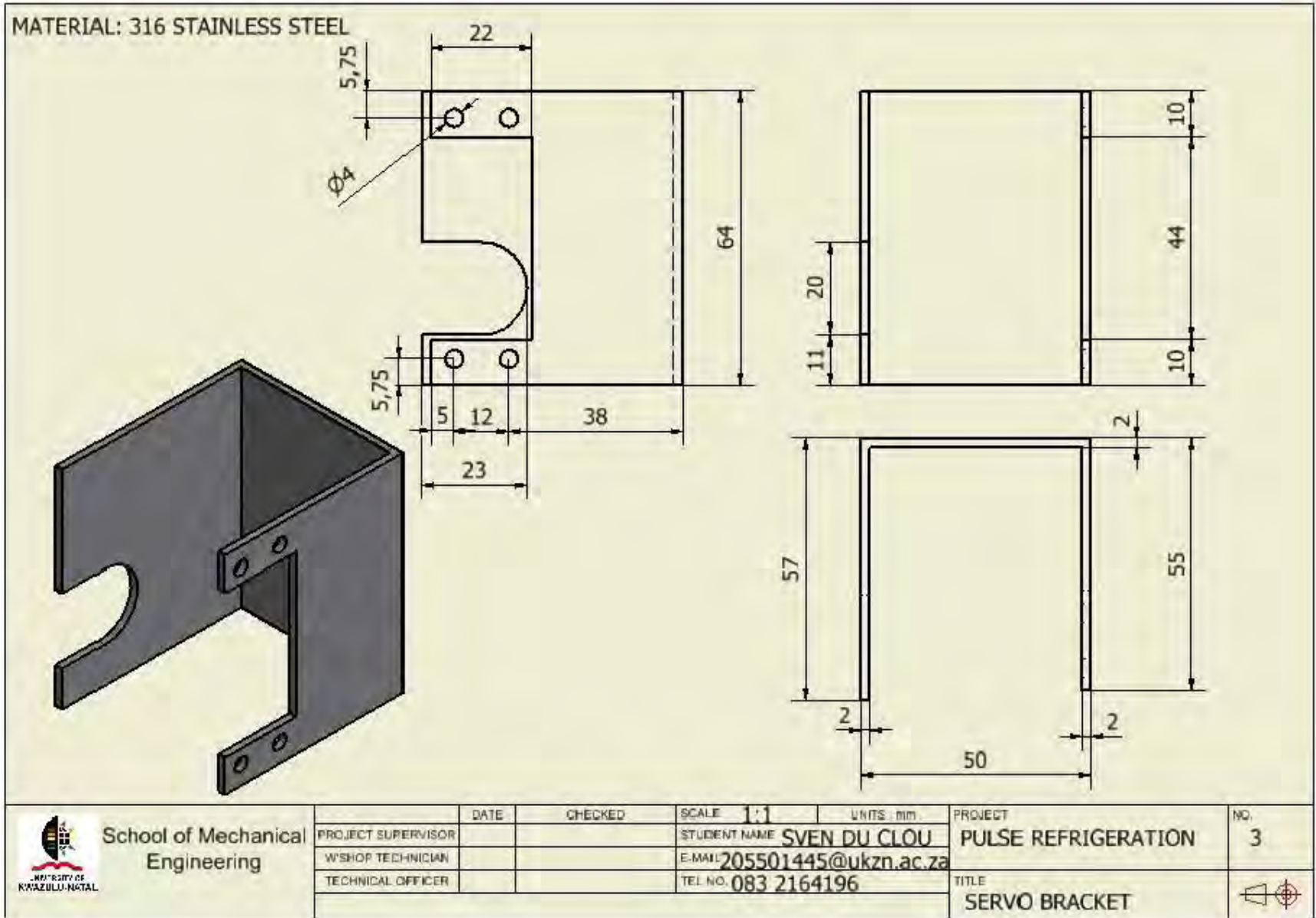
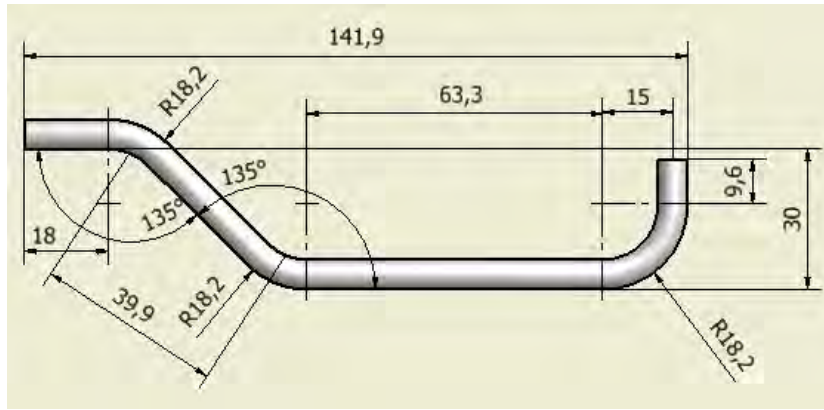


Figure C.4 Boiler block glass cover plate machine drawing

Figure C.5 Servo valve bracket





**Figure C.6** Tube from boiler outlet to the 3-way valve





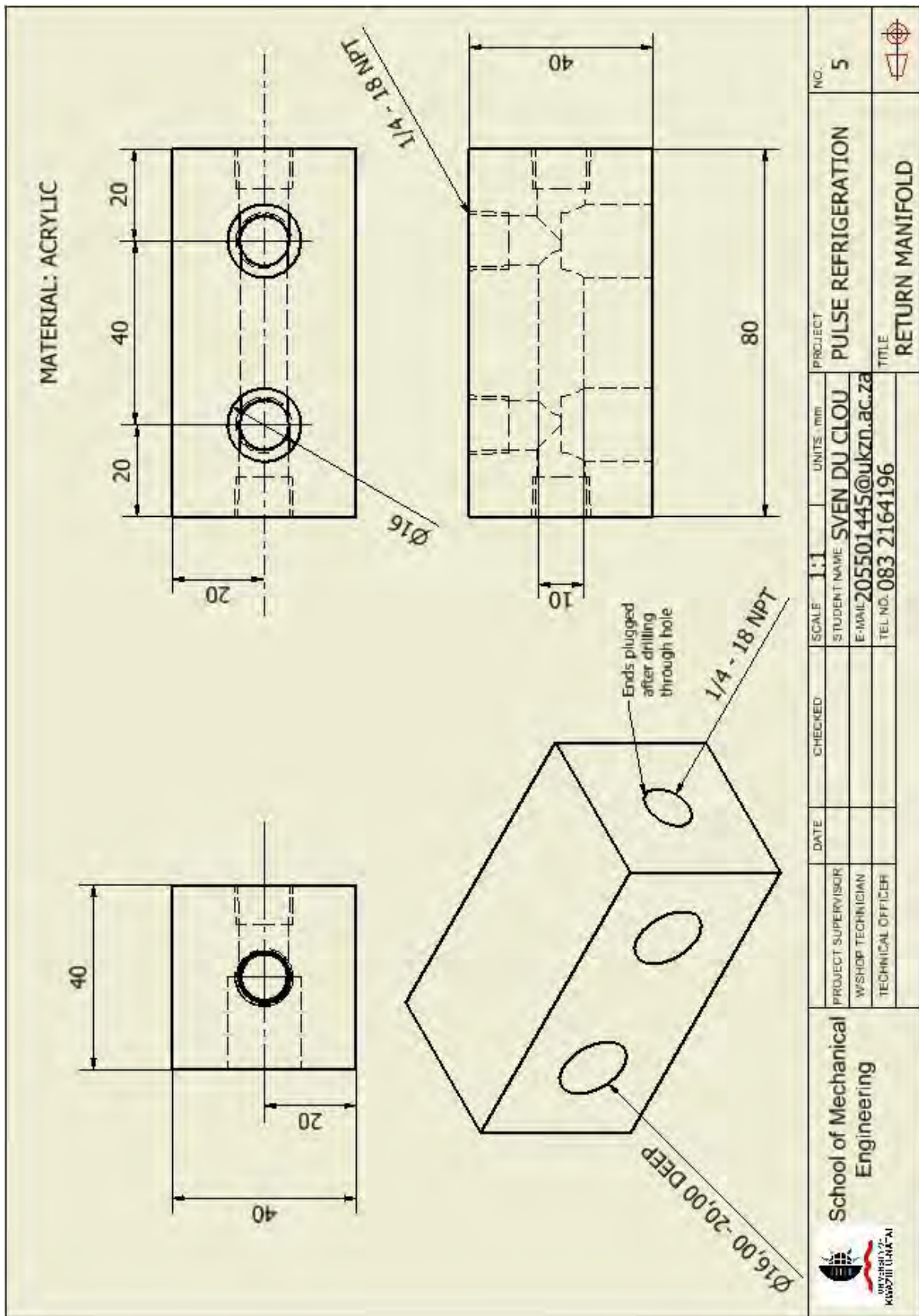
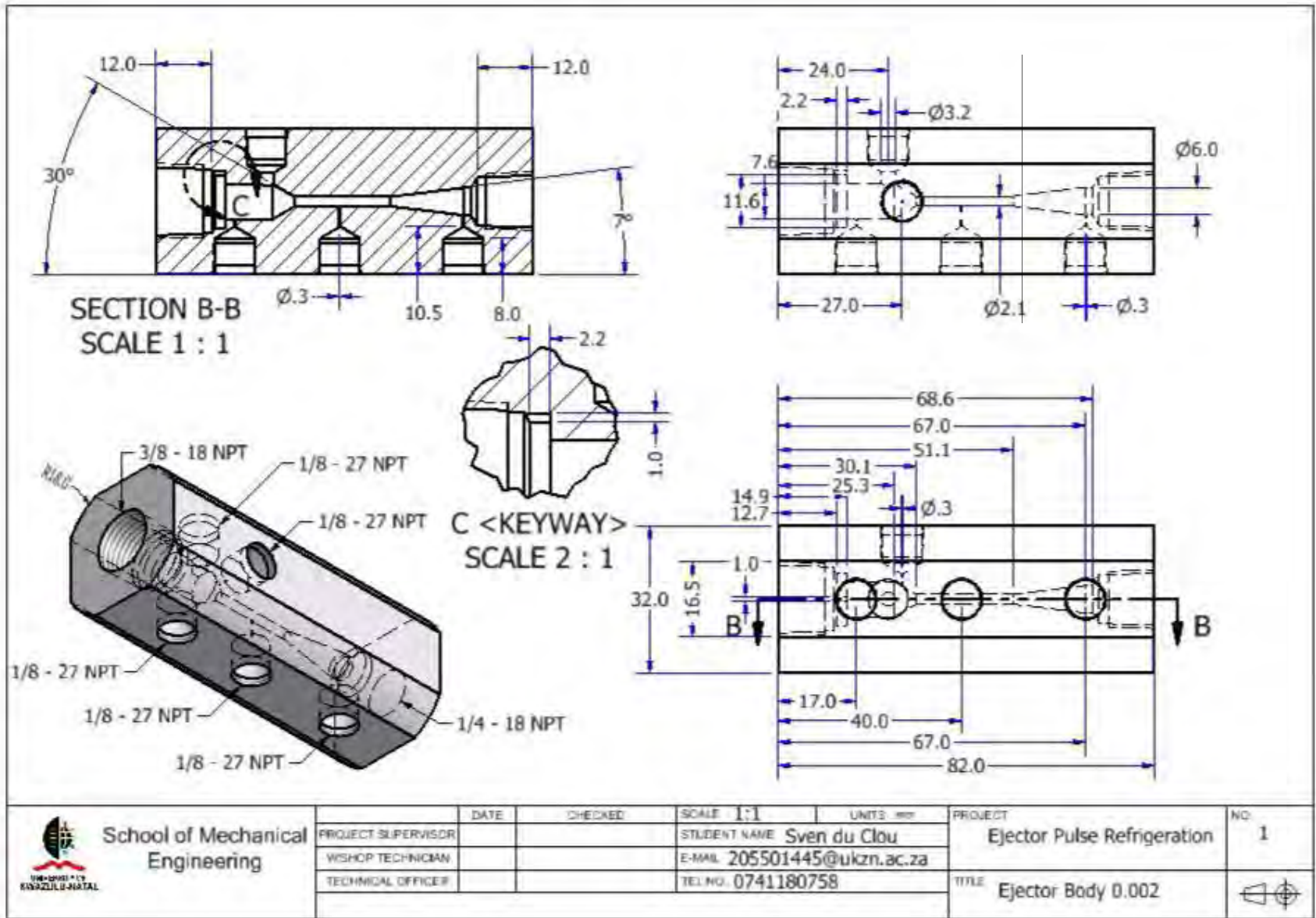


Figure C.8 Condenser return manifold

Figure C.9 Ejector body (design)





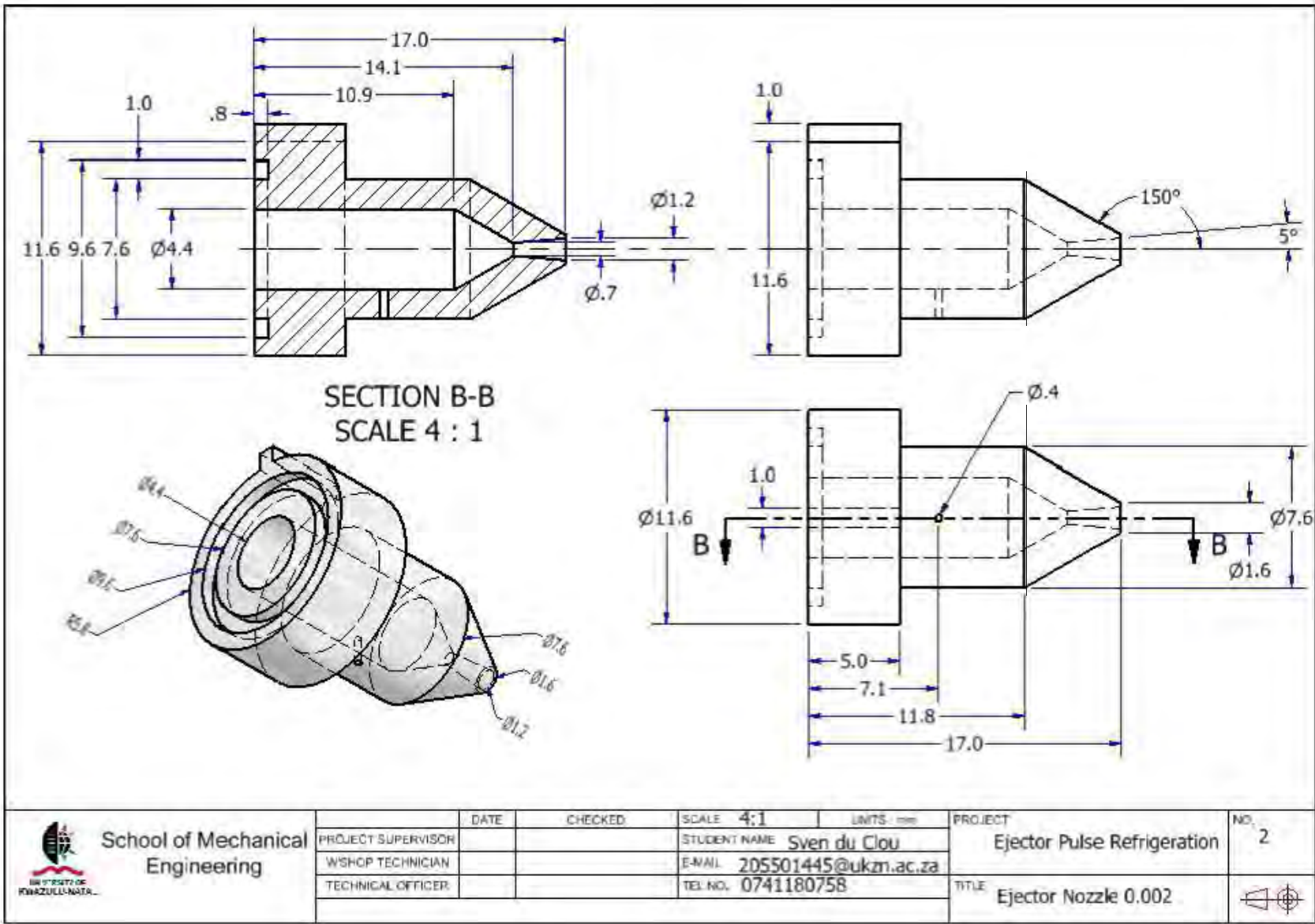
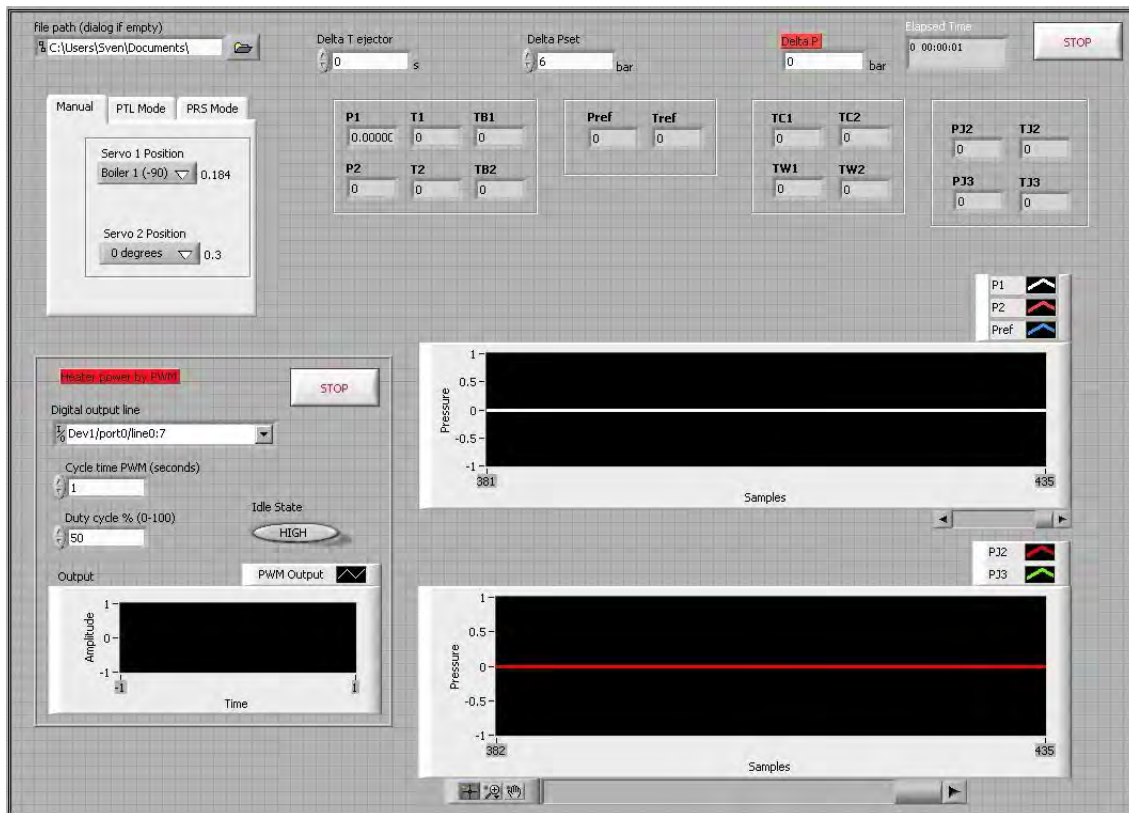


Figure C.10 Ejector nozzle (design)

## D. DATA ACQUISITION SOFTWARE AND HARDWARE

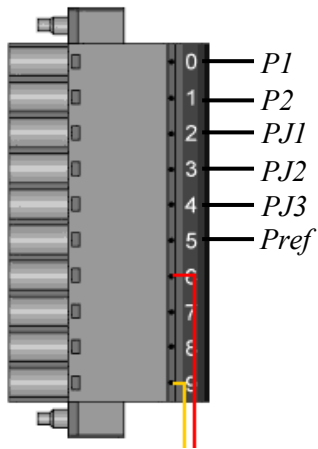
### D.1. LabVIEW GUI



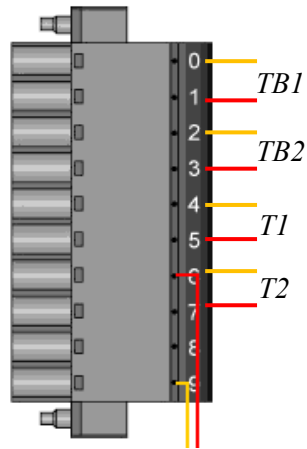
**Figure D.1** LabVIEW GUI. The tabbed control is used to select manual, PTL, or PRS operating modes.  $\Delta P_{set}$  and  $Q$  can be varied on demand. The application .VI is available on the included disk.

## D.2. DAQ chassis and modules

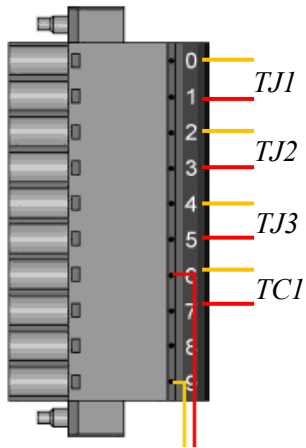
NI – 9203 (Pressure)



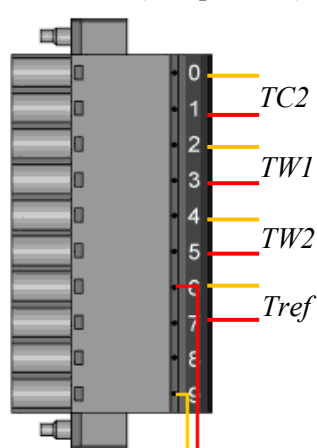
NI – 9211 (Temperature)



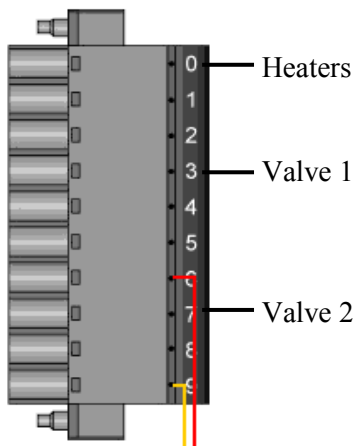
NI – 9211 (Temperature)



NI – 9211 (Temperature)



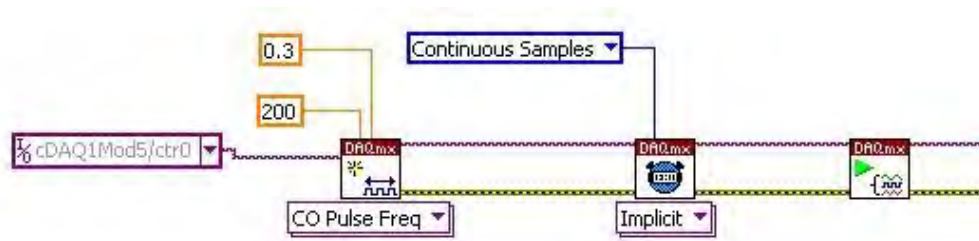
NI – 9474 (Digital output)



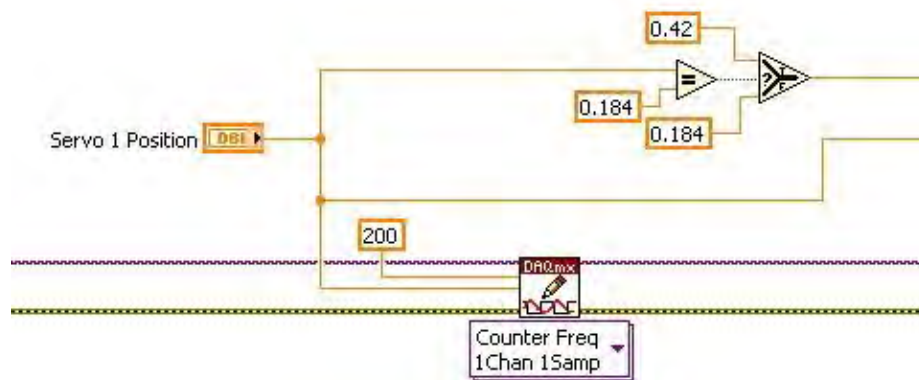
NI Compact DAQ - 9172

Figure D.2 NI module connections and DAQ chassis

### D.3. VI diagrams



**Figure D.3** Generate 200 Hz frequency signal for servo 1 with a 30% duty cycle from the NI 9474 module counter, and start the task. This is repeated for servo 2.



**Figure D.4** Manual servo control with user defined duty cycle. The sub-VI writes the task to the output channel. The logic computes the alternative servo position ( $\pm 90^\circ$ ) which is used in the PTL and PRS automated control logic. This is repeated for servo 2.

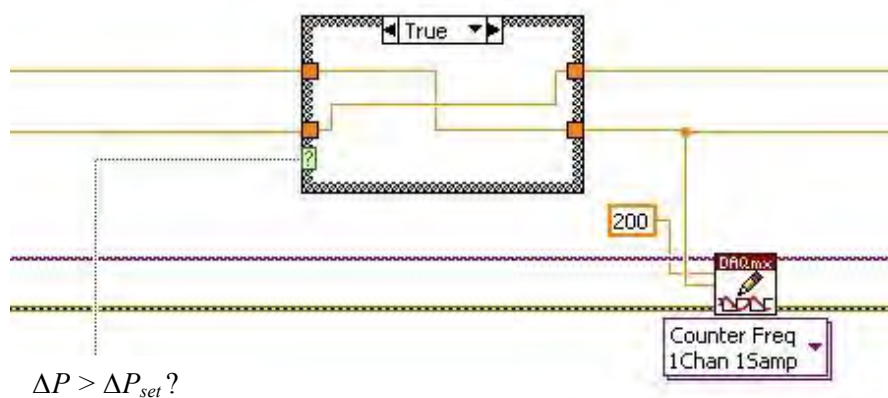
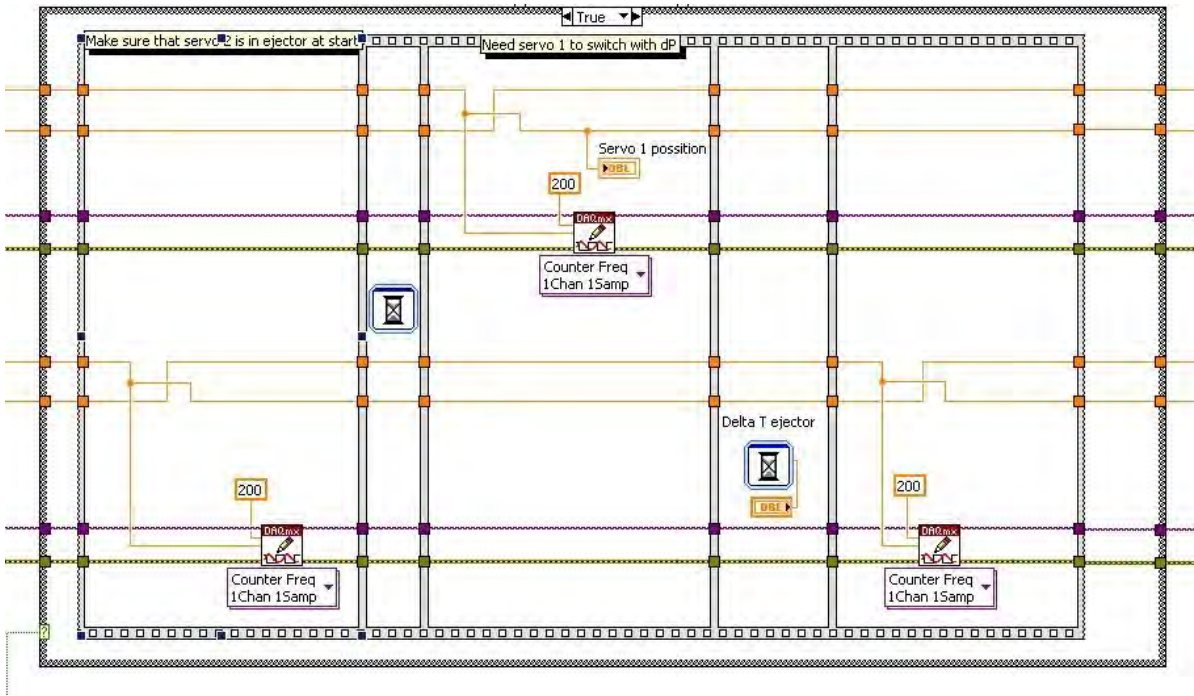
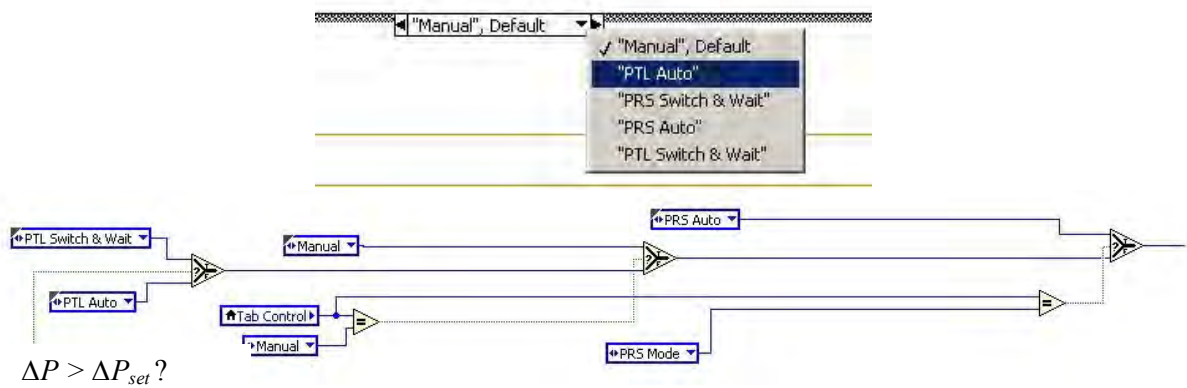


**Figure D.5** PTL automated valve toggling. Writes the new position to the output task and computes the alternative position. The embedded loop only executes when the input is true, ( $\Delta P > \Delta P_{set}$ )



$$\Delta P > \Delta P_{set} ?$$

**Figure D.6** PRS automated valve toggling for variant I, using a flat sequence structure. There are four steps to the sequence when the input condition is true; i) actuate second servo valve to ejector loop, ii) a small time delay is imposed, iii) actuate the boiler servo valve to pulse refrigerant through the ejector loop, iv) a small time delay is imposed and, v) actuate ejector servo valve to allow the latter portion of the pulse to pass through the VTL bypass. The same case structure is applied to variant II with steps i and iii swapped.



$$\Delta P > \Delta P_{set} ?$$

**Figure D.7** Tabbed control is manually selected on the front panel to enable manual, PTL automated or PRS automated operation. The logic structure is used to determine which operating mode is selected. The included switch and wait tabs prevent unwanted valve cycling since  $\Delta P$  may not reduce before the next iteration causing the valve to cycle unnecessarily.



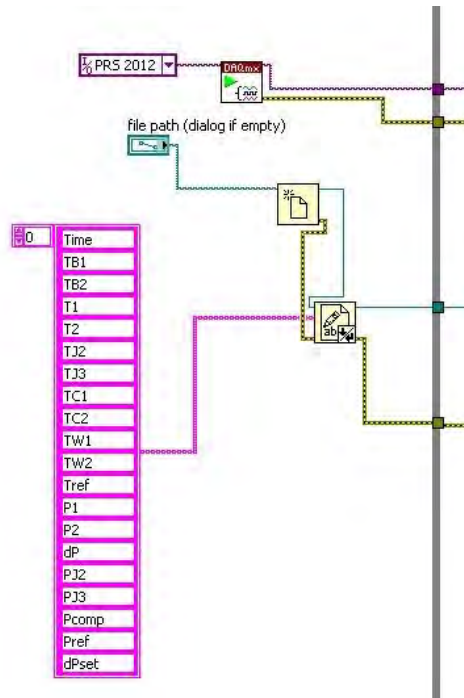


**Figure D.8** The start task acquires and initializes the signals from the DAQ modules. A spreadsheet file is created, opened, and the column labels are assigned. The file is left open to improve the loop iteration speed.

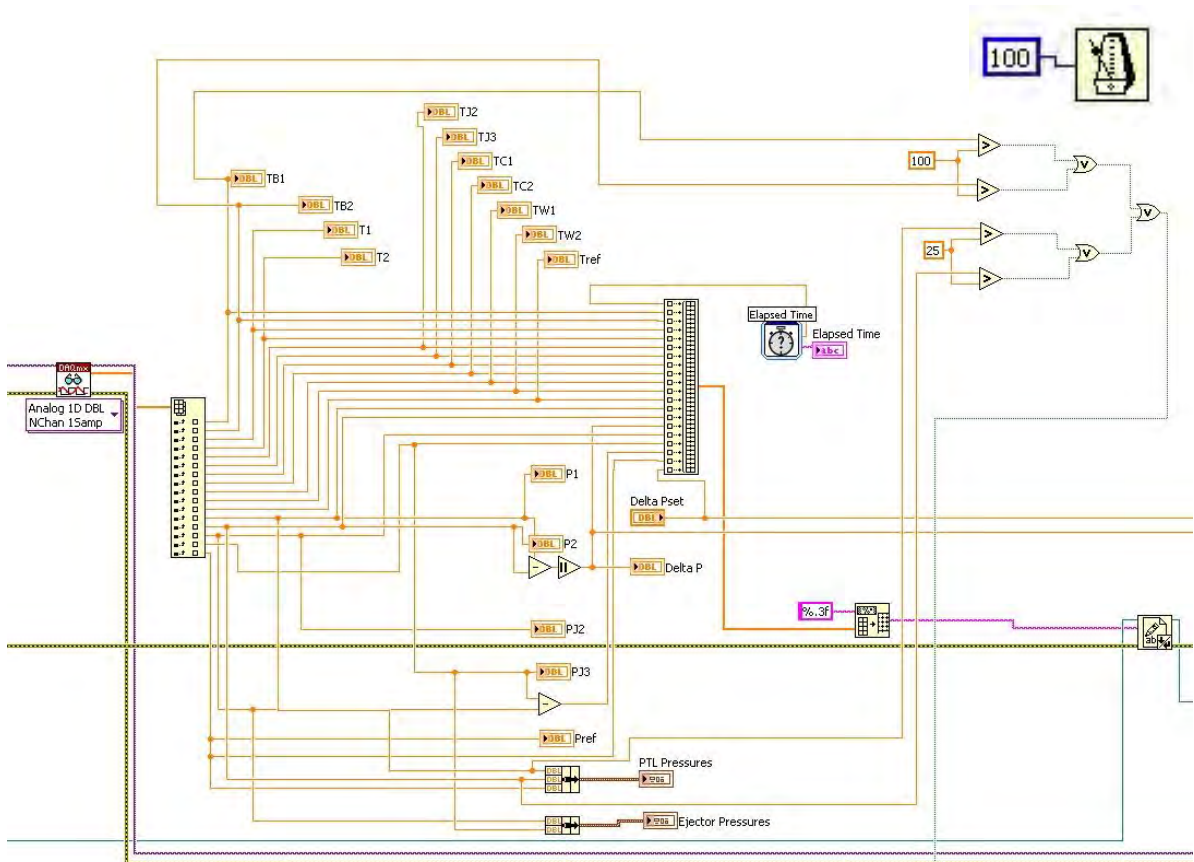


**Figure D.9** Measurement loop. The data are unbundled, displayed, and written to a spreadsheet file at a frequency of 10 Hz.

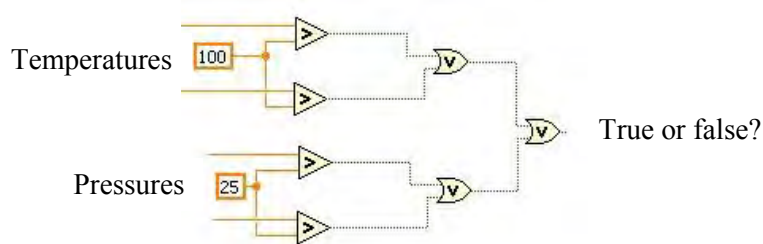


**Figure D.10** Fail-safe logic. The pressure and temperature limits are compared with the real-time measurements. If the output logic is true, the heaters are turned off.

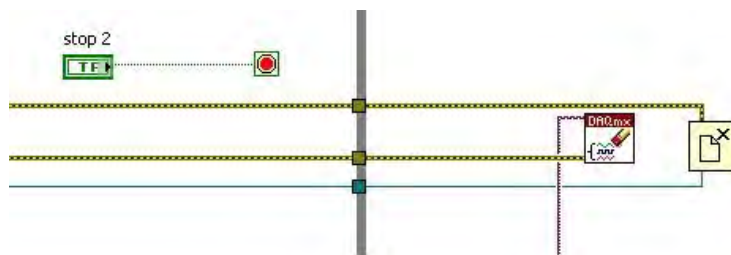


**Figure D.11** The stop button terminates the loop. The tasks are cleared and the spreadsheet file is closed.

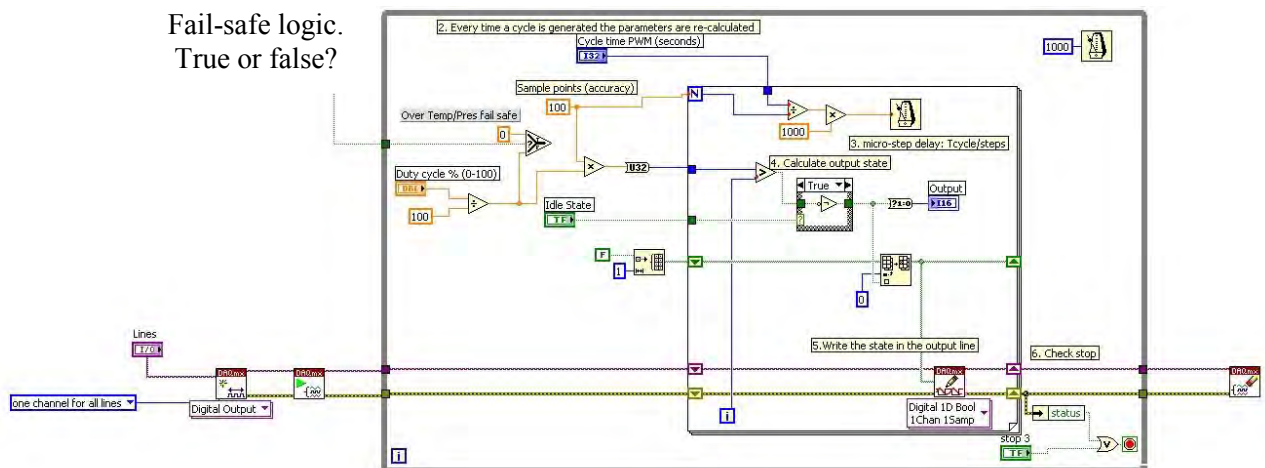
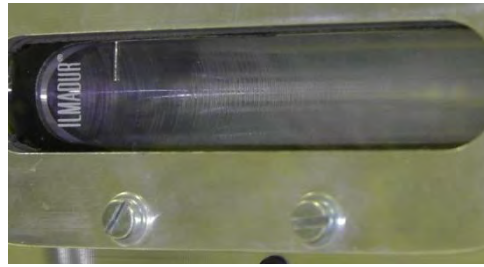


**Figure D.12** Software generated PWM loop for the heater power control.

## E. PHOTOGRAPHY

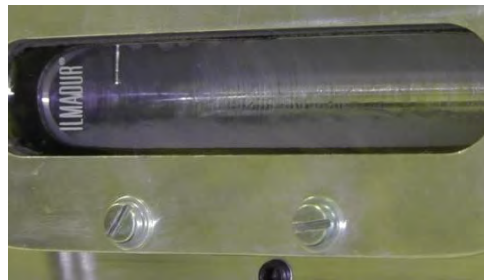
1. Liquid vaporizes as it is injected into the chamber, cooling the block.



2. Liquid injection continues until the  $\Delta P$  reduces to close the inlet check valve.



3. Pool boiling occurs where vapor bubbles form at nucleation sites on the surface.



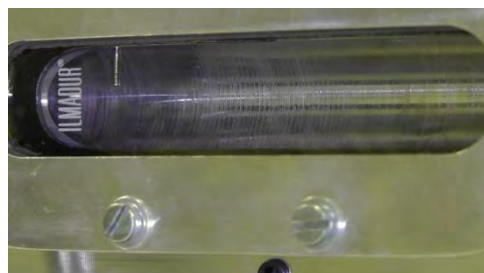
4. Pool boiling may approach the critical heat flux limit where some parts of the surface are exposed to vapor.



5. Pressure increases and the outlet valve opens at  $\Delta P_{set}$ . The refrigerant instantly vaporizes as it expands into the VTL and condenser. The high pressure pulse forces refrigerant into the alternate boiler.



6. The emptied boiler decreases in pressure whilst the alternate boiler pressurizes.



Injection

Boiling & pressurizing

Pulsing

**Figure E.1** Photographs of nominal refrigerant injection, boiling and pulsing. Flow is from right to left. Video of this process is given on the disk in Appendix G.

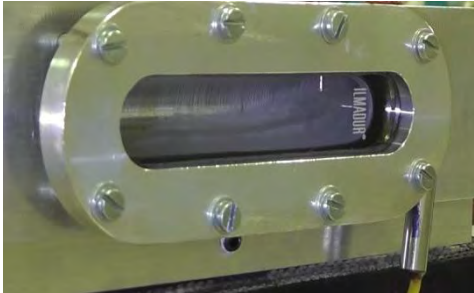
← - - - - - Flow direction - - - - -



1. Liquid vaporizes as it is injected into the chamber, cooling the block.



2. Excess liquid is injected due to the high mass content in the system.



3. Initially, heat transfer is dominated by natural convection. The R-134a liquid level is visible halfway up the sight glass.



4. Pool boiling occurs and small bubbles detach from the surface.



5. Pressure increases and the outlet valve opens at  $\Delta P_{set}$ . The refrigerant slowly vaporizes as it expands into the VTL and condenser. Vaporization is limited due to liquid occupying a greater portion of the loop.



6. The emptied boiler decreases in pressure whilst the alternate boiler pressurizes.



Injection

Boiling & pressurizing

Pulsing

**Figure E.2** Photographs of refrigerant injection, boiling and pulsing with excess mass. Flow is from left to right. Video of this process is given on the disk in Appendix G.

----- Flow direction ----->



**Figure E.3** Pull down resistor of  $10\text{ k}\Omega$  grounds floating signals present in PWM.

Additional photography is available on the included disk.